FZR-430

Wissenschaftlich-Technische Berichte
FZR-430 August 2005 ISSN 1437-322X

U. Rohde, S. Kliem, B. Hemström, T. Toppila,
Y. Bezrukov

The European project FLOMIX-R: Description of the slug mixing and buoyancy related experiments at the different test facilities
Final report on WP 2

Editor: S. Kliem

Forschungszentrum
Rossendorf

Wissenschaftlich-Technische Berichte
FZR-430
August 2005

U. Rohde, S. Kliem, B. Hemström, T. Toppila,
Y. Bezrukov

The European project FLOMIX-R: Description of the slug mixing and buoyancy related experiments at the different test facilities
Final report on WP 2

Editor: S. Kliem

Forschungszentrum
Rossendorf

EUROPEAN COMMISSION
5th EURATOM FRAMEWORK PROGRAMME 1998-2002
KEY ACTION : NUCLEAR FISSION

FLOMIX-R

FIKS-CT-2001-00197

Deliverable D09

Description of the slug mixing and buoyancy related experiments at the different test facilities (Final report on WP 2)

U. Rohde, S. Kliem, B. Hemström, T. Toppila, Y. Bezrukov

Dissemination level :

PU: Public

Content

1 Introduction

The quantitative assessment of the mixing of coolant with different quality inside the reactor coolant system during normal operation or hypothetical accidents is in the focus of experimental and numerical investigations, for several years now. These different quality might be different temperatures, different densities and/or different concentrations of additives. The most relevant additive to the primary coolant in pressurized water reactors (PWR) is boron acid used for the control of reactivity. In some cases, dependent on the scenario of the transient, both temperature and boron acid concentration might be different in the slug mixed with ambient water, in some cases density differences due to temperature gradients can be neglected with respect to mixing.

A slug of lower borated water can be formed in the primary circuit by various mechanisms. Causes might be injection of coolant with less boron content from interfacing systems (external dilution) or separation of the borated reactor coolant into highly concentrated and diluted fractions (inherent dilution).The mixing of these lower borated slugs with water of higher boron concentration is the most mitigative mechanism against serious reactivity accidents in local boron dilution transients, and therefore, is one of the most important, nuclear safety related issues of mixing. Significant advantage in boron dilution transient analysis can be achieved, if realistic mixing data are used ([Gru94], [Kli04]).

The goal of the work described in this report was the experimental investigation of the mixing of coolant with different quality on the way from the cold leg through the downcomer and lower plenum to the core inlet in a systematic way. The obtained data should help in the clarification of the mixing mechanisms and should form a data basis for the validation of computational fluid dynamics (CFD) codes.

For these purposes, experiments on slug mixing have been performed at two test facilities, modelling different reactor types in scale 1:5, the Rossendorf and Vattenfall test facilities. The corresponding accident scenario is the start-up of first main coolant pump (MCP) after formation of a slug of lower borated water during the reflux-condenser mode phase of a small break loss of coolant accident (LOCA). The matrices for the experiments were elaborated on the basis of the key phenomena, being responsible for the coolant mixing during pump start-up [Roh02]. Slug mixing tests have also been performed at the VVER-1000 facility of EDO Gidropress to meet the specifics of this reactor type.

The mixing of slugs of water of different quality is also very important for pre-stressed thermal shock (PTS) situations. In emergency core cooling (ECC) situations after a LOCA, cold ECC water is injected into the hot water in the cold leg and downcomer. Due to the large temperature differences, thermal shocks are induced at the reactor pressure vessel (RPV) wall. Temperature distributions near the wall and temperature gradients in time are important to be known for the assessment of thermal stresses.

One of the important phenomena in connection with PTS is thermal stratification, a flow condition with a vertical temperature profile in a horizontal pipe. The fluid is in single-phase regime unlike in case when the upper part of the pipe is filled with steam, which is not elaborated within this context. Typically a stratified condition builds up, when a low-velocity cold fluid enters to a low-velocity warm fluid in a horizontal pipe. Stable stratification is not particularly dangerous for the pipe itself in structural integrity sense. However, in a real process there are often disturbances that make the temperature boundary to move vertically. Velocity difference between the colder and warmer fluids may also cause wave formation in the temperature boundary. All this may cause thermal fatigue in the pipe. Besides of thermal fatigue, a single thermal shock can also be relevant for structural integrity, if it is large enough, especially in the case, that the brittle fracture temperature of the RPV material is reduced due to radiation embrittlement. Therefore, additional to the investigations of slug mixing during re-start of coolant circulation, the mixing of slugs or streams of water with higher density with the ambient fluid in the RPV was investigated. The aim of these investigations was to study the process of turbulent mixing under the influence of buoyancy forces caused by the temperature differences. Heat transfer to the wall and thermal conductivity in the wall material have not been considered.

Experiments on density driven mixing were carried out at the Rossendorf and the Fortum PTS facilities.

2 Slug mixing experiments at the ROCOM test facility

2.1 Methodology of mixing experiments at ROCOM

The test facility ROCOM (Rossendorf Coolant Mixing Model) was erected for the investigation of coolant mixing in the reactor pressure vessel of PWR. The experiments at ROCOM are carried out with the goal, to measure the time-dependent distribution of the boron concentration inside the complex geometry of the pressure vessel with its internals. The distribution at the inlet into the reactor core is of highest importance. Measurement positions on the way of the coolant from the inlet into the vessel trough the downcomer and the lower plenum serve for the clarification of the phenomena taking place during the mixing processes. Further, all the data can be used to validate theoretical methods for the description of the coolant mixing, especially computational fluid dynamics codes. The boundary conditions for the experiments are the coolant flow rates in the loops of the test facility and the boron concentration at the different inlet nozzles. These boundary conditions can be constant or even time-dependent.

It is assumed, that the transport of the boron with the coolant can be described by the transport equation for a scalar. A scalar is a quantity, spread by fluid convection and diffusion in a fluid without feedback from the scalar concentration to the fluid properties, like e.g. density or viscosity. In the test facility as well as in the original reactor, the flow is turbulent. At turbulent flow regimes, the transport of a scalar is determined by the turbulent dispersion, the corresponding molecular diffusion of the boron plays a secondary role. Therefore it is possible, to replace the mixing of the boron by the mixing of a tracer, which is solved in the coolant of the test facility as the boron in the coolant of the original reactor. Sodium chloride is used as tracer in the test facility. The concentration is determined by measuring the conductivity. In the experiments, a maximum conductivity of 200 µS/cm is used. At that low concentrations, the direct proportionality of conductivity and concentration is ensured.

The time dependent distribution of the tracer concentration C(x,y,z,t) is transformed into a dimensionless mixing scalar θ(x,y,z,t) by relating it to a lower and an upper reference value. The conductivity of the coolant in the facility before the experiment serves as lower reference value C_0 in most of the cases. The determination of the upper reference value C_1 depends on the type of the carried out experiment. The conductivity of the injected salt tracer solution is used in some experiments. In other experiments the maximum conductivity measured at the inlet into the vessel or the time and spatially averaged conductivity at the sensor in the inlet nozzle serves as upper reference value. Due to the proportionality between concentration and conductivity, the dimensionless mixing scalar is calculated according to:

$$\Theta(x,y,z,t) = \frac{C(x,y,z,t) - C_0}{C_1 - C_0} = \frac{\sigma(x,y,z,t) - \sigma_0}{\sigma_1 - \sigma_0} \qquad \text{(Equ. 2.1.1)}$$

The distribution of the boron concentration can be derived using:

$$C_B(x,y,z,t) = \Theta(x,y,z,t) \cdot (C_{B,1} - C_{B,0}) + C_{B,0} \qquad \text{(Equ. 2.1.2)}$$

Hereby, $C_{B,1}$ and $C_{B,0}$ are the corresponding reference values for the boron concentration of the slug and the ambient coolant. The mixing scalar is obtained at discrete positions in the geometry of the test facility determined by the geometry and the arrangement of the measurement devices.

It is worth to be noted, that in the turbulent flow field, temperature differences between different parts of the coolant can be treated in a similar way as difference in boron concentration or salt concentration. The mixing of water with different temperature is based on the same microscopic turbulent exchange. Therefore, the coolant mixing during i.e. overcooling transients can be described on the basis of the mixing scalar determined in the ROCOM experiments. This assumption is true unless density differences in the coolant do not feed back onto the velocity field. The experience showed, that fully developed natural circulation flow and flow conditions at running pumps are sufficient to fulfill this requirement.

2.2 Facility

2.2.1 Design

ROCOM is a 1:5 model of a PWR of German KONVOI type. The test facility was designed for the investigation of a wide spectrum of mixing scenarios.

The design parameters of the test facility are presented in the following table together with the data of the original reactor.

Tab. 2.1 Comparison original PWR - ROCOM with water at 20°C

Value	**Unit**	**Reactor**	**ROCOM**
Inner diameter of the vessel	mm	5000	1000
Height of the pressure vessel	mm	~12 000	~2400
Inner diameter of the inlet nozzle	mm	750	150
Width of the downcomer	mm	315	63
Coolant flow rate per loop	$\frac{m^3}{h}$	23 000	350 (max.) 185 (nominal)
Coolant inlet velocity	m/s	14.5	5.5 (max.) 2.91 (nominal)
Velocity in the Downcomer	m/s	5.5	2.1 (max.) 1.1 (nominal)
Reynolds-number in the inlet nozzle	-	$8.4 \cdot 10^{7}$	$8.3 \cdot 10^{5}$ (max.) $4.4 \cdot 10^{5}$ (nominal)
Re Downcomer	-	$2.7 \cdot 10^{7}$	$2.6 \cdot 10^{5}$ (max.) $1.4 \cdot 10^{5}$ (nominal)
Re Reactor/Re ROCOM	-	1	~100 (max.) ~190 (nominal)
Travelling time Reactor/ROCOM	-	1	1 (nominal)

The pumps were limited to a pressure head of 15 m at a maximum flow rate of 350 m^3/h due to the use of acrylic glass for the vessel. At these conditions, the Reynolds-numbers in the test facility are smaller by a factor of 100 in comparison to the original reactor. The Reynolds-number in the downcomer, where it is the smallest one, is $2.6\ 10^{5}$. That means, the flow is turbulent. Only for flow rates of 3 – 5 m^3/h the Reynolds-number belongs to the laminar-turbulent transition region. Such regime are partly present in the beginning of a pump start-up experiment or during the simulation of natural circulation conditions.

For the used scale of 1:5, transferability of experimental results to reactor conditions was investigated extensively [Hoe98,Hoe99]. It was found on the basis of numerical scale-up investigations, that the influence of the scaling is negligible in the turbulent flow regimes. The results of mixing experiments at original reactors, i.e. at different power plants with VVER-440 reactors were used in these transferability analysis, too.

These experimental results are in good agreement with stationary mixing experiments at an air-operated model of this reactor carried out by Dräger [Dra87]. That can be assessed as a proof of the transferability.

2.2.2 Reactor pressure vessel

The reactor pressure vessel is made from acrylic glass. It is shown in Fig. 2.2.1 and Fig. 2.2.2. To have free access to the downcomer region, the vessel was manufactered as three parts. The reactor core itself is represented by a hydraulic resistance of the fuel elements, only. A core basket consisting of 193 aluminium tubes is inserted being a hydraulic short circuit between core inlet and outlet. In the current design, the model of the pressure vessel is equipped with a plane vessel head, which can be replaced by a spherical head according to the original reactor. The upper plenum does not contain any internals. Mixing in the upper plenum was no subject of investigations in the FLOMIX-R project.

The cylindrical part of the vessel consists of two half shells from acrylic glass with a thickness of 20 mm. They are glued along the longitudinal joints and are centered by glued flanges, also made from acrylic glass. The spherical bottom is connected to the lower end and the nozzle region to the upper end by similar flanges. Only the flanges itself and the vessel head are connected by steel bolts. The sieve drum in the lower plenum (to be seen on Fig. 2.2.1) consists of a removable annulus with all holes and cut-outs according to the original one. It is made from acrylic glass, too. Above the sieve drum, the lower core support plate is located being the basis for the 193 fuel elements in the original reactor. This plate (Fig. 2.2.3) has a thickness of 106 mm and consists of different plates connected by glue and bolts.

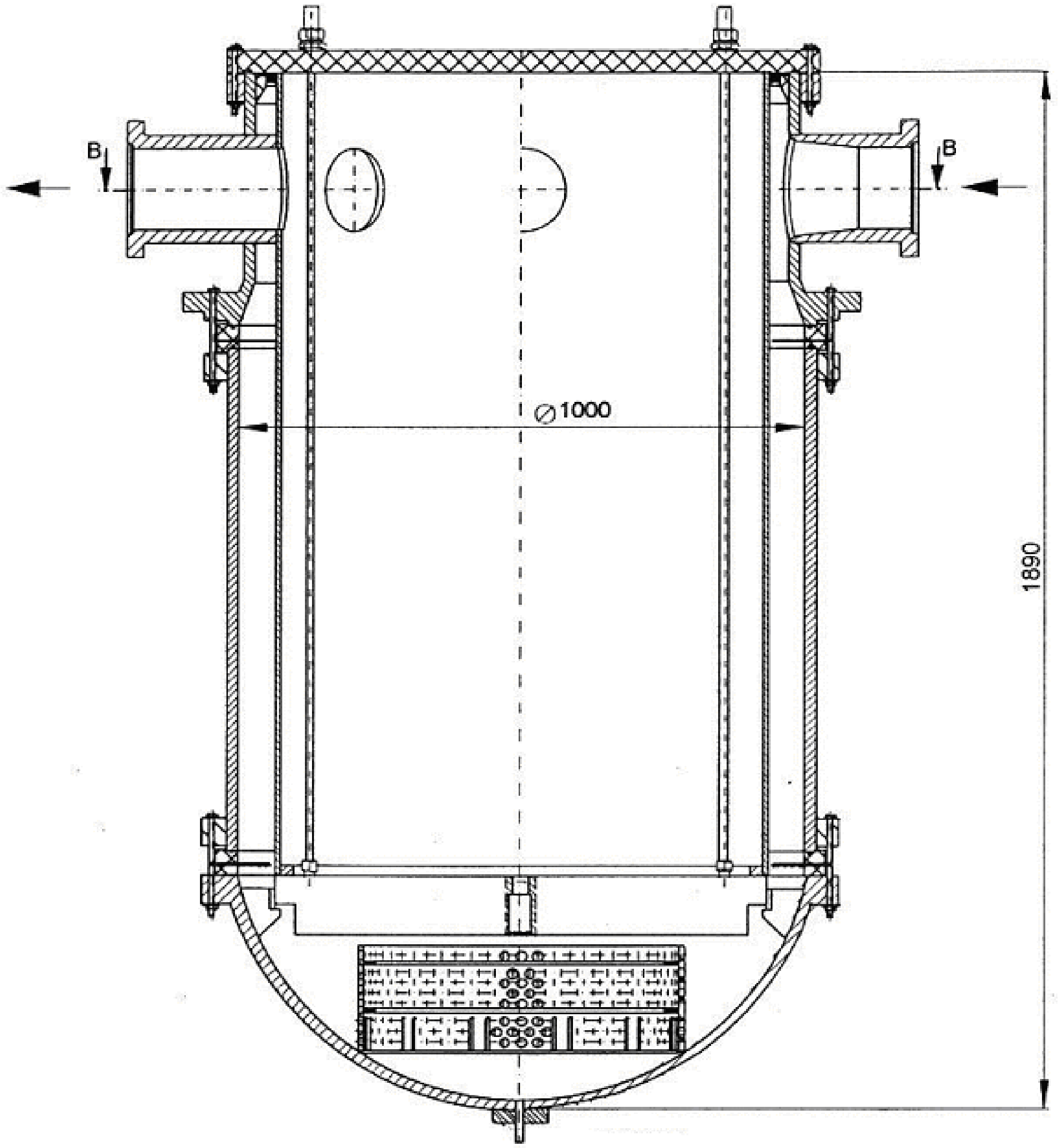

Fig. 2.2.1 Model of the reactor vessel, vertical section

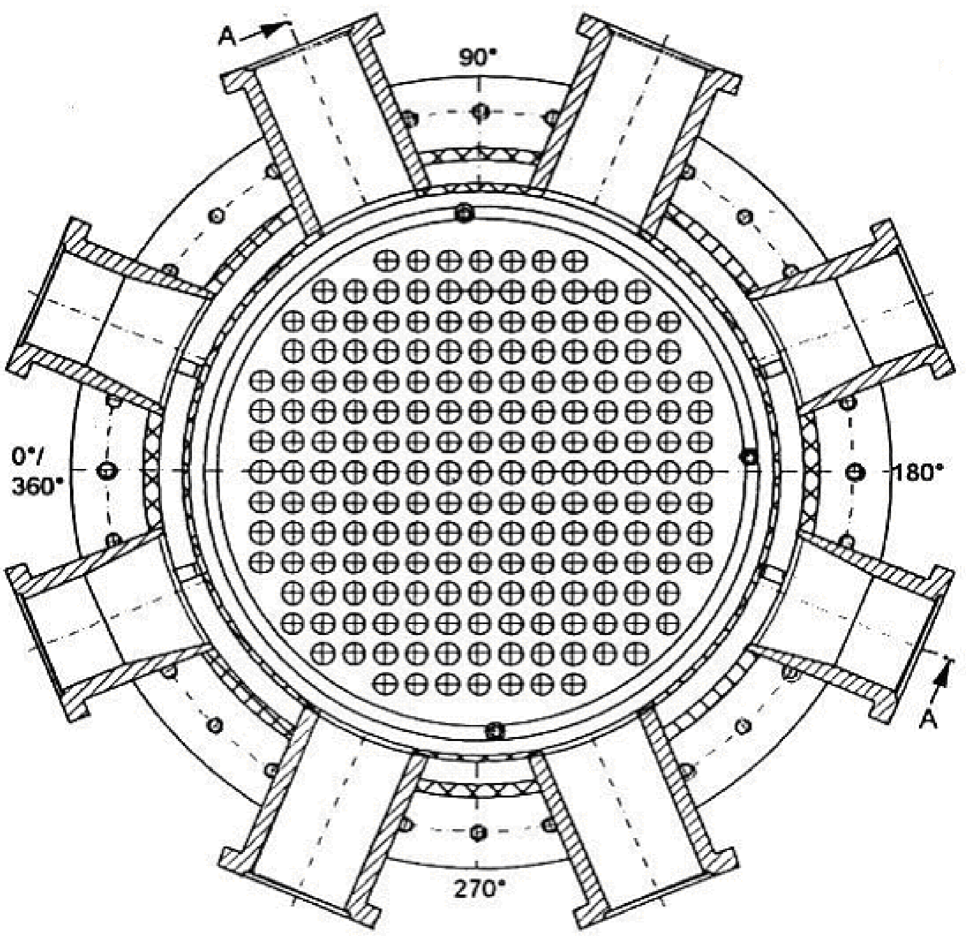

Fig. 2.2.2 Model of the reactor vessel, transverse section in the nozzle region

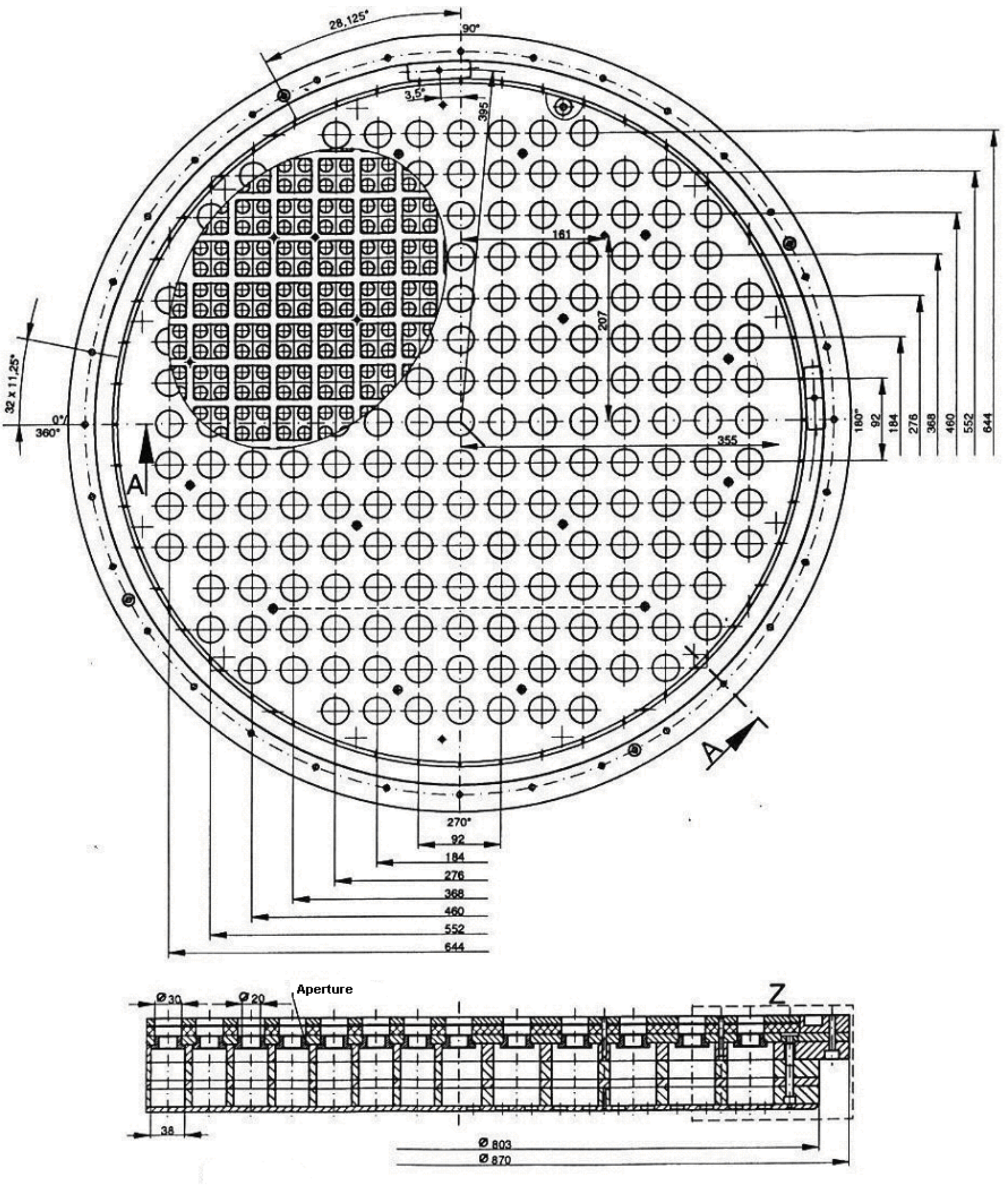

Fig. 2.2.3 Model of the lower core support plate

The penetrations for the coolant flow to the fuel elements are made according to the original reactor. A detail is shown on Fig. 2.2.4. At the position of the entry into each fuel assembly, an orifice with a diameter of 30 mm is located, containing one measurement position of the integrated core inlet wire mesh sensor. At these positions, additional apertures are inserted to adjust the hydraulic resistance of the fuel elements to the values of the original reactor.

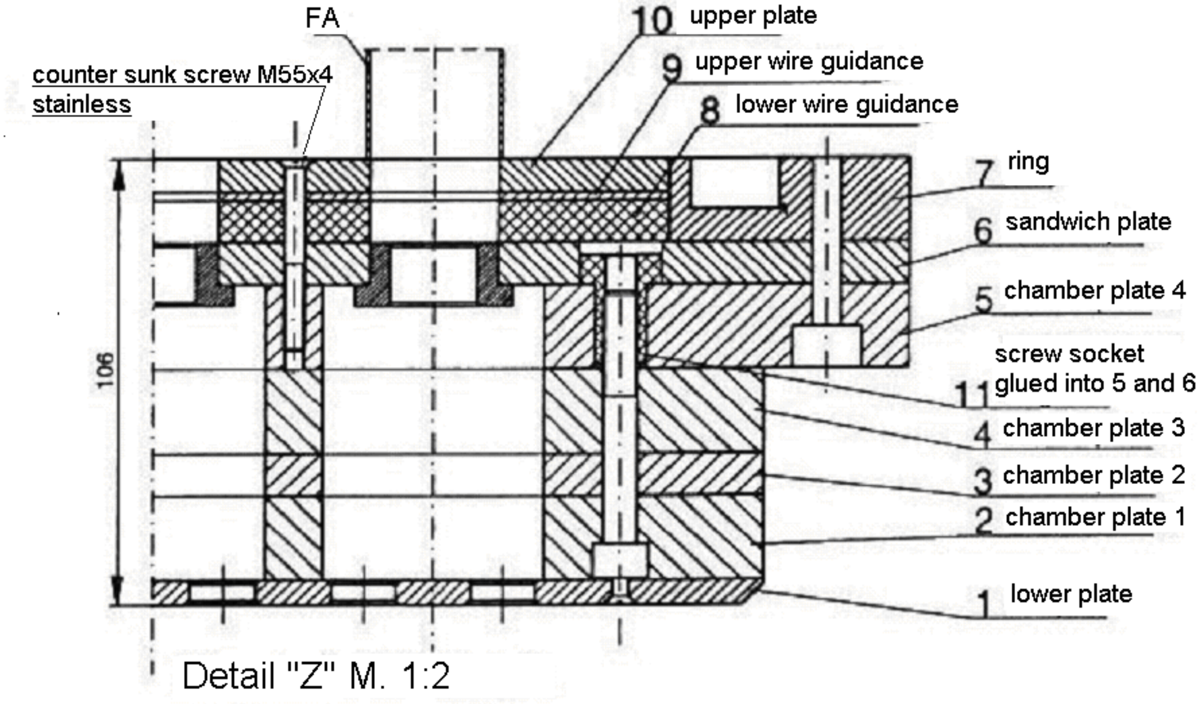

Fig. 2.2.4 Model of the lower core support plate, Detail: Coolant flow into the fuel assembly

The two sensors in the downcomer are located between the flanges connecting the cylindrical part of the vessel with the lower plenum and with the nozzle region. The reactor inlet sensor is situated in the cold leg 1 (position 22.5°) just before the inlet nozzle. Working principle and construction of the sensors is described in chapter 2.3. Fig. 2.2.5 shows the main dimensions of the test facility and the positions of the wire mesh sensors.

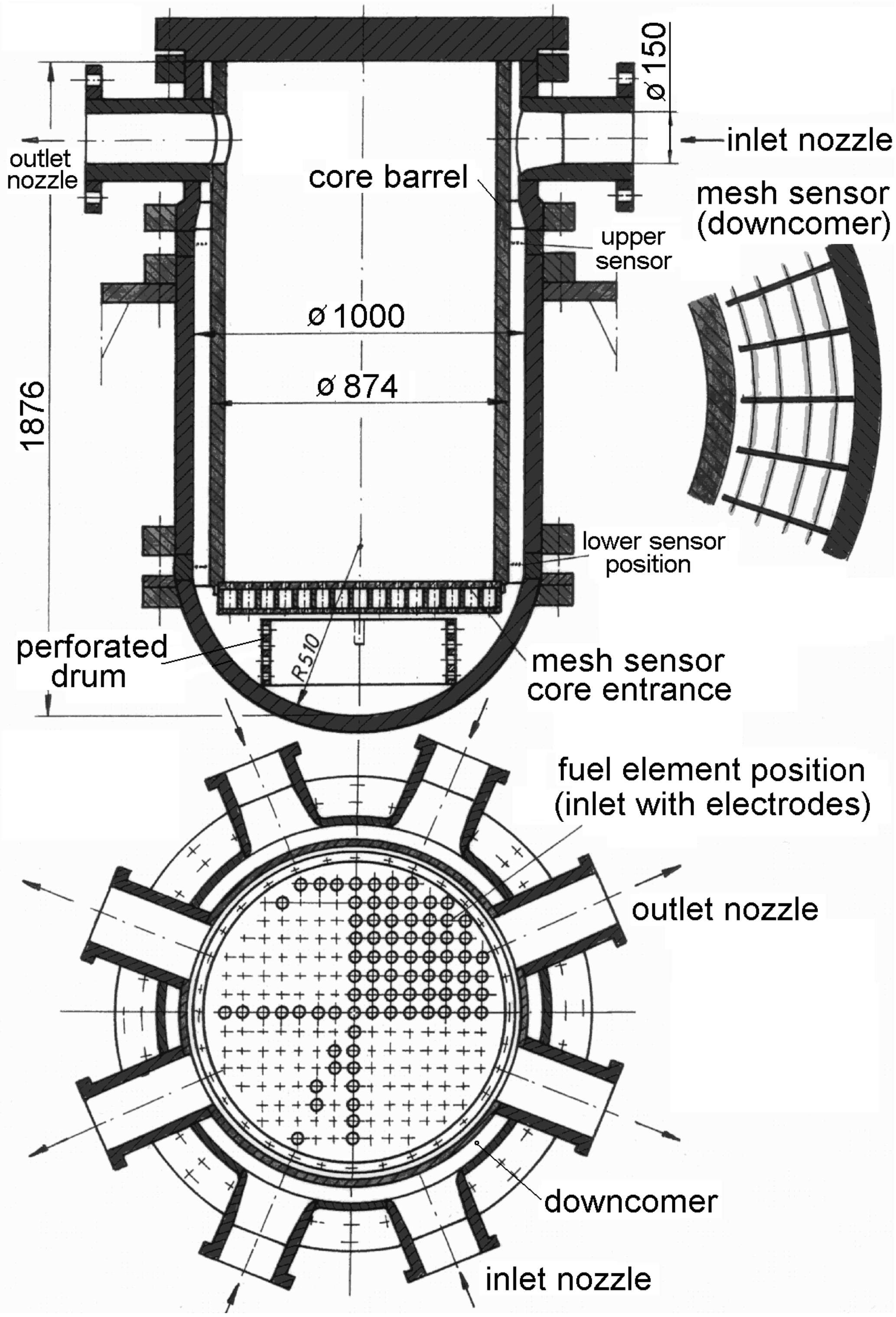

Fig. 2.2.5 Scheme of the model of the vessel with positions of the wire mesh sensors

2.2.3 Circuit

ROCOM is equipped with four loops (Fig. 2.2.6) with a speed controllable circulation pump in each of them. These circulation pumps are controlled by individual frequency transformers. That allows to realize nearly any desired combination of flow rates in the single loops, starting from natural circulation conditions up to nominal and even higher flow rates.

Each loop has a gate valve, mounted at the outlet of the corresponding pump. Further, each loop is equipped with a cylindrical reservoir simulating the steam generator. The reservoir of loop 4 is open to the environment and serves for the pressure equalization.

The geometry of the loops can be seen from Fig. 2.2.6, and the realization in Fig. 2.2.7. The pipes are made from polyvinyl chloride (PVC) with an inner diameter of 150 mm and a rated pressure of 1.0 MPa. It was not possible to keep the full similarity of the loops with the original due to special requirements of the used pumps and the flow meters. The boundary of full similarity between original reactor and test facility is located behind the first bends in the cold and in the hot legs closest to the vessel. That means, these bends are included into the similar representation of the original reactor in the given scale. The volume ratio of vessel and loop is identical between test facility and original reactor to ensure identical coolant travelling times. The total water volume of the test facility is 3.05 m^3.

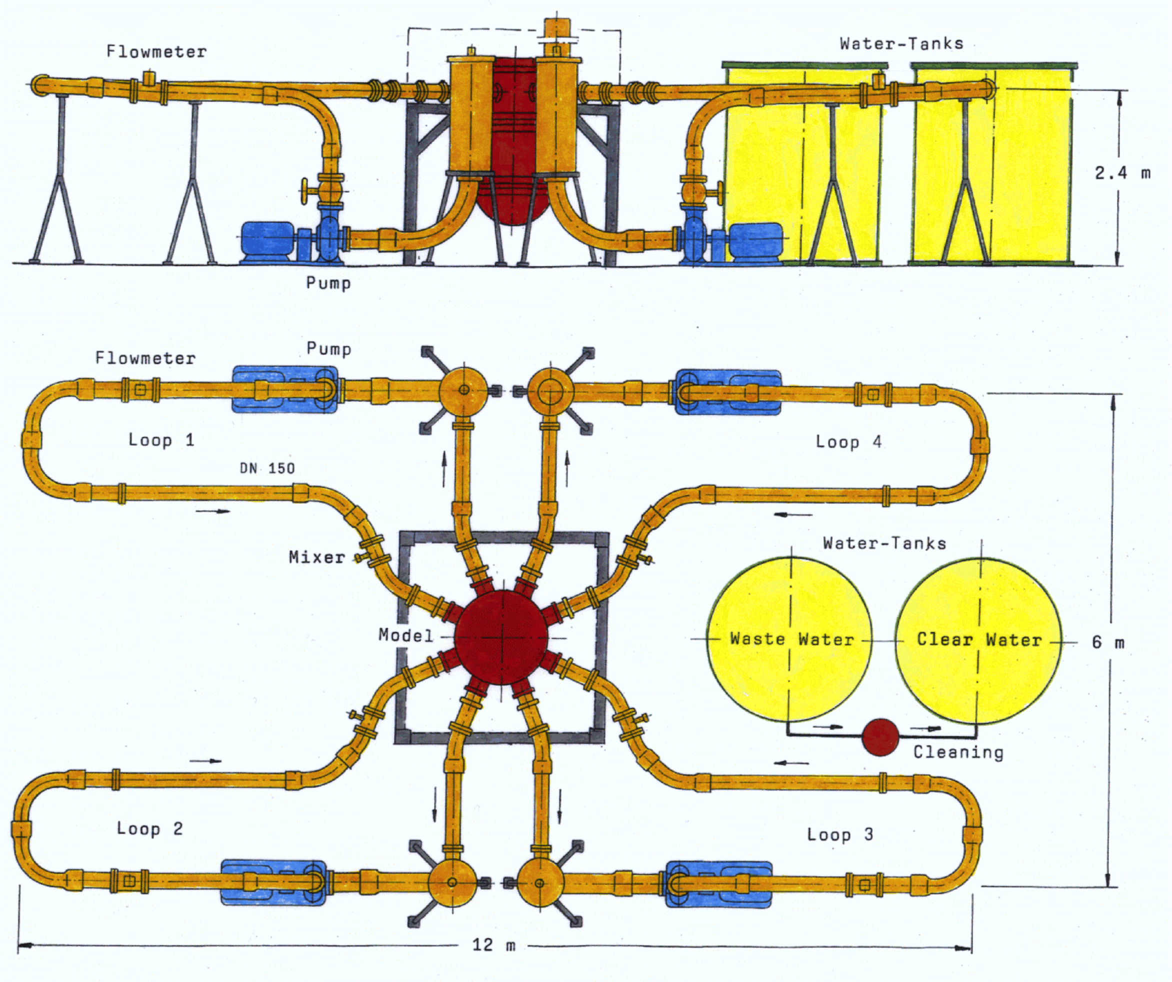

Fig. 2.2.6 Sketch of the ROCOM test facility

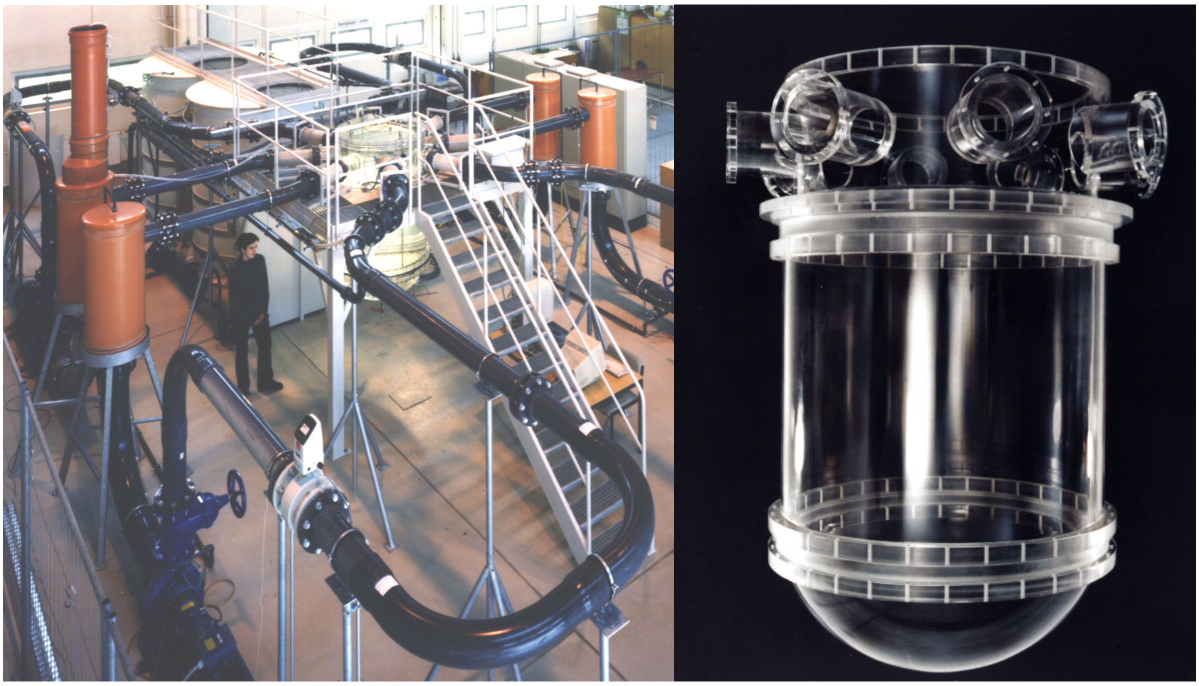

Fig. 2.2.7 View of the test facility and the model of the pressure vessel

2.2.4 Auxiliary systems

A number of auxiliary systems is installed for the proper operation of the test facility. These are a pure water tank and waste water tank made from PVC with a volume of 8 m^3 each of them, pumps for the water supply system and the cleaning system. For the cleaning of the water, an ion exchanger is used. For the cleaning of the test facility inventory (3.05 m^3) about 3 hours are necessary.

As described above, the installed wire mesh sensors measure the local conductivity of the water. Water with a higher content of salt (sodium chloride) is injected into the test facility through a special injection system (Fig. 2.2.8), equipped with two pneumatic valves. The activation of the pneumatic valves is controlled by a special computer program. This program is embedded into the program which controls the wire mesh sensor data acquisition. That ensures an accurate assignment of measurement data and tracer injection, what also allows the superposition of experimental runs with identical boundary conditions. Opening and closing time can be given with an accuracy of 0.005 s.

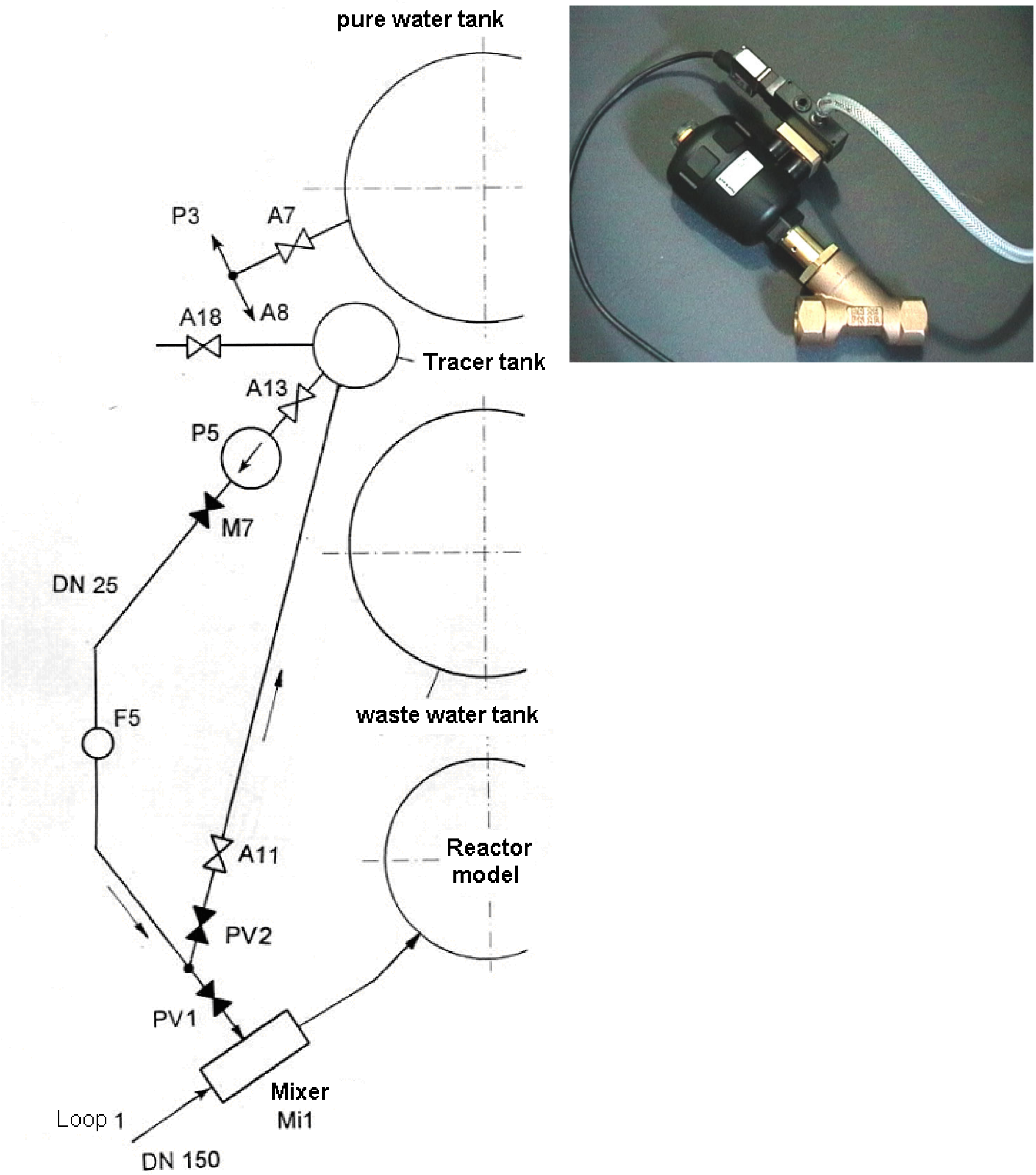

A: Scheme of the injection system

B: View of the pneumatic valve (pos. PV1)

Fig. 2.2.8 Injection system

A mixing device (Fig. 2.2.9) is installed in the loop 1 at the position of the tracer injection. This mixer consists of a pipe with an inner diameter of 25 mm, which is introduced into the loop perpendicularly. Five small pipes with an inner diameter of 10 mm are arranged across the pipe. The are made from stainless steel. As can be seen from Fig. 2.2.9, the tracer enters the small pipes through 4 holes with an diameter of 5 mm. From there, and also from the entry pipe, the tracer mixes into the main coolant flow through altogether 98 holes with a diameter of 2.5 mm. The holes are arranged in such a way, that an uniform distribution of the tracer according to the existing velocity profile is reached. Corresponding measurement results confirm that assumption for long term as well as for short term injection of tracer. The installed mixing device proved successful, because it provides sharp concentration edges, especially at high volume flow rates.

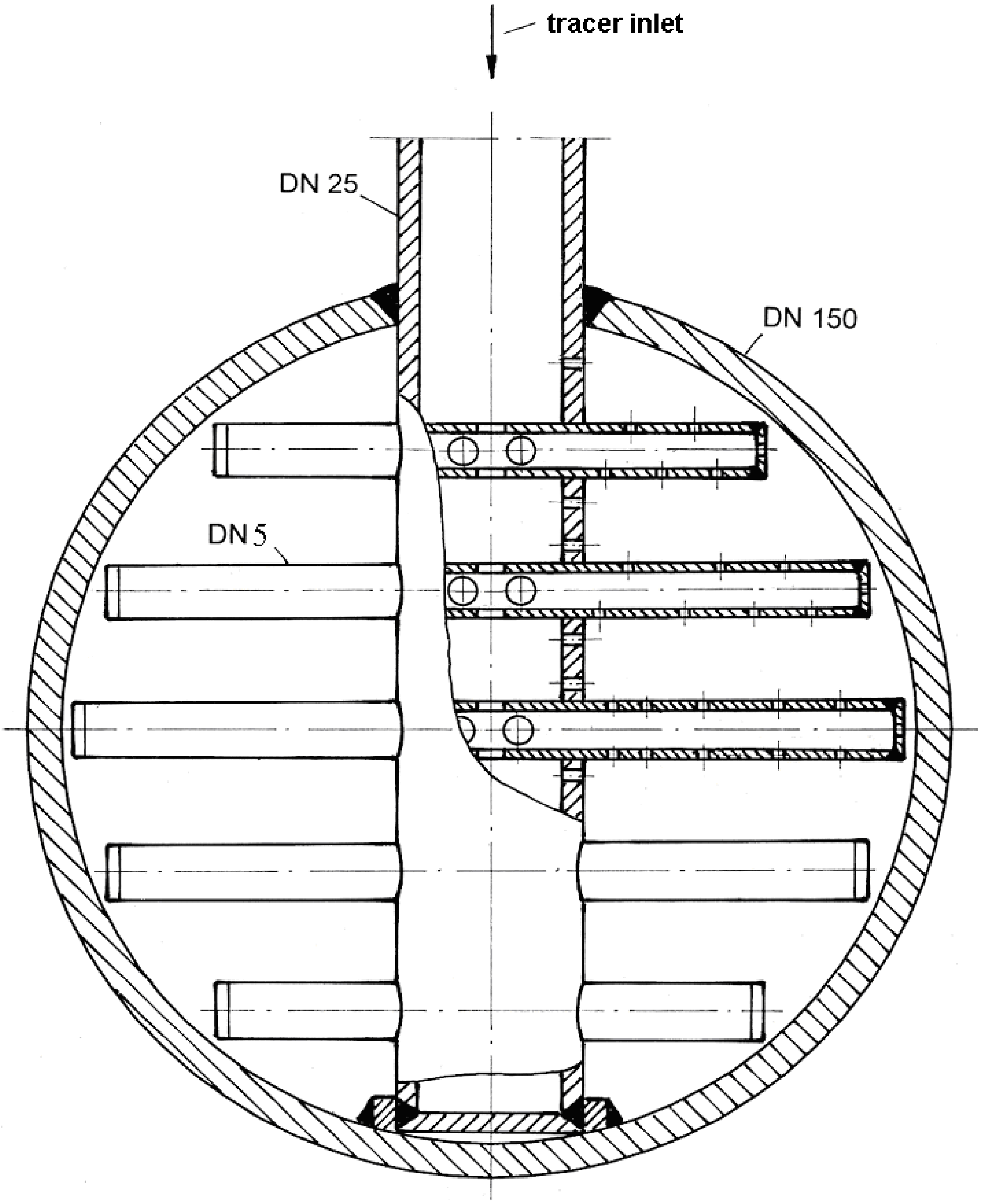

Fig. 2.2.9 Mixing device of the test facility

2.3 Measurement Technique

2.3.1 Wire mesh sensors

The distribution of the conductivity in the test facility is measured by special wire mesh sensors, developed by FZR for the investigation of coolant mixing.

The wire mesh sensor realizes the measurement of the instantaneous local conductivity of the medium in its vicinity. It consists of two planes of electrodes, being a mesh in the flow cross section. The planes are located in short distance one from each other, in most of the cases. The angle between the electrodes is 90°, mainly. All electrodes are insulated against each other and against the wall of the facility and the wall of the sensor base itself. The electrodes of the first plane (transmitter) are provided with short voltage pulses, consecutively. At each single electrode of the second plane (receiver) a current is formed, being directly proportional to the conductivity of the medium in the vicinity of the measuring position. These currents are registered, submitted and stored on a data acquisition PC. Special measures are introduced to avoid crosstalks between the electrodes as well as electrolysis and polarization. The measured values represent directly the electrical conductivity at each measurement position, formed at the cross of one transmitter and one receiver electrode.

The data acquisition unit of the ROCOM test facility contains altogether 32 driver for transmitter electrodes and 32 input positions for the receiver electrodes. At all, 1024 measurement positions can be realized with this unit. The available positions were distributed onto four different sensors with 16x16 measurement positions in each of them. Two sensors each share the use of either 16 receiver or 16 transmitter positions.

The data acquisition unit is connected to a PC by a special ISA-Bus parallel interface for data storage purposes. That configuration allows a maximum measurement frequency of 300 Hz. In the experiments carried out in the frame of the FLOMIX-R project, the measurement frequency was 200 Hz. 10 successive measurements were averaged and the data were stored. In that way, the effective measurement frequency was 20 Hz.

2.3.1.1 Construction of the wire mesh sensors

Wire mesh sensor in the cold leg nozzle

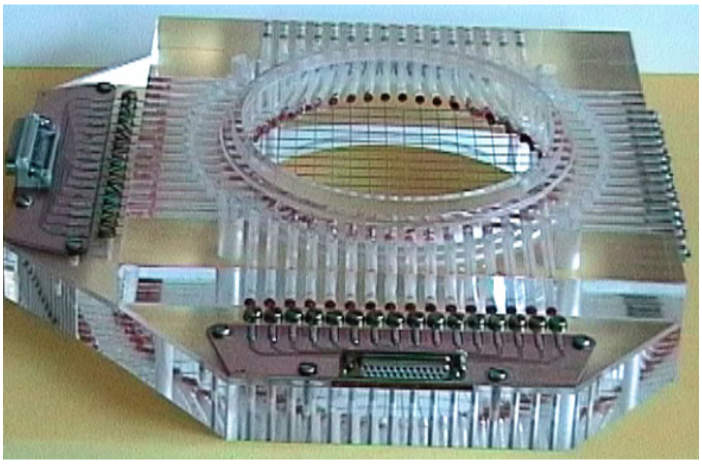

Fig. 2.3.1 Wire mesh sensor for the inlet nozzle (2 x 16 electrodes)

The sensor in the inlet nozzle consists of two planes of electrodes arranged perpendicularly to each other, each of them consisting of 16 wires with a diameter of 0.5 mm. The distance between the two planes is 2.0 mm and the pitch between two parallel wires is 8.9 mm. This pitch determines the spatial resolution. The wires are made from stainless steel and put into a frame of acrylic glass. The frame has an inner diameter of 150 mm, what corresponds to the diameter of the cold leg at the test facility. The sensor is mounted between two flanges connecting the loop with the nozzle of the reactor pressure vessel. Hereby, the electrodes are positioned in an angle of 45° oriented to the horizontal. The sensor has 256 measurement positions. Due to the construction of the frame, some of the measurement positions do not belong to the flow cross section. Altogether 216 measurement positions are located inside the free flow area.

Wire mesh sensors in the downcomer

In the downcomer of the test facility, two identical sensors are located (Fig. 2.3.2). They are situated at the positions, where the central part of the vessel is flanged to the upper and lower construction elements. The base of the sensors is a ring made from acrylic glass, whose inner diameter corresponds to the inner diameter of the vessel. These rings fit into the flanges of the vessel. The transmitter electrodes are represented by 64 radial fixing rods with a diameter of 3 mm, mounted into the ring with a pitch of 5.625°. The rods are provided with orifices for four circular electrode wires. Rods and wires are separated electrically by small ceramic insulation beads. The pitch in radial direction is 13 mm. The 4x64 measurement positions form a 16x16 measuring matrix.

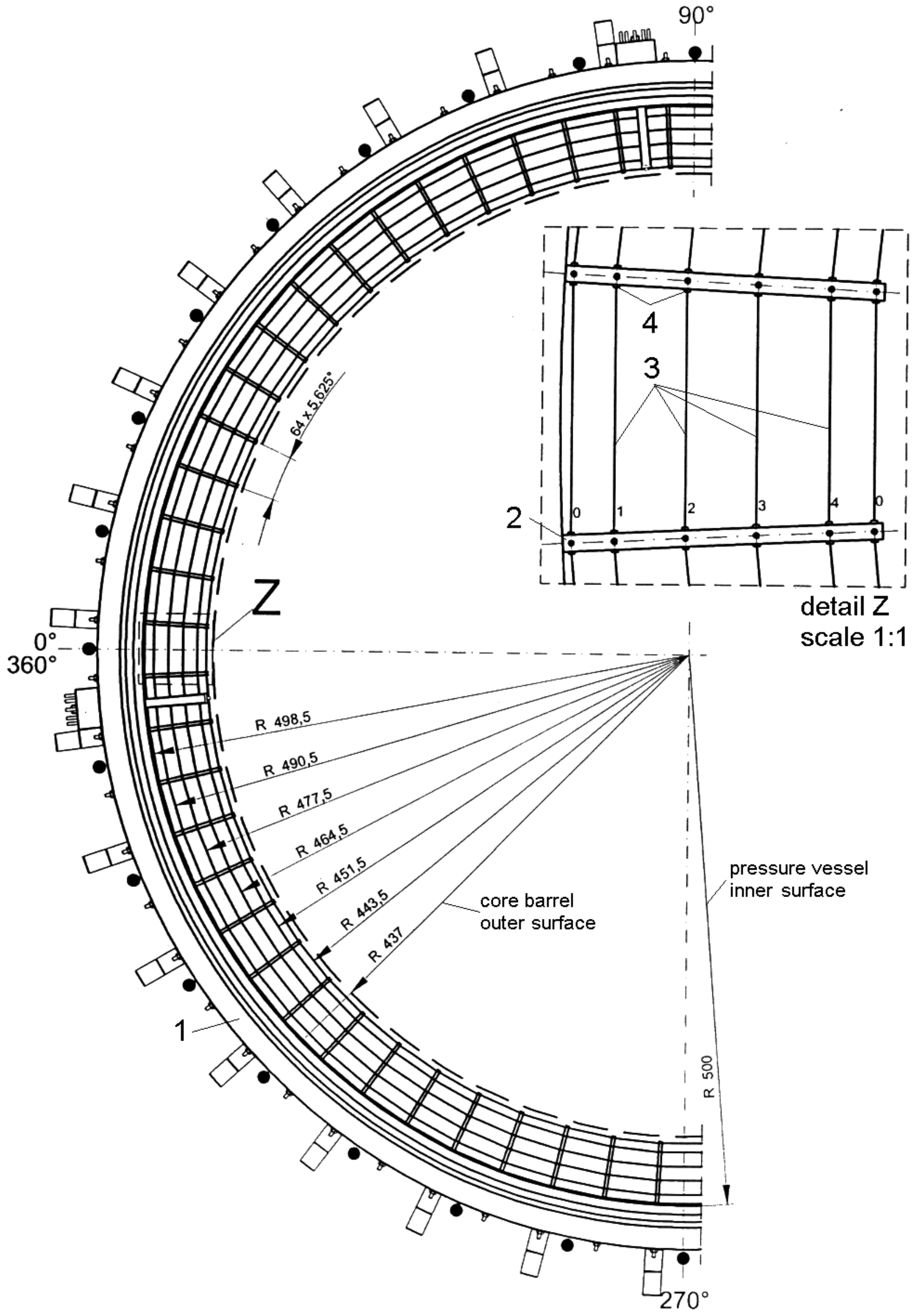

Fig. 2.3.2 Mesh sensor for the downcomer (4x64 measurement positions) (1. RPV wall, 2. wire fixing rod/transmitter electrode, 3. receiver electrode, 4. ceramic insulation pearls)

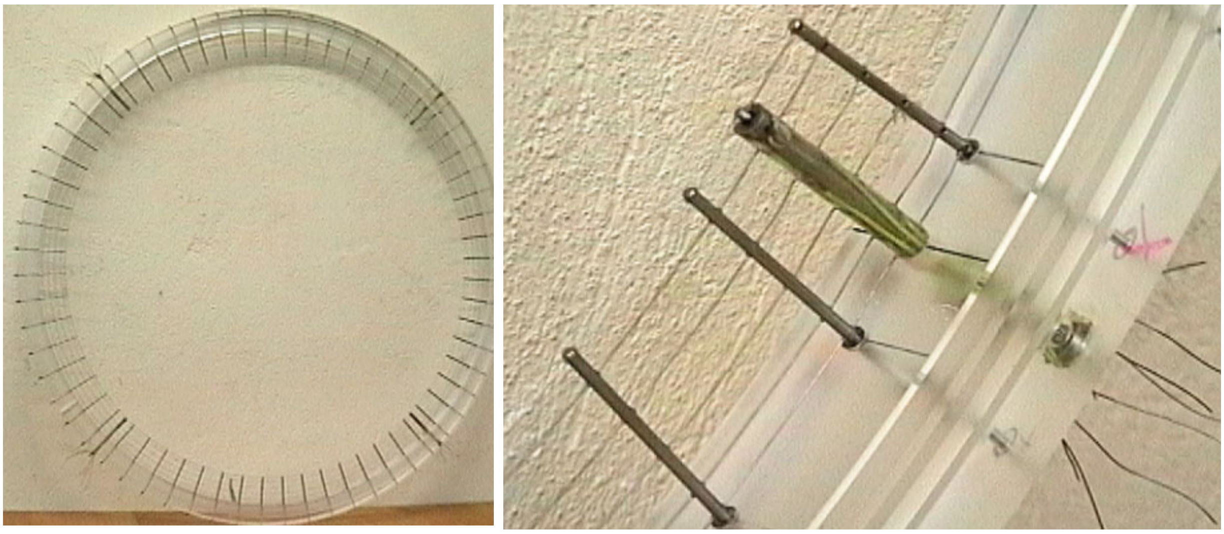

A) total view B) detailed view on the electrodes

Fig. 2.3.3 Pictures of the wire mesh sensor for the downcomer

Wire mesh sensor at the core inlet

The fourth sensor is integrated into the lower core support plate (Fig. 2.3.4). The PWR KONVOI contains 193 fuel elements in 15x15 matrix. Some positions in the edges are not used to give the reactor core a more ore less cylindrical surface. The lower core support plate contains one circular hole for each fuel assembly. This plate was reproduced in the given scale from acrylic glass. The transmitter and receiver electrodes are integrated into the plate in such a way, that one crossing point of two electrodes is located in the middle of each hole. The sensor contains 15 transmitter and 15 receiver electrodes, so that one column and one row are not used in the matrix. The diameter of the sensor wires is 0.5 mm and the axial distance is 2.0 mm. All of the 193 fuel element inlet positions are equipped with one measurement positions.

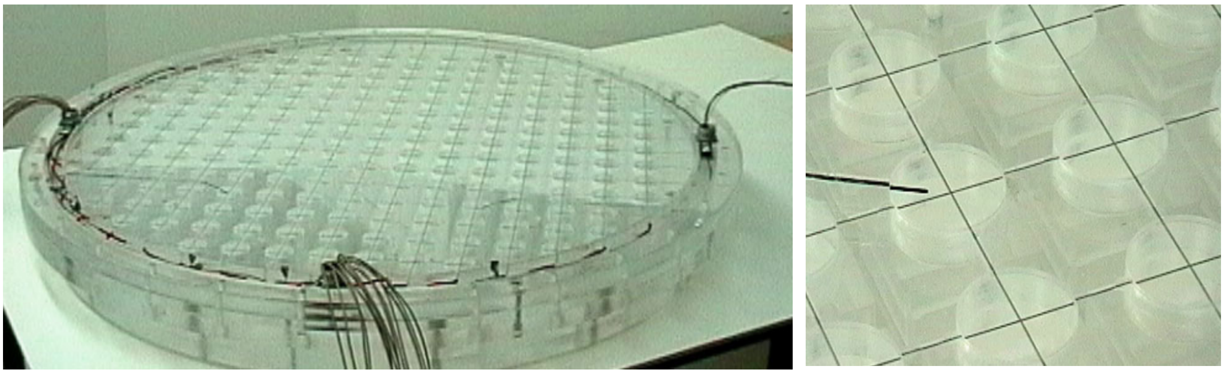

A) total view B) electrodes

Fig. 2.3.4 Lower core support plate with integrated wire mesh sensor

2.3.1.2 Calibration of the wire mesh sensors and determination of the mixing scalars

The calibration curve represents the relation between the measured current at the measurement position and the local conductivity. For the determination of the calibration curve, sampling points are needed, which are recorded for a well-known conductivity of the water. For that purpose, the circumstance is used, that after a certain time at running all pumps, the salt content becomes equal in the whole test facility. The conductivity of the water is identical at all measurement positions and is measured by a reference measurement device for the conductivity. Using these sampling points, calibration curves are adjusted by means of polynomials of the order n.

$$\sigma(x_i, y_i, z_i, t) = \sum_{j=0}^{n} p_{i,j} \cdot U(x_i, y_i, z_i, t) - U_0(x_i, y_i, z_i))^j \qquad \text{(Equ. 2.3.1)}$$

The determination of the coefficients $p_{i,j}$ is carried out by solving a least square deviation problem for each measurement position individually. The order of the polynomials can be prescribed for each sensor, individually. The experience showed, that a linear curve is a good representation of the sampling points. So, two calibration coefficients should be stored for each measurement position. The experiments start at a basic conductivity of >10 µS/cm in order to exclude the non-linear region.

To determine the mixing scalar, the transient distribution of the conductivity $\sigma(x_i,y_i,z_i,t)$ should be calculated using the calibration coefficients, in the first step. Then, the transient distribution of the mixing scalar $\theta(x_i,y_i,z_i,t)$ is calculated using the lower and upper reference value according to equ. (2.1.1).

2.3.2 Auxiliary measurement devices

Magneto-inductive flow meters are used to measure the volume flow rate in the four loops of the test facility. They are working in water with a minimal conductivity of > 5 µS/cm. For flow rates higher than 30 m^3/h, the measurement accuracy is ± 0.5 %. In the injection loop, a turbine flow meter is installed to control the injection flow rate. A measurement device for the conductivity with a measurement region of 0 - 200 µS/cm is used to measure the reference conductivity for the sampling points. The temperature compensation of the probe is deactivated in order to measure the real conductivity value, what is also present at the wire mesh sensors. The display accuracy is four significant digits. At conductivity values of less than 20 µS/cm, two decimal digits are displayed, the display accuracy is ± 0.005 µS/cm. At higher values, the device switches to one decimal digit, the display accuracy is now ± 0.05 µS/cm. For the determination of the conductivity in the injection loop, an identical measurement device is used.

2.4 Error analysis

2.4.1 Introduction

In this chapter, an error analysis for the measured conductivity values and the mixing scalars determined on that basis is provided. The following three sources of errors are included into the examination:

- Deviation from the calibration curve
- Discretisation error of the primary measurement value
- Statistical fluctuations of the measured values

2.4.2 Calibration curve

For the calibration curves, equations of the type (2.3.1) are used. They are based on the sampling points, determined in the current measurement series. Fig. 2.4.1 shows the sampling points and the fitted calibration curve for one measurement point of each sensor. It turned out, that a linear fitting curve represents the sampling points in a sufficient manner. A linear calibration curve is also meaningful from the physical point of view. It is worth to be mentioned that values above 1800 mV are not considered as sampling points, because they are outside of the saturation level of the signal amplifiers.

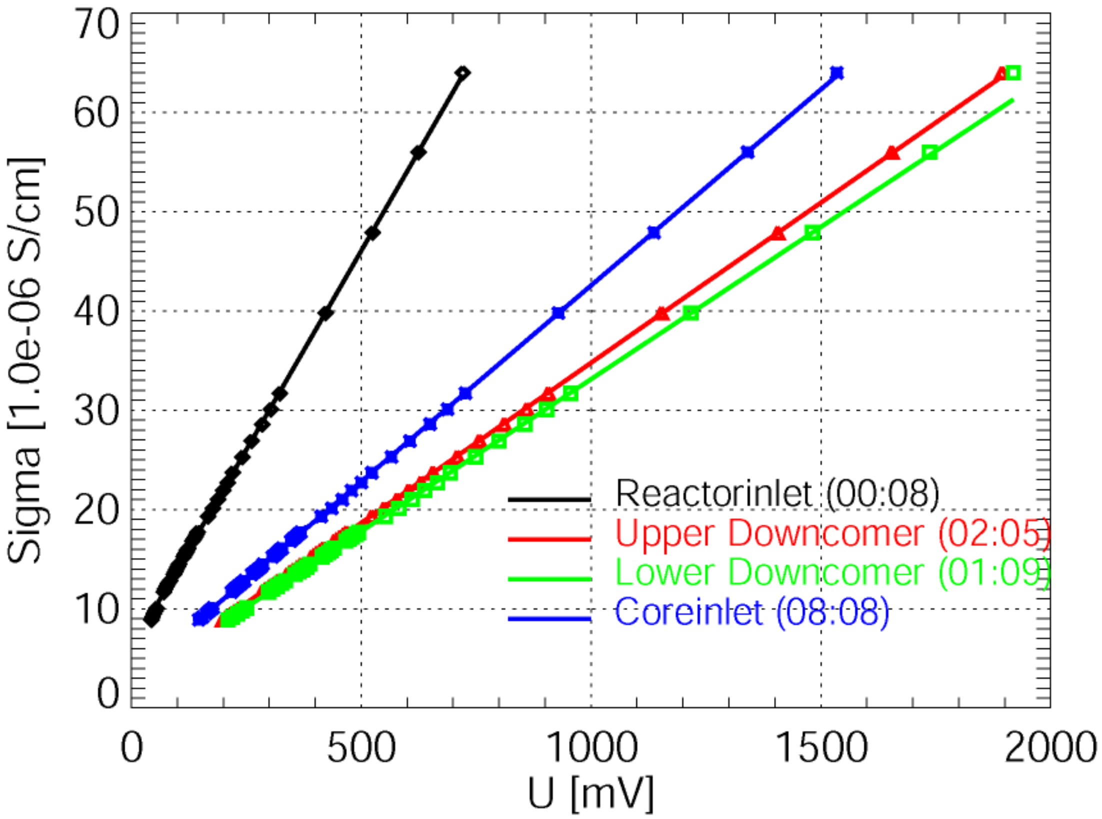

Fig. 2.4.1 Calibration curve (line) and measured values (points) for one measurement position of each sensor

As far as each measurement position has its individual calibration curve the deviations between sampling points and this curve differ from measuring point to measuring point. The points selected for the error analysis are representative for the corresponding sensor.

Tab. 2.2 contains a comparison of the measured sampling point and the corresponding calibration value for the selected measurement point of the wire mesh sensor in the reactor inlet nozzle. As mentioned above, the experiments only start with a basic conductivity of 10 µS/cm. In that relevant area, the maximum deviation between calculated and sampling value is:

$$\Delta\sigma_{\text{calibmax}} = \pm\ 0.29\ \mu\text{S/cm}.$$

The first values in the table underline the non-linearity for conductivity values below 10 µS/cm.

Tab. 2.2 Comparison of the measured sampling point and the calculated calibration value for the measurement position 00:08 at the sensor in the inlet nozzle

U [mV]	σ_{meas} [µS/cm]	σ_{cal} [µS/cm]	$\sigma_{meas} - \sigma_{cal}$ [µS/cm]	U [mV]	σ_{meas} [µS/cm]	σ_{cal} [µS/cm]	$\sigma_{meas} - \sigma_{cal}$ [µS/cm]
44	8.89	9.48	- 0.59	133	16.83	16.62	+ 0.21
46	9.16	9.64	- 0.48	136	17.03	16.86	+ 0.17
49	9.49	9.88	- 0.39	139	17.25	17.10	+ 0.15
52	9.78	10.12	- 0.34	142	17.50	17.34	+ 0.16
55	10.07	10.37	**- 0.29**	144	17.70	17.50	+ 0.20
71	11.69	11.65	+ 0.04	167	19.30	19.35	- 0.05
73	11.99	11.81	+ 0.18	178	20.10	20.23	- 0.13
77	12.27	12.13	+ 0.14	189	21.00	21.11	- 0.11
80	12.55	12.37	+ 0.18	200	21.90	21.99	- 0.09
84	12.86	12.69	+ 0.14	210	22.70	22.79	- 0.09
92	13.46	13.33	+ 0.13	221	23.70	23.67	+ 0.03
95	13.73	13.57	+ 0.16	242	25.30	25.36	- 0.06
98	13.96	13.81	+ 0.15	262	26.90	26.96	- 0.06
101	14.22	14.05	+ 0.17	285	28.60	28.80	- 0.20
104	14.48	14.29	+ 0.19	304	30.10	30.33	- 0.23
114	15.25	15.10	+ 0.15	323	31.70	31.85	- 0.15
116	15.46	15.26	+ 0.20	423	39.80	39.87	- 0.07
119	15.66	15.50	+ 0.16	525	47.90	48.05	- 0.15
121	15.88	15.66	+ 0.22	625	56.00	56.06	- 0.06
124	16.09	15.90	+ 0.19	721	64.00	63.76	+ 0.24

The evaluation of the data at the measurement position of the sensor in the upper downcomer shows a maximum deviation of

$$\Delta\sigma_{calibmax} = \pm\ 0.16\ \mu S/cm,$$

what is nearly only the half of the value at the first sensor. A non-linearity of the data below 10 µS/cm is not to be seen. The maximum error for the sensor in the lower part of the downcomer is

$$\Delta\sigma_{calibmax} = \pm\ 0.27\ \mu S/cm.$$

The non-linearity is not present, too. The two highest values (1894 and 1919 mV) are not used for the determination of the calibration coefficients.

The maximum deviation for the measurement position at the sensor in the core support plate is:

$$\Delta\sigma_{calibmax} = \pm\ 0.30\ \mu S/cm.$$

The standard deviation of the calibration curve from the sampling points s_{calib} can be determined on the basis of the deviation at each measured sampling point according to:

$$s_{calib} = \sqrt{\frac{\sum_i^n \left(\sigma_{meas} - \sigma_{cal}(U_{meas})\right)^2}{n-2}} \qquad \text{(Equ. 2.4.1)}$$

From that standard deviation, the region can be calculated, where the error induced by the calibration curve can be found with a given statistical confidence. To obtain the error, the standard deviation has to be weighted with the corresponding factor of the Student distribution. For the selected four representative measurement positions, the following error for a statistical confidence of 95.4 % is calculated using equ. (2.4.1) and (2.4.2).

$$\Delta\sigma_{calib(P=95.4\%)} = t_P \cdot s_\sigma \qquad \text{(Equ. 2.4.2)}$$

Reactor inlet (pos. 00:08):	$\Delta\sigma_{\mathrm{calib}}$ (P = 95.4 %) = ± 0.34 µS/cm
Upper Downcomer (pos. 02:05):	$\Delta\sigma_{\mathrm{calib}}$ (P = 95.4 %) = ± 0.16 µS/cm
Lower Downcomer (pos. 01:09):	$\Delta\sigma_{\mathrm{calib}}$ (P = 95.4 %) = ± 0.22 µS/cm
Core inlet (pos. 08:08):	$\Delta\sigma_{\mathrm{calib}}$ (P = 95.4 %) = ± 0.21 µS/cm.

2.4.3 Discretisation error of the primary measurement values

A 11 bit digital number is the primary measurement value, representing the current at the corresponding crossing point of two wires. This current is proportional to the local conductivity at the measurement position. Each measurement position has its individual characteristic (dependence of the conductivity from the measured current). This characteristic differs for different sensors (Fig. 2.4.1). At one sensor, the differences between the single measurement positions are small. The steepness of the curve determines the value of the discretisation error. It corresponds to the change of the conductivity caused by a change of the primary measured value by 0.5. As far as all experiments are carried out in the region of an almost linear dependency of the conductivity fro the measured values (see above), the discretisation error of one measuring series is constant and can directly be calculated from the gradient of the calibration curve. For the selected representative measurement positions, the absolute discretisation error is:

Reactor inlet (pos. 00:08):	$\Delta\sigma_{\text{Diskr}} = \pm 0.040$ µS/cm
Upper Downcomer (pos. 02:05):	$\Delta\sigma_{\text{Diskr}} = \pm 0.016$ µS/cm
Lower Downcomer (pos. 01:09):	$\Delta\sigma_{\text{Diskr}} = \pm 0.015$ µS/cm
Core inlet (pos. 08:08):	$\Delta\sigma_{\text{Diskr}} = \pm 0.020$ µS/cm.

2.4.4 Statistical fluctuations of the measured values

Electrical noise acting on the sensors from outside, fluctuations of conductivity or temperature of the water in the facility as well as the noise of the used electronic devices lead to statistical fluctuations of the signals. They are present in the measured conductivity values as a statistical error. These errors can be determined by analyzing the measurement values at the single wire mesh sensors before the injected tracer reaches the measuring cross section. In the left part, Fig. 2.4.2 shows the fluctuations of the measured value at a selected measurement position at each sensor. At the sensor in the inlet nozzle, the fluctuations reaches maximum values of about 0.1 µS/cm. At the remaining three sensors, the fluctuations reach values of about 0.05 µS/cm. The discrete signals for the shown time span of 6 s (121 measuring values) were analyzed in a statistical way. In the right part of the fig., the result of this statistical analysis is shown as the probability density and the frequency of the values.

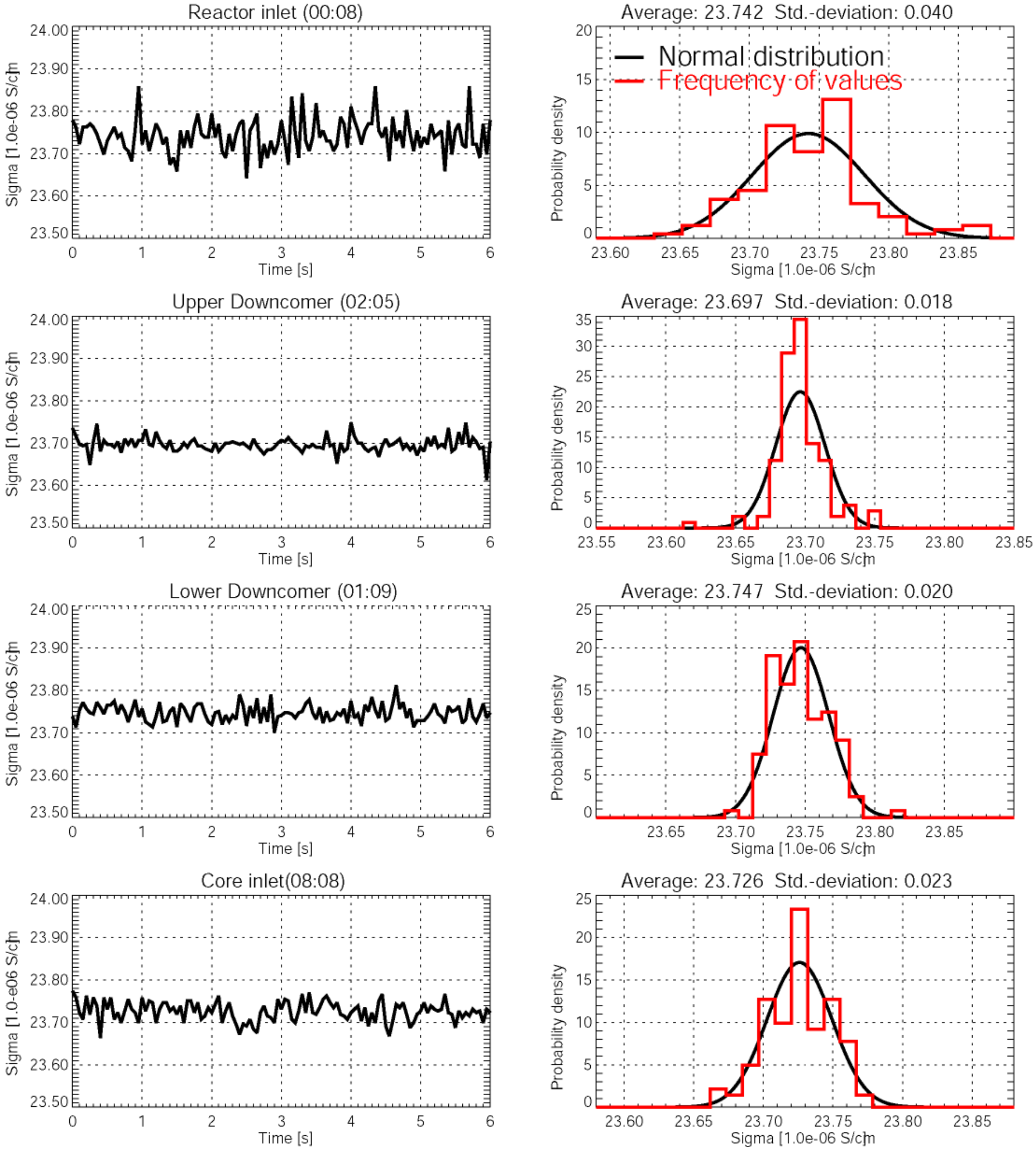

Fig. 2.4.2 Time signal and statistical analysis of the conductivity at one measurement position of each sensor before the tracer injection

The statistical nature of the fluctuations is clearly to be seen. At all four sensors, the average value is the most probable one. The shown standard deviation s_{fluct} was recalculated into an absolute error $\Delta\sigma_{fluct}$ of the corresponding measurement points, which bounds the measured values with a statistical confidence of P = 95.4 % (for a sufficient high number of values, as in Fig. 2.4.2, the expression $\Delta\sigma_{(P=95.4\%)} = 2 \cdot s_{fluct}$ can be used):

Reactor inlet (pos. 00:08): $\Delta\sigma_{\text{fluct}}$ (P = 95.4 %) = ± 0.080 µS/cm

Upper Downcomer (pos. 02:05): $\Delta\sigma_{\text{fluct}}$ (P = 95.4 %) = ± 0.036 µS/cm

Lower Downcomer (pos. 01:09): $\Delta\sigma_{\text{fluct}}$ (P = 95.4 %) = ± 0.040 µS/cm

Core inlet (pos. 08:08): $\Delta\sigma_{\text{fluct}}$ (P = 95.4 %) = ± 0.046 µS/cm

2.4.5 Summation of the single error types

The single contributions to the total error were determined as absolute errors with a statistical confidence of P = 95.4 %. The absolute total error of a directly measured value is given as the sum of the contributions together with the smallest statistical confidence. That means for a instantaneous measured conductivity value:

$$\Delta\sigma_{(P=95.4\%)} = \Delta\sigma_{calib} + \Delta\sigma_{Diskr} + \Delta\sigma_{fluct} \qquad \text{(Equ. 2.4.3).}$$

For the representative measurement positions, these are:

Reactor inlet (pos. 00:08) $\Delta\sigma_{(P = 95.4\,\%)}$ = ± 0.40 µS/cm

Upper Downcomer (pos. 02:05): $\Delta\sigma_{(P = 95.4\,\%)}$ = ± 0.17 µS/cm

Lower Downcomer (pos. 01:09): $\Delta\sigma_{(P = 95.4\,\%)}$ = ± 0.21 µS/cm

Core inlet (pos. 08:08): $\Delta\sigma_{(P = 95.4\,\%)}$ = ± 0.22 µS/cm.

The mixing scalar (equ. 2.1.1) is an indirectly determined quantity. Three different conductivity values contribute to this mixing scalar. Therefore, the absolute maximum error is calculated acc. to [Her95] with:

$$\Delta\Theta(t,x,y,z) = \pm\left(\left|\frac{\partial\Theta}{\partial\sigma(t,x,y,z)}\right| \cdot \Delta\sigma + \left|\frac{\partial\Theta}{\partial\sigma_0(x,y,z)}\right| \cdot \Delta\sigma_0 + \left|\frac{\partial\Theta}{\partial\sigma_1}\right| \cdot \Delta\sigma_1\right)$$

(Equ. 2.4.4).

The contributors are the instantaneous conductivity at the measurement position ($\sigma(t,x,y,z)$), the averaged conductivity at the measurement position before the tracer reaches the position ($\sigma_0(x,y,z)$) and the reference conductivity (σ_1) at the inlet into the reactor, each of them with their own deviations.

When a value is calculated by averaging a number of instantaneous conductivity values, so the standard deviation reduces and together with them the statistical error components, too. That concerns the discretisation error and the stochastic fluctuations of the signal, but it do not concern the systematic errors, in our case the calibration error. All statistical errors reduces in comparison with a single value with a factor of $1/\sqrt{n}$, where n is the number of used single measurements.

Considering the single contributions to the errors and the statistical nature of the fluctuations and the discretisation error, the following formula for the calculation of the absolute maximum error of an instantaneous value of the mixing scalar is obtained:

$$\Delta\Theta(t,x,y,z) = \pm \left(\begin{array}{l} \dfrac{\Delta\sigma_{calib}}{(\sigma_1-\sigma_0)^2} \cdot \left(|\sigma_1-\sigma_0| + |\sigma-\sigma_1| + |\sigma_0-\sigma| \right) + \\ + \dfrac{\Delta\sigma_{fluct}+\Delta\sigma_{Diskr}}{(\sigma_1-\sigma_0)^2} \cdot \left(|\sigma_1-\sigma_0| + \dfrac{|\sigma-\sigma_1|}{\sqrt{n}} + \dfrac{|\sigma_0-\sigma|}{\sqrt{m}} \right) \end{array} \right) \qquad \text{(Equ. 2.4.5)}$$

and after combining some terms:

$$\Delta\Theta(t,x,y,z) = \pm \frac{2\Delta\sigma_{calib}}{(\sigma_1-\sigma_0)} + \frac{\Delta\sigma_{fluct}+\Delta\sigma_{Diskr}}{(\sigma_1-\sigma_0)^2} \cdot \left(|\sigma_1-\sigma_0| + \frac{|\sigma-\sigma_1|}{\sqrt{n}} + \frac{|\sigma_0-\sigma|}{\sqrt{m}} \right)$$

or

$$\Delta\Theta(t,x,y,z) = \pm \frac{1}{\sigma_1-\sigma_0} \cdot \left(2\Delta\sigma_{calib} + \left(\Delta\sigma_{fluct}+\Delta\sigma_{Diskr}\right) \cdot \left(1 + \frac{\frac{1}{\sqrt{n}}\cdot(\sigma_1-\sigma) + \frac{1}{\sqrt{m}}\cdot(\sigma-\sigma_0)}{\sigma_1-\sigma_0} \right) \right)$$

(Equ. 2.4.6)

Hereby n is the number of measurement values for the determination of σ_0 and m for the determination of σ_1. As follows from equ. 2.4.6, the error of a certain value of the mixing scalar depends on the local conductivity. This dependency reduces with an increasing number of values used for the determination of the reference values σ_0 and σ_1. Due to the fact, that the calibration error is the dominating one, for great m and n can be written:

$$\Delta\Theta(t,x,y,z) \cong \pm \frac{1}{\sigma_1 - \sigma_0} \cdot \left(2\Delta\sigma_{calib} + \Delta\sigma_{fluct} + \Delta\sigma_{Diskr}\right) \qquad \text{(Equ. 2.4.7).}$$

Equ. (2.4.6) and (2.4.7) show that the error of the mixing scalar increases with decreasing amplitude of the perturbation $\sigma_1 - \sigma_0$.

Fig. 2.4.3 shows the mixing scalar and the error according to equ. (2.4.7) for the selected reference experiment for a certain time point.

Along an azimutal line in the outer part of the core, it is demonstrated, that the dependancy of the measurement error on the absolute value of the mixing scalar is negligible (Fig. 2.4.4).

For the determination of stationary mixing coefficients, the instantaneous mixing scalars are averaged at the saturation plateau level. The absolute maximum error of the mixing coefficient is derived from equ. (2.4.4) and can be calculated as:

$$\Delta\Theta(x,y,z) = \pm \left(\begin{array}{l} \frac{\Delta\sigma_{calib}}{(\sigma_1 - \sigma_0)^2} \cdot \left(|\sigma_1 - \sigma_0| + |\sigma - \sigma_1| + |\sigma_0 - \sigma|\right) + \\ \cdot + \frac{\Delta\sigma_{fluct} + \Delta\sigma_{Diskr}}{(\sigma_1 - \sigma_0)^2} \cdot \left(\frac{|\sigma_1 - \sigma_0|}{\sqrt{l}} + \frac{|\sigma - \sigma_1|}{\sqrt{n}} + \frac{|\sigma_0 - \sigma|}{\sqrt{m}} \right) \end{array} \right) \qquad \text{(Equ. 2.4.8),}$$

where l is the number of the instantaneous values of the mixing scalar used for the averaging at the plateau. Consequently, the statistical error of the measured value σ reduces in comparison to the calibration error. The error of the mixing coefficent can be written in simplified form:

$$\Delta\Theta(x,y,z) \cong \pm \frac{2\Delta\sigma_{calib}}{\sigma_1 - \sigma_0} \qquad \text{(Equ. 2.4.9).}$$

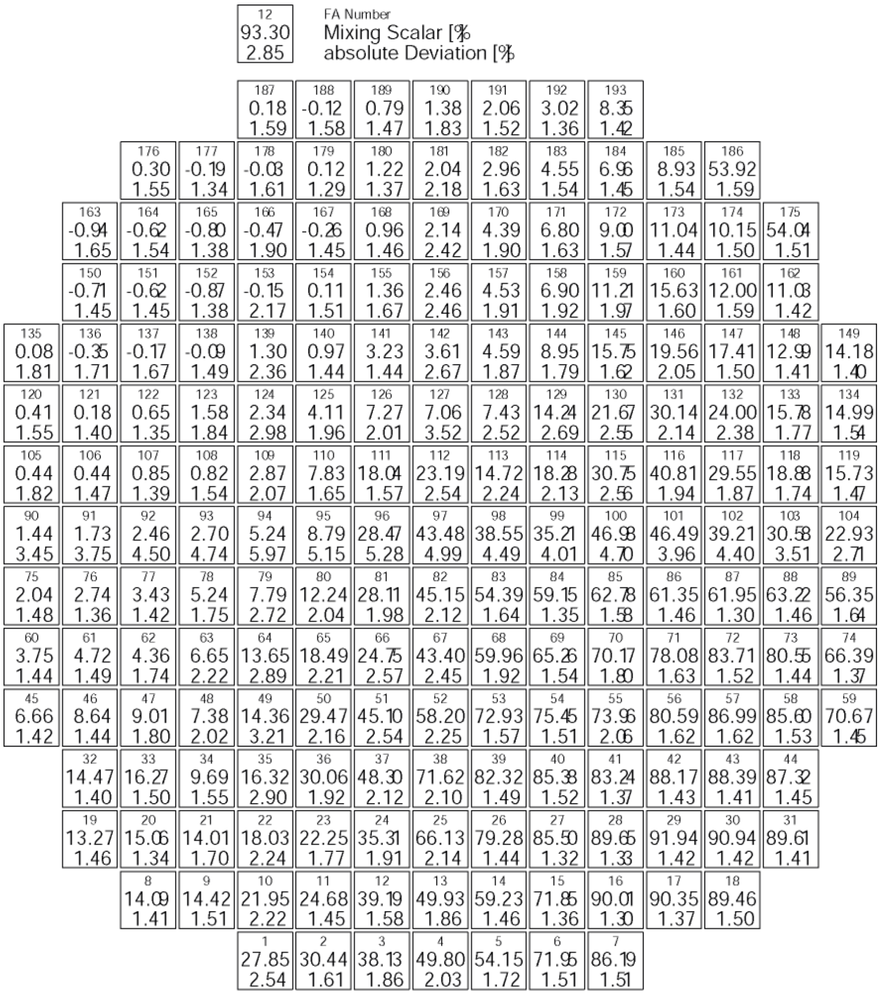

12 93.30 2.85	FA Number Mixing Scalar [% absolute Deviation [%

				187 0.18 1.59	188 -0.12 1.58	189 0.79 1.47	190 1.38 1.83	191 2.06 1.52	192 3.02 1.36	193 8.35 1.42				
		176 0.30 1.55	177 -0.19 1.34	178 -0.03 1.61	179 0.12 1.29	180 1.22 1.37	181 2.04 2.18	182 2.96 1.63	183 4.55 1.54	184 6.96 1.45	185 8.93 1.54	186 53.92 1.59		
	163 -0.94 1.65	164 -0.62 1.54	165 -0.80 1.38	166 -0.47 1.90	167 -0.26 1.45	168 0.96 1.46	169 2.14 2.42	170 4.39 1.90	171 6.80 1.63	172 9.00 1.57	173 11.04 1.44	174 10.15 1.50	175 54.04 1.51	
	150 -0.71 1.45	151 -0.62 1.45	152 -0.87 1.38	153 -0.15 2.17	154 0.11 1.51	155 1.36 1.67	156 2.46 2.46	157 4.53 1.91	158 6.90 1.92	159 11.21 1.97	160 15.63 1.60	161 12.00 1.59	162 11.03 1.42	
135 0.08 1.81	136 -0.35 1.71	137 -0.17 1.67	138 -0.09 1.49	139 1.30 2.36	140 0.97 1.44	141 3.23 1.44	142 3.61 2.67	143 4.59 1.87	144 8.95 1.79	145 15.75 1.62	146 19.56 2.05	147 17.41 1.50	148 12.99 1.41	149 14.18 1.40
120 0.41 1.55	121 0.18 1.40	122 0.65 1.35	123 1.58 1.84	124 2.34 2.98	125 4.11 1.96	126 7.27 2.01	127 7.06 3.52	128 7.43 2.52	129 14.24 2.69	130 21.67 2.55	131 30.14 2.14	132 24.00 2.38	133 15.78 1.77	134 14.99 1.54
105 0.44 1.82	106 0.44 1.47	107 0.85 1.39	108 0.82 1.54	109 2.87 2.07	110 7.83 1.65	111 18.04 1.57	112 23.19 2.54	113 14.72 2.24	114 18.28 2.13	115 30.75 2.56	116 40.81 1.94	117 29.55 1.87	118 18.88 1.74	119 15.73 1.47
90 1.44 3.45	91 1.73 3.75	92 2.46 4.50	93 2.70 4.74	94 5.24 5.97	95 8.79 5.15	96 28.47 5.28	97 43.48 4.99	98 38.55 4.49	99 35.21 4.01	100 46.98 4.70	101 46.49 3.96	102 39.21 4.40	103 30.58 3.51	104 22.93 2.71
75 2.04 1.48	76 2.74 1.36	77 3.43 1.42	78 5.24 1.75	79 7.79 2.72	80 12.24 2.04	81 28.11 1.98	82 45.15 2.12	83 54.39 1.64	84 59.15 1.35	85 62.78 1.58	86 61.35 1.46	87 61.95 1.30	88 63.22 1.46	89 56.35 1.64
60 3.75 1.44	61 4.72 1.49	62 4.36 1.74	63 6.65 2.22	64 13.65 2.89	65 18.49 2.21	66 24.75 2.57	67 43.40 2.45	68 59.96 1.92	69 65.26 1.54	70 70.17 1.80	71 78.08 1.63	72 83.71 1.52	73 80.55 1.44	74 66.39 1.37
45 6.66 1.42	46 8.64 1.44	47 9.01 1.80	48 7.38 2.02	49 14.36 3.21	50 29.47 2.16	51 45.10 2.54	52 58.20 2.25	53 72.93 1.57	54 75.45 1.51	55 73.96 2.06	56 80.59 1.62	57 86.99 1.62	58 85.60 1.53	59 70.67 1.45
	32 14.47 1.40	33 16.27 1.50	34 9.69 1.55	35 16.32 2.90	36 30.06 1.92	37 48.30 2.12	38 71.62 2.10	39 82.32 1.49	40 85.38 1.52	41 83.24 1.37	42 88.17 1.43	43 88.39 1.41	44 87.32 1.45	
	19 13.27 1.46	20 15.06 1.34	21 14.01 1.70	22 18.03 2.24	23 22.25 1.77	24 35.31 1.91	25 66.13 2.14	26 79.28 1.44	27 85.50 1.32	28 89.65 1.33	29 91.94 1.42	30 90.94 1.42	31 89.61 1.41	
		8 14.09 1.41	9 14.42 1.51	10 21.95 2.22	11 24.68 1.45	12 39.19 1.58	13 49.93 1.86	14 59.23 1.46	15 71.85 1.36	16 90.01 1.30	17 90.35 1.37	18 89.46 1.50		
				1 27.85 2.54	2 30.44 1.61	3 38.13 1.86	4 49.80 2.03	5 54.15 1.72	6 71.95 1.51	7 86.19 1.51				

Fig. 2.4.3 Instantaneous mixing scalar and absolute error acc. to equ. (2.4.7) for a certain time point in the experiment

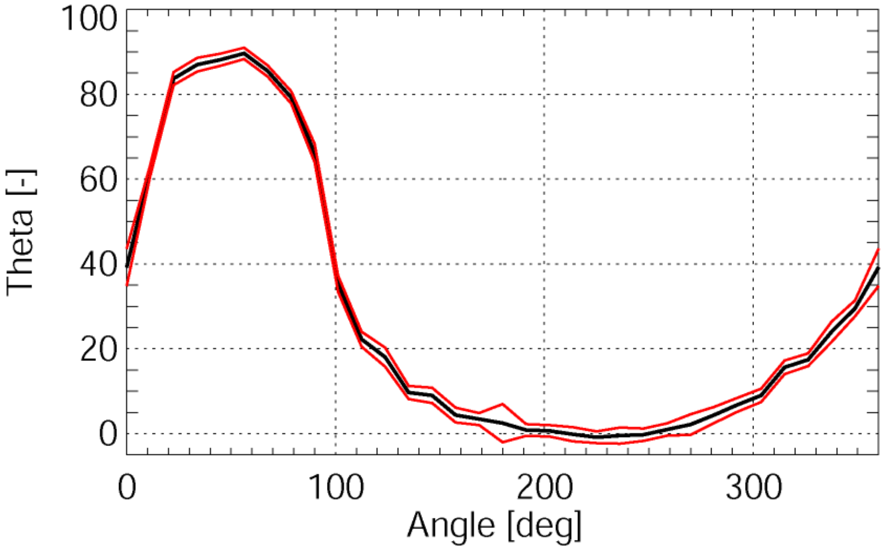

Fig. 2.4.4 Instantaneous mixing scalar and absolute error on a line in the outer part of the core

Tab. 2.3 contains the results of the error analysis for the selected experiment for all measurement positions along the azimuthal line in the outer part of the core inlet sensor. The first column contains the instantaneous conductivity value for a certain time point. In the next columns, the single error contributions and the total error (equ. 2.4.3) are printed. Column 6 contains the mixing scalar calculated acc. to (equ. 2.1.1). The total error of the mixing scalar under full consideration of all components (equ. 2.4.6) can be found in column 7. The comparison with column 8 (error calculated using the simplified equ. 2.4.7) demonstrates the usefulness of the simplification. Further, the plateau averaged mixing scalar is shown together with the error assessment according to equ. (2.4.8) and (2.4.9). The simplified determination of the error according to equ. (2.4.9) is a good approximation, as can be concluded comparing column 10 and 11.

Tab. 2.3 Conductivity, instantaneous and plateau averaged mixing scalar incl. error values acc. to the equations on an azimuthal line in the outer part of the core inlet sensor (reference experiment)

0	1	2	3	4	5	6	7	8	9	10	11
FA	**σ_{meas}**	**$\Delta\sigma_{calib}$**	**$\Delta\sigma_{fluct}$**	**$\Delta\sigma_{diskr}$**	**$\Delta\sigma_{sum}$ (2.4.3)**	**$\Theta(t)$ (2.1.1)**	**$\Delta\Theta$ (2.4.6)**	**$\Delta\Theta$ (2.4.7)**	**Θ (2.1.1)**	**$\Delta\Theta$ (2.4.8)**	**$\Delta\Theta$ (2.4.9)**
	[µS/cm]					**[%]**					
M12	27.21	0.157	0.052	0.020	0.229	15.63	1.62	1.60	14.39	1.34	1.30
L13	29.13	0.146	0.053	0.019	0.217	17.41	1.53	1.50	17.47	1.25	1.20
K13	28.73	0.251	0.052	0.020	0.323	24.00	2.41	2.38	24.32	2.12	2.08
J13	30.60	0.187	0.057	0.020	0.264	29.54	1.89	1.87	34.68	1.59	1.55
H13	33.03	0.496	0.040	0.021	0.557	39.21	4.42	4.40	47.15	4.18	4.15
G13	36.35	0.125	0.045	0.019	0.189	61.95	1.31	1.30	60.94	1.07	1.03
F13	41.96	0.148	0.052	0.020	0.220	83.72	1.54	1.52	76.98	1.26	1.23
E13	44.05	0.160	0.052	0.020	0.231	86.99	1.63	1.62	82.27	1.35	1.32
D12	43.39	0.143	0.040	0.020	0.203	88.17	1.44	1.43	84.49	1.21	1.19
C11	44.11	0.130	0.043	0.020	0.193	89.65	1.35	1.33	86.74	1.10	1.07
C10	42.82	0.128	0.043	0.020	0.191	85.50	1.33	1.32	83.02	1.09	1.06
C09	41.23	0.143	0.041	0.020	0.204	79.28	1.45	1.44	72.36	1.21	1.19
C08	38.66	0.225	0.046	0.020	0.292	66.13	2.16	2.14	49.47	1.90	1.87
C07	30.47	0.195	0.049	0.020	0.265	35.31	1.93	1.91	26.88	1.66	1.62
C06	28.16	0.185	0.038	0.020	0.243	22.25	1.79	1.77	18.41	1.56	1.53
C05	27.29	0.238	0.046	0.020	0.303	18.04	2.26	2.24	16.94	2.01	1.97
D04	26.73	0.155	0.045	0.020	0.220	9.69	1.57	1.55	12.01	1.32	1.28
E03	25.17	0.186	0.044	0.020	0.250	9.01	1.83	1.80	8.04	1.57	1.54
F03	24.43	0.178	0.044	0.020	0.242	4.36	1.77	1.74	4.96	1.52	1.48
G03	24.10	0.141	0.041	0.020	0.202	3.43	1.44	1.42	3.16	1.20	1.17

H03	24.02	0.510	0.038	0.021	0.568	2.46	4.52	4.50	2.35	4.29	4.25
J03	23.81	0.131	0.053	0.020	0.204	0.85	1.41	1.39	0.91	1.13	1.08
K03	23.67	0.130	0.048	0.019	0.197	0.65	1.37	1.35	0.53	1.11	1.07
L03	23.52	0.169	0.047	0.019	0.235	-0.17	1.69	1.67	-0.33	1.44	1.40
M04	23.56	0.133	0.049	0.020	0.202	-0.87	1.41	1.38	-0.81	1.14	1.10
N05	23.55	0.194	0.050	0.020	0.264	-0.47	1.93	1.90	-0.42	1.66	1.61
N06	23.63	0.142	0.049	0.019	0.210	-0.26	1.48	1.45	-0.36	1.21	1.17
N07	23.79	0.140	0.053	0.019	0.212	0.97	1.48	1.45	0.69	1.20	1.16
N08	24.21	0.257	0.051	0.020	0.327	2.14	2.45	2.42	1.97	2.17	2.13
N09	24.95	0.193	0.053	0.020	0.265	4.38	1.93	1.90	4.76	1.64	1.60
N10	25.60	0.164	0.048	0.019	0.231	6.80	1.66	1.64	8.00	1.40	1.36
N11	25.54	0.157	0.046	0.019	0.222	9.00	1.59	1.57	9.91	1.34	1.30

2.4.6 Conclusions on error assessment

- The quality of the calibration curve influences the value of the error bands of the finally determined mixing scalar, significantly.
- The discretisation error and the error caused by statistical fluctuations of the signal are one magnitude smaller than the calibration error.
- An higher amplitude of the perturbation (use of the maximal possible increase of the conductivity) in the experiments decreases the absolute error of the mixing scalar.
- The error of the mixing scalar does not depend on the primary measurement value itself.
- The calculated error bands for the measurement positions of one sensor show small differences, only.
- The calculated error bands are clearly smaller than the fluctuations of the measured values caused by the turbulent nature of the flow in the test facility.

2.5 Slug mixing experiments

2.5.1 Matrix of the experiments

The test matrix of the ROCOM experiments was based of the requirements, elaborated in the frame of the determination of the key phenomena [Roh02]. The list of aspects to be covered by the slug mixing experiments described in the current report contains:

- Velocity measurements in the downcomer during pump start-up
- Scaling of the Reynolds-number
- Scaling of the Strouhal number
- Impact of the status of unaffected loops
- Transition from buoyancy driven to momentum controlled mixing
- Effects of downcomer geometry and lower plenum structures

The consideration of the listed items led to the following variations in the boundary conditions of the slug mixing experiments at the ROCOM test facility:

- Length of the pump ramp
- Final mass flow rate of the loop with the starting–up pump
- Volume of the injected slug
- Initial position of the slug in the cold leg
- Status of the unaffected loops

The influence of the density on the mixing was investigated in separate experiments (see chapter 5), the influence of the geometry is assessed by comparing the experimental results at different test facilities.

Tab. 2.4 Test matrix on ROCOM slug mixing experiments

Run	**Ramp length [s]**	**Final volume flow rate [m³/h]**	**Slug volume [m³]***	**Initial slug position [m]***	**Status of unaffected loops**	**Single realisations**
ROCOM-01	14	185.0	40.0	10.0	Open	5
ROCOM-02	14	185.0	20.0	10.0	Open	5
ROCOM-03	14	185.0	4.0	10.0	Open	5
ROCOM-04	14	185.0	4.0	2.5	Open	5
ROCOM-05	14	185.0	4.0	22.5	Open	5
ROCOM-06	14	185.0	4.0	40.0	Open	5
ROCOM-07	14	185.0	20.0	10.0	Closed	5
ROCOM-08	28	92.5	4.0	10.0	Open	5
ROCOM-09	56	46.3	4.0	10.0	Open	5
ROCOM-10	14	148.0	4.0	10.0	Open	5
ROCOM-11	14	222.0	4.0	10.0	Open	5
ROCOM-12	14	185.0	8.0	10.0	Open	5

* related to the original reactor

All experimental data of the carried out matrix (Tab. 2.4) are documented in [Kli03]. That documentation contains the boundary conditions and the experimental results in graphical and digital form.

2.5.2 Conduction of an experiment

The general conduction of an experiment is described on the example of the experiment ROCOM_02, chosen as benchmark test for the code validation. This experiment refers to the nominal start-up of the first main coolant pump, when a lower borated slug has been accumulated in the pump loop seal.

In the initial state, the coolant is stagnant in the whole test facility. The main gate valves are open. The pump in loop 1 is controlled by a linear frequency ramp. The duration of the frequency ramp is the same as at the original reactor: 14 s. The final value of the frequency ramp was determined in special hydraulic experiments, where the frequency value was determined necessary to have the desired flow rate, in case of ROCOM_02 185.0 m^3/h. At t = 0 s, the experiment is started, the frequency is changed linearly until the plateau value. The volume flow rate is recorded with a frequency of 10 Hz and afterwards recalculated into the corresponding velocity. Fig.

2.5.1 shows the frequency ramp for the experiment ROCOM_02 and the measured velocity in all four loops.

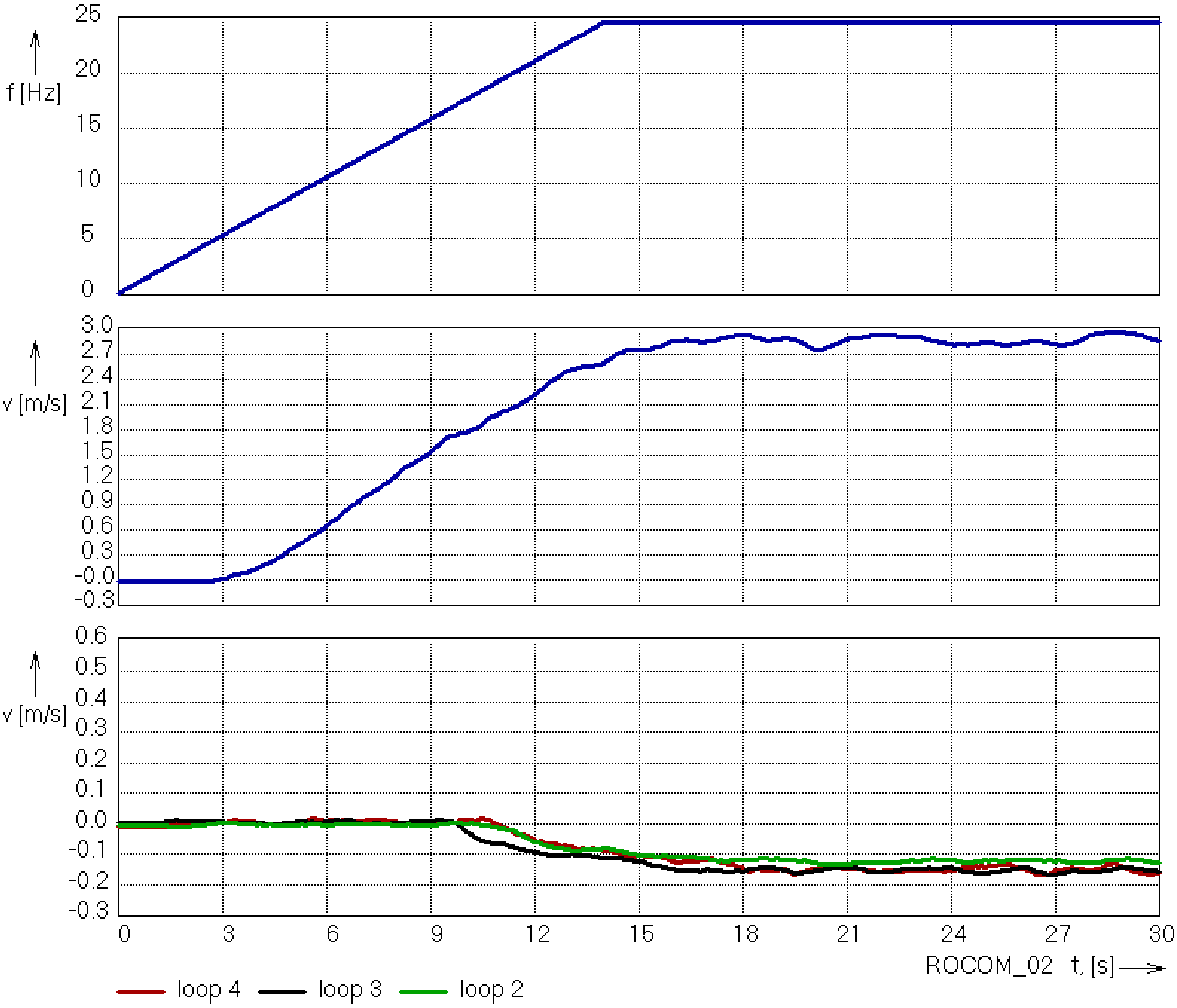

Fig. 2.5.1 Frequency of the pump 1, measured velocity in the loops 1-4

The start of the circulation is delayed with respect to pump start-up due the inertia of the water column. The plateau value of the velocity is reached about 2 s after the end of the frequency ramp. According to the boundary conditions, the gate valves in the passive loops are open. Therefore, a reverse flow establishes in these loops. The maximum value of this reverse flow is about 5 % of the nominal value in each of the loops.

A slug of deborated coolant resting in a loop can be characterized by two parameters:

- Position of the slug, characterized by the initial distance of the front edge from the inlet into the reactor vessel

- Volume of the deborated coolant.

In the ROCOM slug experiments, carried out in the frame of the current project, the initial position of the slug is determined by the time difference between start of the frequency ramp and opening of the injection valve. The volume of the slug is determined by the time duration of injection. The time points for opening and closing of the injection valves are determined in special hydraulic experiments, where the pump was started and no salt water was injected. In these hydraulic experiments, the distance of coolant movement during the pump start-up process was calculated on basis of the measured volume flow rate:

$$L_1(t) = \int_0^t \dot{V}(t) \big/ A_{Loop} \cdot dt \qquad \text{(Equ. 2.5.1)}$$

where A_{Loop} is the cross section of the pipe. During the integration along the flow path the opening and the closure time points for the injection valves were calculated according to the assumptions mentioned above. The obtained values are transferred to reactor conditions with a factor of 5 for the velocity and 125 for the volume. Considering the delay time constants of the valves, the real valve action time points were calculated.

2.5.3 Experimental results on mixing

2.5.3.1 ROCOM_02

The experiment ROCOM_02 was selected as the reference case for the validation calculations carried out in work package 4 of the FLOMIX-R project. Here, it is now used to describe the phenomenology of the process in detail. Fig. 2.5.2 shows the average value and the maximum value of the mixing scalar determined over all measurement positions of the corresponding sensor. The salted tracer is injected with a constant flow rate into the loop with increasing flow rate due to starting up of the pump. That causes the decrease of the tracer concentration during time, what is not typical for the behaviour of the deborated slug in the real reactor. Than, the slug enters the pressure vessel and moves through the measurement cross section of all sensors. During the transport, the slug mixes with the ambient coolant in the vessel and the perturbation reduces, as can be concluded from the decreasing maximum values reached at the different sensor positions.

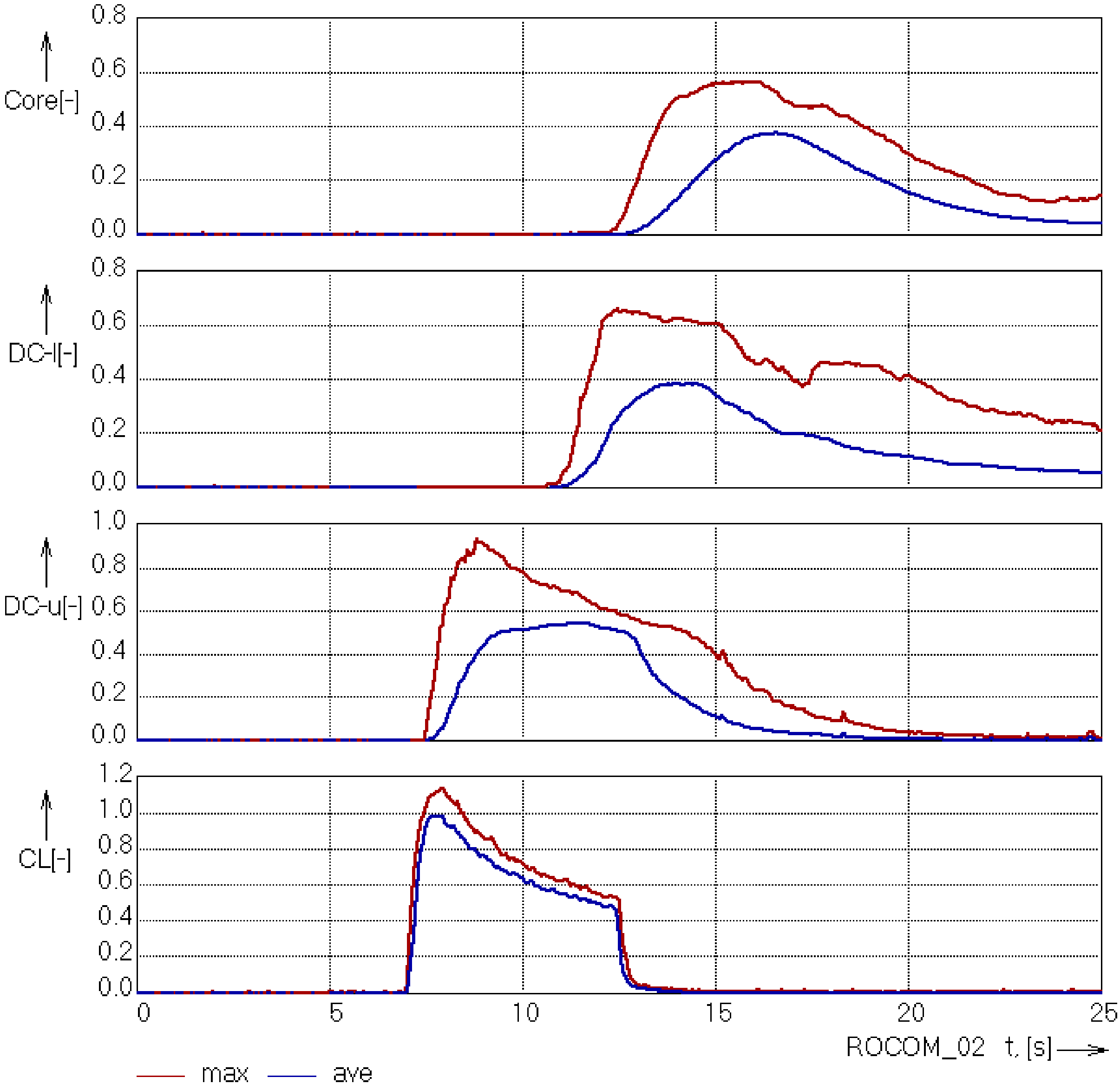

Fig. 2.5.2 Maximum and average mixing scalar a the four sensors in the test facility during the ROCOM_02 experiment

Fig. 2.5.3 shows the time evolution of the mixing scalar at the two sensors in the downcomer. Both sensors are shown in an unwrapped view, the position of the loop with the starting up pump is marked by the red arrow. From the visualization is clearly to be seen, that the deborated coolant passes around the core barrel instead of flowing directly downstream. At the upper sensor, the tracer arrives still below the affected inlet nozzle. With growing time, the tracer spreads in the azimuthal direction. Subsequently, at the lower sensor two maxima of the tracer at azimuthal positions on the back side of the downcomer are observed.

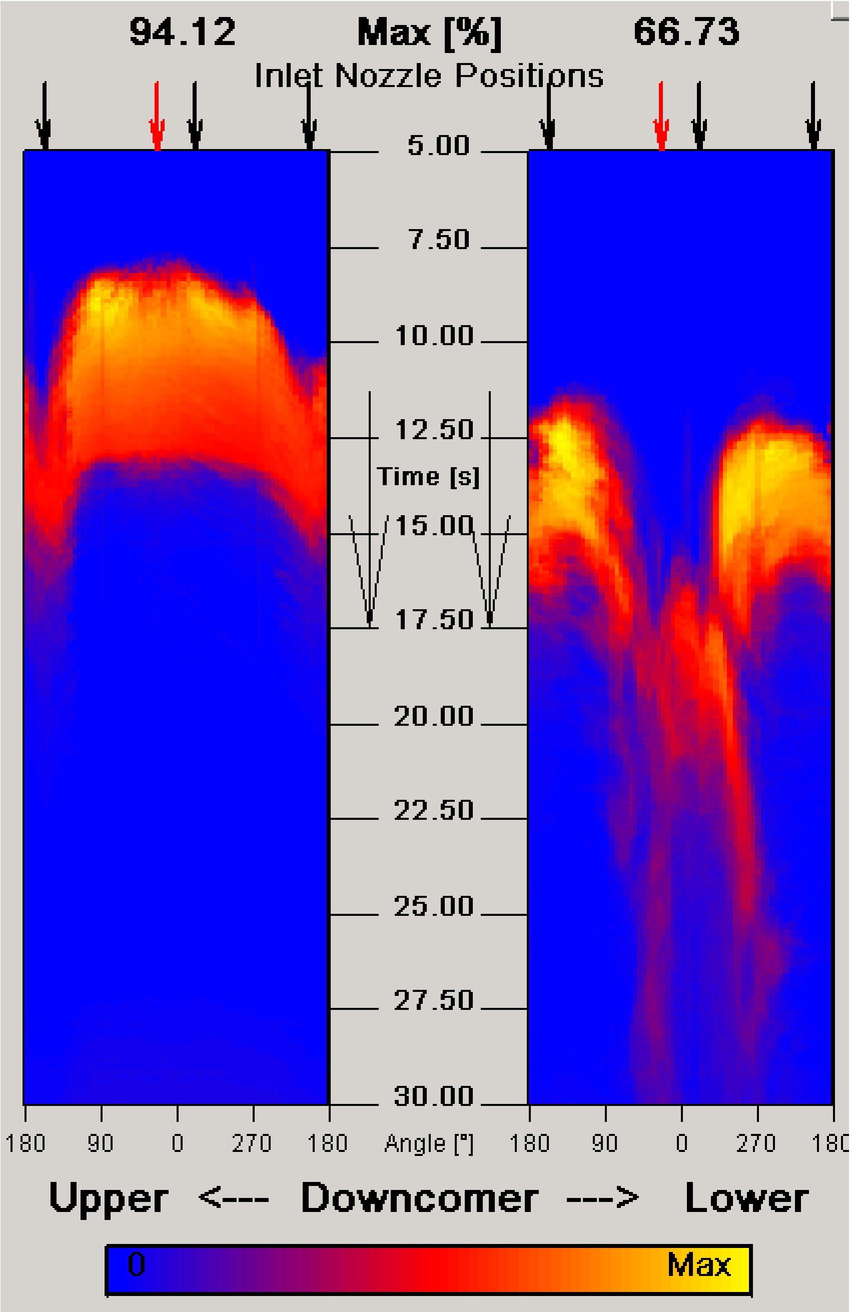

Fig. 2.5.3 Time evolution of the mixing scalar at the two downcomer sensors in the experiment ROCOM_02

A sequence of instantaneous mixing scalar distributions at the core inlet plane are shown on Fig. 2.5.4. The tracer enters the plane of the sensor in the core inlet at the same azimuthal positions as it occurs in the lower part of the downcomer first. These positions are opposite to the active loop. Only with growing time, the part of the core inlet plane, directly below the position of the loop with the starting pump is covered by tracer. The last tracer leaves the core inlet plane from that region.

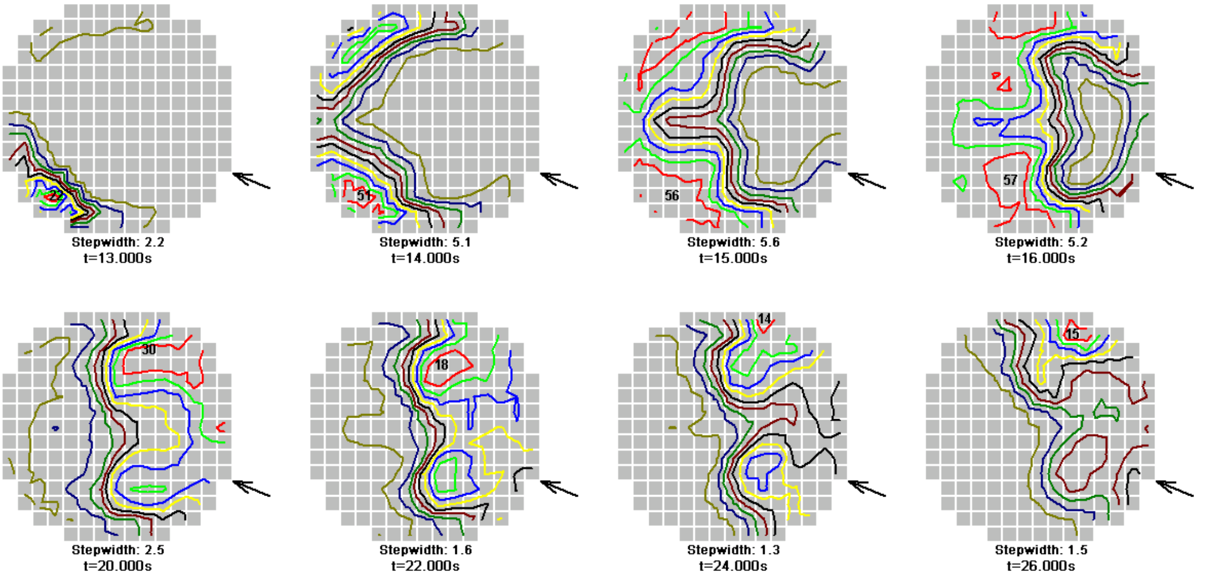

Stepwidth: 2.2 t=13.000s
Stepwidth: 5.1 t=14.000s
Stepwidth: 5.6 t=15.000s
Stepwidth: 5.2 t=16.000s
Stepwidth: 2.5 t=20.000s
Stepwidth: 1.6 t=22.000s
Stepwidth: 1.3 t=24.000s
Stepwidth: 1.5 t=26.000s

Fig. 2.5.4 Time sequences of the mixing scalar a the core inlet plane in the experiment ROCOM_02

2.5.3.2 Uncertainty analysis of the experimental results

It is known from earlier experiments and it was proved during the experimental work in the frame of the FLOMIX-R project, that the time behaviour of the resulting mixing scalar at identical positions in the pressure vessel differ in each single realization of an experiment with identical boundary conditions. Two examples are shown in Fig. 2.5.5. Fluctuations of the flow field in the reactor pressure vessel are the reason for these deviations between single realizations of one experiment. These fluctuations are due to the turbulent nature of the flow, and therefore they appear by chance to a certain degree. As can be seen from Tab. 2.4, all experiments in the current project were repeated five times. The results of these single realizations were averaged. These averaged data are documented and used for further analysis. That was done to damp the statistical fluctuations mentioned above.

It is possible to use the data of the single realizations to carry out an uncertainty analysis of the obtained results. That was done for all experiments and the results of this uncertainty analysis were included into the documentation [Kli03]. This analysis is described for the experiment ROCOM_02 as an example.

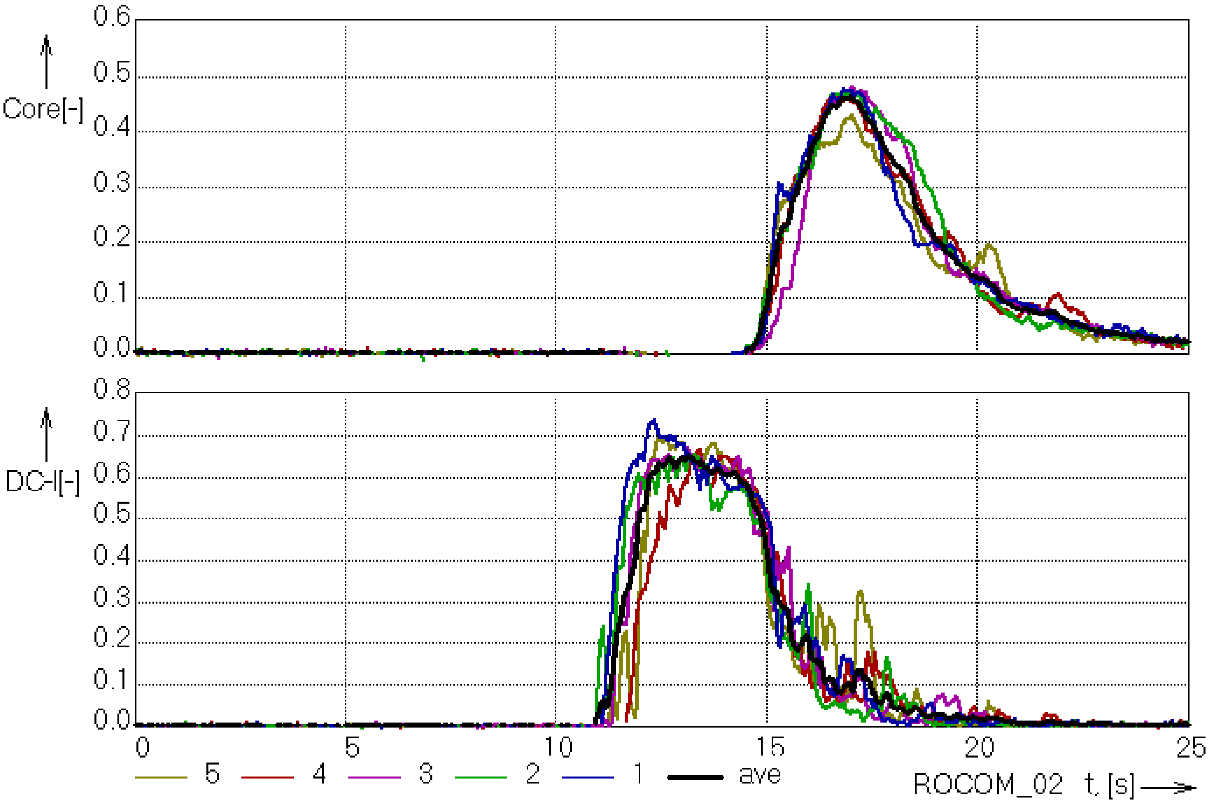

Fig. 2.5.5 Mixing scalar at one measurement position in the downcomer and at the core inlet in the single realizations of the experiment ROCOM_02

In the first step, the minimum error amount $FS_{\min,\Theta}$ for each local value of the mixing scalar at each time point is calculated according to equ. (2.5.2) using the averaged values and the n single realizations.

$$FS_{\min,\Theta}(x,y,z,t)=\sum_{k=1}^{n}(\theta_{ROCOM,k}(x,y,z,t)-\bar{\theta}_{ROCOM}(x,y,z,t))^2 \qquad \text{(Equ. 2.5.2)}$$

The standard deviation is calculated according to

$$s_\Theta(x,y,z,t)=\sqrt{\frac{FS_{\min,\Theta}(x,y,z,t)}{n-1}} \qquad \text{(Equ. 2.5.3).}$$

In the last step, the confidence intervals can be calculated using equ. (2.5.4).

$$u_{z,\Theta}(x,y,z,t)=\pm t_P.\frac{s_\Theta(x,y,z,t)}{\sqrt{n}} \qquad \text{(Equ. 2.5.4)}$$

This confidence interval characterizes the interval around the average value in which the measured value can be found with a given probability of the statistical confidence. Hereby, t_p is the value of the Student-factor. This factor varies with the selected statistical confidence. In the frame of the FLOMIX-R project, the confidence intervals for 68.4 % (corresponds to 1 σ), for 95.4 % (2 σ) and 99.5 % (3 σ) were calculated and included into the documentation, whereby σ is the square root of the variance of the distribution. For five realizations the value of the Student-factor for these three confidence interval is:

P = 68.3 %	tp = 1.11
P = 95.4 %	tp = 2.57
P = 99.5 %	tp = 4.03.

Using eq. (2.5.2) to (2.5.4), the time curves for the confidence intervals were calculated for each measurement position of the three wire mesh sensors inside the reactor pressure vessel. Fig. 2.5.6 shows an example for the measurement position of the core inlet sensor, shown already in Fig. 2.5.5, and additionally for the average and the maximum mixing scalar at that sensor.

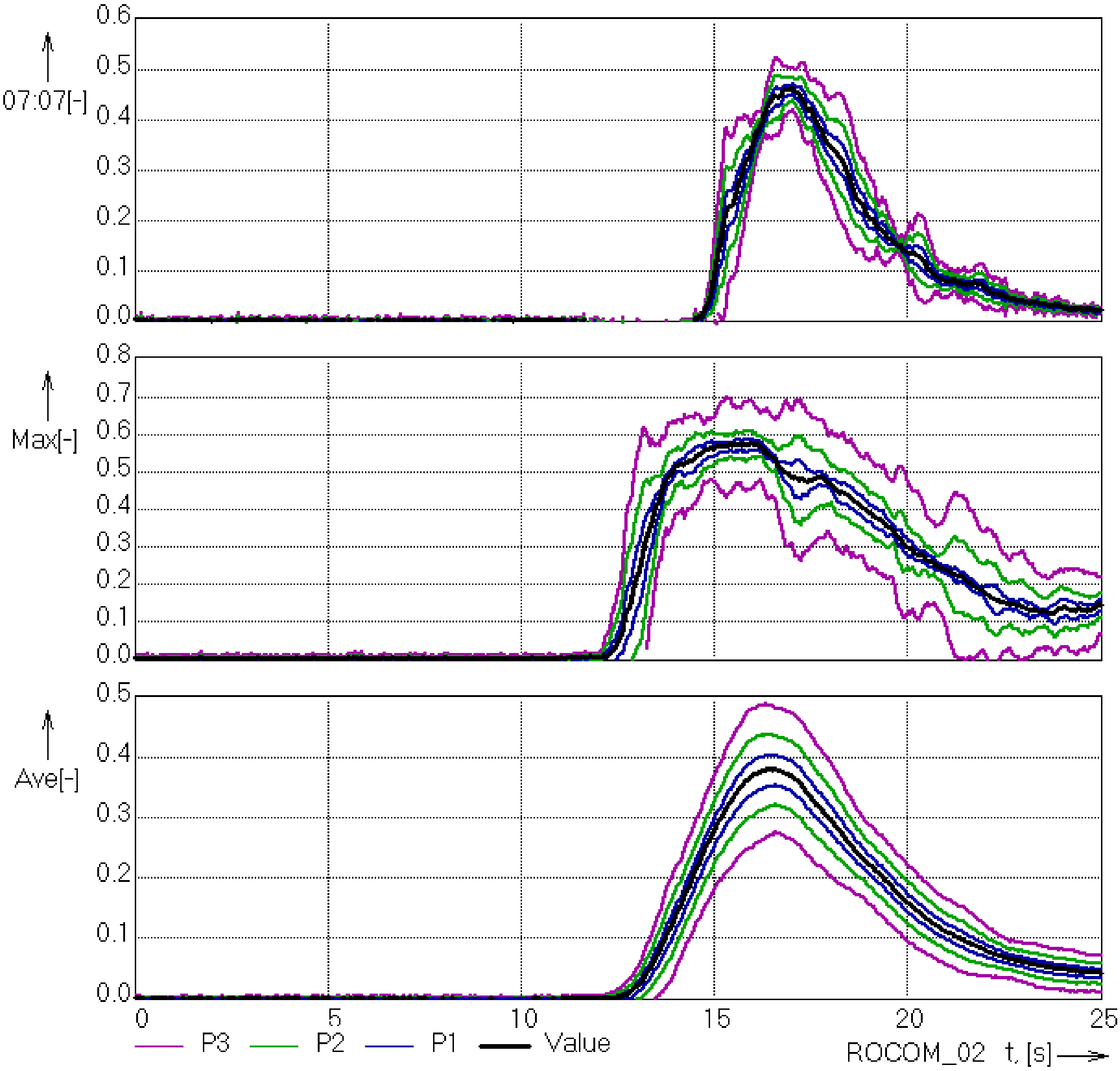

Fig. 2.5.6 Confidence intervals for the average and maximum mixing scalar at the core inlet and for one certain measurement position in the experiment ROCOM_02

In the following sections, the impact of the different variations of the conditions and the parameters of the pump start-up transient are discussed.

2.5.3.3 Influence of the initial slug size

In the experiments ROCOM_01; 02; 03 and 12, the initial slug size was varied. All other boundary conditions are identical. The initial slug size can vary in real boron dilution transients depending on the amount of low borated water that has been accumulated in the loop during a LOCA event. Fig. 2.5.7 shows the time evolution of the maximum mixing scalar at all four sensor positions. At the sensor in the cold leg inlet nozzle, the start of the mixing scalar increase occurs in all experiments at the same time. This should be the case because of the same position for injection start times of the slugs of different volumes. The fulfillment of this conditions in the experiments underlines the reproducibility of the experiments at the ROCOM test facility. At all other sensors, the starting time point is identical, too. With growing slug volume, the reached maximum value is growing, too. Only between ROCOM_02 (20 m^3) and ROCOM_01 (40 m^3) the maximum value is no more increasing. That is connected with the injection technology in the ROCOM experiments already mentioned above. The hydraulic slug volume is determined on the basis of front and the back edge of the mixing scalar at the first sensor. The decreasing of the mixing scalar during increasing loop flow rate leads to the fact, that the rear part of the slug does not contribute to the maximum mixing scalar. But the overall salt volume input in ROCOM_01 is greater than in ROCOM_02 , what results in an increasing average mixing scalar (Fig. 2.5.8).

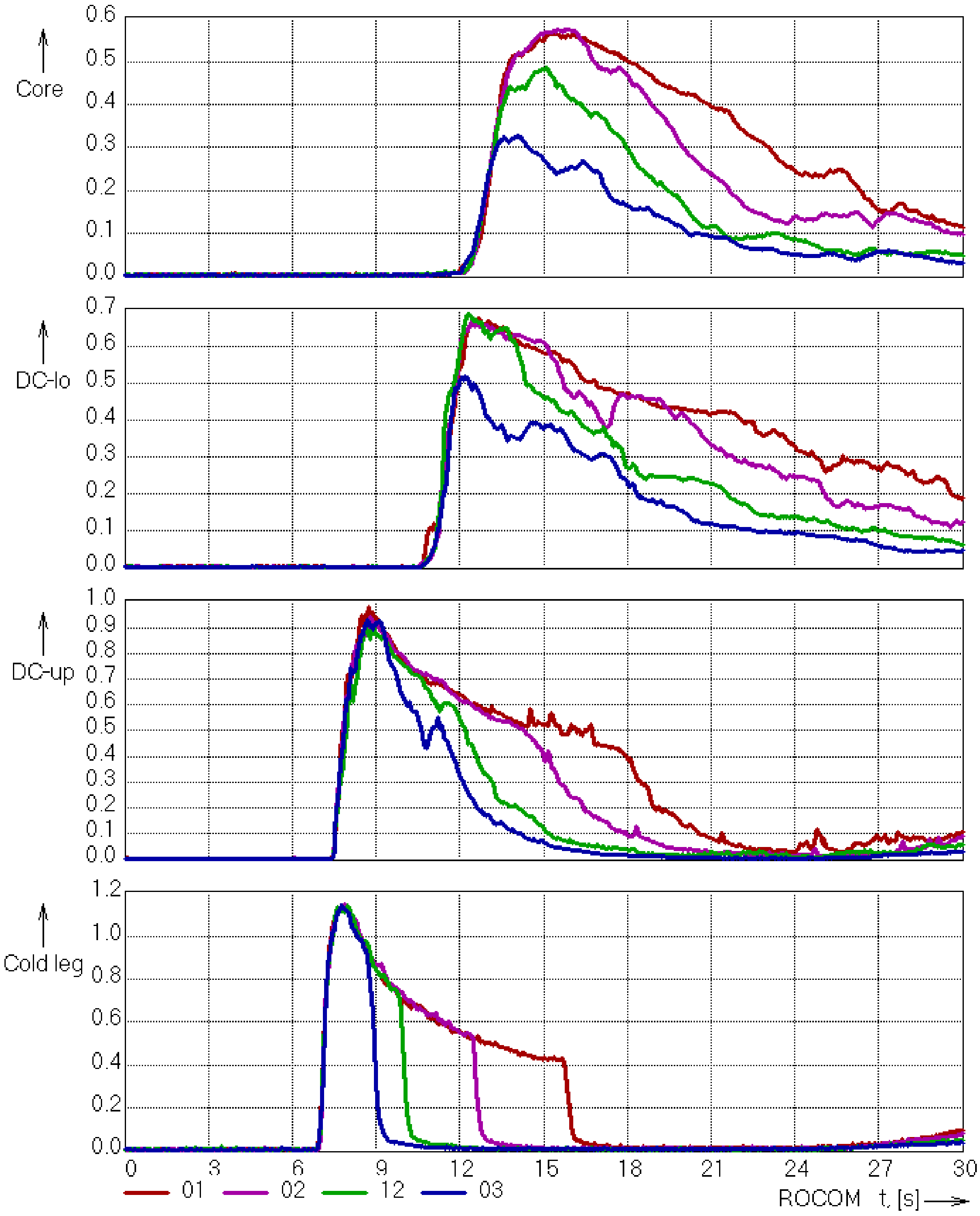

Fig. 2.5.7 Maximum mixing scalar at the different sensors in the test facility during the experiments with variation of slug size

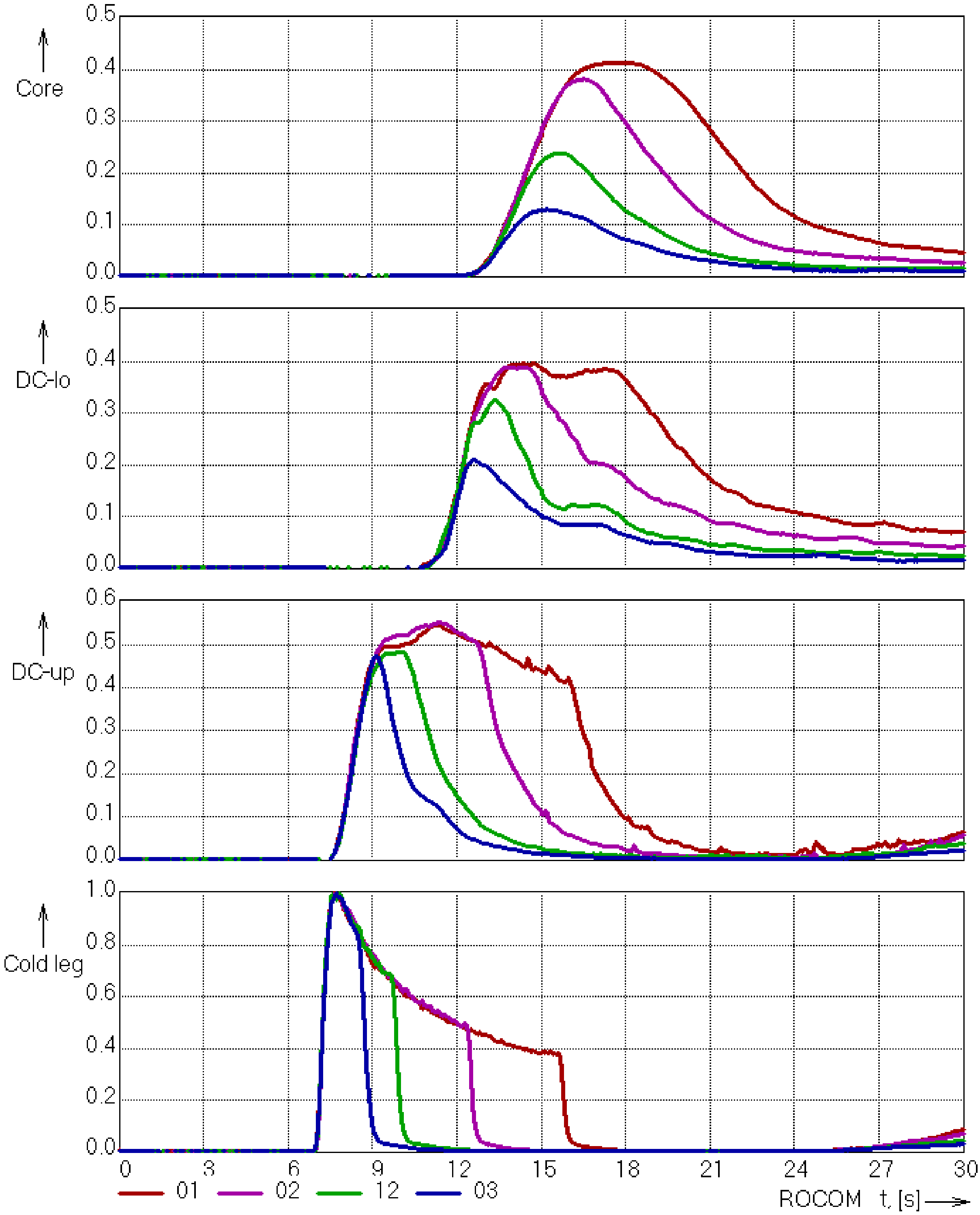

Fig. 2.5.8 Average mixing scalar at the different sensors in the test facility during the experiments with variation of slug size

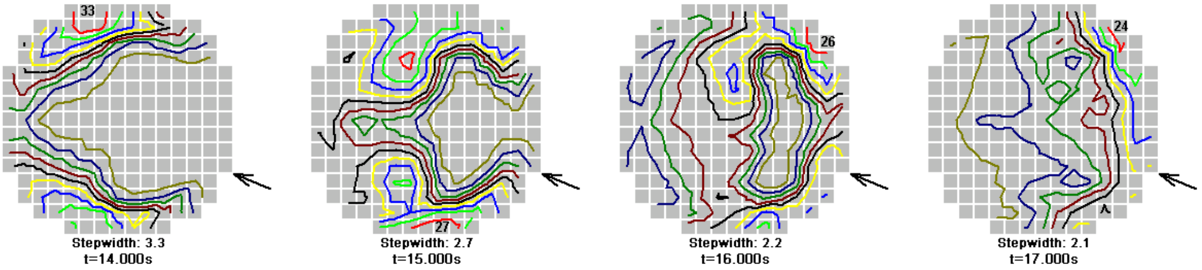

Rocom_03; V_{slug}= 4.0 m^3;

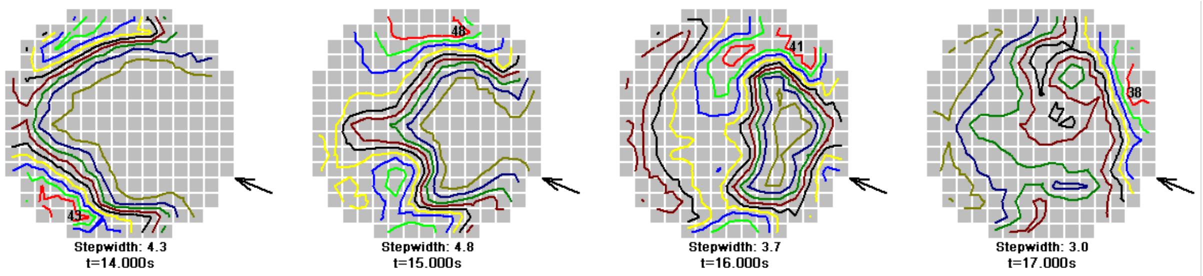

Rocom_12; V_{slug}= 8.0 m^3;

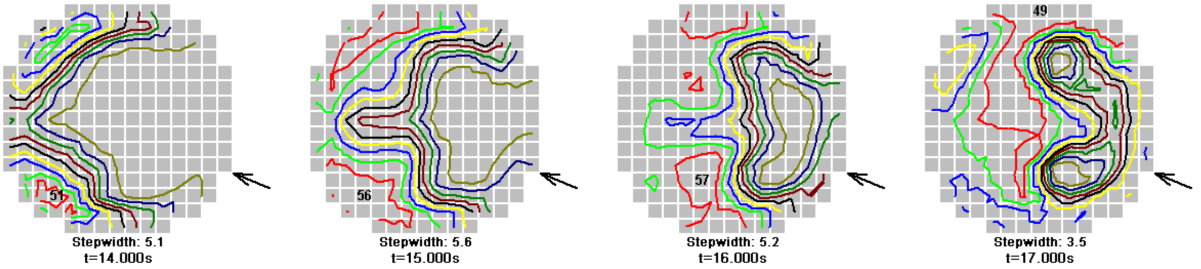

Rocom_02; V_{slug}= 20.0 m^3;

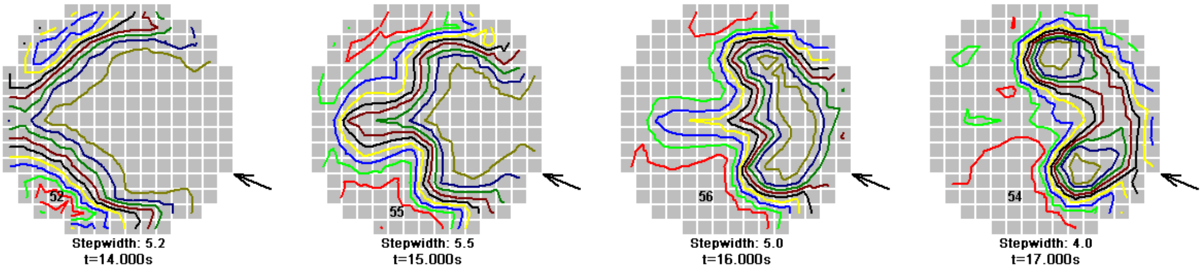

Rocom_01; V_{slug}= 40.0 m^3;

Fig. 2.5.9 Comparison of time sequences of the instantaneous mixing scalar at the core inlet in the different experiments with variation of initial slug volume

Fig. 2.5.9 shows time sequences of the instantaneous mixing scalar at the inlet into the reactor core in the experiments with variation of the initial slug volume. From the qualitative point of view, the transport of the tracer through the core inlet plane looks rather similar in the various tests. The maximum concentration increases with increasing slug volume. The shift of the tracer maximum from the opposite side to the position of the loop with the starting up pump is faster in the experiments with smaller slug volume. The process of tracer transport through the core inlet plane goes faster, too.

The results for the maximum and averaged mixing scalar are summarized in Tab. 2.5

Tab. 2.5 Maximum of the mixing scalar and maximum of the average including corresponding time points of occurrence

Experiment	**Slug volume [m^3]**	**Maximum of the average mixing scalar [%]**	**Time of the maximum of the average mixing scalar [s]**	**Overall maximum of the mixing scalar [%]**	**Time of the overall maximum of the mixing scalar [s]**
ROCOM_03	4	13.4	14.95	36.3	13.65
ROCOM_12	8	23.8	15.85	48.5	15.15
ROCOM_02	20	38.2	16.55	57.5	15.95
ROCOM_01	40	41.5	18.00	56.6	15.30

2.5.3.4 Influence of the initial slug position

The initial distance of the slug from the pressure vessel was 2.5 m in the experiment ROCOM_04 and 40 m in the experiment ROCOM_06. Fig. 2.5.10 compares the time evolution of the mixing scalar at the two sensors in the downcomer. In the first experiment, the most part of the tracer passes the cross section of the upper sensor directly below the loop with the starting up pump, at the lower sensor no tracer is found on the opposite side of the downcomer. In the second experiment, the tracer reaches the back side of the downcomer already in the upper part. The distribution at the time point of maximum at the core inlet for all four experiments with variation of the initial slug position shows the same tendency (Fig. 2.5.11). With increasing initial distance, the maximum at the core inlet moves to the side opposite to the position of the loop with the starting up pump. Further, the first experiment shows a significantly lower maximum value. That indicates, that a qualitative change of the flow conditions takes place during the pump start-up process. The typical velocity field, being responsible for the maximum at the opposite side of the core inlet cross section, establishes with a time delay of some seconds, only. Therefore, slugs entering the vessel at an early stage of the process, flow more or less directly down, instead of flowing to the opposite side.

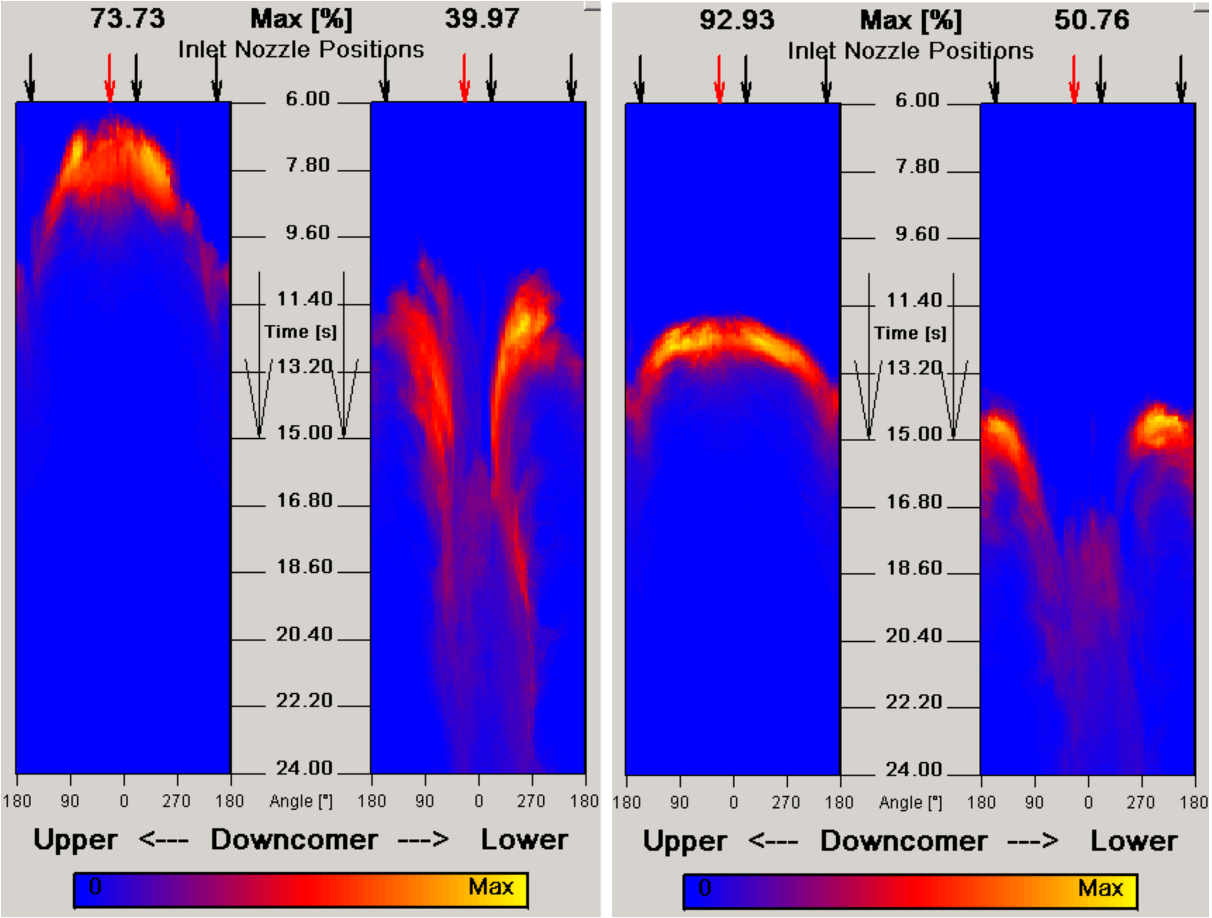

Fig. 2.5.10 Time evolution of the mixing scalar at the two downcomer sensors in the experiment ROCOM_04 (left) and ROCOM_06 (right)

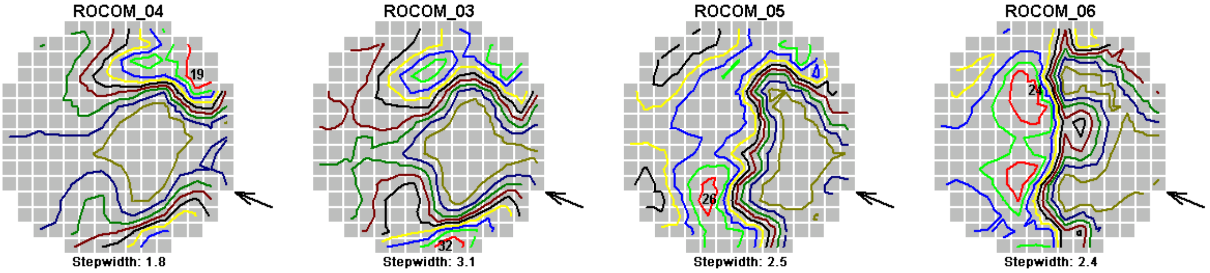

Fig. 2.5.11 Core inlet distribution of the mixing scalar at the time point of maximum in the experiments with variation of the initial distance

2.5.3.5 Final flow rate

In the experiments ROCOM_03, ROCOM_10 and ROCOM_11, the final flow rate was varied. The ramp length was held constant, 14 s in all three cases. Fig. 2.5.12

shows the time evolution of the velocity and the traveled distance of the slug. The different final flow rates lead to different steepness of the velocity curve, what results in differences in the traveled distance for slugs starting from the same initial position. The time evolution of the average mixing scalar in the upper part of Fig. 2.5.12 confirms that the slug in each experiment passes the cross section of the sensor in the inlet nozzle after a distance of 2.0 m (corresponding to 10 m in the original reactor). Fig. 2.5.13 shows the time evolution of the maximum mixing scalar at all sensors in the pressure vessel. The shape of the time evolution and reached maximum value are identical between the three experiments The time shift due to the different final flow rates is the only difference what can be observed between the experiments.

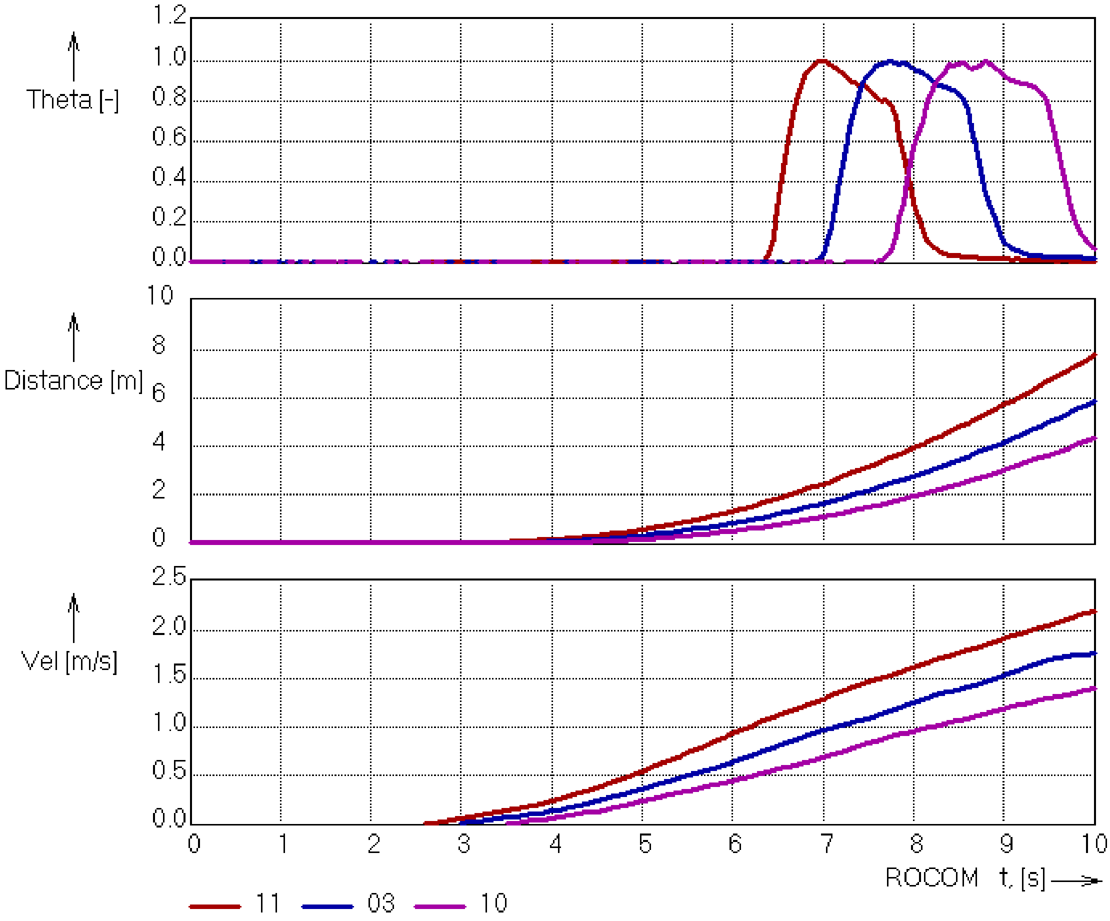

Fig. 2.5.12 Time evolution of the coolant velocity, the traveled distance and the average mixing scalar at the inlet nozzle in the three experiments with variation of the final flow rate

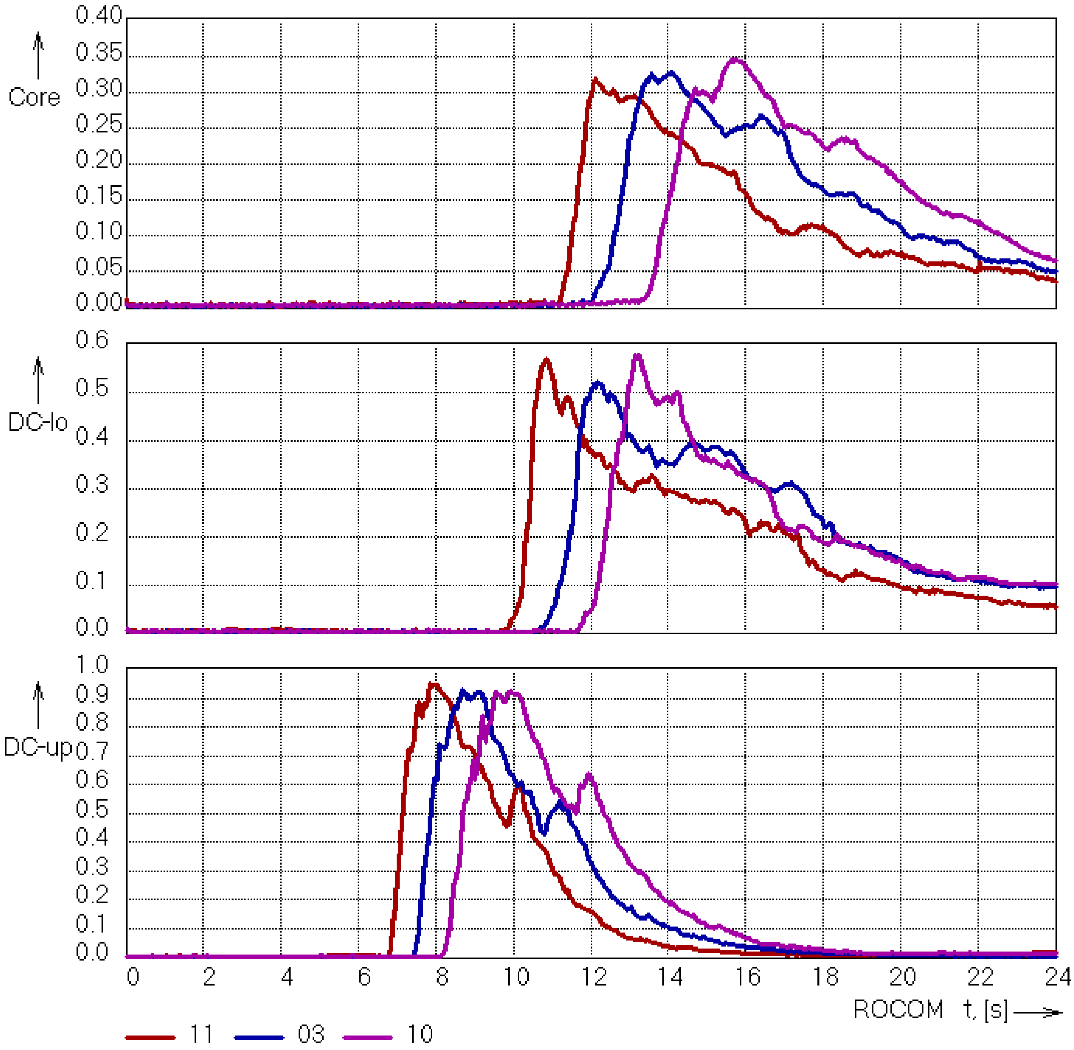

Fig. 2.5.13 Time evolution of the maximum mixing scalar at the sensors in the pressure vessel in the three experiments with variation of the final flow rate

2.5.3.6 Status of the passive loops

The experiment ROCOM_07 differs from experiment ROCOM_02 only by the status of the passive loops. In the experiment ROCOM_07, they are closed, so that a reverse flow is not possible. The volume flow rate in the loop with the starting up pump is practically not affected by the closed loops. The tracer is injected at the same time in both experiments.

In Fig. 2.5.14 to Fig. 2.5.16, the time course of the maximum and average mixing scalar at all three sensor positions inside the reactor vessel is shown. The bands for the confidence interval of 95.4 % are included into the figs. These bands were calculated separately for each experiment.

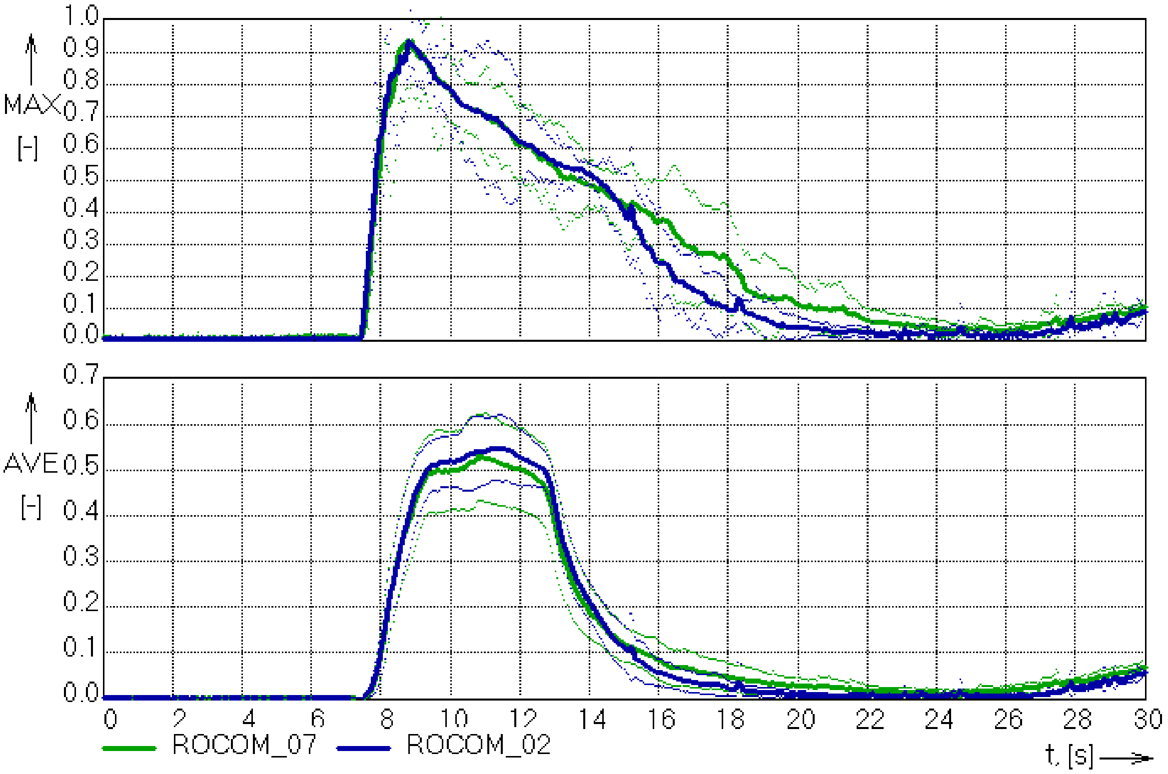

Fig. 2.5.14 Time evolution of the average mixing scalar at the upper downcomer sensor in the experiments ROCOM_02 and ROCOM_07 including the confidence interval of 95.4 %

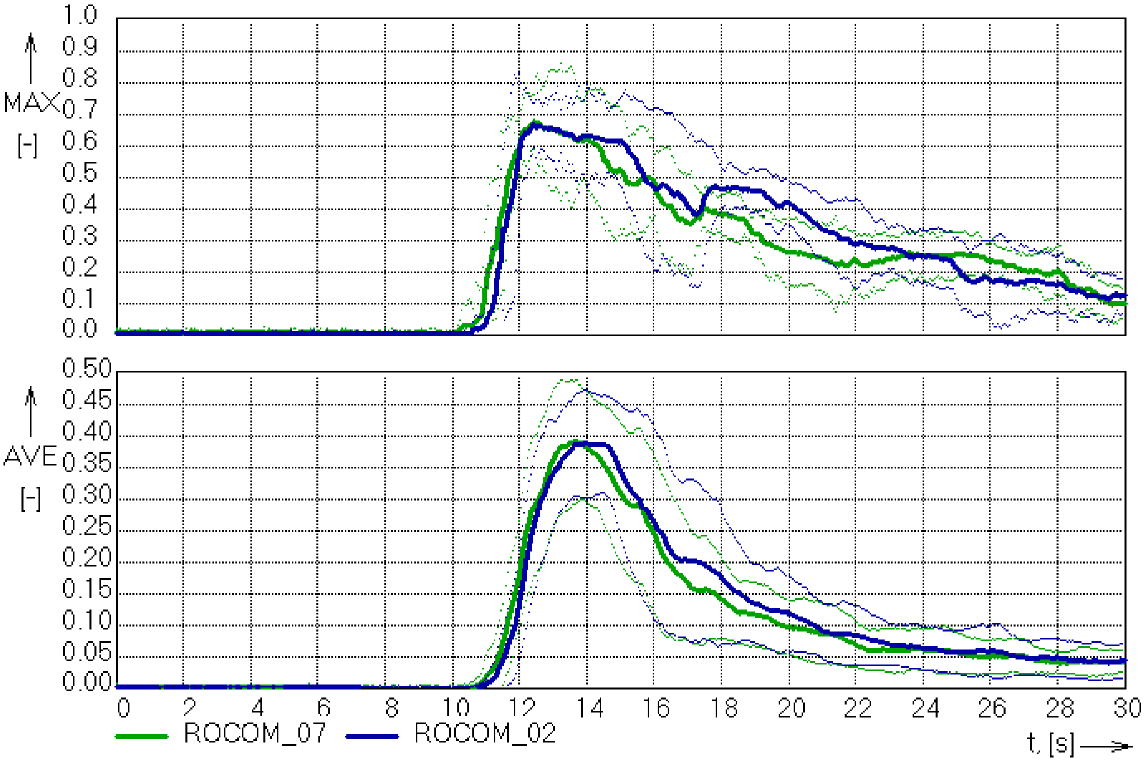

Fig. 2.5.15 Time evolution of the average mixing scalar at the lower downcomer sensor in the experiments ROCOM_02 and ROCOM_07 including the confidence interval of 95.4 %

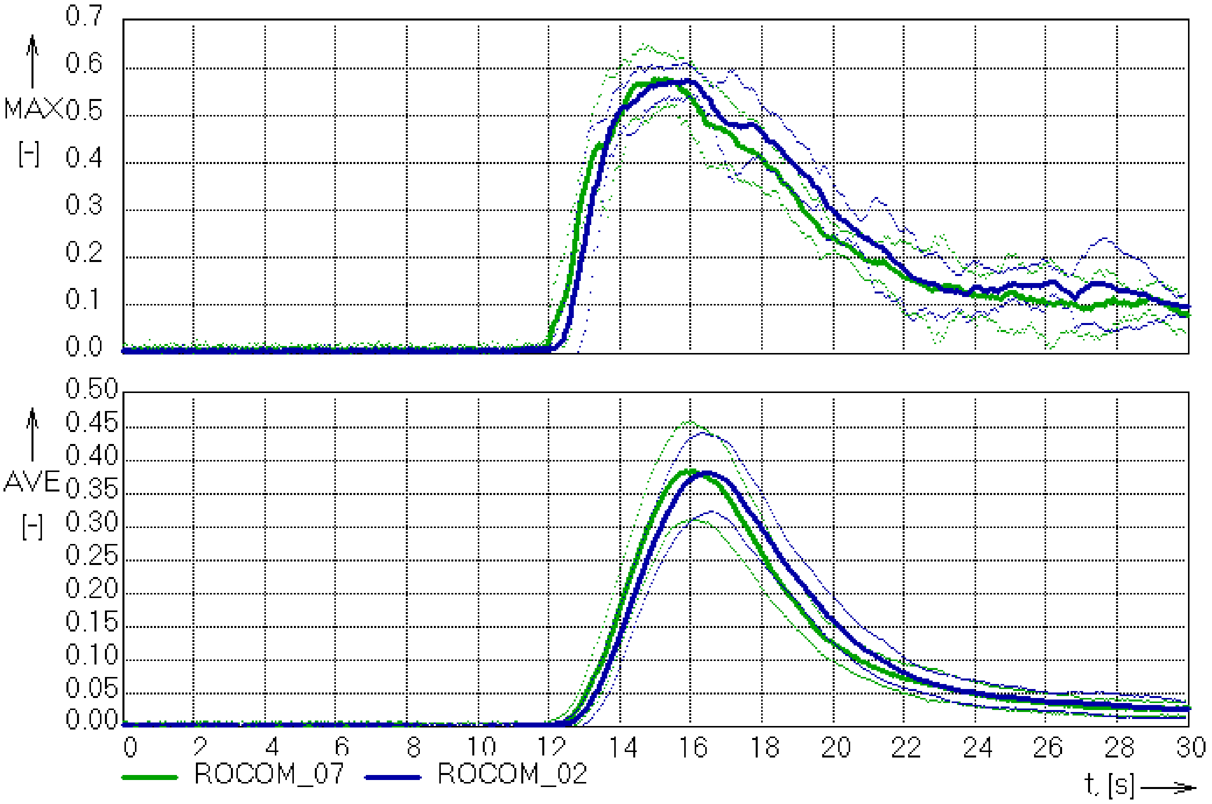

Fig. 2.5.16 Time evolution of the average mixing scalar at the core inlet sensor in the experiments ROCOM_02 and ROCOM_07 including the confidence interval of 95.4 %

For all sensors, the time course of the average and the maximum mixing scalar are very close between the two experiments. The status of the loops has almost no influence on the mixing inside the reactor pressure vessel. The calculated confidence intervals of the experiments are overlapping, so that the average of one experiment belongs to the confidence interval of the other one trough all the time. The tracer arrives at the lower downcomer sensor and at the core inlet sensor slightly earlier in the experiment with closed gate valves as can be concluded from the starting of the increase of the mixing scalar at these sensor positions. That is connected with a higher resulting velocity in the downcomer due to the absence of reverse flow. This observation is the only difference between the two experiments.

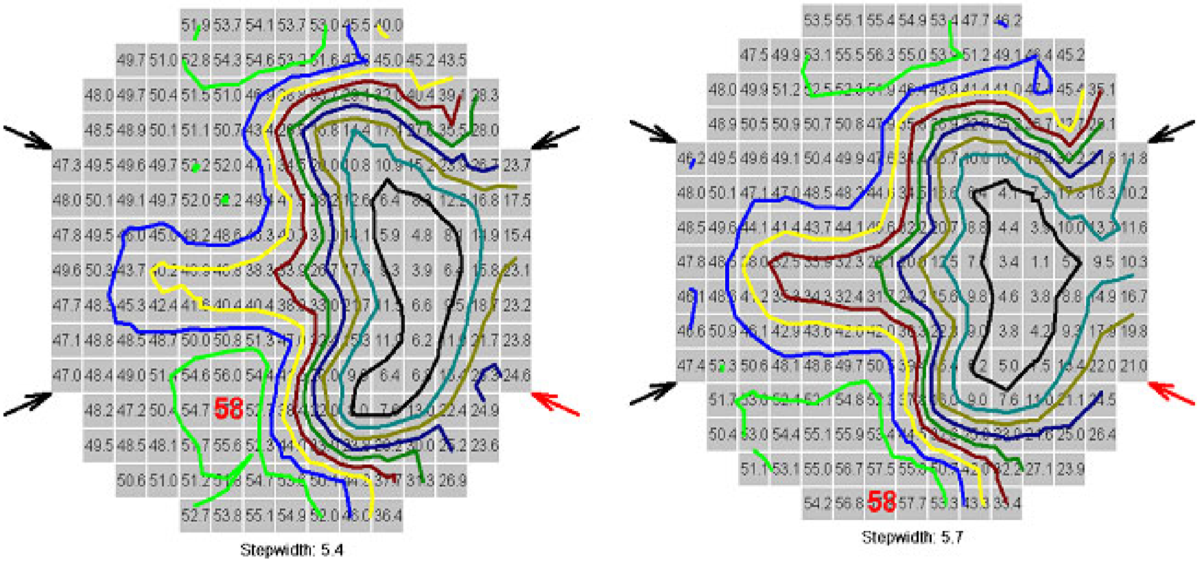

Fig. 2.5.17 Mixing scalar at the time point of maximum in the experiments ROCOM_02 (left) and ROCOM_07 (right)

Fig. 2.5.17 shows the distribution of the mixing scalar at the core inlet plane at the time point of maximum in the experiments with open and closed gate valves. As can be seen, the shape of the distribution is identical. The maximum value reached is identical, too and the position belongs to the same region of the core inlet plane.

2.5.3.7 Variation of the Reynolds-number at constant Strouhal-number

The experiments ROCOM_03, ROCOM_08 and ROCOM_09 were carried out to investigate the influence of the Reynolds-number at constant Strouhal-number in transient experiments. The Strouhal-number Sr is defined as follows:

$$Sr = \frac{L}{w * \tau} \qquad \text{(Equ. 2.5.5),}$$

where L is the characteristic length, w the velocity and τ the time. To hold the Sr-number constant, the product from velocity and time should be constant. For the transient experiments under consideration, the velocity is the velocity on the plateau after the ramp, the time is the time of reaching the plateau value. To be able to compare the time histories of tracer concentrations, the time axes should be stretched according to the scaling factor. Fig. 2.5.18 shows the measured velocity in the loop with the starting up pump in the three experiments in the lower part. In the upper part, the velocity curves for the experiments ROCOM_08 and ROCOM_03 were stretched with the corresponding scaling factor (2.0 for ROCOM_08; 4.0 for ROCOM_03) to bring all three experiments into the same time scale. Fig. 2.5.19 show the average of the mixing scalar at the inlet into the reactor vessel in the three experiments (original and scaled time curves). For the experiments ROCOM_08 and ROCOM_09, fully coincidence was achieved, while ROCOM_03 starts about 2 s to earlier. Fig. 2.5.20 shows the time history of the maximum mixing scalar at all three sensor positions in the vessel. At the upper downcomer sensor, the shape and reached maximum value are nearly identical between the three experiments, at the lower downcomer sensor, the curve for the experiment ROCOM_09 deviates starting from t = 45 s. The same tendency can be observed at the core inlet plane, the reached maximum value in the experiment ROCOM_09 is lower, too. Fig. 2.5.21 shows the maximum value, reached at the core inlet, together with the confidence intervals for 2 σ and 3 σ. The spreading of the confidence intervals is very high. Although the measured maximum mixing scalar for the experiments ROCOM_03 and ROCOM_08 are higher than the value for the experiment ROCOM_09, the confidence intervals for 3 σ are overlapping. Due to this unusual high spreading in the confidence intervals of the latter experiment it is assumed, that during the experiment ROCOM_09 some disturbance from outside takes place (e.g. pump control or something similar). For the other two experiments, the scaling of the Reynolds-Number at constant Strouhal-Number works properly.

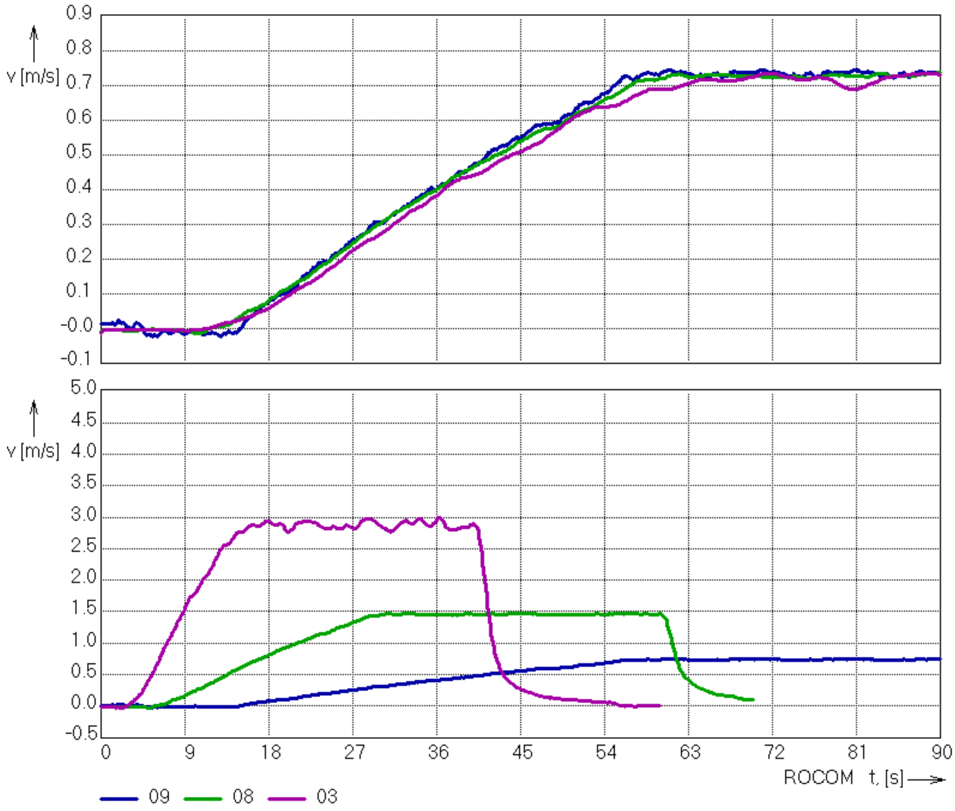

Fig. 2.5.18 Velocity in loop 1 (original and scaled) in the experiments ROCOM_03, ROCOM_08 and ROCOM_09

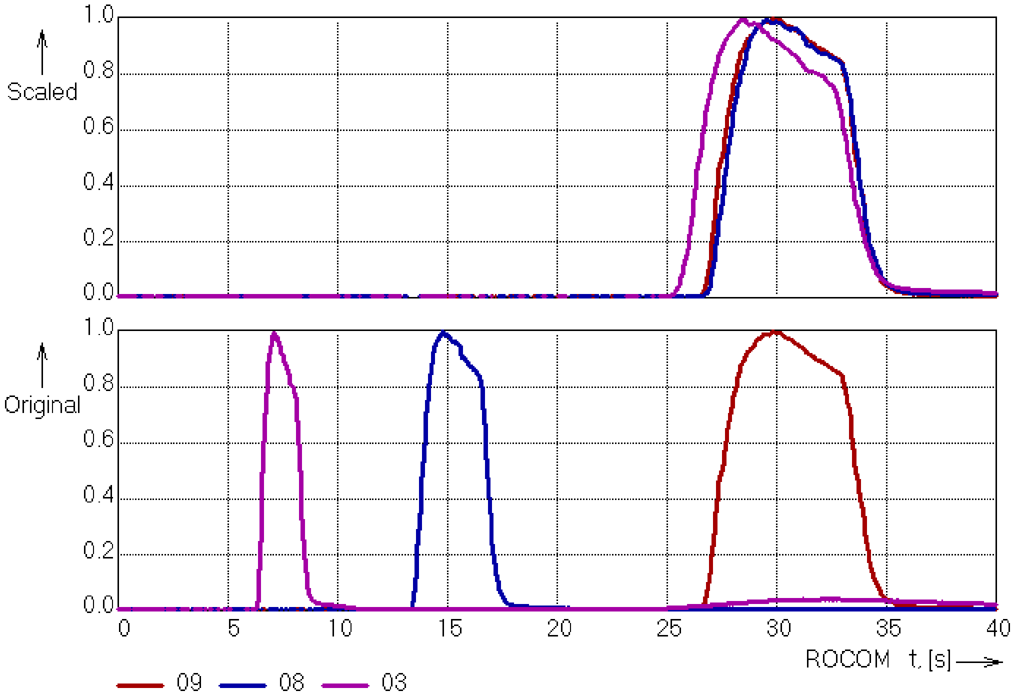

Fig. 2.5.19 Time evolution of the average mixing scalar (original and scaled) at the inlet into the vessel

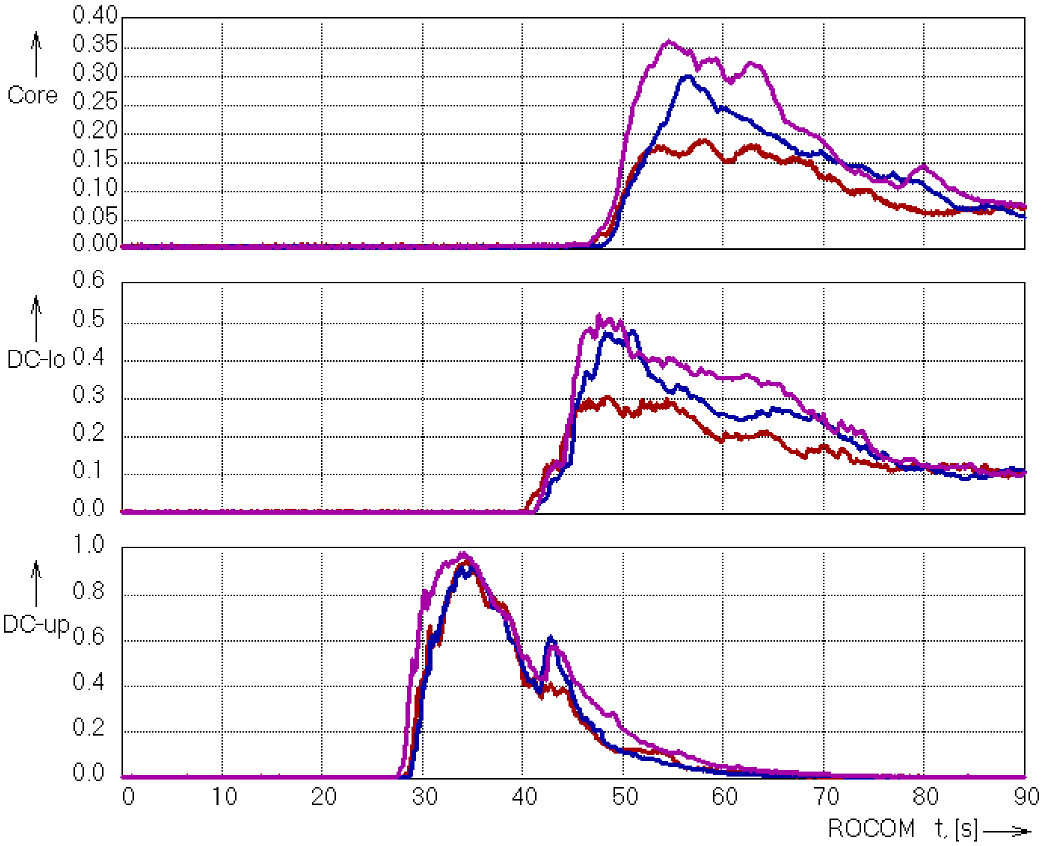

Fig. 2.5.20 Time evolution of the maximum mixing scalar at the sensor positions in the vessel

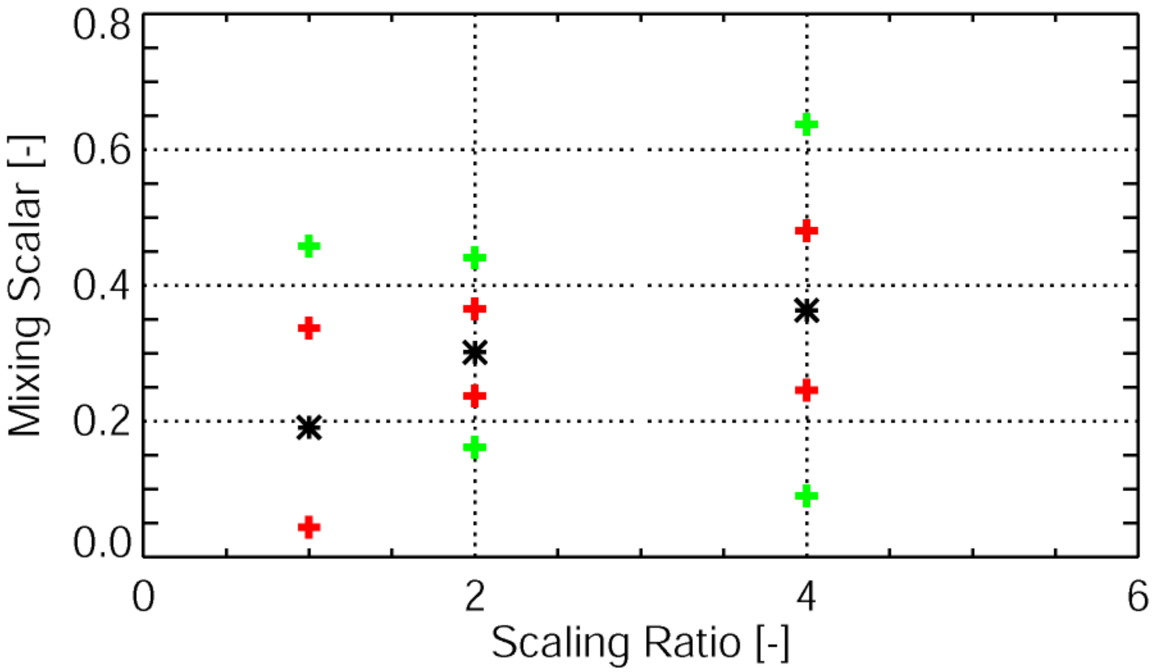

Fig. 2.5.21 Maximum mixing scalar a the core inlet in the scaling experiments with confidence intervals of 2 σ and 3 σ

2.5.4 Velocity measurements during pump start-up process

2.5.4.1 Measurement system and positions

The measurements of the velocity were carried out by means of a laser Doppler anemometer of the Fa. Dantec (Fig. 2.5.22).

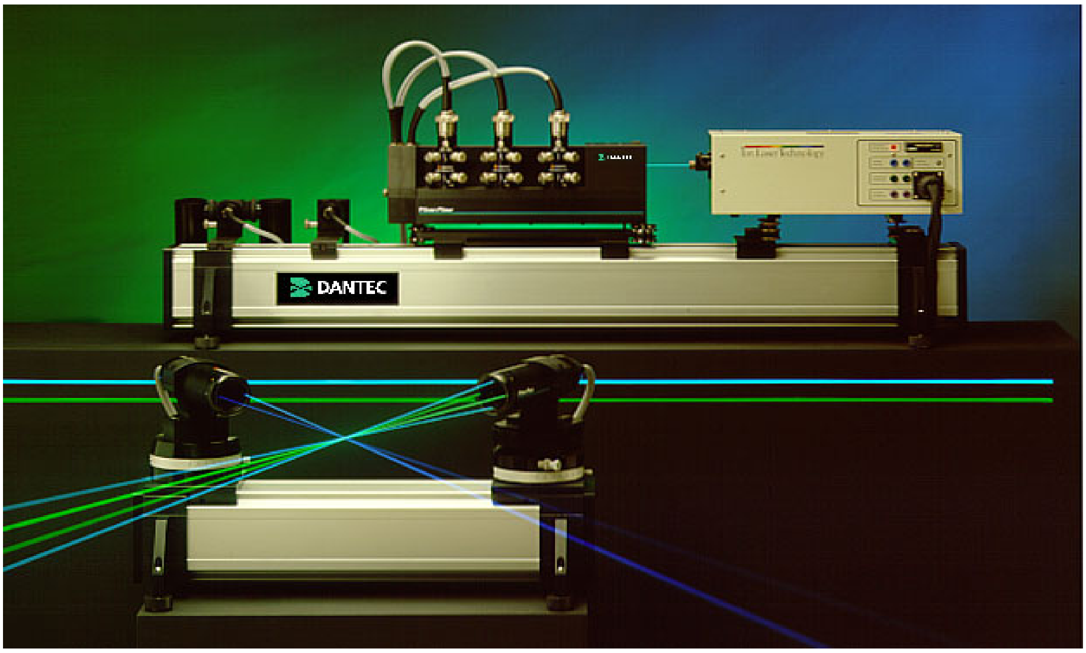

Fig. 2.5.22 Laser Doppler anemometer used for the transient velocity measurements

The velocity was measured at the outlet of the downcomer in a plane 1045 mm below the middle of the nozzle region. Measurements of the vertical velocity component were made at 16 positions equally distributed around the circumference of the downcomer. In radial direction, the measurement position was in the middle of the downcomer.

2.5.4.2 Measurement results

The velocity was measured for the start-up process of the first MCP. The start-up ramp is shown on Fig. 2.5.1.

For the transient velocity measurements, the experiments were carried out in the following way: The pump in loop 1 was started at t = 0 s according to the frequency ramp shown on Fig. 2.5.1. After reaching the plateau value the final frequency was hold until t = 30 s. At this time, the pump was switched off, data were recorded until t = 60 s. This process was repeated five times, all bursts occurring during the measurement time were recorded. The described process was repeated for all mentioned 16 angle positions. The corresponding data are documented in [Kli03]. The upper part of Fig. 2.5.23 shows the volume flow rate averaged over the five realizations of the experiment, the lower part shows all measured by LDA data for three different angle positions.

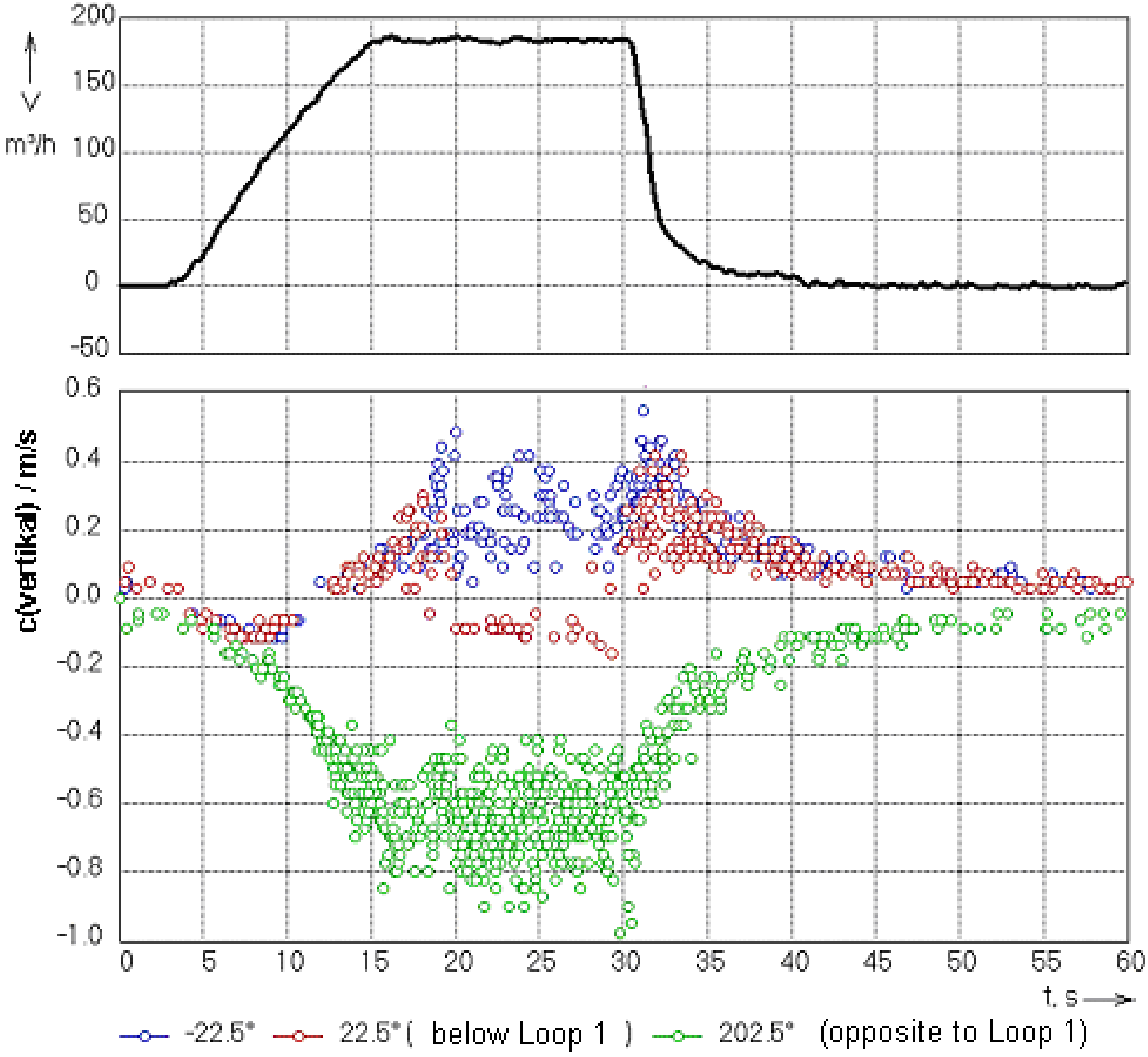

Fig. 2.5.23 Volume flow rate in Loop 1 and LDA data for three angle positions

The number of measured values (registered bursts) is not constant over time. In the parts of the transient with low velocity, sometimes no data were recorded over several seconds. Nevertheless, the obtained data allow to draw conclusions about the flow behaviour during the start-up process.

The time evolution of the velocity at three characteristic angle positions is shown on Fig. 2.5.23. The position 22.5° is directly below the nozzle with the staring-up pump, the position 202.5 is on the opposite side of the downcomer. The position –22.5° corresponds to the angle position of the neighboring loop. This position was included into the Fig. 2.5.23 due to the fact, that there the maximum upwards directed velocity values were measured (Downwards directed velocity values have the sign “-“, upwards directed the sign “+”.).

At about t = 7.5 s, the velocity at all three positions starts to increase, the whole fluid comes in motion, accelerated in a similar way. Only after that, a secondary flow starts to establish. A recirculation area appears in the downcomer, therefore the velocity below the nozzle with the starting-up pump decreases again. Then, the velocity below this nozzle changes the sign. That means, the flow direction changes, the water in that area flows against the main flow direction. The highest values of the upwards directed velocity were measured below the neighboring inlet nozzle (-45° according to the position of the loop with the starting-up pump).

A t = 20 s, that means 5 s after reaching the final flow rate, the velocity below the inlet nozzle with the running pump changes the sign, again. The reverse flow below the neighboring nozzle remains until the switch-off of the pump.

After switching-off of the pump, the flow rate in loop 1 decreases fast. After 10 s, the flow meter in the loop does not measure any flow. Contrary to that, areas with moving fluid still exist over a longer time in the downcomer (Fig. 2.5.23). This is connected with the swirls rotating in the downcomer. They are decaying over a longer time.

The start of very intensive fluctuations of the velocity at all positions in the downcomer is observed in the time between t = 12.5 s and t = 17.5 s. Obviously, swirls of lower spatial extension start to appear at that time.

For different time points, the azimuthal velocity distribution is shown on Fig. 2.5.24. The development of the characteristic velocity distribution described above is good to be seen.

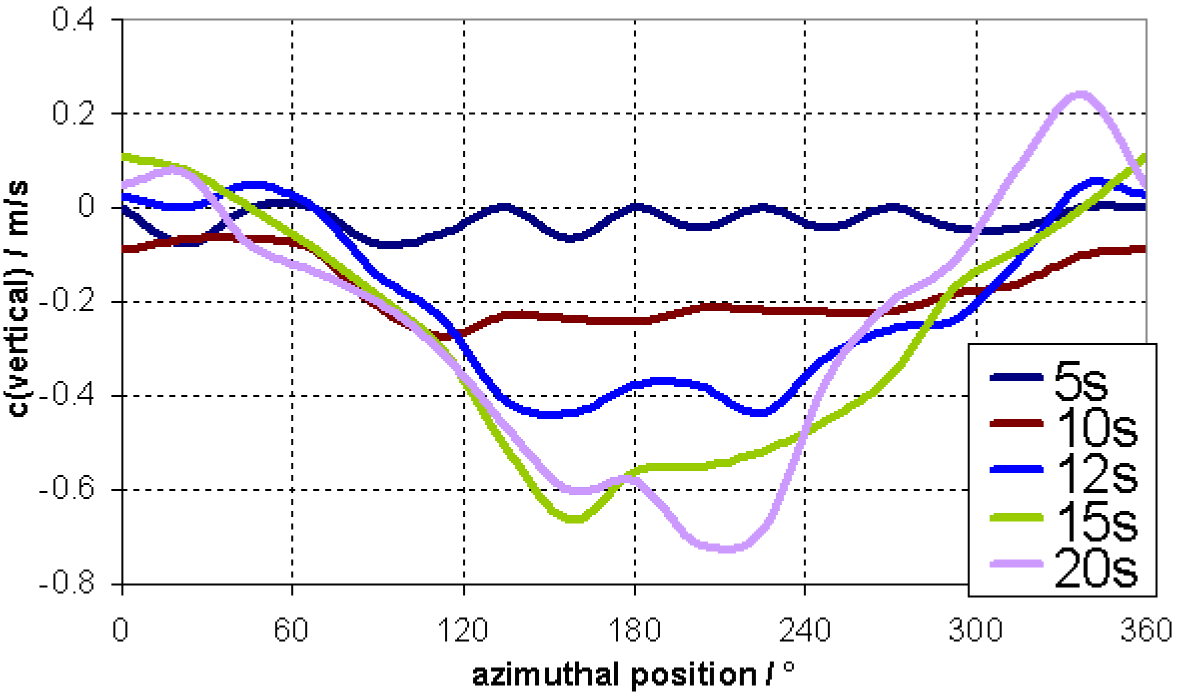

Fig. 2.5.24 Angular distribution of the measured velocity at different time points

3 Slug mixing experiments at the Vattenfall test facility

3.1 Introduction

The work presented in this report deals with a category of Rapid Boron Dilution Events characterized by a rapid start of a MCP with a slug of unborated water present in the reactor coolant system (RCS) pipe. Model tests have been done at Vattenfall Utveckling AB in a 1:5 scale model of a Westinghouse PWR.

The experimental work models how a slug of unborated water is diluted on its way to the core. The results can be used in determining critical volumes of unborated water.

Experiments are made for the four different scenarios shown in Tab. 3.1:

Tab. 3.1 Description of test cases

Test case	**Slug volume in plant (m^3)**	**Final volume flow rate in model (m^3/h)**	**Ramp length (s)**
VATT-01	14	429	16
VATT-02	8	429	16
VATT-03	4.5	429	16
VATT-04	8	173	40

In the plant, the final volume flow rate is 6 m^3/s and the ramp length (i.e. the approximate time from zero flow rate to maximum flow rate) is 40 seconds. In test case VATT-04 the transit time for the slug, i.e. the time it takes for the slug to travel from its initial position to the inlet to the core, is the same as in the plant. The other three tests cases are run with a higher flow rate in order to increase the Reynolds number, and thereby decrease the Reynolds number scaling effects. Strouhal number scaling is used to determine the ramp length for these tests. Scaling rules are discussed in 3.2.2.

Experiments are made for three different slug sizes (4.5 m^3 (VATT-03), 8 m^3 (VATT-02 and VATT-04) and 14 m^3 (VATT-01)). The initial position of the front of the slug is the same in all tests (the front of the slug being 9.8 m, in the plant, from the inlet to the downcomer). The two idle loops are open in all tests.

The following experimental work was done:

- Measurements of boron concentration at the inlet to the core
- Visualisations. The following types of visualisations were made:
  - Local injections of dye during steady state flow and during a transient.
  - Visualisations of a coloured slug passing through the downcomer during a transient.
  - Laser sheet visualisations of a slug passing through the downcomer during a transient.
- LDV measurements of vertical and tangential/circumferential velocity in the downcomer during steady state and transient conditions.

Earlier performed model tests in the same model are documented in references ([Tin93], [And94], [Hem94], [Ala95], [And95], [Hem95], [Hem97]).

3.2 Description of test facility

3.2.1 Geometry

A picture of parts of the model is shown in Fig. 3.2.1. A schematic sketch of the model is shown in Fig. 3.2.2, a section of the model in Fig. 3.2.3 and pictures from a CAD model in Fig. 3.2.4, Fig. 3.2.5, Fig. 3.2.6. The geometry is also supplied in the IGS file FLOMIX-R_VATT_MODEL.IGS. The geometric scale of the model is 1:5. All measures given below are for the model, not the plant.

In the upstream end of the model there is a big tank, the tap-water tank, with a volume of 15 m^3. The tank is a horizontal cylinder with a length of 6 m and a diameter of 1.8 m. The water level is kept at approximately 200 mm below the roof of the tank and is relatively stable during a boron transient.

The model uses tap water. The water is heated to 53±4°C in order to maximize the Reynolds number.

4.5 m downstream of the tank there is a pump (P1). This pump runs at full speed both before and during a transient. Immediately downstream of the pump there is a possibility to by-pass the flow back to the tank.

1.7 m downstream of the pump there is a manually controlled gate-valve (V2). V2 can be used to control the flow rate through the model. In these tests, however, V2 is fully open during the whole transient.

3.3 m downstream of the manually controlled gate-valve (V2) there is a motor-operated gate-valve (V3). The movement of this valve controls the flow rate increase during a transient. The position of the gate of the valve is linear in time, which creates a well-defined flow increase during a transient. From this position to the inlet to the downcomer the inner diameter of the pipe is 150 mm, and the pipe is horizontal.

840 mm or 6 diameters downstream from the motor-operated gate-valve there is a flow straightener. Its purpose is to decrease the erosion of the slug due to swirl and to variations in axial velocity distribution across the pipe radius and to create a well-defined boundary condition for CFD calculations. The flow straightener consists of a tube bundle with a tube diameter of 20 mm and a length of 150 mm. At both ends of the tube bundle there are perforated plates with an open porosity of around 50%. These plates will create a flow resistance that will decrease the variation of axial velocity across the pipe radius. The tube bundle will cancel out all swirl in the flow. The relatively low momentum of the flow through the outlet plate is believed to create only a small amount of swirl downstream of the flow straightener. 0.7 m or 4.6 diameters from the flow straightener there is an electromagnetic flow-meter.

0.92 m and 4.59 m from the flow meter, respectively, there are two valves (V4 and V5) that encompass the slug before the start of a transient (i.e. at t=0). V5 is positioned at the same place for all tests. For test case VATT-03, the small slug volume, V4 is moved to 2.55 m from the flow meter. For the large slug volume (VATT-01) the position of V4 is the same as for the medium slug volume (VATT-02 and VATT-04), but the diameter is increased to 250 mm for a length of the pipe of 0.5 m at the centre of the pipe. Both area changes occur over a distance of 1.1 m.

Before each transient run the pipe section between the valves V4 and V5 is evacuated and filled with salt water. The salt-water is prepared in and pumped from a separate salt-water tank.

From 0.25 m from V5 to 0.55 m from V5 the pipe is made in plexiglas, in order to be able to visualize the slug during a transient.

Fig. 3.2.1 Picture of model

Fig. 3.2.2 A schematic sketch of the model

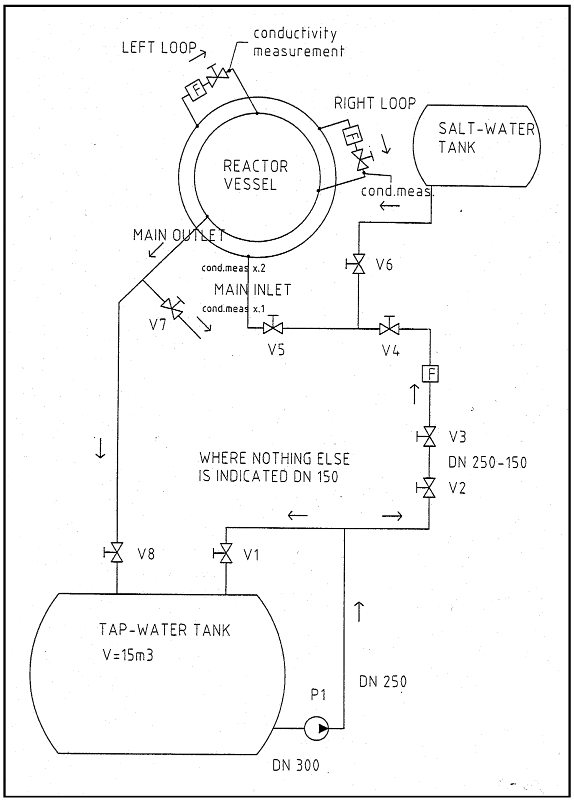

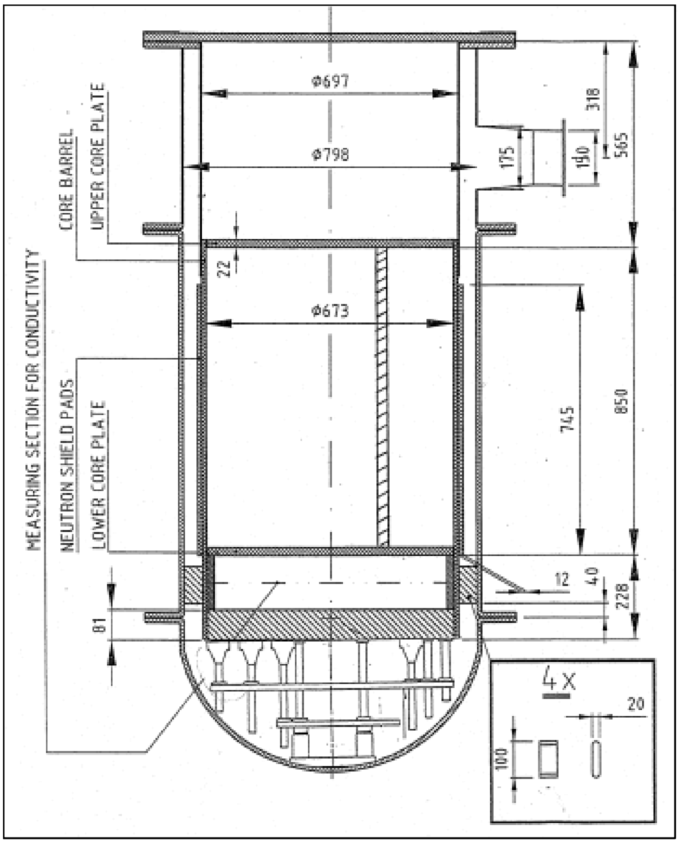

Fig. 3.2.3 A section of the model

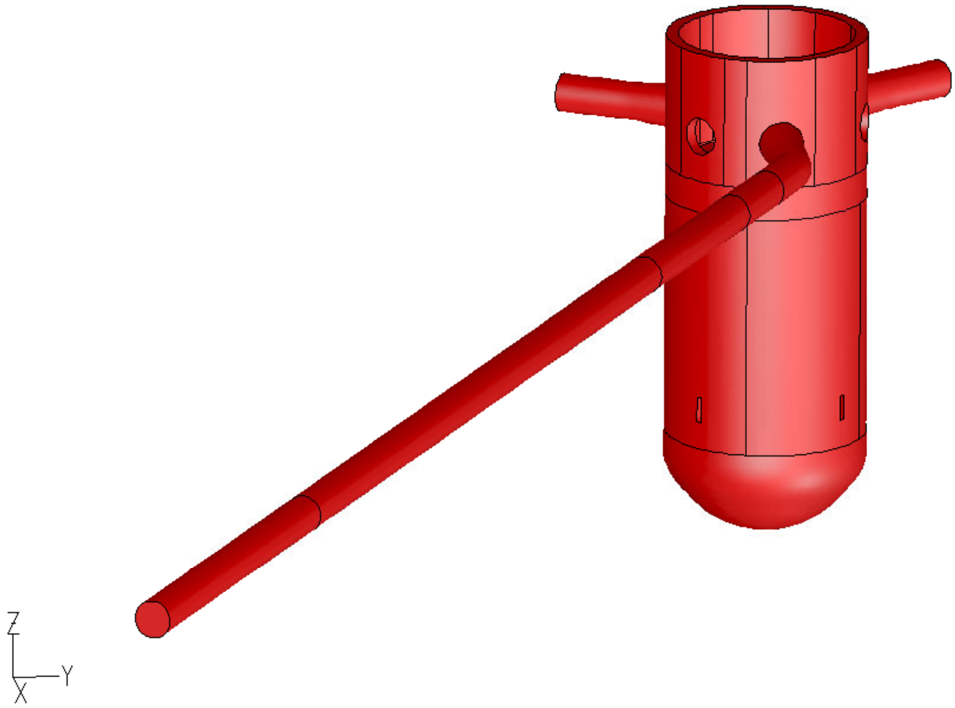

Fig. 3.2.4 Outline of the CAD model. Perspective view

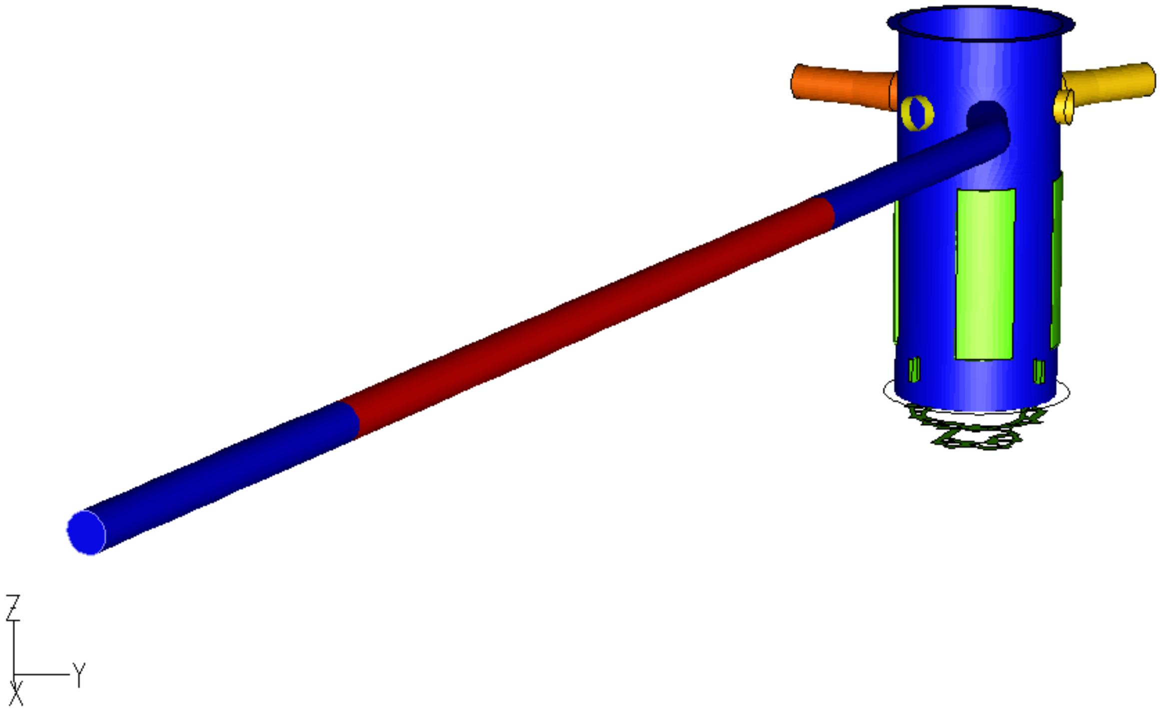

Fig. 3.2.5 Outline of the CAD model. Perspective view

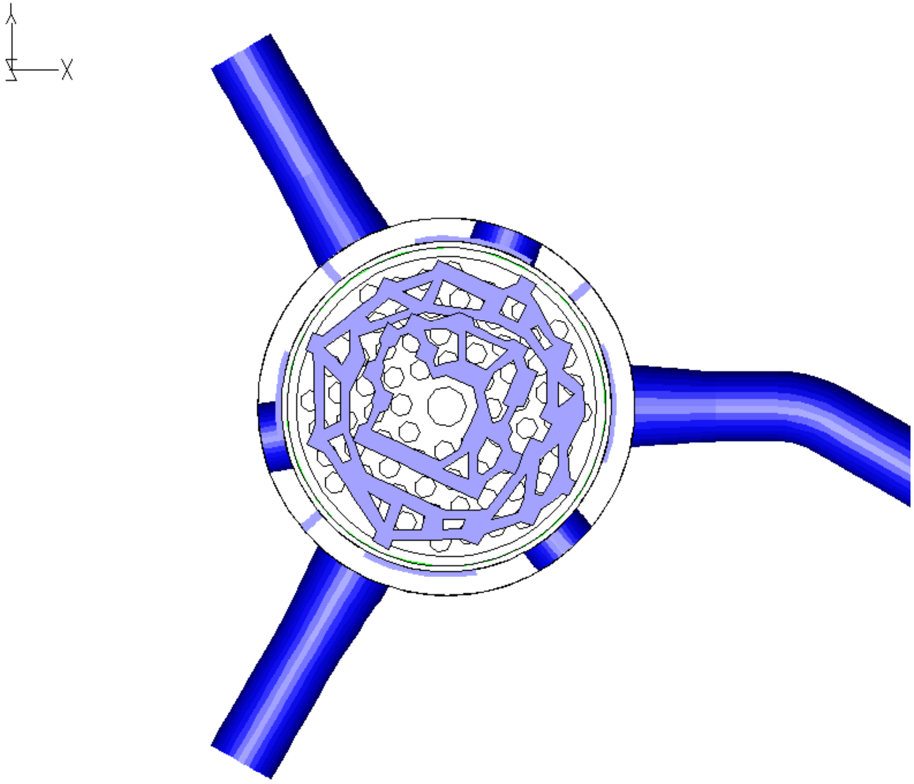

Fig. 3.2.6 Outline of the CAD model. View from below

1.96 m from V5 the inlet pipe enters the downcomer. Between V5 and the downcomer there is a 30 degrees to the left bend. The upstream end of the bend is 0.4 m from the inlet to the downcomer. This bend is present also in the plant. The bend will change the velocity distribution at the inlet to the downcomer, which to some extent will change also the flow pattern in the downcomer.

In the global coordinate system referenced below, z, the vertical coordinate, is 0 at the level of the centre of the main inlet pipe, the RCS pipe. z is directed upwards. x and y are both zero at the centre of the core. x is directed towards the RCS pipe.

To describe tangential positions in the model an additional cylindrical coordinate system is defined, with the axis at the centre of the core. Angle=0° is defined as the angular position where the main inlet pipe enters the downcomer (at x=0.405 m and y=0 m). Positive angles are to the right of this position, negative angles are to the left, when looking at the model from the outside standing at angle=0°.

At the inner downcomer walls, in the middle part of the downcomer, there are four thermal shields (light green in Fig. 3.2.6). The width of these shields (in the radial direction) is 12 mm. The total width of the downcomer is 50 mm. The tangential positions are given in Fig. 3.2.6. These shields are not completely symmetrically placed relative to the main inlet pipe, which means that they to some extent will create a non-symmetric flow pattern in the downcomer. The thermal shields are located from z= -1.06 m up to z= -0.32 m. The edges of the shields have chamfers (see Fig. 3.2.7).

There are four supports in the lower part of the downcomer (light green in Fig. 3.2.5). The tangential positions are shown in Fig. 3.2.6. The vertical extension of these supports is 100 mm and the extension in the tangential direction is 20 mm. They are located from z= -1.18 m up to z= -1.08 m (see Fig. 3.2.7).

In the upper part of the downcomer, at z=0, there are three pipes passing through the downcomer (see Fig. 3.2.4, Fig. 3.2.5, Fig. 3.2.6), consisting of the outlet pipe from the model and of the two idle loop pipes. These pipes will act as obstructions for the flow and will distort the flow pattern.

The structures in the lower plenum are also modelled (see Fig. 3.2.5, Fig. 3.2.6 and Fig. 3.2.7). The model of the structures differs from the plant only in small details. The model in the CAD model, as shown in Fig. 3.2.5 and Fig. 3.2.6 is however a simplified model of the structure being built. The lower horizontal structure in the lower plenum are at z= -1.50 m. The upper horizontal structure in the lower plenum are at z= -1.39 m.

The plate between the lower plenum and the core inlet (see Fig. 3.2.3 and Fig. 3.2.6) is modelled in geometrical detail. The height is 81 mm. All holes except the central hole, which has a diameter of 84 mm, have a diameter of 46 mm. The distance between the small holes is 61 mm. The vertical position is from z = -1.288 to z = -1.207 m.

The model of the core models the vertical and horizontal flow resistance in the core region, as well as the resistance from the inlet and outlet plates. The latter two plates are modelled in geometrical detail. These have a hole diameter of 21 mm. The distance between the holes is 37 mm. The height of the plates is 22 mm. The core model consists of a tube bundle with a pitch of 43 mm and a tube diameter of 30 mm. The core inlet is located at z= -1.06 m. The core outlet is located at z=-0.188 m.

The idle loops are modelled as pipes with a length of 3.9 m and a diameter of 0.15 m. In the CAD model, see Fig. 3.2.4, Fig. 3.2.5 and Fig. 3.2.6, the full length of the loops are not modelled. The maximum flow rate in the loops is controlled using gate valves. The maximum flow rate in each loop is approximately 10% of the maximum flow rate in the RCS pipe. The flow rate is measured in each loop using electromagnetic flow- meters.

At the outlet from the model the flow is dumped into a free water surface in a vertical pipe connected to the 15 m^3 tap-water tank.

The test starts when the valves V4 and V5 starts to open. Both valves are driven by air pressure in order to achieve a fast and controlled opening. The valves open during a period of approximately 2 seconds. Immediately when V4 and V5 are fully open the motor-valve (V3) starts to open and the flow through the model consequently starts to increase. The start time of a test, t=0, is defined as the time when V3 starts to open.

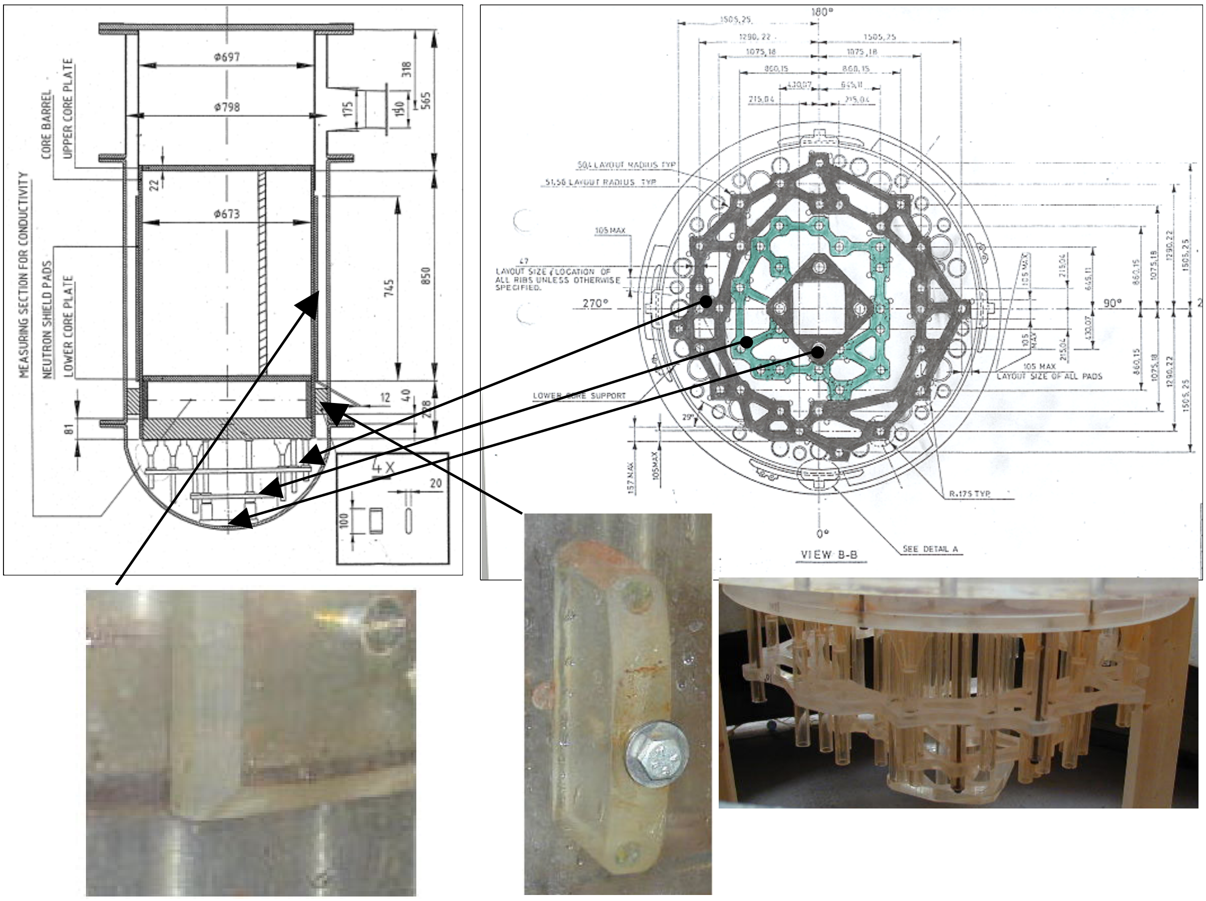

Fig. 3.2.7 Model drawings and pictures

3.2.2 Model scaling

The main rule of scaling is to have the same Strouhal number (Sr) in model and plant. The Strouhal number is the ratio between forces due to transient acceleration and forces due to convective acceleration. For this particular situation the Strouhal number can be defined as:

$$Sr = \frac{U \cdot \tau}{L} \qquad \text{Equ. 3.2.1}$$

U = velocity (m/s)

τ = a characteristic time for the transient, for example the ramp length (s)

L = distance (m)

The geometric scale is 1:5. If we want to use the same ramp length in the model and the plant the velocities in the model must consequently be 5 times lower than in the plant. This will also give the same transit time as in the plant for the slug transport through the model. The VATT-04 case was run in this way. In the plant the ramp time is around 40 s and the maximum volume flow rate around 6 m^3/s. The flow rate in the model is 125 times lower than in the plant, which gives a maximum volume flow rate of 48 l/s in the model. The other three tests were all run with an increased flow rate, with the purpose of increasing the Reynolds number and thereby minimizing the Reynolds number scaling effects. A maximum flow rate of 119 l/s was used in these tests, i.e. the flow rate is around 2.483 times the flow rate in VATT-04. To get the same Strouhal number for the higher flow rate the ramp length must be decreased at the same rate. The opening rate of the gate valve V5 was therefore decreased around 2.483 times.

Fig. 3.2.8 shows the measured mass flow rate for the VATT-02 and VATT-04 cases as a function of time. Plotted is the average flow rate from the 15 tests performed for each test case. The flow rate for the VATT-01 and VATT-03 cases are very similar to the flow rate for the VATT-02 case and therefore not shown here. In Fig. 3.2.8 the flow rate for the VATT-04 case has been scaled in both time and flow rate with the factor 2.483. If the Strouhal numbers are the same these two curves should coincide. This is almost the case for up to around 12 seconds. Unfortunately it was not possible to get the two curves to coincide after this time, due to the way the flow is regulated using the two gate valves in the upstream part of the model. The most important part of the transient, when the lowest concentrations are measured at the inlet to the core, is however within these 12 seconds.

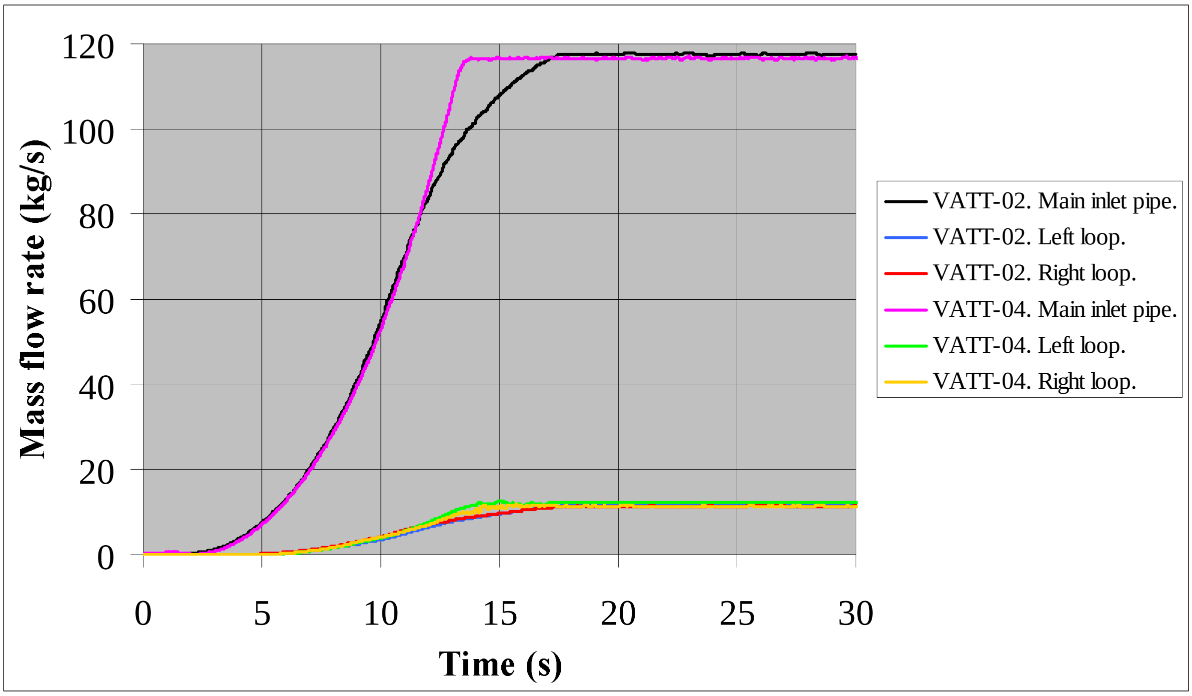

Fig. 3.2.8 Mass flow rate as a function of time for the VATT-02 and VATT-04 cases

One potential problem in all scale models of turbulent flow is Reynolds number sensitivity. The Reynolds number is 25 times lower in the model than in the plant for the VATT-04 test, not taking into account temperature differences between plant and model. For the VATT-01, VATT-02 and VATT-03 tests the velocity is 2.5 times higher than for the VATT-04 tests and the Reynolds number is therefore 10 times lower than in the plant for these tests. These three tests were run with the Reynolds numbers shown in Tab. 3.2.

Tab. 3.2 Values of the Re-number at different positions

Test case	**Value**
Re_1	290 000
Re_2	29 000
Re_3	78 000
Re_4	170 000

$$\mathrm{Re} = \frac{U \cdot D}{\nu}$$

Equ. 3.2.2

Re_i = Reynolds number

U = velocity (m/s)

D = equivalent diameter (m)

ν = kinematic viscosity = $0.6 \cdot 10^{-6}$ m²/s

- Re_1 = Inlet Pipe Reynolds number when the front of the salt-water slug reaches the downcomer. Re_1 is based on the inlet pipe diameter of 0.15 m and on the main flow rate (e.g. the flow in the RCS pipe).
- Re_2 = Downcomer Reynolds number when the front of the salt-water slug reaches the downcomer. Re_2 is based on the main flow rate and on the horizontal area of the downcomer at z=0.
- Re_3 = Downcomer Reynolds number when the front of the salt-water slug reaches the measuring plane below the core. Re_3 is based on the main flow rate minus the loop flow rates and on the horizontal area of the downcomer at z=0.
- Re_4 = Maximum Downcomer Reynolds number. Re_4 is based on the maximum main flow rate and on the horizontal area of the downcomer. This Reynolds number is not very interesting, as most of the slug has already passed the core inlet when the maximum flow rate is reached.

For steady state flow, turbulence usually starts to occur at a Reynolds number of around 10^4. For accelerating flow, as in this case, onset of turbulence occur at a much higher Reynolds number, maybe at Reynolds numbers as high as 10^5. This would mean that laminar conditions would prevail in the downcomer, at least in parts, for almost the whole of the interesting part of the transient. In the inlet pipe, however, the Reynolds number is well above 10^5 at the time when the front of the slug enters the downcomer.

From the LDV measurements and to some extent also from the visualisations with local injections of dye during a transient, we can get indications on when turbulent behaviour starts to occur. Fig. 3.2.9 shows a measured vertical velocity as a function of time at an angle of 30 degrees at the lower part of the downcomer (z=-1.033 m). Here we can see that unstable behaviour, indicating onset of turbulence, starts at around 8.5 seconds.

The velocity at the same tangential position but at the mid position in the downcomer (z=-0.773 m) is shown in Fig. 3.2.10. At this position turbulence seems to occur after 7.5 seconds.

Visualizations (which are made in the lower part of the downcomer, at z=-1.1 m) give an indication of turbulence occurring at this level at around 8-10 seconds.

The front of the slug enters the downcomer at around 7 seconds and reaches the core inlet at around 10 seconds. The slug thus passes the downcomer approximately at the same time as transition from laminar to turbulent conditions take place.

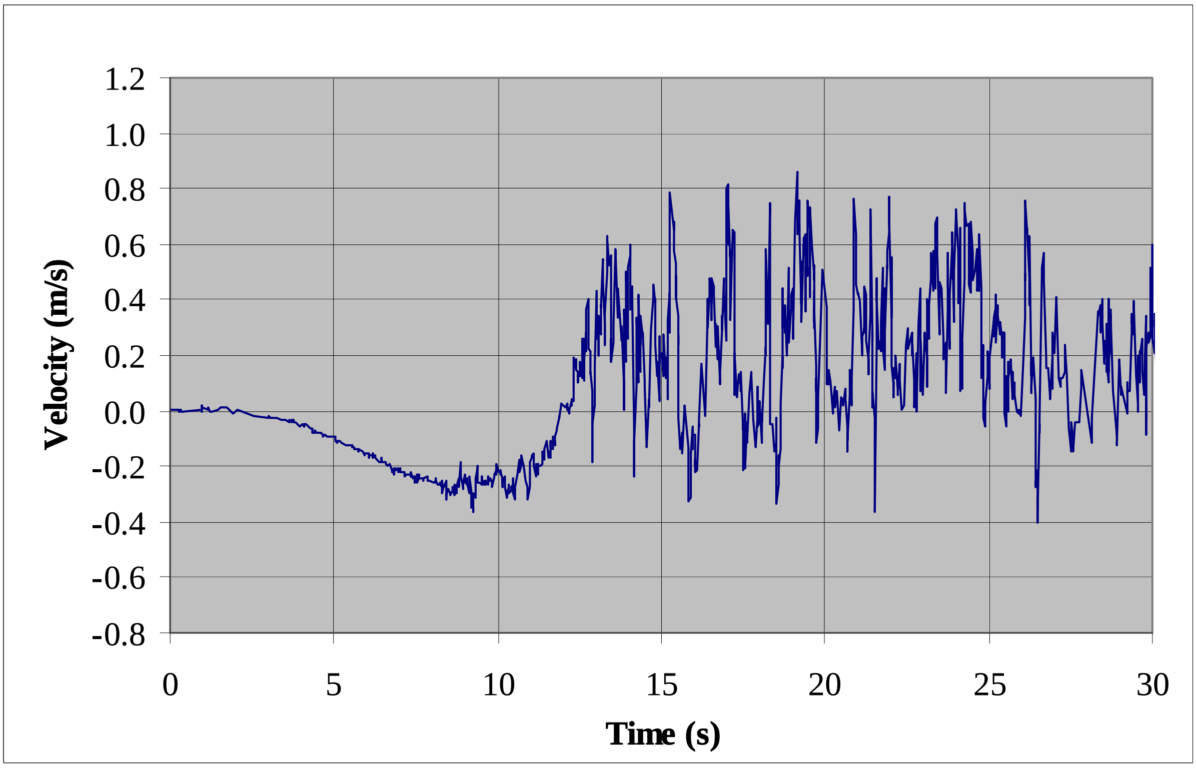

Fig. 3.2.9 VATT-02. Vertical velocity as a function of time at z=-1.033 m and at an angle of +30°

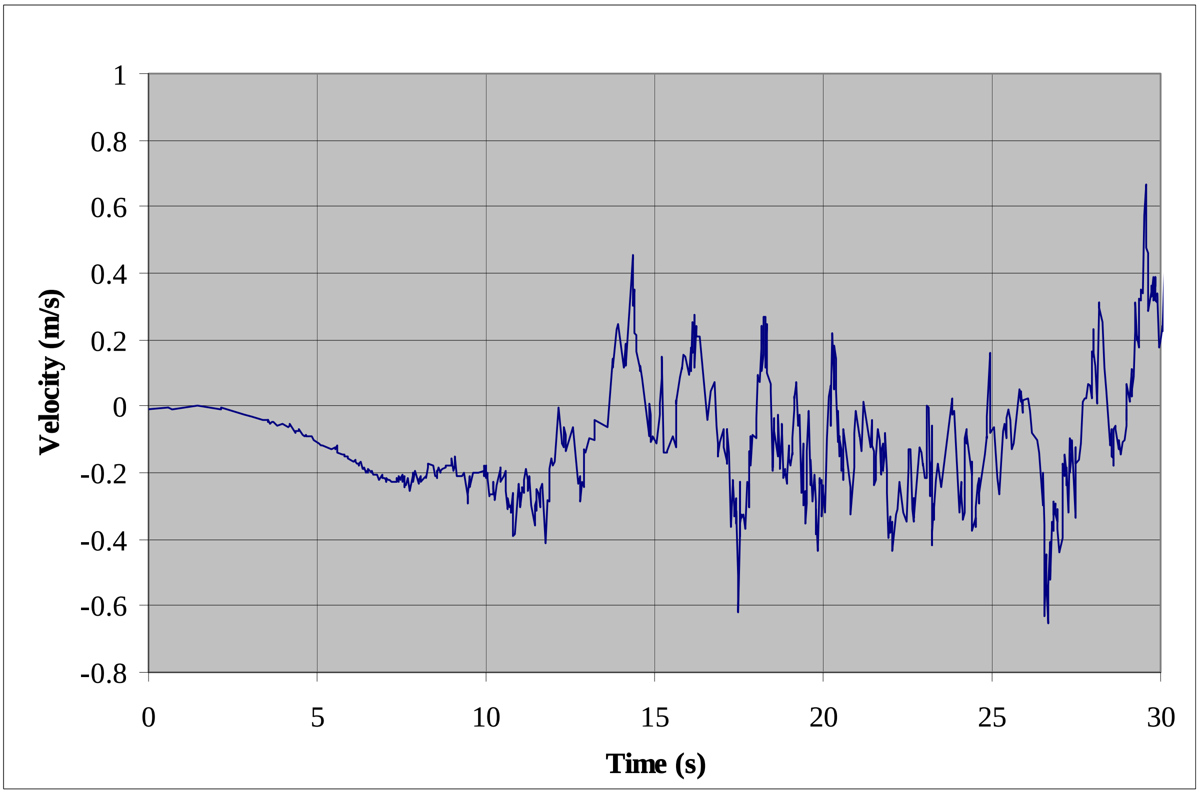

Fig. 3.2.10 VATT-02. Vertical velocity as a function of time at z=-0.773 m and at an angle of +30°

3.3 Results from experiments

3.3.1 Flow rate

The measured mass flow rates for the four test series are given in Fig. 3.2.8 in chapter 3.2.2. The flow rates for VATT-01 and VATT-03 are very similar to that of VATT-02 and therefore not shown in Fig. 3.2.8. The flow rate for VATT-04 has been scaled with a factor of 2.483, both in time and flow rate. At the start of the transient (e.g. at t=0 seconds) the flow rate through the model starts to increase from zero. For the VATT-01, VATT-03 and VATT-04 tests there is a small leakage flow of 0.2 kg/s through the closed motor-valve before t=0. The leakage flow starts to occur only after the valves V4 and V5 have started to open, i.e. 2 seconds before the start of the transient.

The final flow rate in the two idle loops is around 10% of the flow rate in the RCS pipe.

There are indications from the transient velocity measurements in the downcomer and from CFD calculations that the measured flow rates during the first part of the transient are significantly lower than the actual flow rates. This can be due to a built-in time-averaging of the signal from the electromagnetic flow-meters. This averaging is not possible to change.

3.3.2 Boron concentration

3.3.2.1 Measurement technique.

The principle behind the technique for measuring boron concentration is as follows. The slug of water with relatively low boron content is modelled by means of a salt-water solution and the normally borated water by means of tap-water, or rather with tap-water with a lower salt-water content than for the salt-water. The former is from now on called unborated water and the latter for borated water. The unborated water is in the following defined to have a dimensionless boron concentration equal to 0.0 and the borated water a dimensionless boron concentration equal to 1.0. Dimensionless boron concentrations for mixtures of the two solutions are obtained through measurements of conductivity.

Salt can be considered as a passive tracer and to mix at the same rate as boron. Equation 3.3.1 therefore gives an exact expression for dimensionless boron concentration:

$$c = (s_u - s)/(s_u - s_b) \qquad \text{(Equ. 3.3.1)}$$

c = dimensionless boron concentration

s_u = salinity of unborated water (g salt/kg water)

s_b = salinity of borated water (g salt/kg water)

If the conductivity of the salt-water solution can be expressed as a function of salinity, dimensionless boron concentration can be obtained through conductivity measurements. If the relation is linear, equation 3.3.2 can be used:

$$c = (\gamma_u - \gamma)/(\gamma_u - \gamma_b) \qquad \text{(Equ. 3.3.2)}$$

c = dimensionless boron concentration

γ_u = conductivity of unborated water ($1/\Omega$m)

γ_b = conductivity of borated water ($1/\Omega$m)

The relation between conductivity and salinity is, however, not quite linear and is also affected by temperature differences. The inaccuracy occurring from this fact is discussed in Appendix A.1, along with other sources of inaccuracy.

The conductivity measurement technique is described in [Tin93]. The technique was later improved (see [And94]). The probe sensing volume (definition in [Tin93], p. 14) is equivalent to a sphere with a diameter of 1 mm, or smaller. The rise time is very fast, at least in the order of the sampling frequency. The sampling frequency used in the tests is 60 Hz.

The probes were initially calibrated using 5 different salt-water solutions with conductivities ranging from 0.09 1/Ωm to 0.9 1/Ωm. The true conductivity was measured using a separate conductivity-measurement instrument, a "P Series conductivity meter (CM-11P)" from TOA Electronics Ltd. Calibration curves based on an analytical form were then adjusted to the data to give functional relationships between conductivity and voltage for each individual probe.

The initial calibration curves were later linearly corrected based on conductivity measurements for water with known conductivities directly before and after each test series. The reason for adjusting the initial calibration constants was that they changed continuously during the test period. The reason for this was probably deposits and corrosion on the probes. Error estimates for the measured boron concentrations are given in Appendix A.1.

Concentrations are measured at 181 positions at a plane 70 mm beneath the core inlet (at z=-1.13 m), at two positions in the inlet pipe and at four positions in the idle loops (two in each loop). All these probes were, however, not used in the evaluation of the results for all tests as not all of them passed the quality test that was decided on (see Appendix A.1).

When preparing the salt-water for the slug, the density of the salt water was modified using ethanol in order to get approximately the same density as for the tap water surrounding the salt-water slug. Even very small density differences can cause gravity currents, i.e. that the denser fluid starts to dive under the lighter fluid. After the opening of the valves V4 and V5 the flow rate is very low and buoyancy forces can cause gravity currents. By decreasing the density differences these gravity currents are minimized. The densities were checked using an aerometer. The maximum inaccuracy in the determination of density was estimated to be 2 kg/m^3. To validate that this procedure of minimizing density effects was successful the slug was dyed and the plexiglas section of the inlet pipe was filmed during the transient. This was done only for the VATT-02 tests.

3.3.2.2 Conductivities in the inlet pipe.

Conductivities are measured at two positions in the main inlet pipe (the RCS pipe), placed at 101.0 cm (X.1) and 64.5 cm (X.2) upstream of the inlet to the downcomer. The probes are positioned at the centre of the pipe. X.1 and X.2 are used for determining the conductivity of the salt-water slug. An example of the measured conductivities at X.1 and X.2 for one of the tests in VATT-02 is shown in Fig. 3.3.1. One can see that the front of the salt-water slug reaches X.1 after 5.4 seconds and X.2 after 5.8 seconds. The back of the slug reaches X.1 after 8.1 seconds and X.2 after 8.2 seconds. One can also see that a core of the salt-water slug is still undiluted when the slug passes X.1 and X.2, which of course should be the case as dilution only can take place at the edges of the slug, a process that does not have enough time to penetrate very deeply into the 3.6 m long slug.

The time at which the front of the salt-water slug reaches the inlet to the downcomer is approximately 7.0 seconds, based on the measured flow rate and the volume of water in the pipe between the slug front and the inlet to the downcomer. At this time the main flow rate has increased to 19 kg/s or 16% of the maximum main flow rate.

The back of the slug reaches the downcomer inlet at around t = 9.1 s. At this time the main flow rate has increased to 41 kg/s or 35 % of the maximum main flow rate.

3.3.2.3 Dimensionless boron concentrations close to the core inlet.

Dimensionless boron concentrations are measured at a plane halfway between the top of the bottom plate and the bottom of the core (e.g. 70 mm beneath the inlet to the core), at z=-1.13 m. Measurements are made at 181 positions. The distance between the probes is 43 mm. Only 61 probes are used. These are installed in a triangular arrangement in one third (120 degrees sector) of the plane. Measurements are first made for a certain angular position of the probe package. The whole probe package is then rotated 120 degrees, and new measurements are made for the same conditions. The whole probe package is then once again rotated 120 degrees, in the same direction as before, and new measurements are made. The whole plane will consequently be covered. The position and names of the measurement positions are given in Fig. 3.3.2 and in Appendix A.4. The view in Figure 3.3.2 is from above and the tangential position of the main inlet pipe (the RCS pipe) is to the right in Fig. 3.3.2. The three probe package positions (A, B and C) are also given in the figure. Each position in the plane beneath the core was measured five times, except for the position 0:1 at the centre of the model, which was present in all three test-series and therefore measured 15 times.

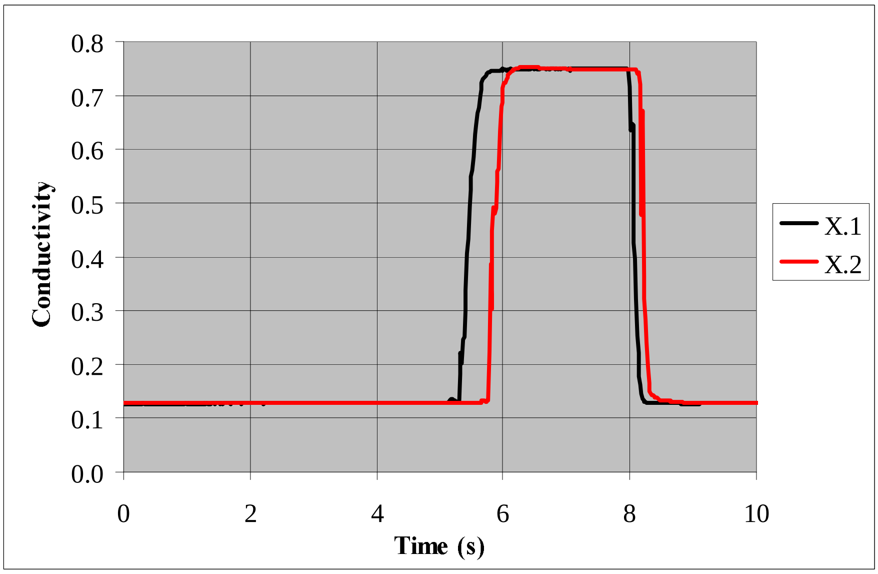

Fig. 3.3.1 Measured conductivities in inlet pipe for one of the tests in VATT-02

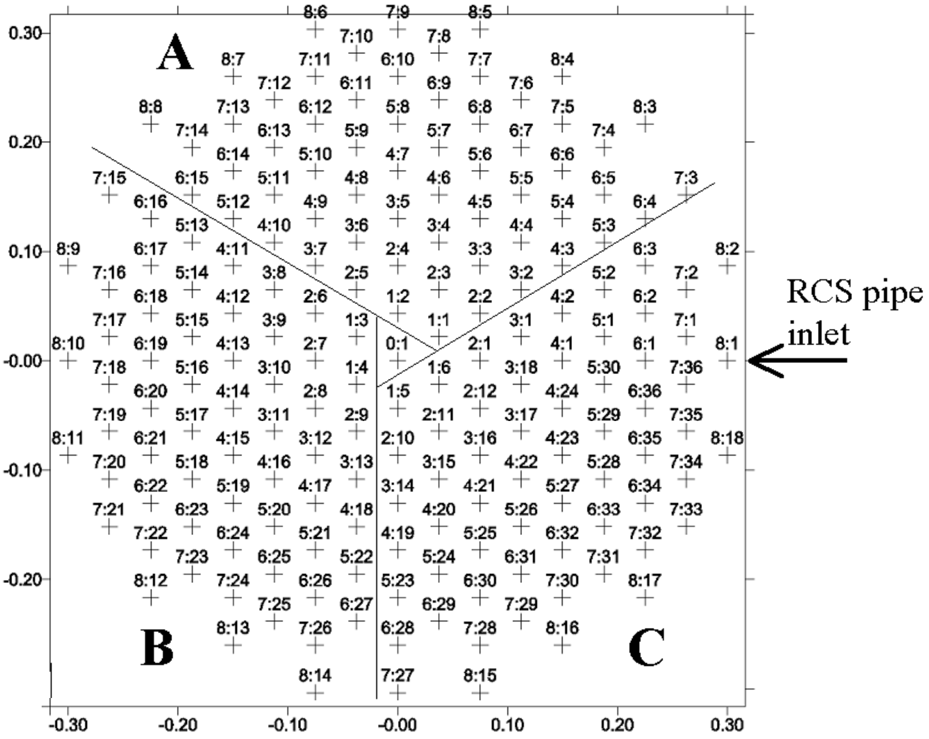

Fig. 3.3.2 Name and position of conductivity measurements points at the core inlet. View is from above

3.3.2.4 Spatially averaged dimensionless boron concentration.

Figure 3.3.3 shows the measured ensemble- and spatially-averaged dimensionless boron concentration over the measurement section for all four test cases. In other words, it shows the mean boron concentration over the whole measurement plane as a function of time. This curve can also be interpreted as the typical (or average) response at the measuring plane. The result from VATT-04 has been scaled in time with a factor of 2.483.

According to Fig. 3.3.3 the unborated water reaches the measurement plane after about 10 seconds. At this time the main flow rate has increased to 56 kg/s or 48% of the maximum main flow rate. VATT-04 is delayed with around 0.4 seconds, compared to the other three test cases. The reason for this delay can be lower accuracy for the measured flow rates for low flow rates. The rate at which concentration decreases for the first second or two is almost the same for all test cases. The mean dimensionless boron concentration at the measurement section then decreases rapidly to reach its minimum value after around 12.5 seconds. The main flow rate has by then increased to 94 kg/s or 80% of the maximum main flow rate. The mean concentration then increases more slowly.

The minimum values are also shown in Tab. 3.3.

Tab. 3.3 Minimum average dimensionless boron concentration

Test case	**Minimum average dimensionless boron concentration.**
VATT-01	0.70
VATT-02	0.80
VATT-03	0.90
VATT-04	0.82

.

The minimum concentration is relatively well scaled with the slug volume. If the minimum concentration for VATT-02 is scaled with the slug volume for VATT-01, the concentration for VATT-01 would be 0.65, which is 0.05 units lower than the measured one. One reason for the higher concentration is that a bigger part of the slug leaves through the loops than in the case for VATT-02. This is discussed in Appendix A.2.

The Reynolds number effect is given by the difference between VATT-04 and VATT-02. The lower Reynolds number case, VATT-04, give a somewhat higher concentration. This in spite of the fact that the turbulence intensity should be lower for this case. The turbulence has, however, more time to develop and the slug more time to mix for the low Reynolds number case. Another reason for the higher concentration is that a bigger part of the slug leaves through the loops than is the case for the high Reynolds number case.

Mass continuity checks for the slugs for the four test cases are given in Appendix A.2.

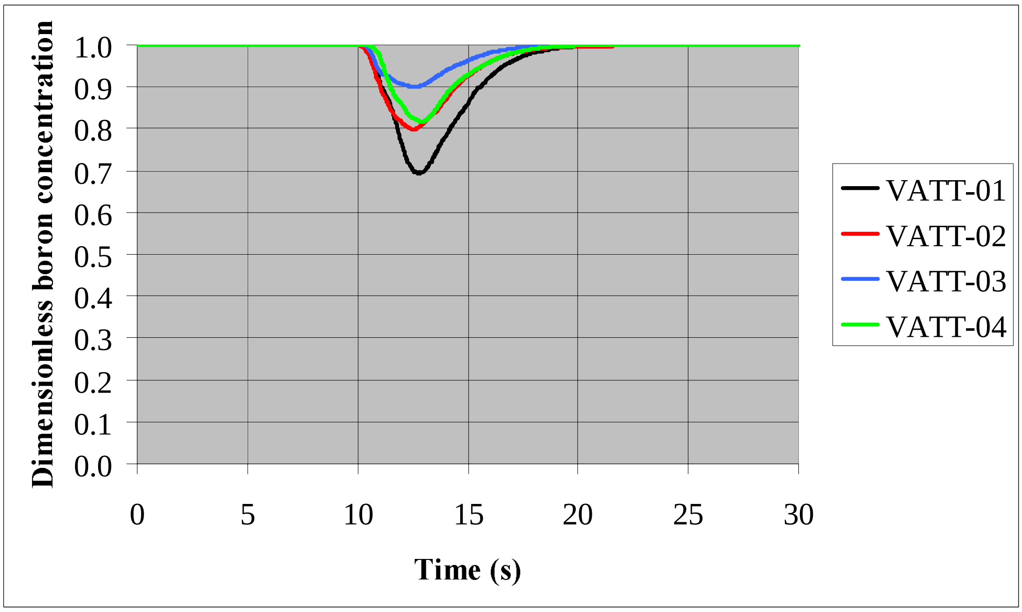

Fig. 3.3.3 Average dimensionless boron concentration at core inlet

3.3.2.5 Extreme values of dimensionless boron concentration.

The minima of the ensemble average (i.e the ensemble average from the five tests performed for each test case) boron concentrations that occur during the transient are shown in Fig. 3.3.4 for all positions. In other words, Fig. 3.3.4 shows the minimum of the ensemble average concentrations for each position, no matter when during the transient the minimum value have occurred. The tangential position of the RCS pipe inlet is to the right in the figures in Fig. 3.3.4.

The lowest ensemble averaged dimensionless boron concentrations measured for each test case are listed in Tab. 3.3 below.

Tab. 3.4 The lowest ensemble averaged dimensionless boron concentrations

Test case	**Lowest ensemble averaged dimensionless boron concentration.**	**at probe**
VATT-01	0.347	4:8
VATT-02	0.403	5:8
VATT-03	0.635	6:27
VATT-04	0.542	6:25

For all test cases there are basically two areas with low boron concentrations, one to the left of the inlet (in the lower half of each figure) and one to the right (in the upper half of each figure).

Comparing the two test cases with the same slug volume but with different Reynolds numbers (VATT-02 and VATT-04) one can see that the concentration field is much more symmetric for the low-Reynolds number case (VATT-04). There is also a slight shift in the positions for the minima. This indicates that the flow pattern is not Reynolds number independent. We know from the LDV measurements in the downcomer that the flow pattern is quite symmetric across a plane through the RCS pipe for low flow rates. At the time when the slug for the VATT-02 case passes through the downcomer there is a drastic transition in flow pattern, and more of the flow will go to the right where the jet from the RCS pipe meets the downcomer. This can explain why the non-symmetric boron concentration pattern evolves. The concentration field can therefore be expected to be more symmetric for VATT-04 than for VATT-02.

For the small slug volume, VATT-03, the concentration field is rather symmetric, but with slightly lower minimum concentration to the left of the inlet. This can also be a Reynolds number effect, as the VATT-03 slug is smaller and therefore subjected to lower Reynolds numbers than the VATT-02 slug.

For VATT-01, the big slug, the minimum concentration is lower at the left of the inlet. The difference between the left and right side is however not as big as for the VATT-02 case. The VATT-01 slug is of course subjected to even higher Reynolds numbers than VATT-02.

Fig. 3.3.5 shows the lowest ensemble average concentrations as a function of slug volume for the four test cases. As expected, the relationship is not linear. Fig. 3.3.6 shows instead the average of the minima for the left and right side of the inlet pipe. For a slug volume of 8 m^3 the value for VATT-04 is the higher mark of the two in Fig. 3.3.6.

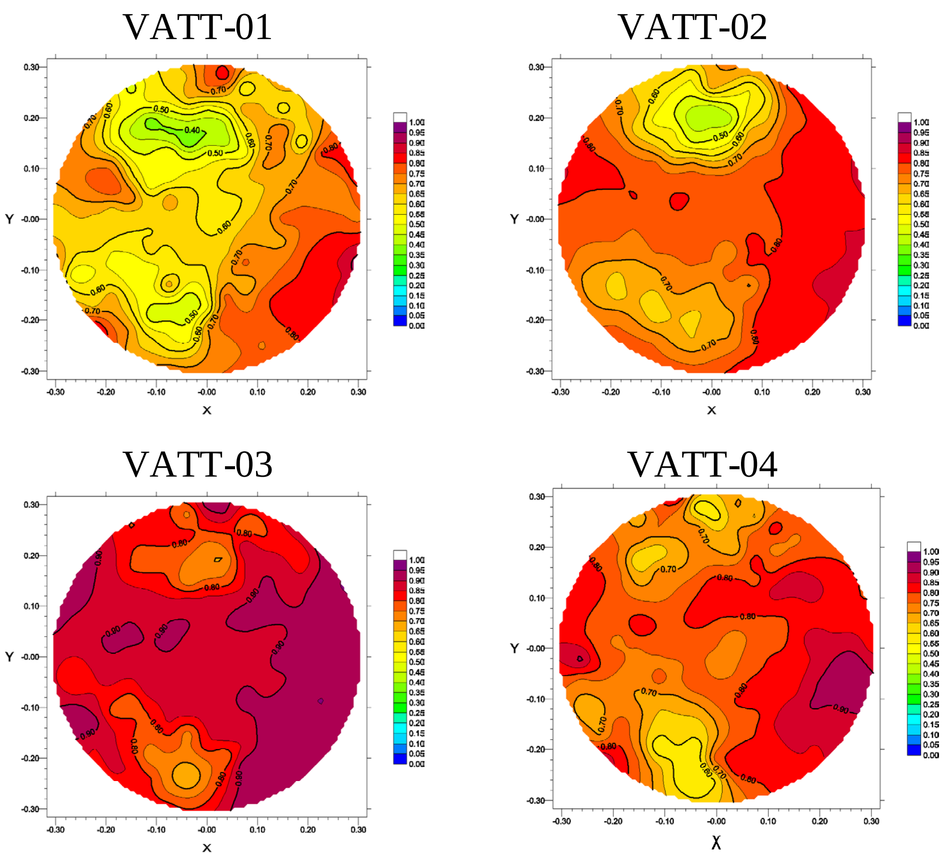

Fig. 3.3.4 Minima of the ensemble average concentrations

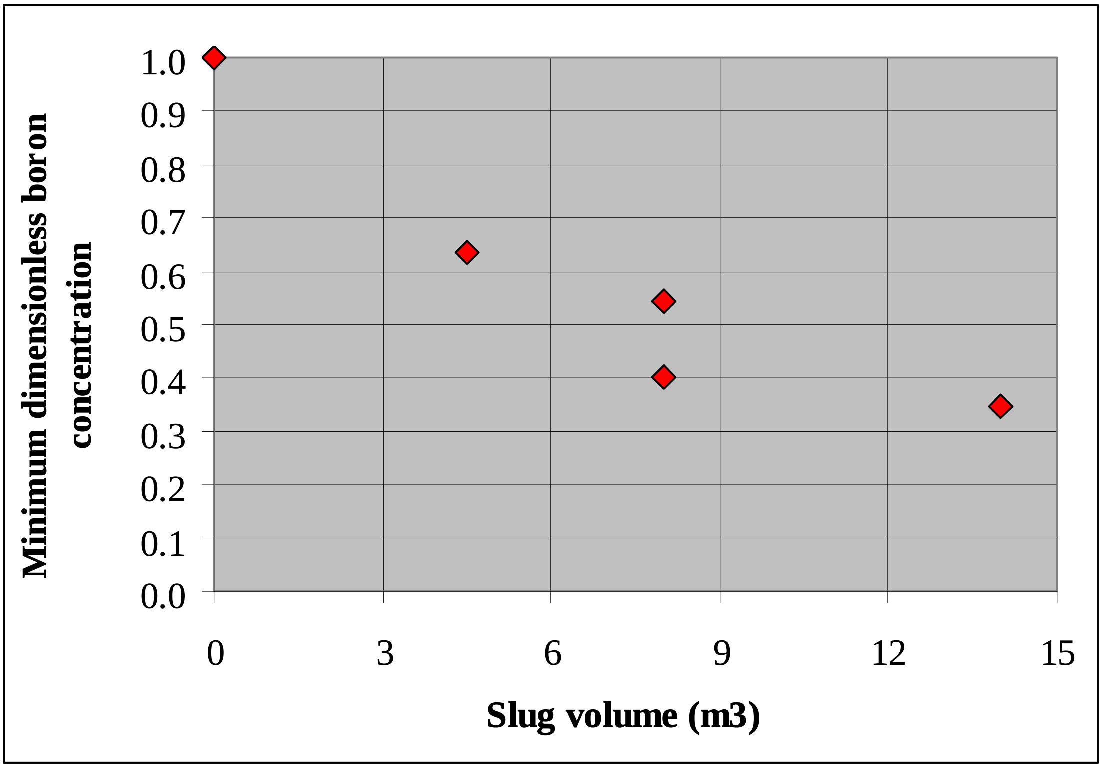

Fig. 3.3.5 Lowest average concentration as a function of slug volume

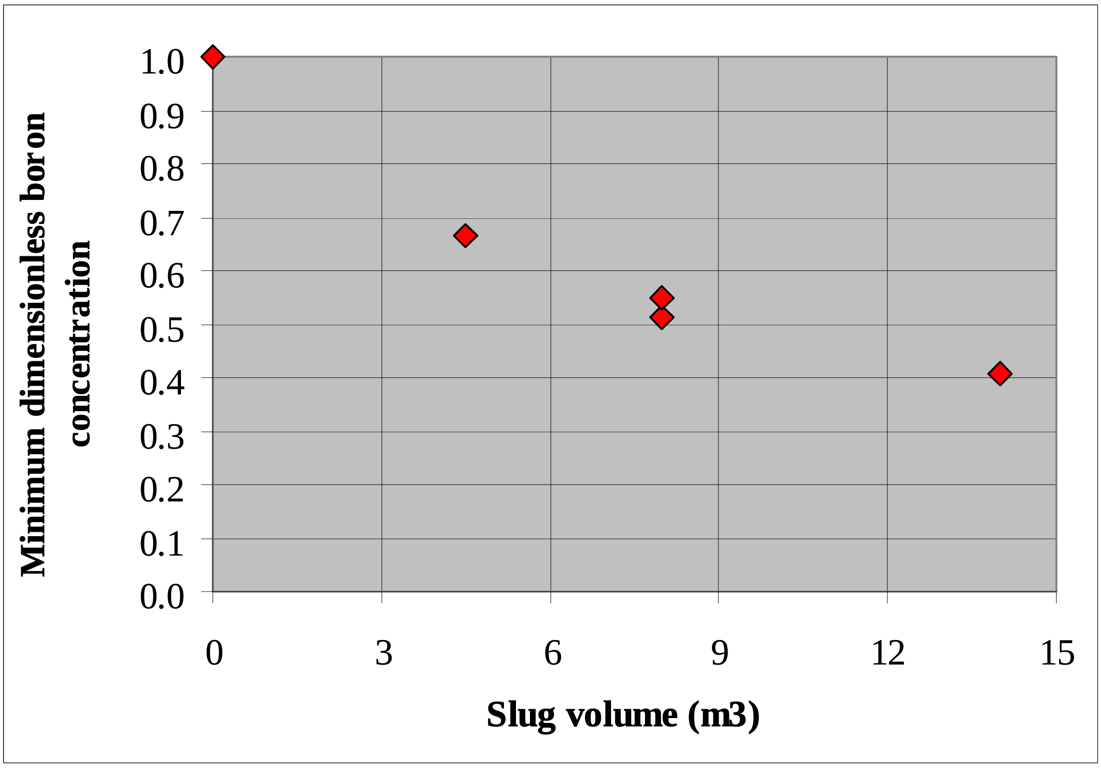

Fig. 3.3.6 Lowest average concentration as a function of slug volume. Average of minimum concentration from left and right side of the RCS pipe

3.3.2.6 Dimensionless boron concentration for different times.

Fig. 3.3.7-Fig. 3.3.22 show boron concentration fields for different times for all test cases. The table below lists which figures that corresponds to which test case.

Tab. 3.5 Overview on the figures

Test case	**Figures**
VATT-01	3.3.7 – 3.3.10
VATT-02	3.3.11 – 3.3.14
VATT-03	3.3.15 – 3.3.18
VATT-04	3.3.19 – 3.3.22

Let us first look at the VATT-02 case, Fig. 3.3.11 – Fig. 3.3.14. For VATT-02 the front of the unborated water slug reach parts of the measurement section after around 10.2 seconds. 0.6 seconds later, an almost symmetric pattern has developed. The positions of the minimum concentrations at this time are almost the same as the minimum concentration that occur during the whole transient (see Fig. 3.3.4). In other words, there is definitely a strong positive correlation between the first affected areas and the areas with the lowest dimensionless boron concentrations. This is expected, as these parts of the slug have not had time to mix so much. Still, the concentration is approximately the same on the left and right sides.

After 11.2 to 11.4 seconds, or 1.0 to 1.2 seconds after the first part is affected, the concentration minima are reached for the strongest affected areas to the right of the inlet. This time, which is around 1 second before the time when the lowest mean concentration is reached (see Fig. 3.3.3), large areas, especially close to the inlet and opposite of the inlet, are still not affected. The pattern is still rather symmetric. If we instead look at the minima for the left side we see that these occur over a much longer time than for the right side, from around 10.8 to 12.2 seconds.

At around 12.6 seconds or 2.4 seconds after the first probe is affected, the lowest spatially averaged dimensionless boron concentration is reached. Almost every part of the measuring plane has by now been reached by some unborated water.

The minimum concentrations are lower to the right side of the inlet than to the left side between 11.0 and 13.8 seconds.

The rest of the transient shows a rather undramatic increase of concentration.

Comparing all tests one can see that the boron concentration is lower on the left side for all tests up to at least around 11.0 seconds. For the low-Reynolds number test (VATT-04) the concentration is slightly lower on the left side up to 13.8 seconds. For the small slug (VATT-03) the concentration field gets rather symmetric after only 11.2 seconds, and stays quite symmetric for the rest of the transient. For VATT-02 the concentration is lower on the right side from around 11.0 seconds to 13.0 seconds. After that it gets quite symmetric. For the big slug (VATT-01) the concentration is lower on the left side up to at least 15 seconds. The tendency is thus to get lower concentrations on the left side for low flow rates and small slug sizes and lower concentration on the right side for higher flow rates and big slug sizes. The reason for the non-symmetry for the low Reynolds number case (VATT-04) can be due to the non-symmetries in the geometry in the downcomer and in the lower plenum. It can also be that the axis of the inlet pipe is not quite perpendicular to the downcomer wall. A small deviation in the angle of the jet from the inlet pipe can have a big influence on the flow field.

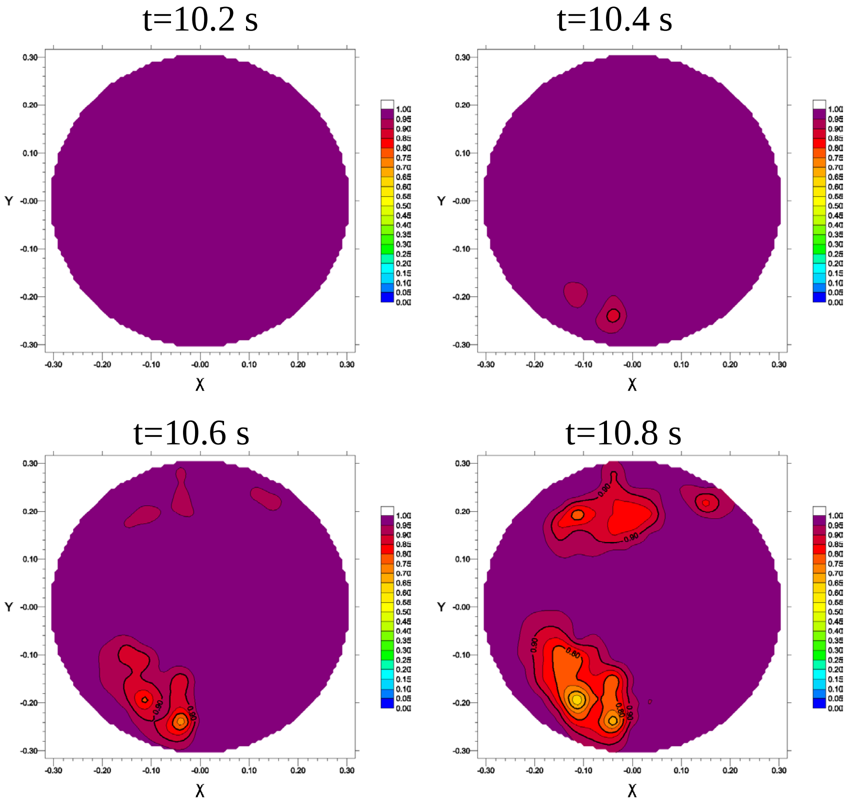

Fig. 3.3.7 VATT-01. Boron concentrations at core inlet for different times

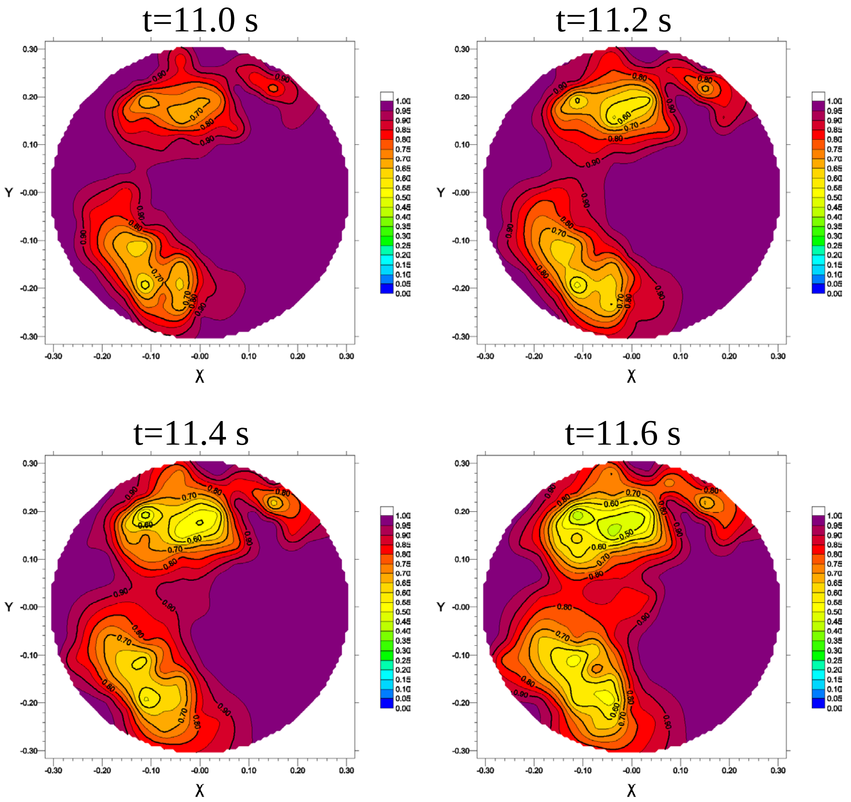

Fig. 3.3.8 VATT-01. Boron concentrations at core inlet for different times

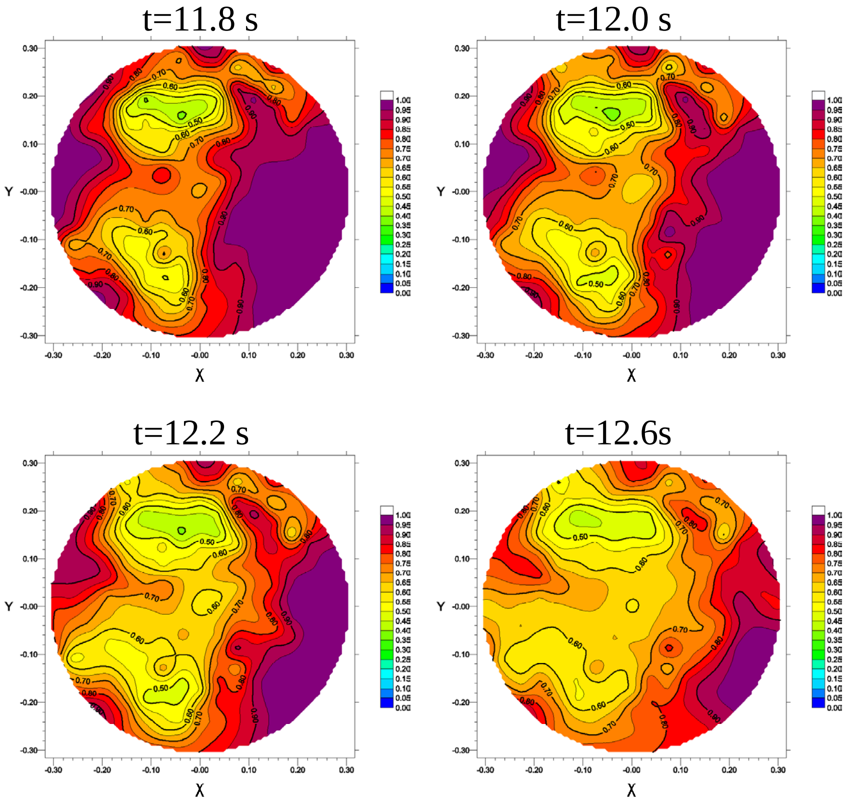
t=11.8 s

t=12.0 s

t=12.2 s

t=12.6s

Fig. 3.3.9 VATT-01. Boron concentrations at core inlet for different times

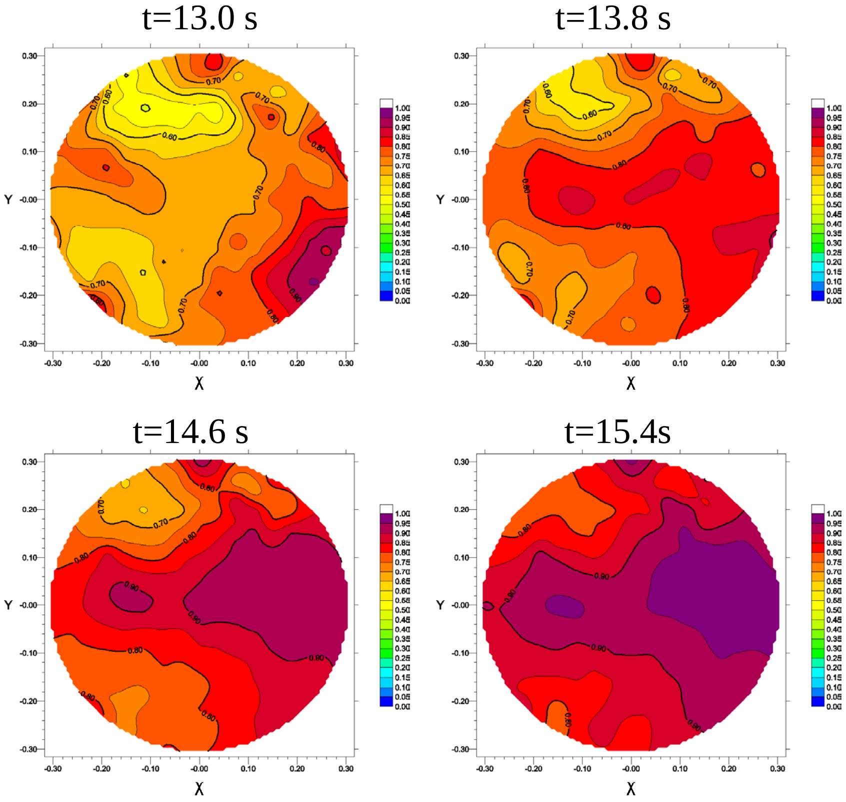
t=13.0 s

t=13.8 s

t=14.6 s

t=15.4s

Fig. 3.3.10 VATT-01. Boron concentrations at core inlet for different times

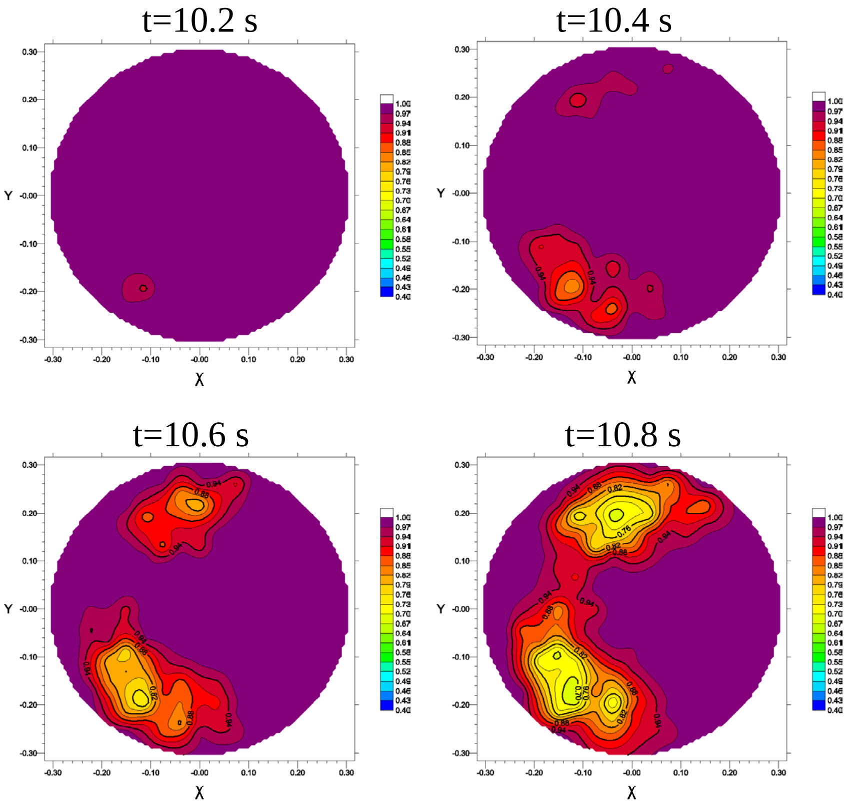

Fig. 3.3.11 VATT-02. Boron concentrations at core inlet for different times

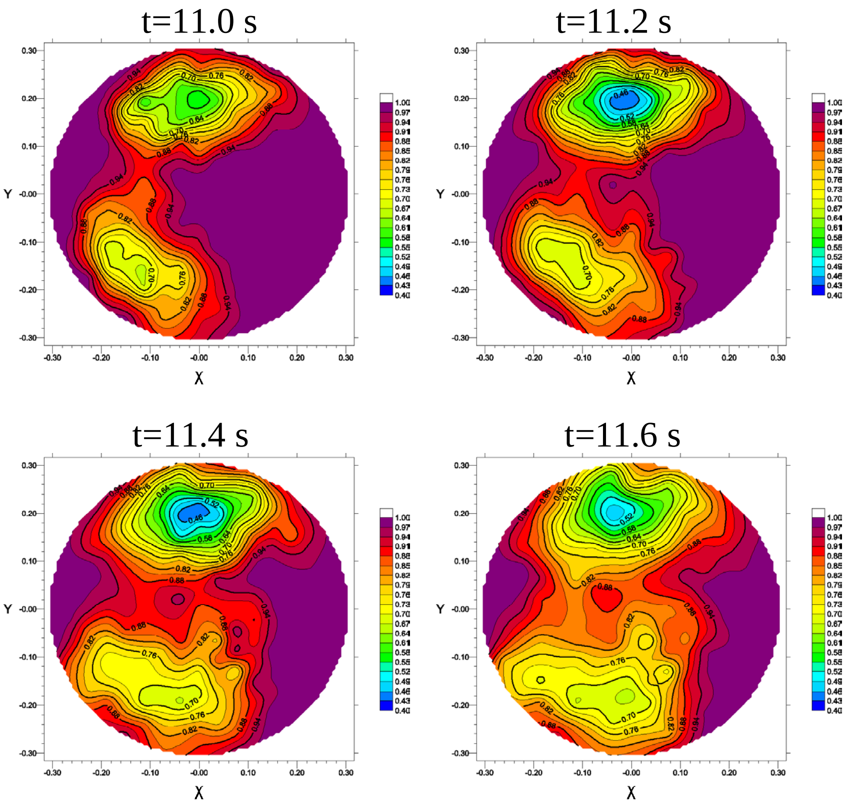

Fig. 3.3.12 VATT-02. Boron concentrations at core inlet for different times

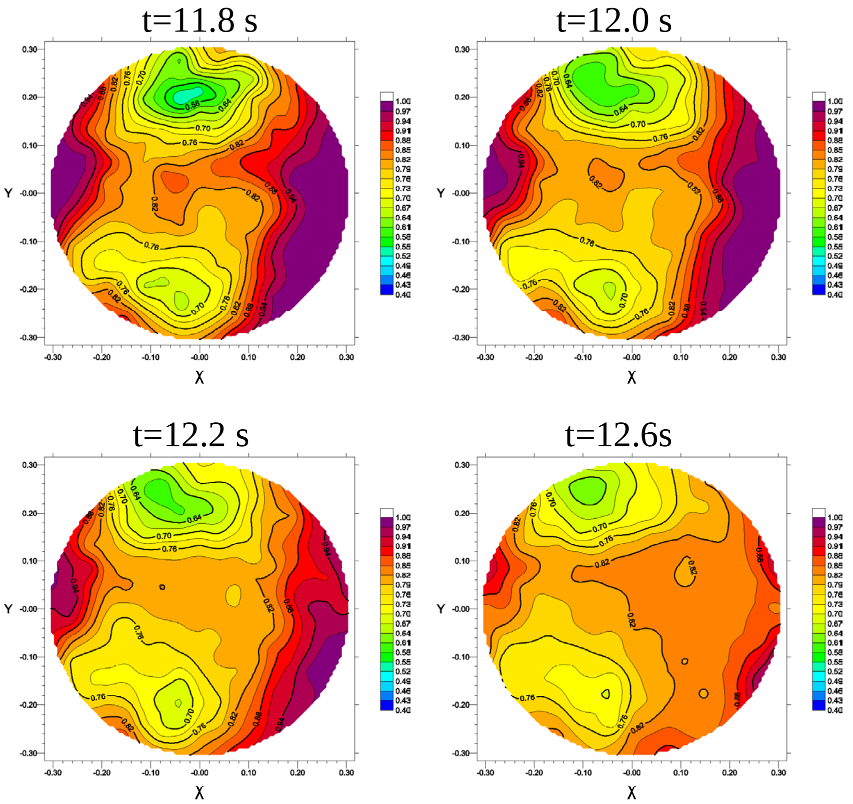
t=11.8 s

t=12.0 s

t=12.2 s

t=12.6s

Fig. 3.3.13 VATT-02. Boron concentrations at core inlet for different times

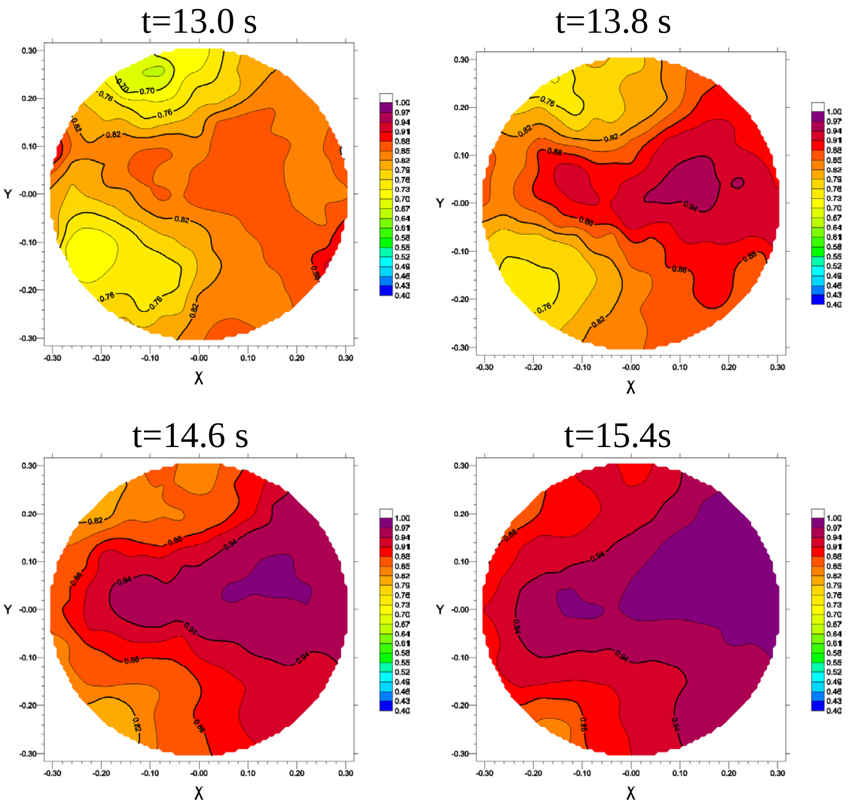
t=13.0 s

t=13.8 s

t=14.6 s

t=15.4s

Fig. 3.3.14 VATT-02. Boron concentrations at core inlet for different times

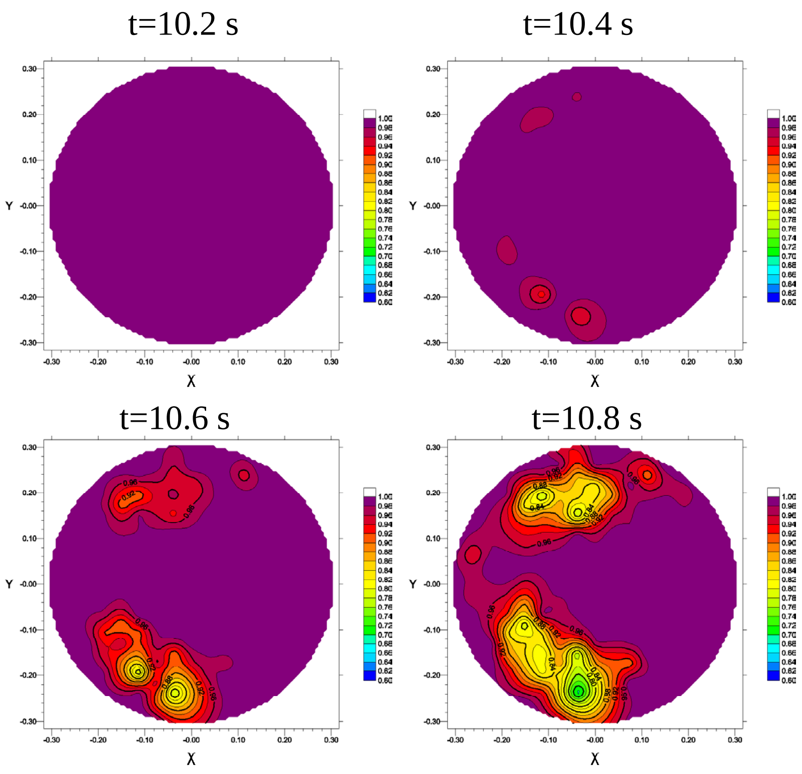

t=10.2 s

t=10.4 s

t=10.6 s

t=10.8 s

Fig. 3.3.15 VATT-03. Boron concentrations at core inlet for different times

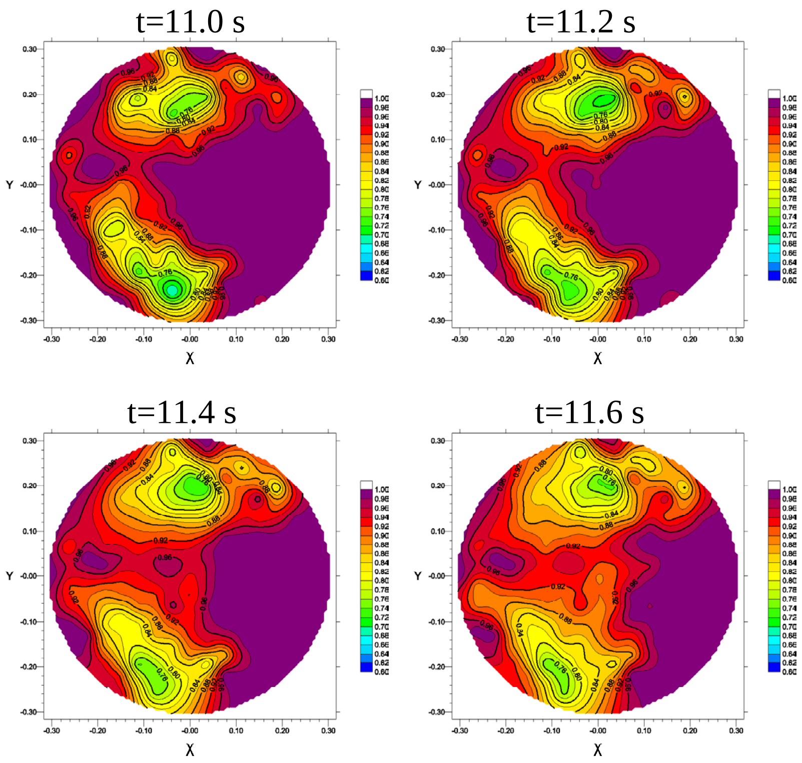

t=11.0 s

t=11.2 s

t=11.4 s

t=11.6 s

Fig. 3.3.16 VATT-03. Boron concentrations at core inlet for different times

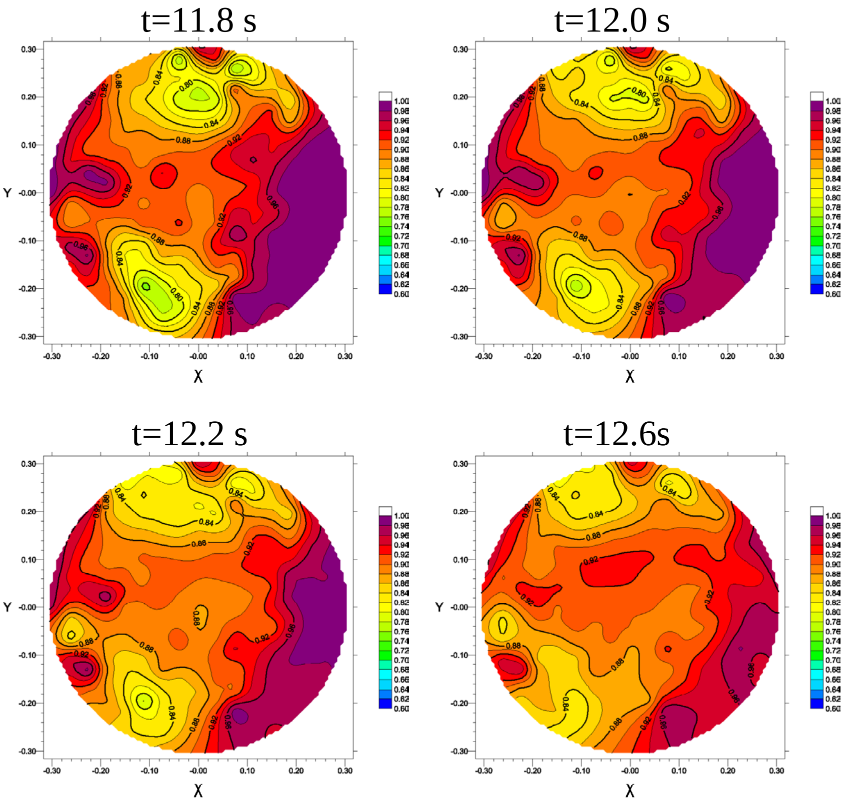
t=11.8 s

t=12.0 s

t=12.2 s

t=12.6s

Fig. 3.3.17 VATT-03. Boron concentrations at core inlet for different times

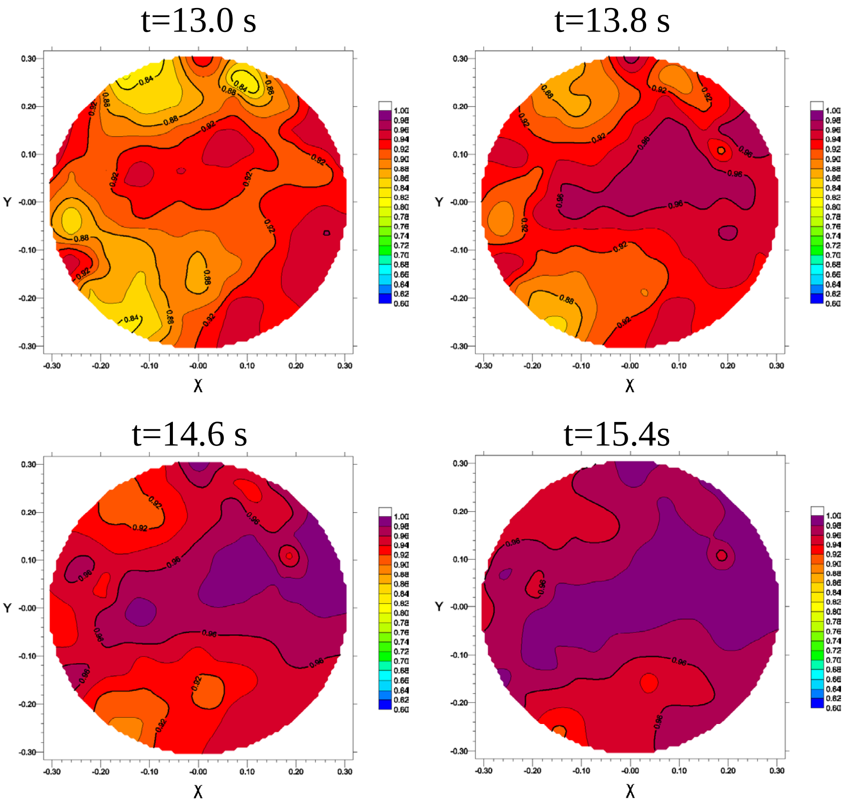
t=13.0 s

t=13.8 s

t=14.6 s

t=15.4s

Fig. 3.3.18 VATT-03. Boron concentrations at core inlet for different times

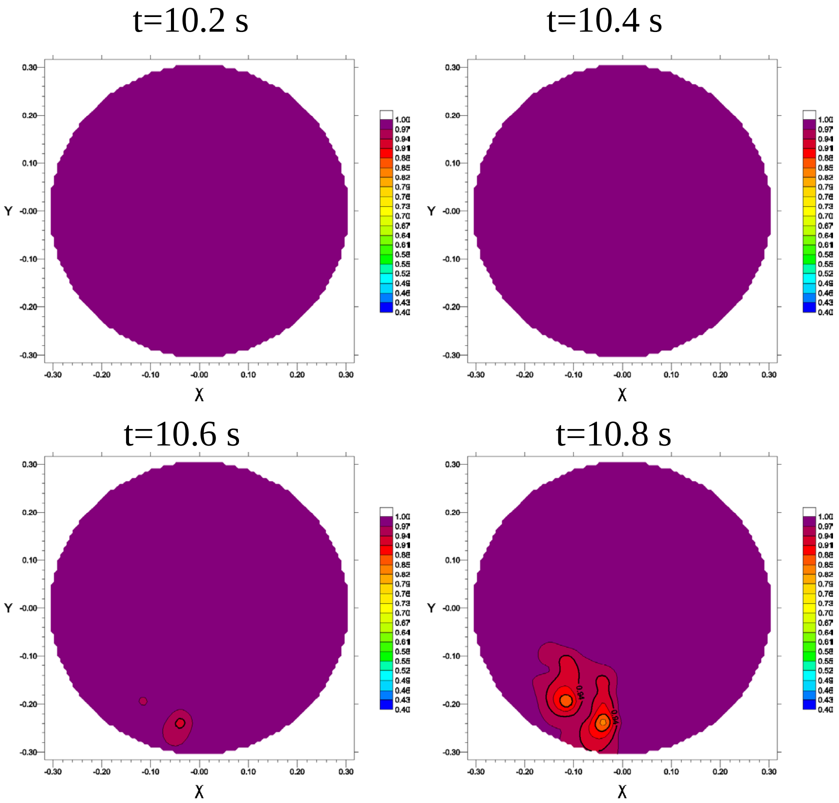

Fig. 3.3.19 VATT-04. Boron concentrations at core inlet for different times

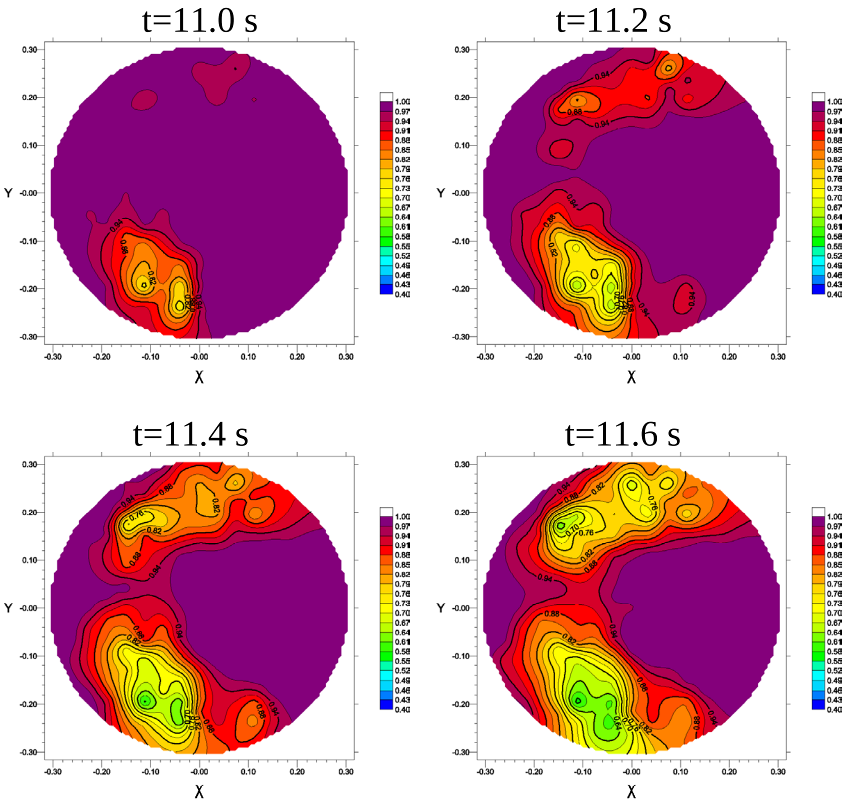

Fig. 3.3.20 VATT-04. Boron concentrations at core inlet for different times

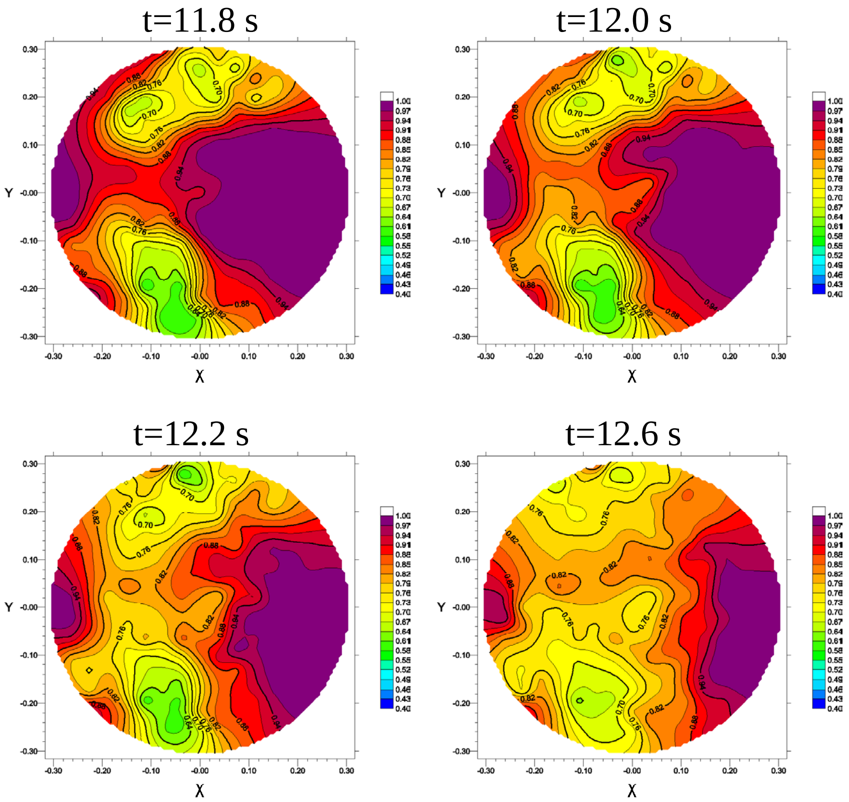

Fig. 3.3.21 VATT-04. Boron concentrations at core inlet for different times

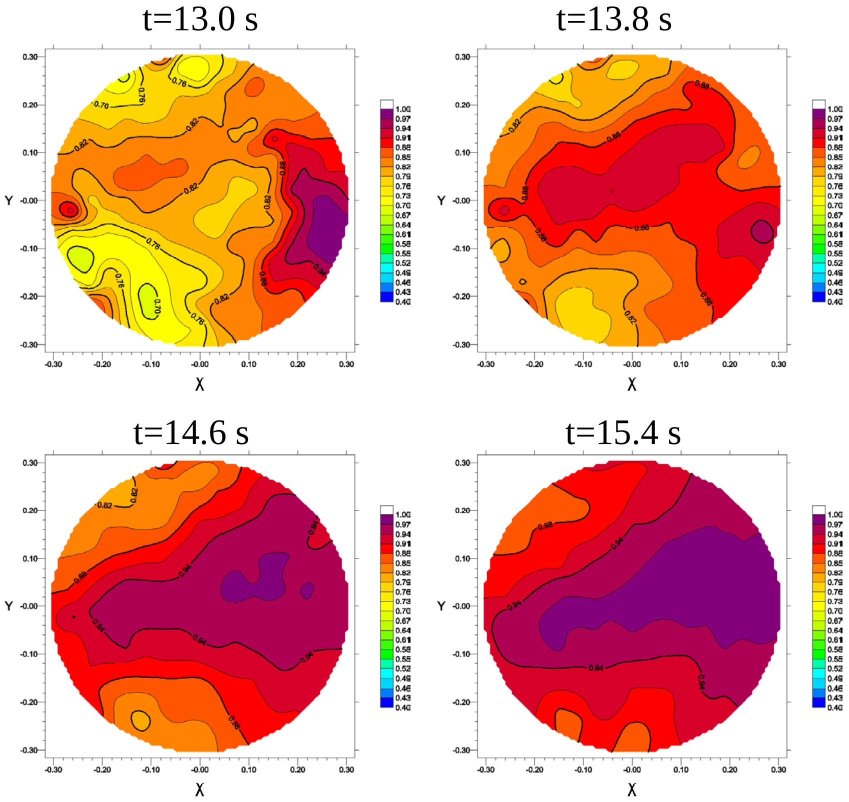

Fig. 3.3.22 VATT-04. Boron concentrations at core inlet for different times

3.3.2.7 Dimensionless boron concentration for individual probes.

In Fig. 3.3.23 - Fig. 3.3.26 boron concentrations for the probes for which the lowest concentrations were measured for each test case (see Tab. 3.4) are plotted as a function of time. Both the average concentration from the five tests (thick black line) in the test series and the concentration for each individual test are plotted.

In Fig. 3.3.27 the average concentration for the same positions are plotted together. Although not at the same positions they give an indication of the behaviour at the "worst" positions.

One can see that the four signals almost coincide for the first part of the transient. For the big slug, VATT-01, the slope of the concentration curve starts to decrease at a concentration of around 0.6. For the VATT-02 case the slope is retained all the way down to a concentration of around 0.4.

One can also see that the curve form is different for VATT-04 and VATT-02.

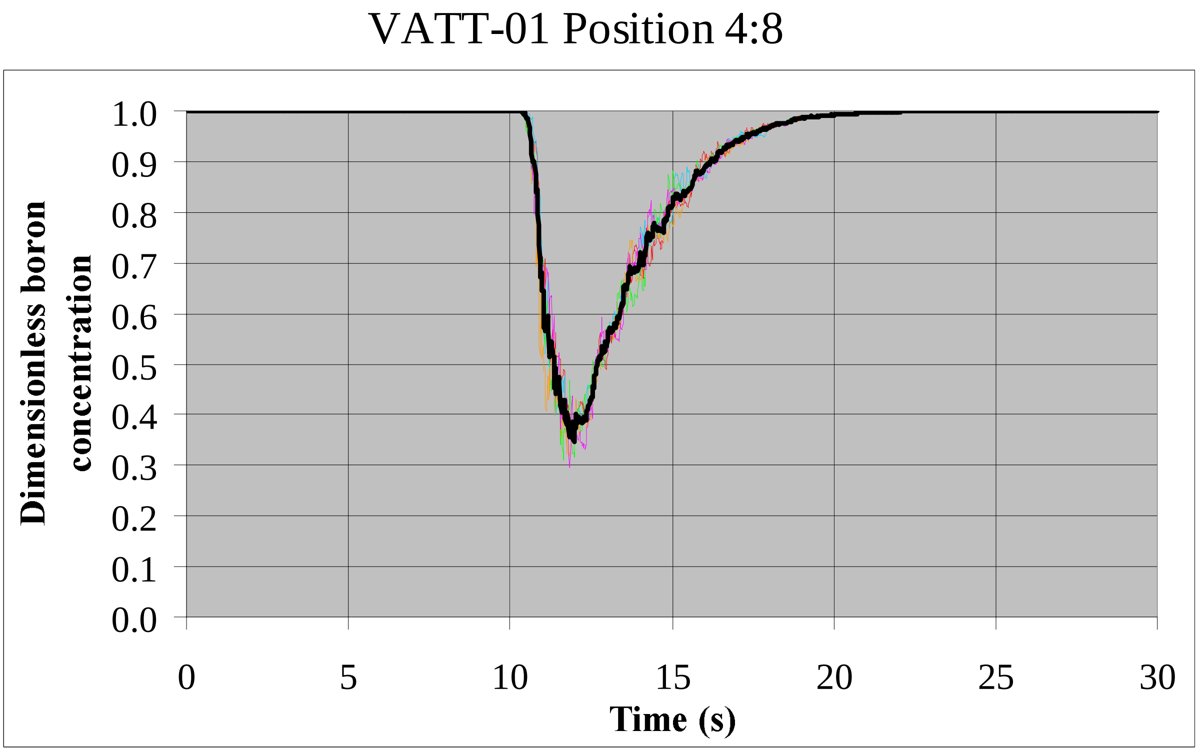

Fig. 3.3.23 Time history of boron concentration for position where lowest minimum concentration was measured for test case VATT-01

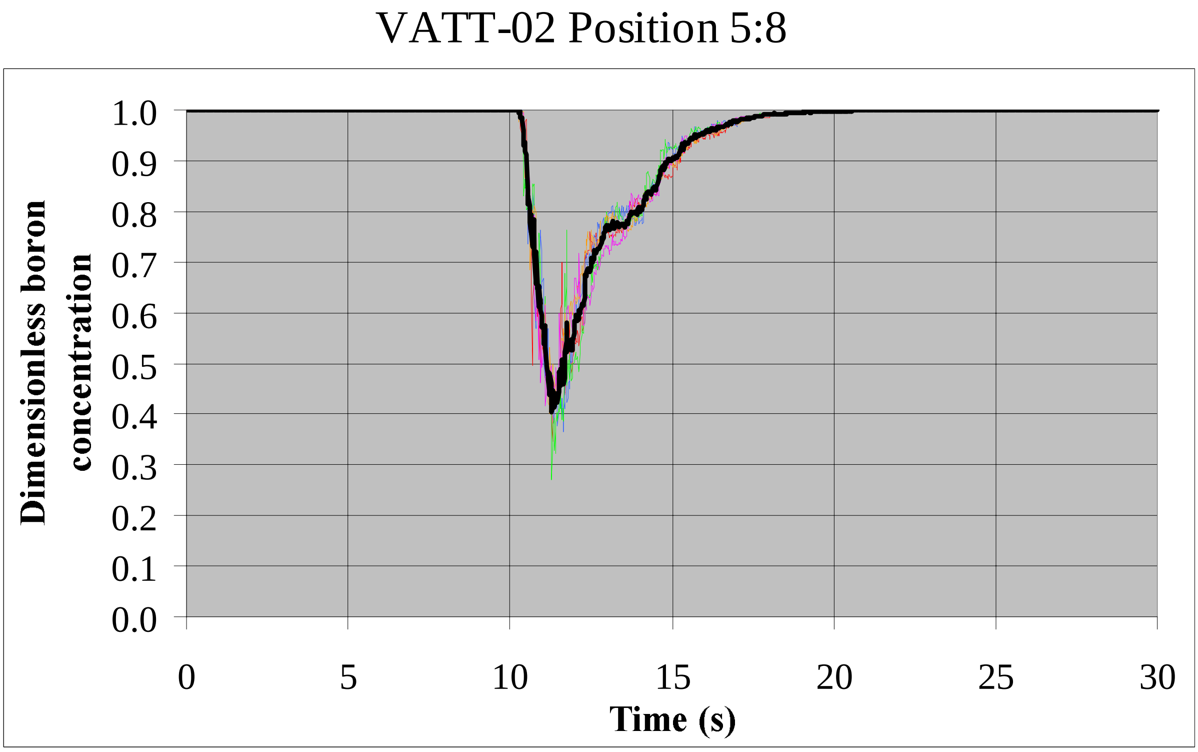

Fig. 3.3.24 Time history of boron concentration for position where lowest minimum concentration was measured for test case VATT-02

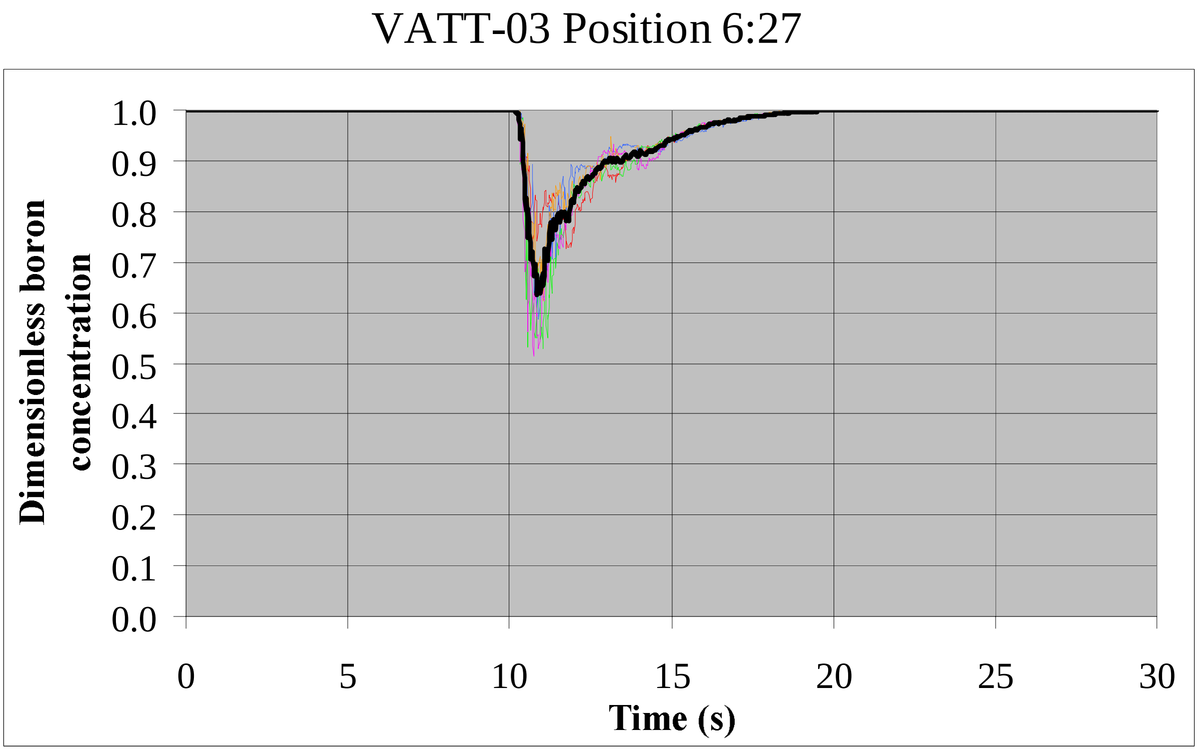

Fig. 3.3.25 Time history of boron concentration for position where lowest minimum concentration was measured for test case VATT-03

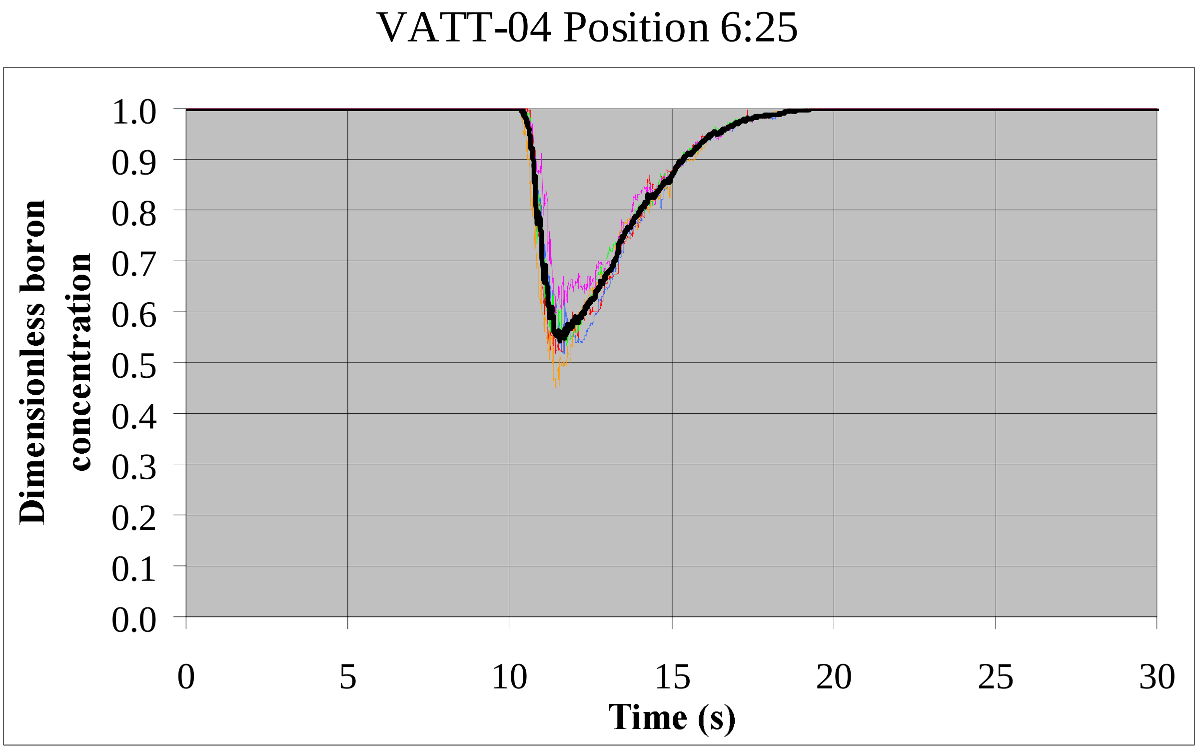

Fig. 3.3.26 Time history of boron concentration for position where lowest minimum concentration was measured for test case VATT-04

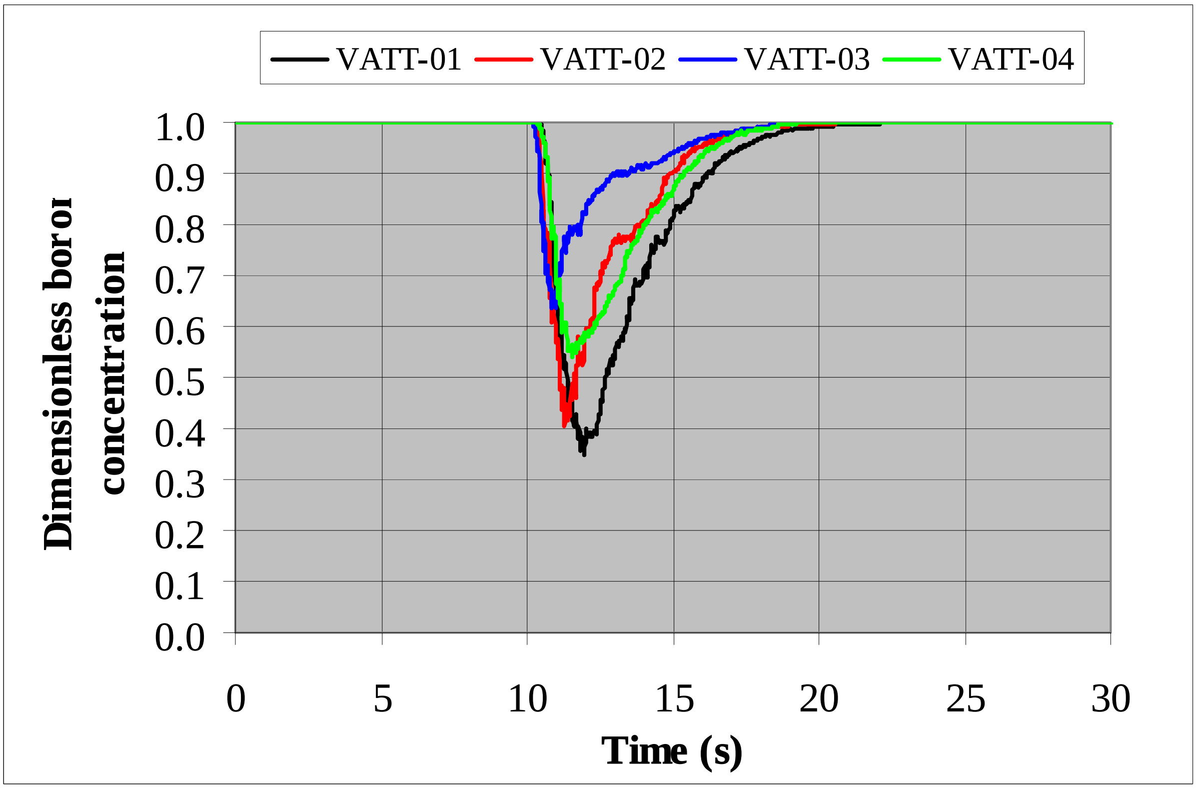

Fig. 3.3.27 Time history of boron concentration for position where lowest minimum concentration was measured for each test case. Only the average from each test series is plotted

3.3.3 Visualisations

The following types of visualisations were made for the Vattenfall VATT-02 case.

- Local injections of dye during steady state flow.
- Local injections of dye during a VATT-02 transient.
- Visualisations of a coloured slug passing through the downcomer during a VATT-02 transient.
- Laser sheet visualisations of a slug passing through the downcomer during a VATT-02 transient.
- Visualisations of slug quality in the inlet pipe during a VATT-02 transient.

These visualisations are described below. A description of the mpg files is given in Appendix A.3.

All visualisations are run with a water temperature of 54±2°C.

3.3.3.1 Local injections of dye during steady state flow

Dye is injected locally during a steady state flow situation with an inlet mass flow rate of 118 kg/s, the same mass flow rate as the maximum mass flow rate during the VATT-02 transient tests. Most injection positions are in the lower part of the downcomer, at around z=-1.1 m (i.e. around 15 cm above the bottom of the downcomer). The radial position of the injection points is not kept track of. There are, however, only small differences in flow pattern between different radial positions in the lower part of the downcomer. The recordings are presented starting at a tangential angle of 0° and then moving anti-clockwise, when seen from above.

To show the angular position in the downcomer, yellow markings and vertical lines have been put on the outer wall of the downcomer for every 5 degrees. The distance between these vertical lines is 11 cm. The height of the yellow angle markings is 3.5-4 cm. There are no markings for vertical positions in the downcomer.

Below are some hints, apart from those presented in chapter 3.2.1, on how to navigate through the model.

- The lowest visible part of the downcomer is at z=-1.19 m.

- Most of the yellow angle-markings near the bottom of the downcomer are at z= -1.13 m.
- The yellow angle-markings further up in the downcomer are at z= -0.54 m.
- The highest visible part of the downcomer is at around z=-0.3 m.

These visualisations will primarily give a qualitative understanding of the direction of flow in the lower part of the downcomer and how this flow direction fluctuates in time. It is hard to get a measure of the velocity magnitude from these visualisations. The LDV measurements will give this information. The streak line from an injection position is difficult to follow for any longer distance due to the rapid dilution of the dye into the surrounding fluid.

Fig. 3.3.28 shows some results from the visualisations. It shows the steady state flow direction at z=-1.1 m, i.e. around 15 cm above the bottom of the downcomer. One can see that the flow is directed almost straight upwards for angles between around +30° and +75° (see red line) and almost straight downwards between +115° and -45° (see black lines). At an angle of 0°, under the inlet pipe, the flow is directed to the left. At an angle of around +95° the flow is directed to the right.

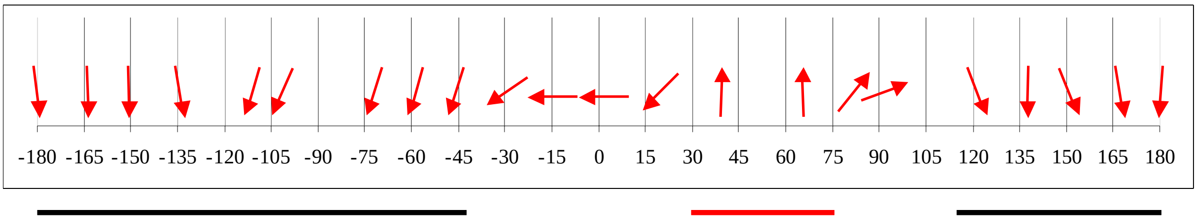

Fig. 3.3.28 Steady state flow direction at z=-1.1 m, as a function of tangential angle

3.3.3.2 Local injections of dye during a VATT-02 transient

Dye is injected locally during a VATT-02 transient. Only a small number of injection positions in the lower part of the downcomer (at around z= -1.1 m, i.e. around 15 cm above the bottom of the downcomer) and from tangential position 0° to +90° are used. It is in this region that the flow tends to be directed upwards during steady state flow.

Each recording starts at approximately the same time as the start of the transient, as defined in chapter 3.2.1.

These visualisations will give the same kind of information as the local injections of dye during steady state flow described above, and show how the flow pattern changes during the transient.

From these visualisations it could be seen that the flow direction changed considerably during the transient. For example, at a tangential position of 0° the flow direction is more or less straight downwards for the first 8-10 seconds, the turns upward and finally ends up being directed straight to the left.

3.3.3.3 Visualisations of a coloured slug passing through the downcomer during a VATT-02 transient

VATT-02 transient tests are run with a coloured slug. The downcomer region is filmed from four different tangential locations, +35°, +110°, -160° and –70°. These recordings are made during separate test runs. Two recordings are made for each camera position.

Each recording starts approximately 5 seconds before the start of the transient.

These visualisations show which parts of the downcomer that are affected by the slug, for different times. Concentrations are hard to determine due to the effect of uneven lightning.

From these visualisation one can, for example, see that the slug front enters the bottom of the downcomer later below the inlet pipe (for angles between -50° to +30°) and opposite of the inlet pipe (for angles between +120° to -170°). This also indicates that the flow pattern is somewhat twisted to the left at the early stages of the transient. This is in accordance with the observations from the boron concentration measurements at the core inlet, for which the concentrations were lower on the left side early on.

One can also see that the tail of the slug moving downwards in the downcomer at around +110° is much more broken up and fluctuating in time compared to the tail on the other side of the downcomer. This can be an effect of the wake behind the idle loop pipe passing through the downcomer at an angle of -50°.

3.3.3.4 Laser sheet visualisations of a coloured slug passing through the downcomer during a VATT-02 transient

VATT-02 transients are being run with laser sheets positioned at six different vertical planes in the downcomer (at 0°, +60°, +120°, 180°, -120°, -60°) and at three different horizontal planes in the downcomer region (at z=-0.48 m (High level), z= -0.78 m (Middle level) and at z= -1.08 m (Lower level). These recordings are made during separate test runs. Two recordings are made for each laser-sheet position.

Each recording starts approximately 5 seconds before the start of the transient. To be able to restrict the illumination to the sheets only, keeping the surrounding fluid black, the scene was kept very dark.

These visualisations show at what times the laser-sheet planes are affected by the slug. Concentrations are hard to determine.

3.3.3.5 Visualisations of slug quality in inlet pipe during a VATT-02 transient

The concentration measurement tests for VATT-02 were run with a coloured slug. The stretch of the inlet pipe, from 23 cm to 62 cm downstream from the initial position of the slug front, which is in plexiglas, was filmed during the transient for 12 of the 15 VATT-02 concentration measurement tests.

Each recording starts approximately 5 seconds before the start of a transient.

These visualisations show that there are very small density currents in this part of the inlet pipe due to density differences between the slug and the water immediately upstream and downstream of the slug.

3.3.4 LDV measurements

LDV measurements are made for steady state and for transient conditions for the VATT-02 case.

Measurements are only made in the downcomer. Here measurements are made for six different tangential positions (at +30°, +90°, +150°, -30°, -90° and -150° and at two different levels (low level: z=-1.033 m and middle level: z = -0.773 m) and at four positions in the radial direction (10 mm, 20 mm, 30 mm and 40 mm from the inside of the outside wall. The inner point of these four points does not exist for the tangential positions -90° and +90° where there are thermal shields. Appendix A3.4 gives the coordinates for the position where velocities were measured. The red dots in Fig. 3.3.29 show where measurements were made.

Vertical and tangential velocities were measured. These were measured simultanously. Tangential velocity is defined as being positive when the flow is directed to the right when looking from an upright position outside the model.

The steady state measurements are made for 60 seconds. Transient measurements are made for 90 seconds. 5 measurements are made for each measurement point.

All measured LDV data are presented in files that are attached to [Hem04].

Fig. 3.3.30 - Fig. 3.3.32 show measured velocities and velocity angle at the lower measuring plane for steady state conditions. Velocity angle, which gives the direction of flow, is defined as being zero when the flow is directed straight downwards, positive when directed to the right when looking from an upright position outside the model. Only the radial averages are shown for each tangential position. One can see that the flow pattern is quite non-symmetric around the angle 0. The flow is directed upwards between around -15° and +70°, if interpolation is made between the angles for which measurements are made. Flow is directed straight to the left at an angle of +30°. This can be compared to the results from the visualisations, presented in chapter 3.3.3.1. These are made only about 10 cm below where the LDV measurements were made, but below the thermal shields. Here the velocity was directed upwards from around +30° to around +100°, i.e. a bit further away from the RCS pipe inlet. Flow was directed straight to the left at an angle of -15° to 0°.

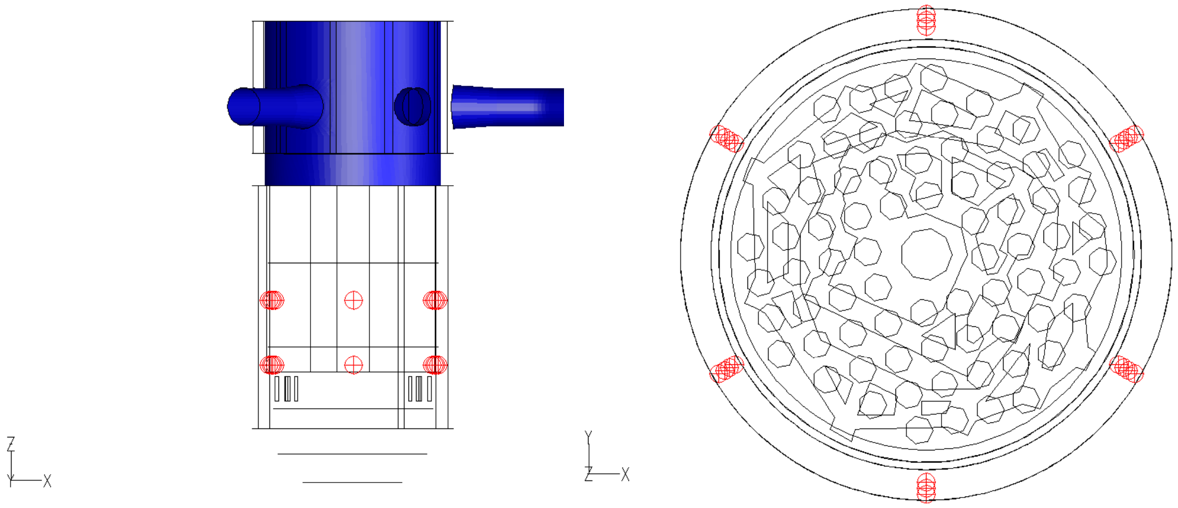

Fig. 3.3.29 Positions for velocity measurements

The maximum velocity measured is -2.55 m/s. This can be compared to the average velocity of around -1.0 m/s.

Fig. 3.3.32 - Fig. 3.3.35 show measured velocities and velocity angle at the middle measuring plane (z=-0.773 m). The flow pattern is similar to the low level, but with smaller variations. There are no measured positive velocities at this level. Fig. 3.3.36 and Fig. 3.3.37 show measured velocities as a function of time. Only the velocity angle, i.e. the direction of flow is presented here. The average velocity from five tests is shown. The red squares show around which time averages were made. One can see that the flow field changes drastically during the transient. Up to around 9 seconds the flow is more or less directed straight downwards at the low level. At 9 seconds the flow pattern suddenly starts to change. Not until around 20 seconds something that looks like the steady state flow pattern have evolved. At the middle level the transition takes place approximately one second earlier. The reason for the changes in flow pattern is probably the transition from laminar to turbulent flow. Two examples of individual velocity time signals were shown in Fig. 3.2.9 and Fig. 3.2.10.

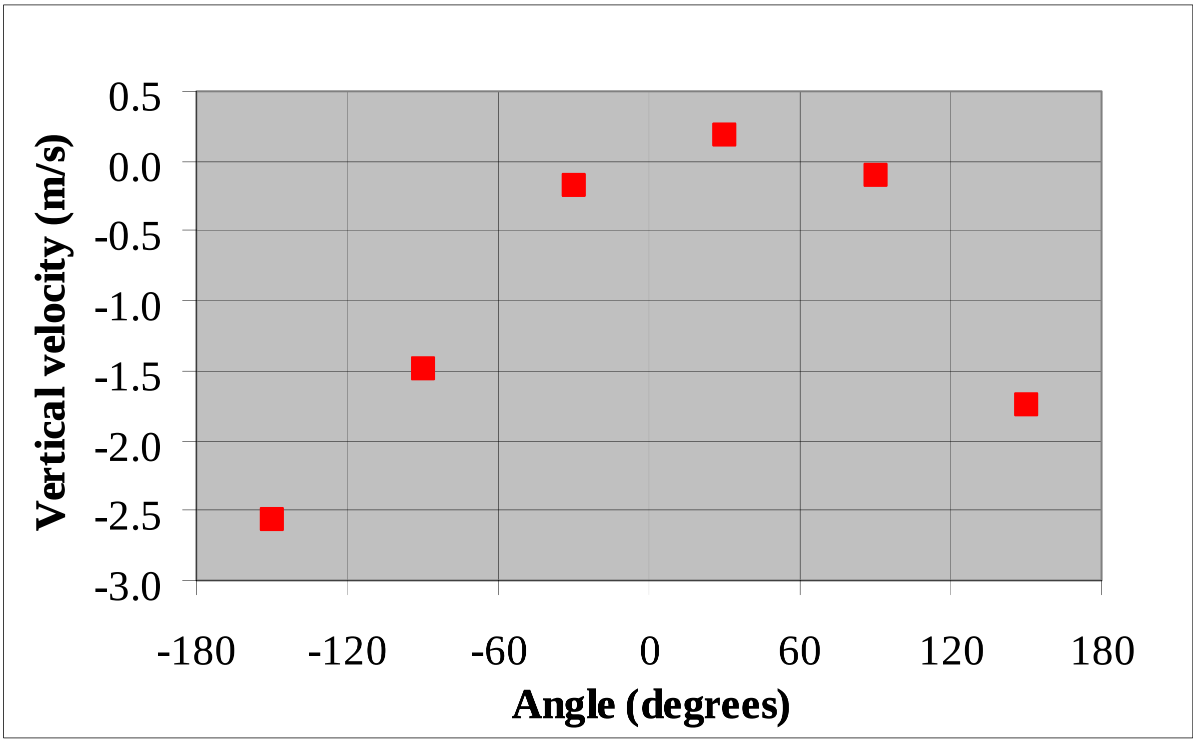

Fig. 3.3.30 Steady state. Vertical velocity at low level (z=-1.033 m)

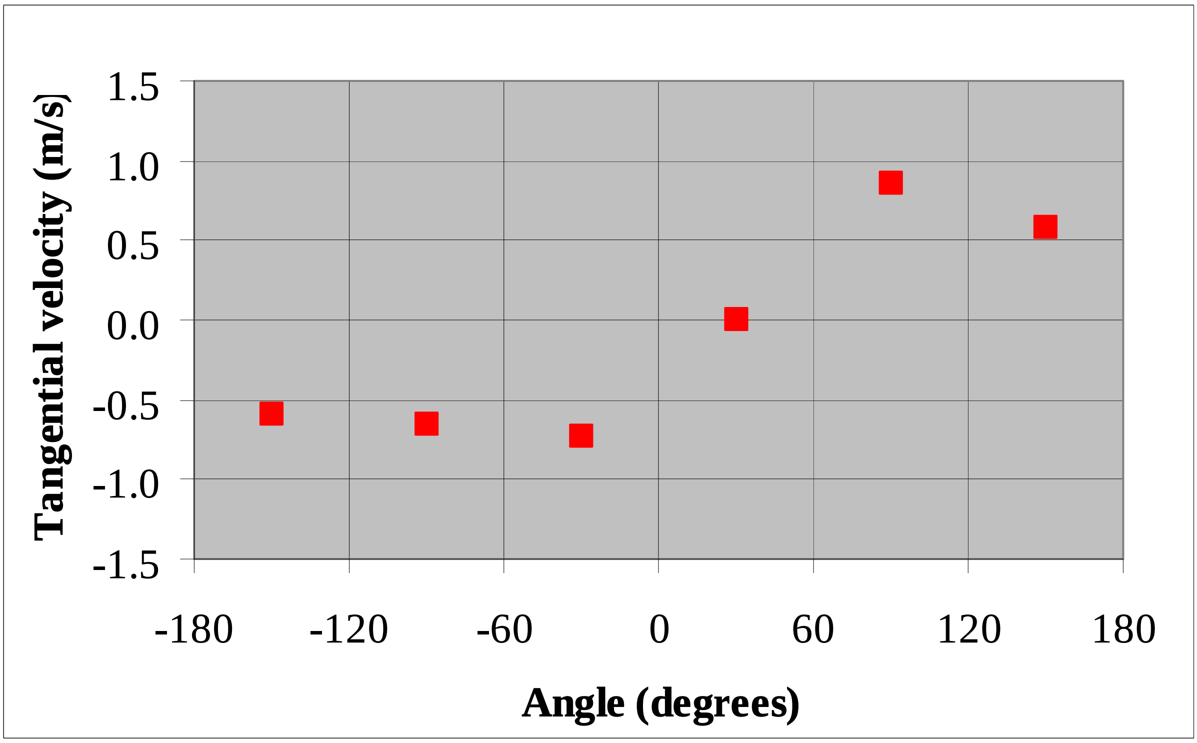

Fig. 3.3.31 Steady state. Tangential velocity at low level (z=-1.033 m)

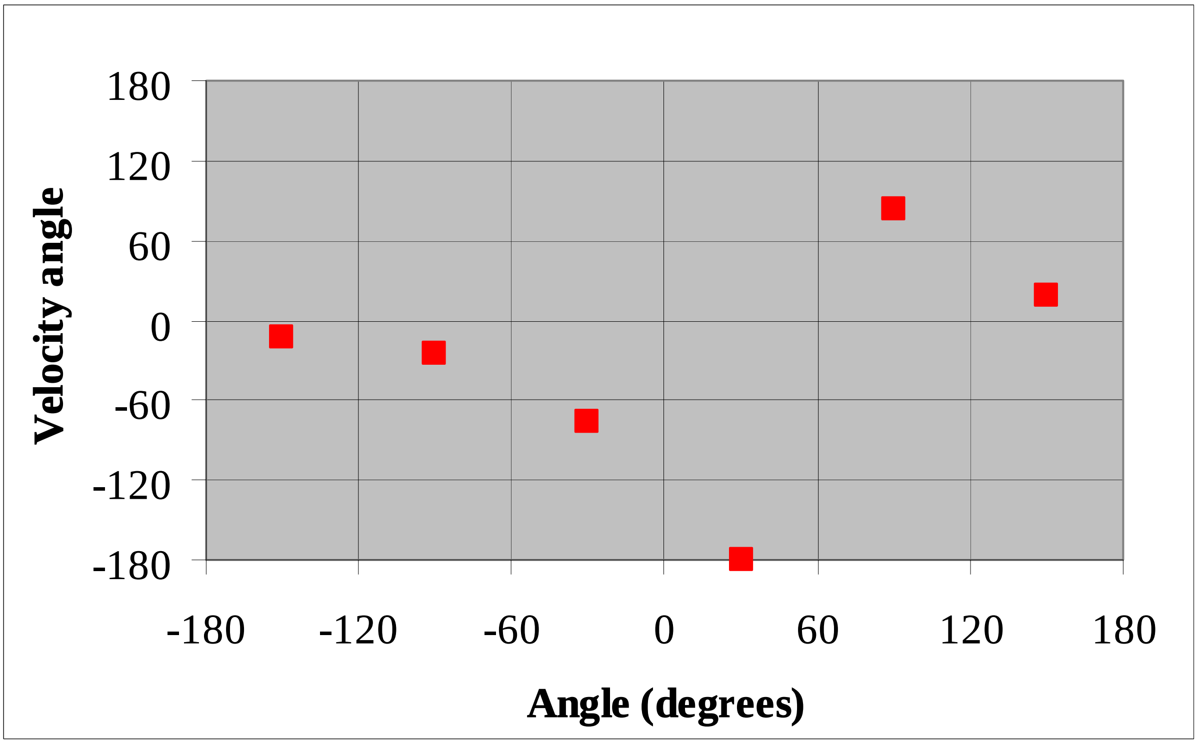

Fig. 3.3.32 Steady state. Velocity angle at low level (z=-1.033 m)

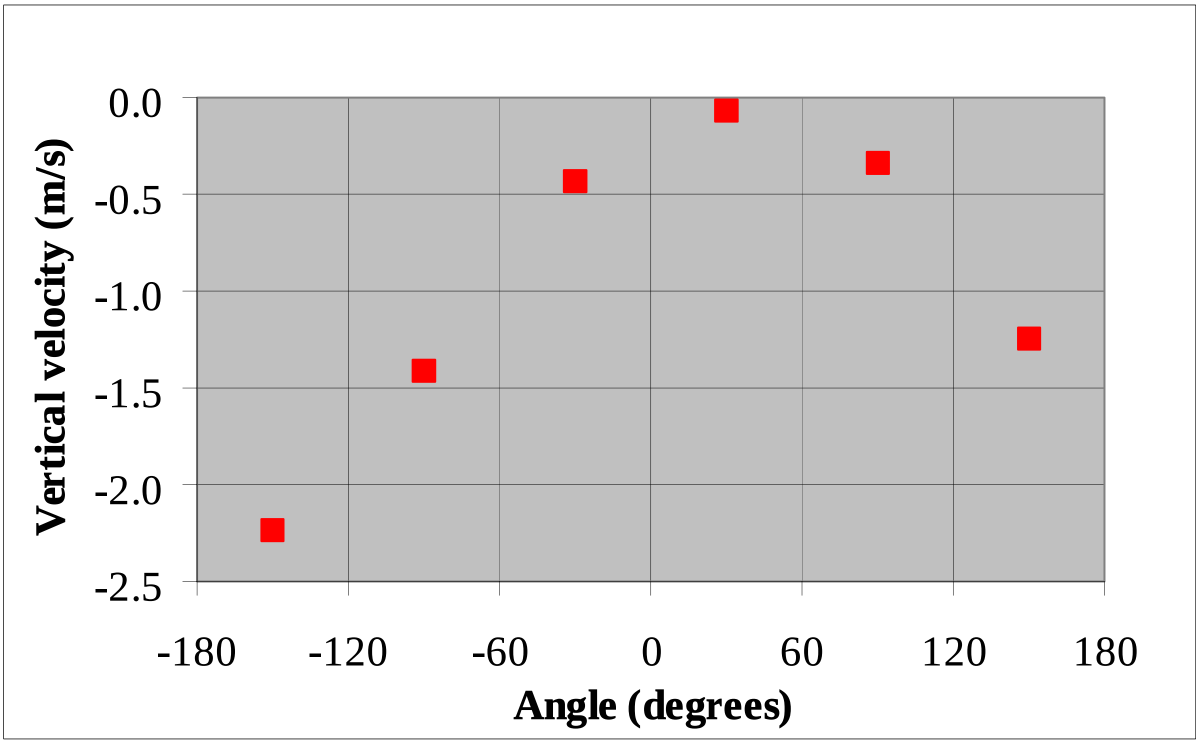

Fig. 3.3.33 Steady state. Vertical velocity at mid level (z=-0.773 m)

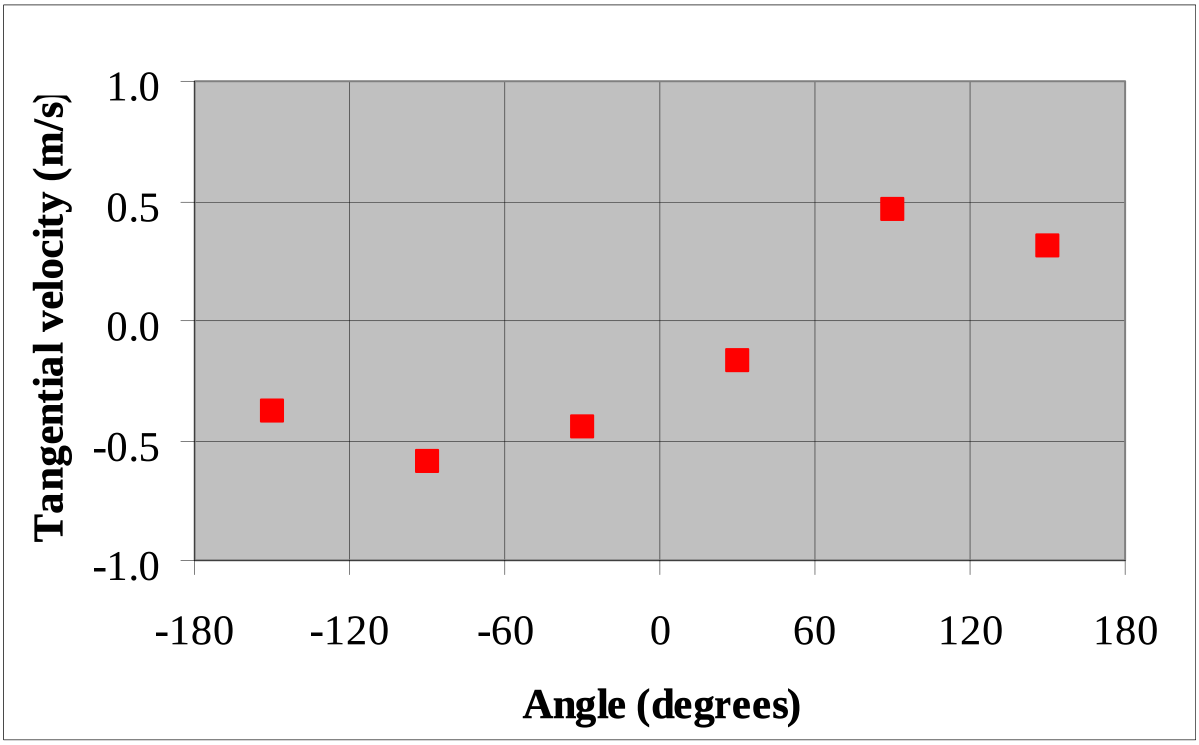

Fig. 3.3.34 Steady state. Tangential velocity at mid level (z=-0.773 m)

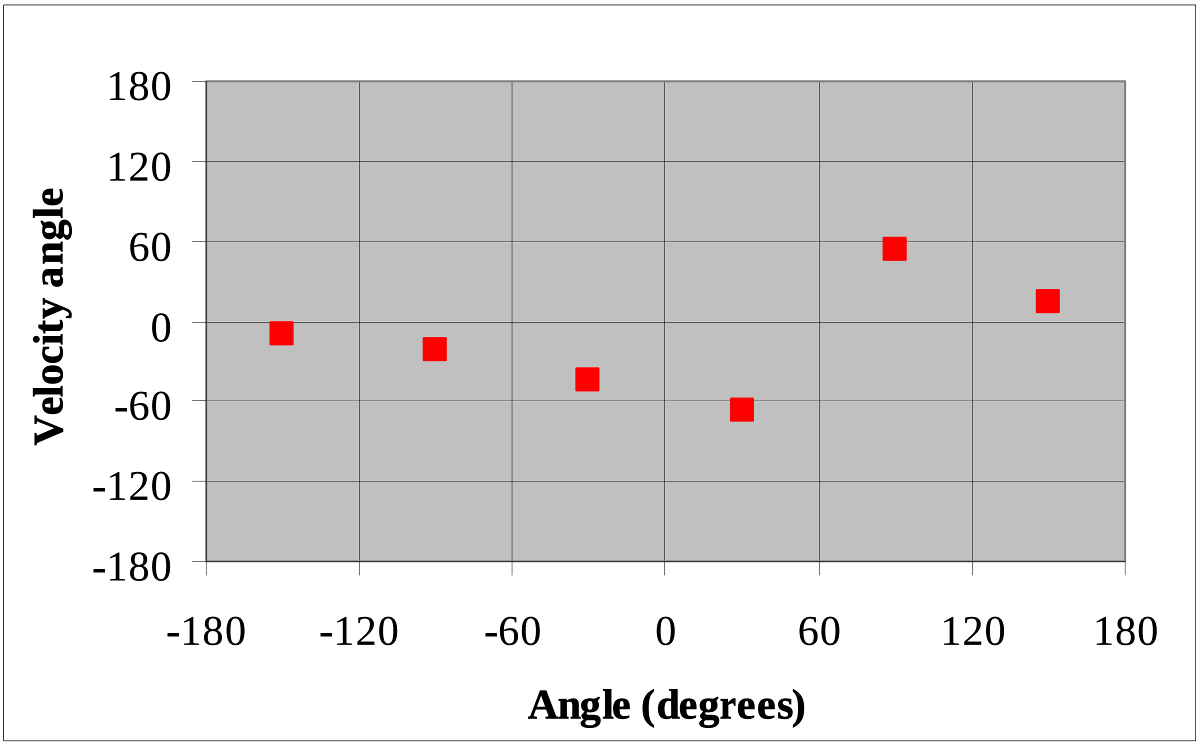

Fig. 3.3.35 Steady state. Velocity angle at mid level (z=-0.773 m)

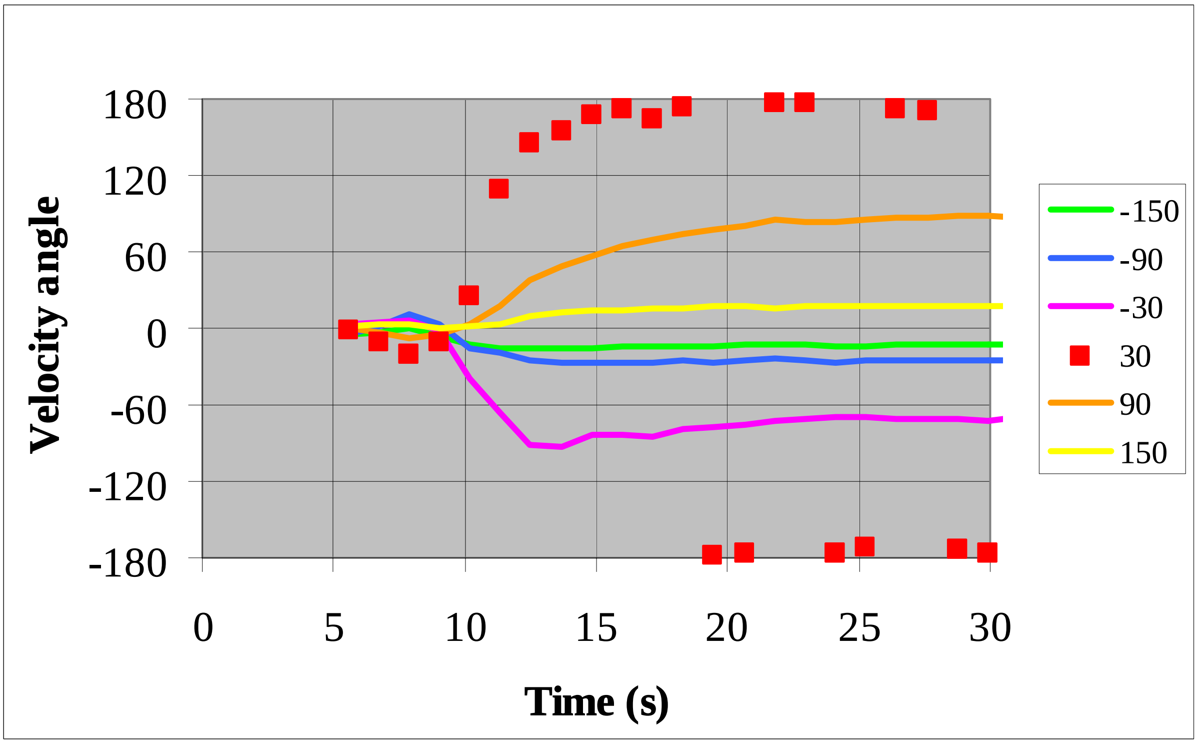

Fig. 3.3.36 Velocity angle as a function of time at the low level (z=-1.033 m)

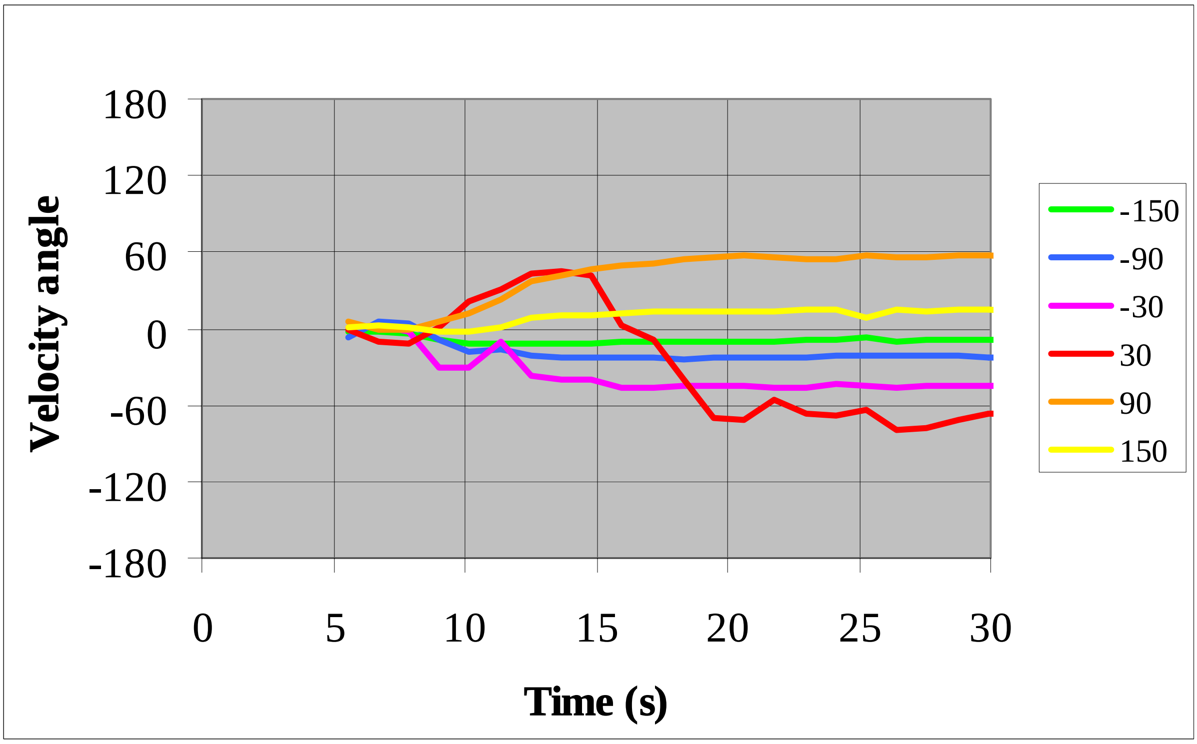

Fig. 3.3.37 Velocity angle as a function of time at the mid level (z=-0.773 m)

4 Slug mixing experiments at the Gidropress test facility

4.1 The event to be studied and its simulation

The start-up of the VVER-1000 reactor circulation loop MCP with the loop seal being filled with coolant with decreased or zero boron concentration was simulated on the experimental facility. It was supposed that the MCP of the loop under consideration is started-up the first. In this case for other three idle loops coolant back flow will occur. To reduce the degrees of freedom of coolant distribution in the reactor inlet chamber the present report deals with the experimental data for the experiments where is no back flow through the idle loops. The gate valves on the idle loops were closed. The entire coolant from the model loop comes into the core inlet.

The volume of the loop seal in the VVER-1000 reactor including the MCP lower part is equal approximately to 8.5 m^3. The volume of the loop seal on the test rig was equal to 74 l that corresponds approximately 1/125 of the full-scale loop seal volume.

The coolant flow rate through the loop was determined according to the ratio obtained from equality of Strouhal number between model and reactor:

$$\frac{W_M \cdot \tau_M}{L_M} = \frac{W_r \cdot \tau_r}{L_r} \qquad \text{(Eq. 4.1.1)}$$

If either time of passage of the slug through the core or the coolant rate in the loop are assumed turn-by-turn as the governing parameter, the range of change in the coolant flow rate through the model loop of the experimental facility can be determined. If the time of the process in the model is equal to that in the real object we shall obtain from the ratio the following:

$$Q_M = Q_r * M^3 \qquad \text{(Eq. 4.1.2)}$$

and in case of equality of velocities of coolant in the model and real object

$$Q_M = Q_r * M^2 \qquad \text{(Eq. 4.1.3)}$$

Thus, with the actual flow rate of 27500 m^3/h (if one MCP is in operation) and a model scale of 1:5 the flow rate through the model loop in the experiments with the MCP start-up shall be over the range as follows:

$$220 \ m^3/h \le Q_M \le 1100 \ m^3/h \qquad \text{(Eq. 4.1.4)}$$

4.2 Description of the test rig

The test rig is based on the metal model of VVER-1000 reactor (the Novo-Voronezh (NV) NPP, Unit 5) on a scale of 1:5. In this rig, one loop with the loop seal and MCP simulator is completely simulated. The remaining three loops are performed as short-closed and only the pressure loss is simulated in them. These loops have valves that allow for these loops to be connected or disconnected. The diagram of this test rig is given in Fig. 4.2.1. Similar test rigs are available in France (test rig BORA-BORA), in Sweden (Vattenfall Utveckling AB, see chapter 3) and in Germany (test rig ROCOM, see chapter 2) with the PWR reactor models being made also on a scale of 1:5. However, it is necessary to note that the PWR reactor flow path (especially the lower vessel part) essentially differs from the VVER-1000 reactor flow path.

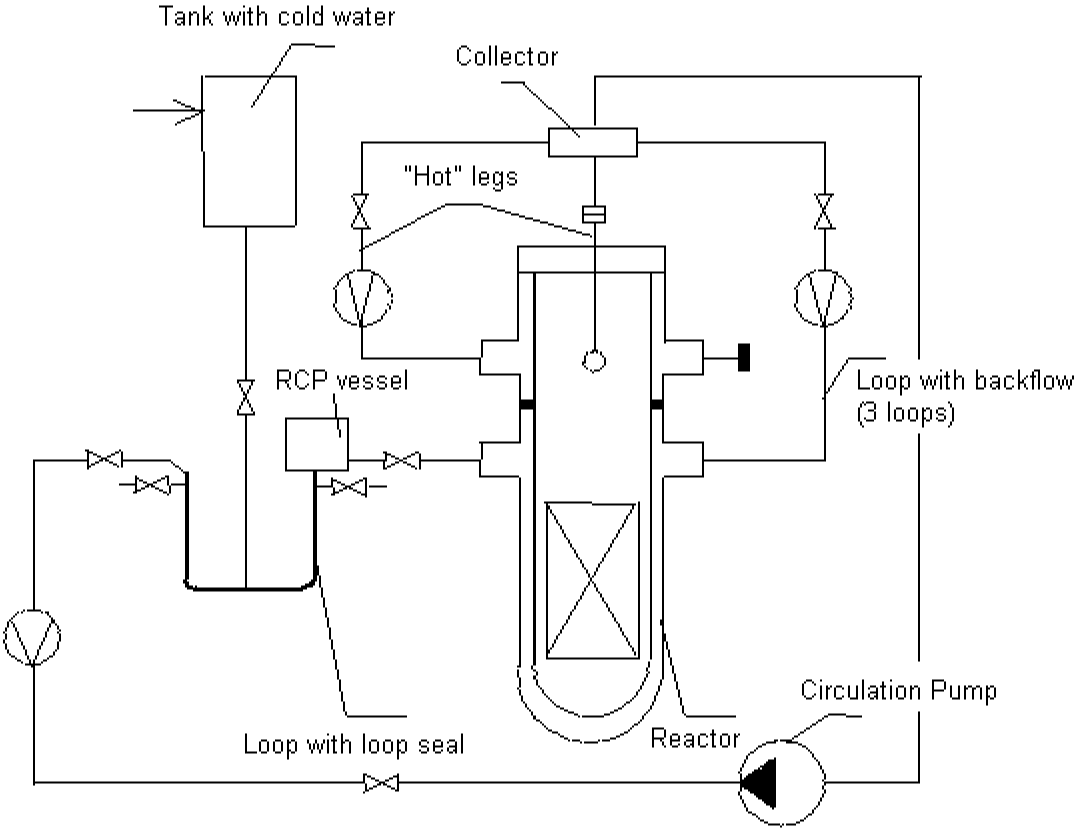

Fig. 4.2.1 Diagram of test rig

The reactor model is shown on Fig. 4.2.2. The basic geometrical dimensions of the flow path of the reactor model downcomer are given in Fig. 4.2.3. The minimum gap between the vessel bottom and core barrel amounted to 17 mm. The design and basic geometrical dimensions of the reactor model core barrel bottom are shown in

Fig. 4.2.4 and Fig. 4.2.5. By means of this model the NV NPP, Unit 5 reactor flow path was simulated. The water comes into the bottom through 1324 holes of d = 8.0 mm being uniformly located on the bottom elliptic grid. The perforation of the supporting tubes of the core barrel bottom (see Fig. 4.2.6) was not geometrically simulated. Only the pressure loss of the full-scale supporting tubes was simulated. The number of supporting tubes of the model core barrel bottom is equal to 151. Each of them has 12 slots of 30x3 mm. All the reactor model components were made of stainless steel.

The geometrical dimensions of the loop seal and supply pipeline are given in Fig. 4.2.7. The geometrical dimensions of the MCP simulator are given in Fig. 4.2.8. The geometry of the flow path of the reactor model inlet section (from the inlet nozzles up to the core inlet) corresponds completely to the full-scale one.

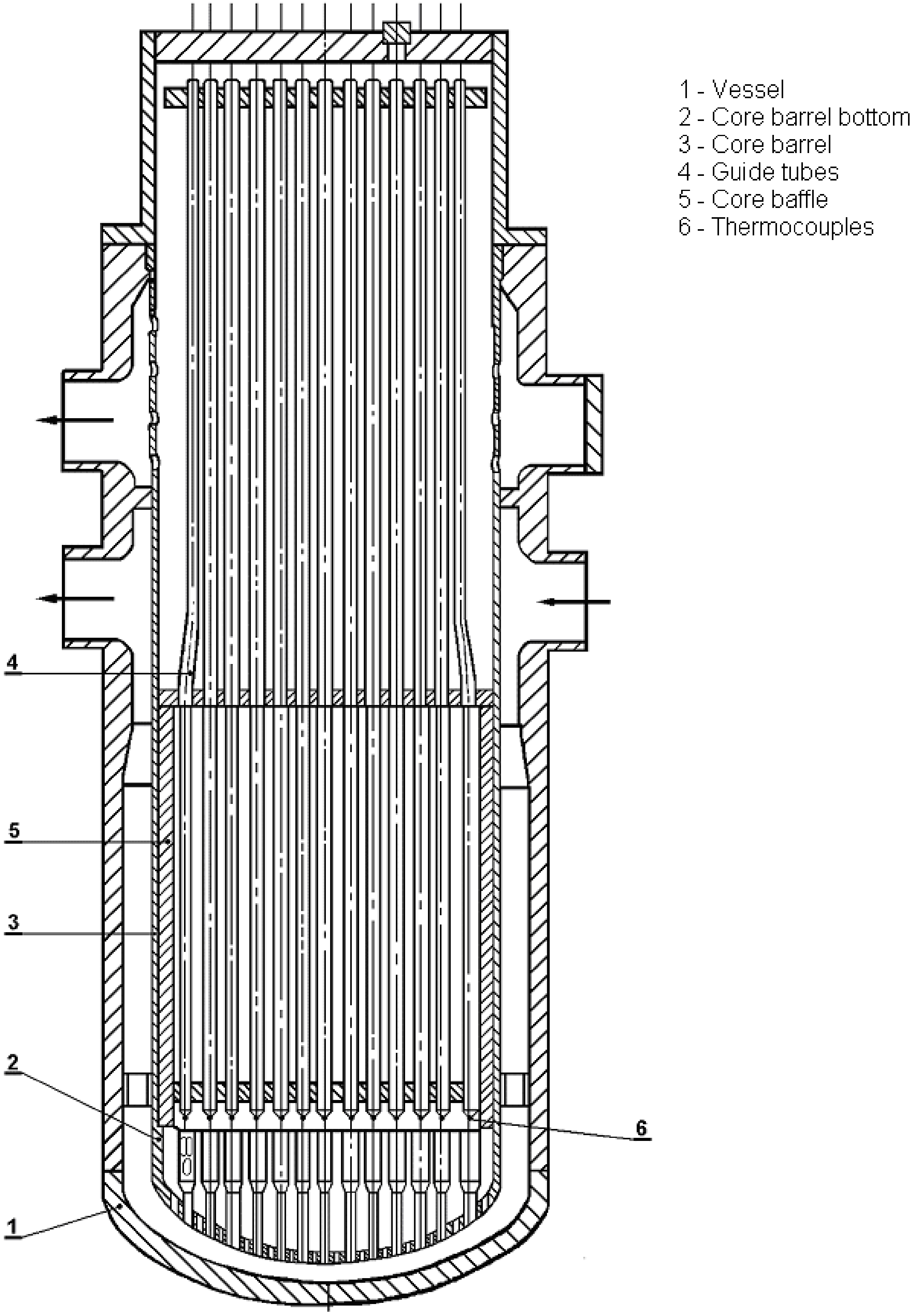

Fig. 4.2.2 Reactor model

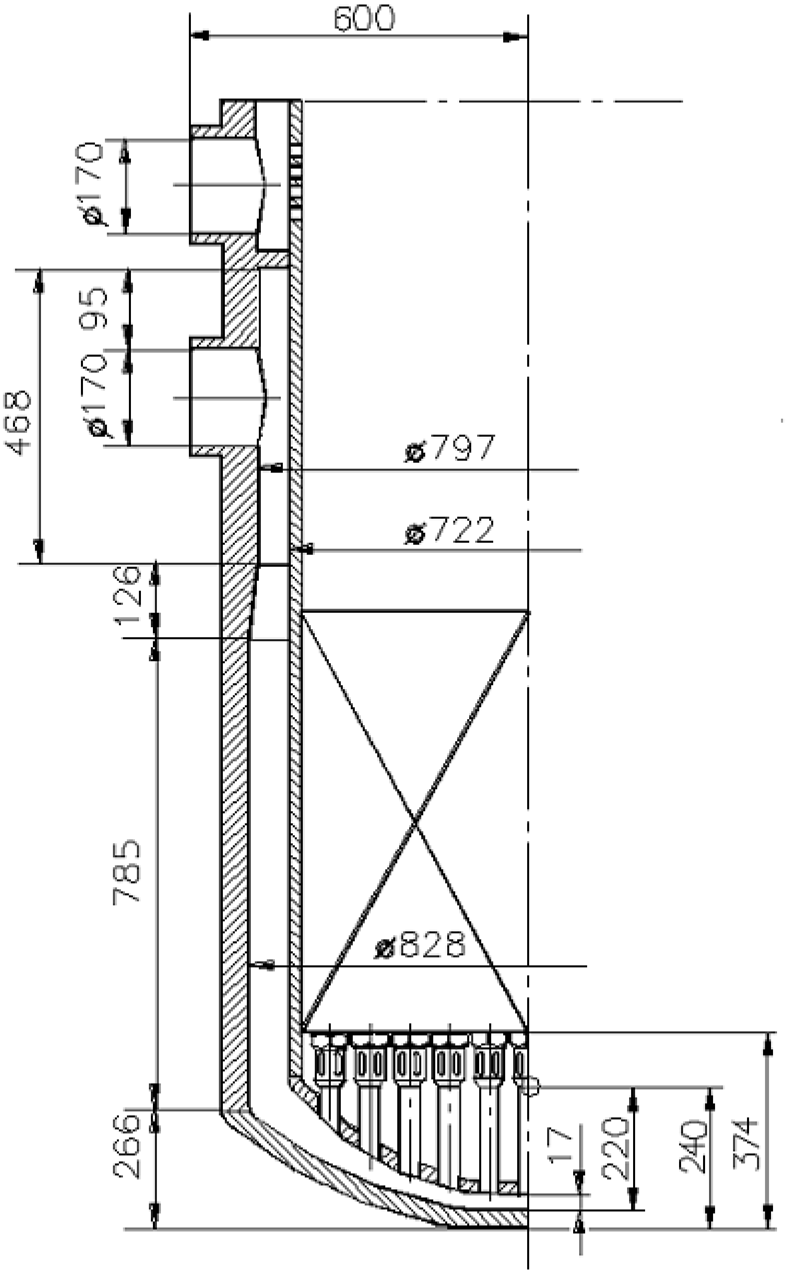

Fig. 4.2.3 Drawing of the downcomer

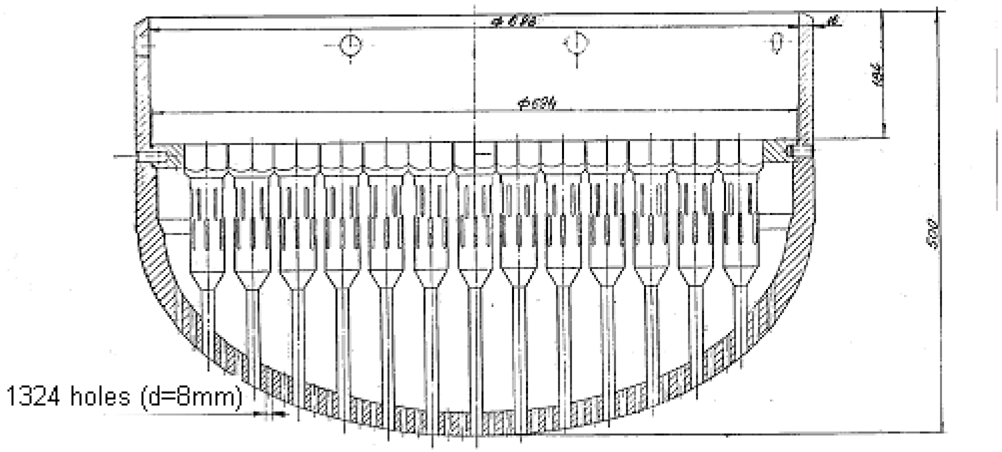

Fig. 4.2.4 Sketch of the core barrel bottom

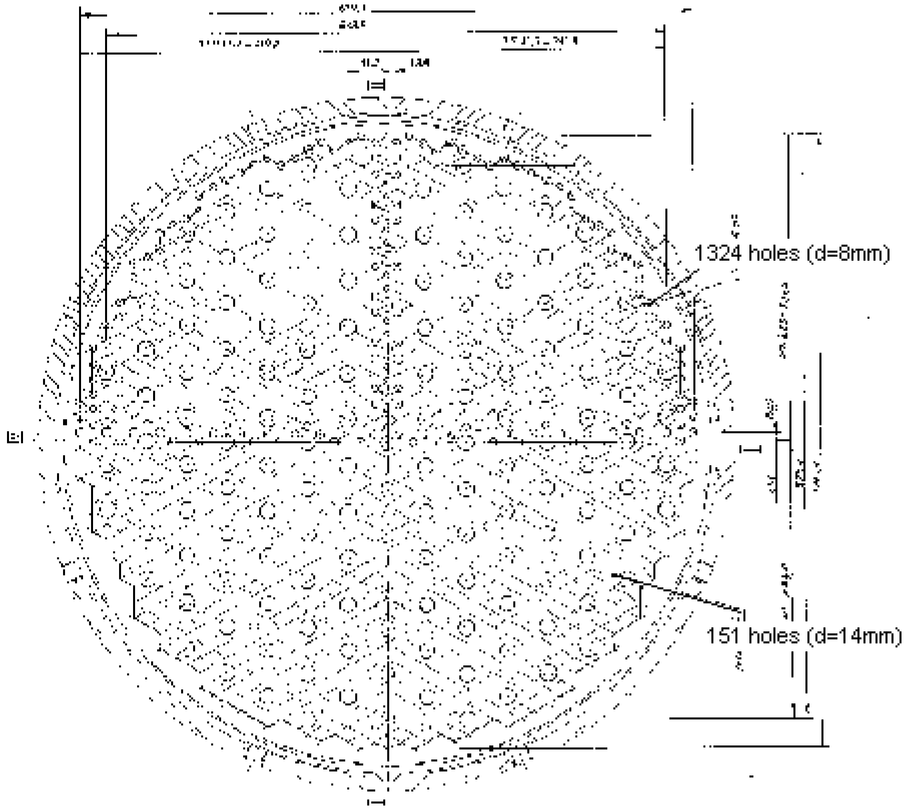

Fig. 4.2.5 Top view of the core barrel bottom

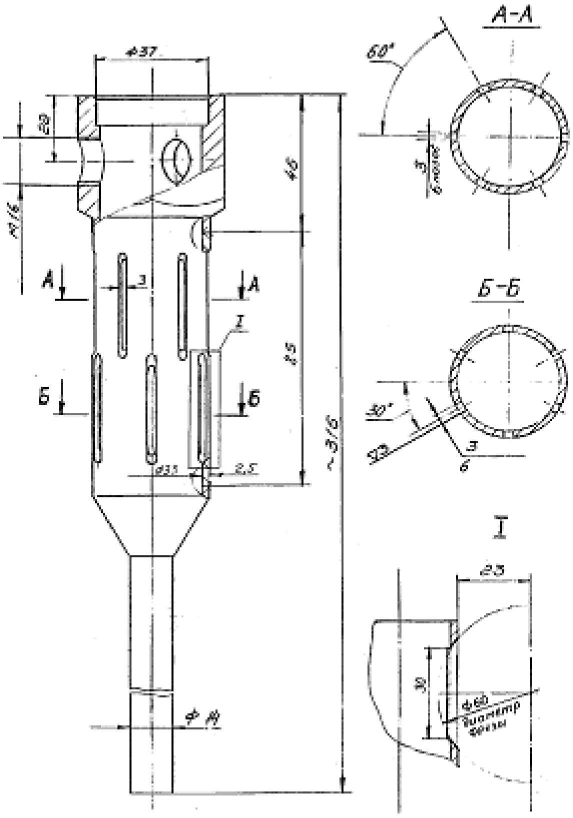

Fig. 4.2.6 Sketch of the supporting tube in the lower part of the reactor model

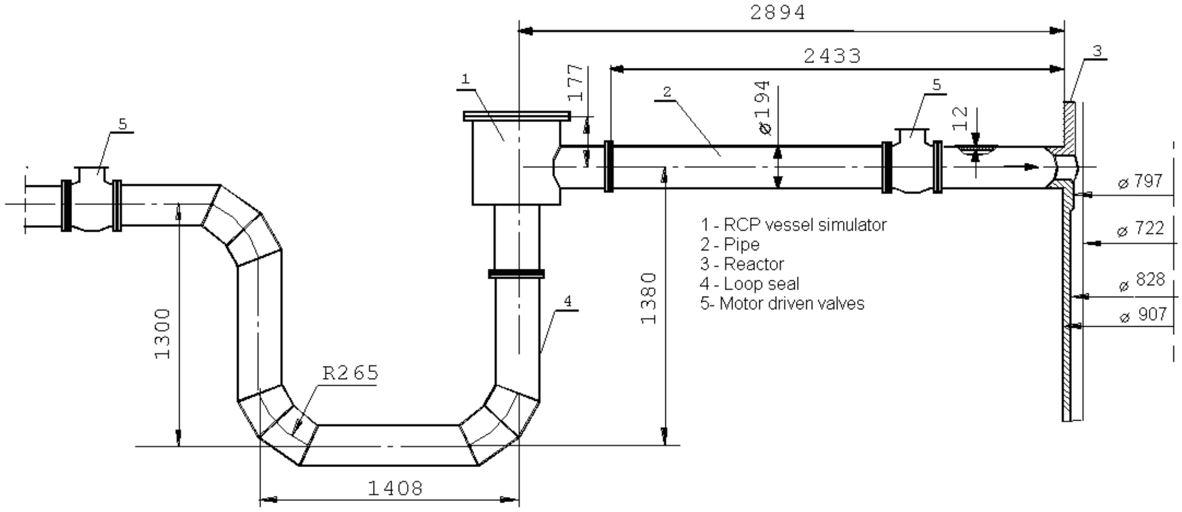

Fig. 4.2.7 Geometrical dimensions of loop seal and inlet pipe

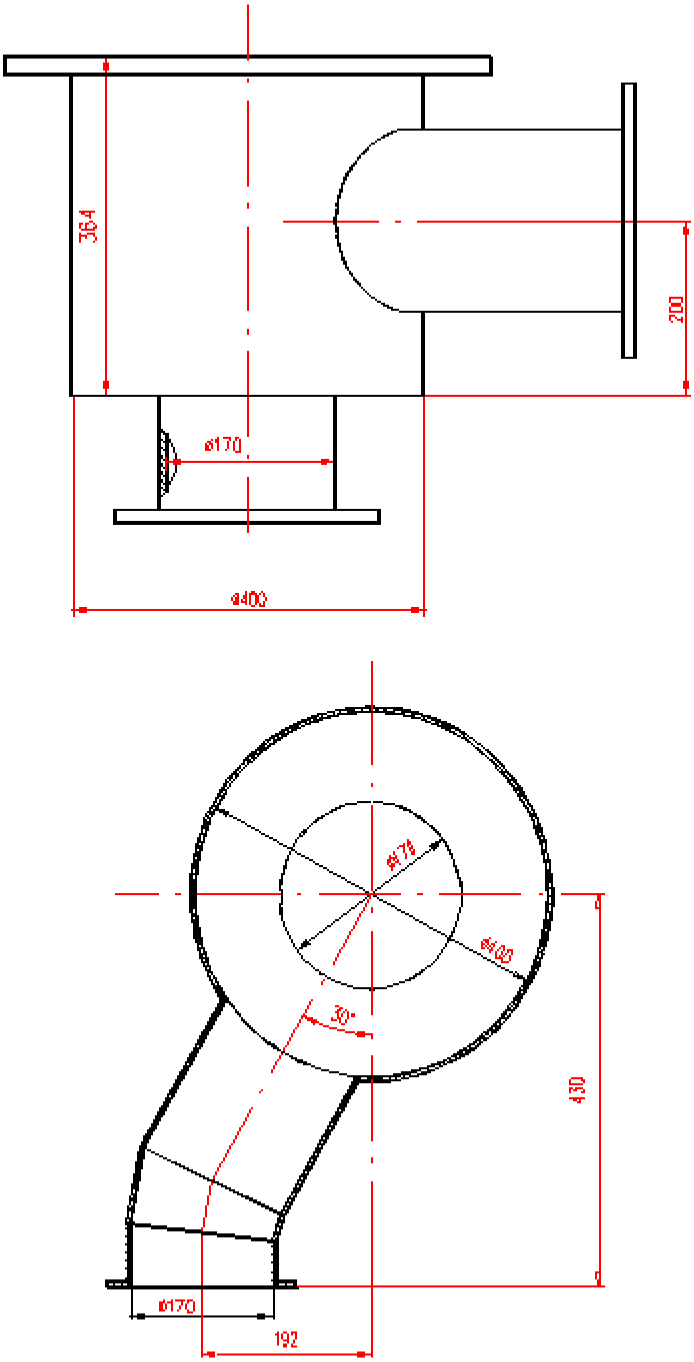

Fig. 4.2.8 Sketch of the MCP simulator

The boron concentration in the reactor model was modeled using the temperature method. The borated primary coolant was simulated by hot water at temperature of 65-75 °C, the condensate slug – by cold water at temperature of 20-30 °C. The circuit was heated up due to the heat released during operation of the circulation pump. About 100 thermocouples were placed into the lower downcomer part and at the core inlet to study mixing of flows. The thermocouples have small dimensions and small time constant (about 0.01 s). A cartogram of arrangement of thermocouples at the core inlet is given in Fig. 4.2.9. The exact coordinates of the positions of the thermocouples at the core inlet are presented in Tab. 4.1.

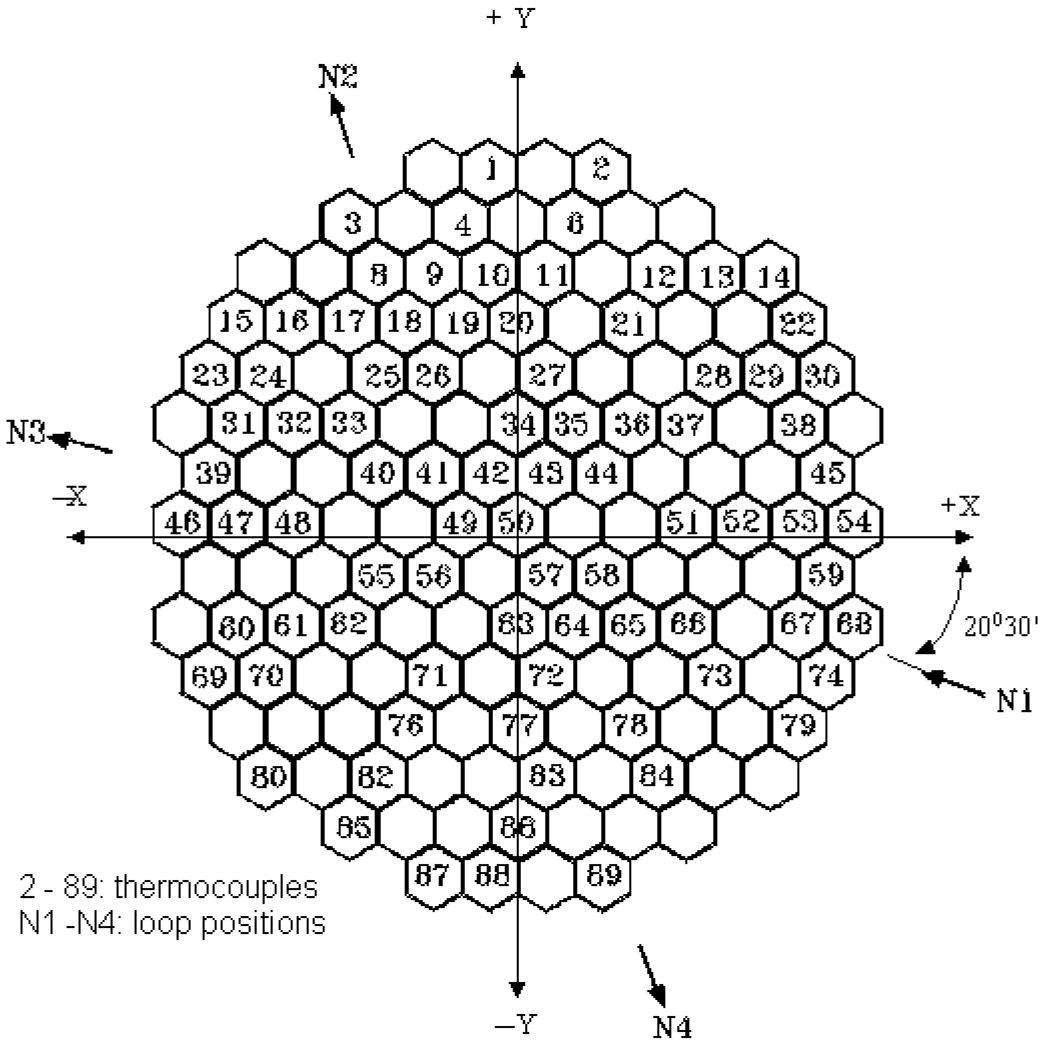

Fig. 4.2.9 Arrangement of thermocouples in the reactor model

Tab. 4.1 Coordinates of the thermocouples at the core inlet

Number of thermo-couple	**Coordinate on axis X, mm**	**Coordinate on axis Y, mm**	**Number of thermo-couple**	**Coordinate on axis X, mm**	**Coordinate on axis Y, mm**
1	-24.1	291.9	46	-289.2	0.0
2	72.3	291.9	47	-241.0	0.0
3	-144.6	250.2	48	-192.8	0.0
4	-48.2	250.2	49	-48.2	0.0
5	-	-	50	0.0	0.0
6	48.2	250.2	51	144.6	0.0
7	-	-	52	192.8	0.0
8	-120.5	208.5	53	241.0	0.0
9	-72.3	208.5	54	289.2	0.0
10	-24.1	208.5	55	-120.5	-41.7
11	24.1	208.5	56	-72.3	-41.7
12	120.5	208.5	57	24.1	-41.7
13	168.7	208.5	58	72.3	-41.7
14	216.9	208.5	59	265.1	-41.7
15	-241.0	166.8	60	-241.0	-83.4
16	-192.8	166.8	61	-192.8	-83.4
17	-144.6	166.8	62	-144.6	-83.4
18	-96.4	166.8	63	0.0	-83.4
19	-48.2	166.8	64	48.2	-83.4
20	0.0	166.8	65	96.4	-83.4
21	96.4	166.8	66	144.6	-83.4
22	241.0	166.8	67	241.0	-83.4
23	-265.1	125.1	68	289.2	-83.4
24	-216.9	125.1	69	-265.1	-125.1
25	-120.5	125.1	70	-216.9	-125.1
26	-72.3	125.1	71	-72.3	-125.1
27	24.1	125.1	72	24.1	-125.1
28	168.7	125.1	73	168.7	-125.1
29	216.9	125.1	74	265.1	-125.1
30	265.1	125.1	75	-	-
31	-241.0	83.4	76	-96.4	-166.8
32	-192.8	83.4	77	0.0	-166.8
33	-144.6	83.4	78	96.4	-166.8
34	0.0	83.4	79	241.0	-166.8
35	48.2	83.4	80	-216.9	-208.5
36	96.4	83.4	81	-	-
37	144.6	83.4	82	-120.5	-208.5
38	241.0	83.4	83	24.1	-208.5
39	-265.1	41.7	84	120.5	-208.5
40	-120.5	41.7	85	-144.6	-250.2
41	-72.3	41.7	86	0.0	-250.2
42	-24.1	41.7	87	-72.3	-291.9
43	24.1	41.7	88	-24.1	-291.9
44	72.3	41.7	89	72.3	-291.9
45	265.1	41.7			

Special experiments were carried out to evaluate the influence of unsteady heat exchange between the cold slug and heated parts of the reactor model for transferability of the mixing processes. During the experiments the following parameters were recorded:

- initial temperatures of the hot and cold water;
- water temperature in the lower downcomer part;
- water temperature at 80 positions at the core inlet;
- water flow rate at the model inlet and through the non-operating loops.

These parameters were recorded by the fast-acting data acquisition system based on the NATIONAL INSTRUMENTS equipment.

The test procedure was the following: The circulation circuit together with the reactor model was heated up to temperature 65-75°C. Upon reaching the required water temperature in the circuit the circulation pump was disconnected. The gate valves at the loop seal inlet and outlet were closed. The valve in the loop seal lower part (see Fig. 4.2.10) was opened connecting it with the cold water tank. Then the valves on the left and right branches of the loop seal (on the upper borders of the filled section) opened, and the hot water from the loop seal lower part started to be slowly displaced. Filling of the loop seal and drainage of water from it were performed before equalizing the temperatures of the cold water and loop seal walls. After filling the loop seal for 25 s the readings of all thermocouples at the core inlet and in the loop seal were recorded. The arrangement of thermocouples is shown in Fig. 4.2.9. On the basis of these records the average values of the hot water temperature for the reactor model and cold water in the loop seal, and also the root-mean-square deviation of the readings of the single thermocouples at the core inlet from the average value were determined. The water volume in model loop seal was equivalent to 8.5 m^3 in the full-scale reactor.

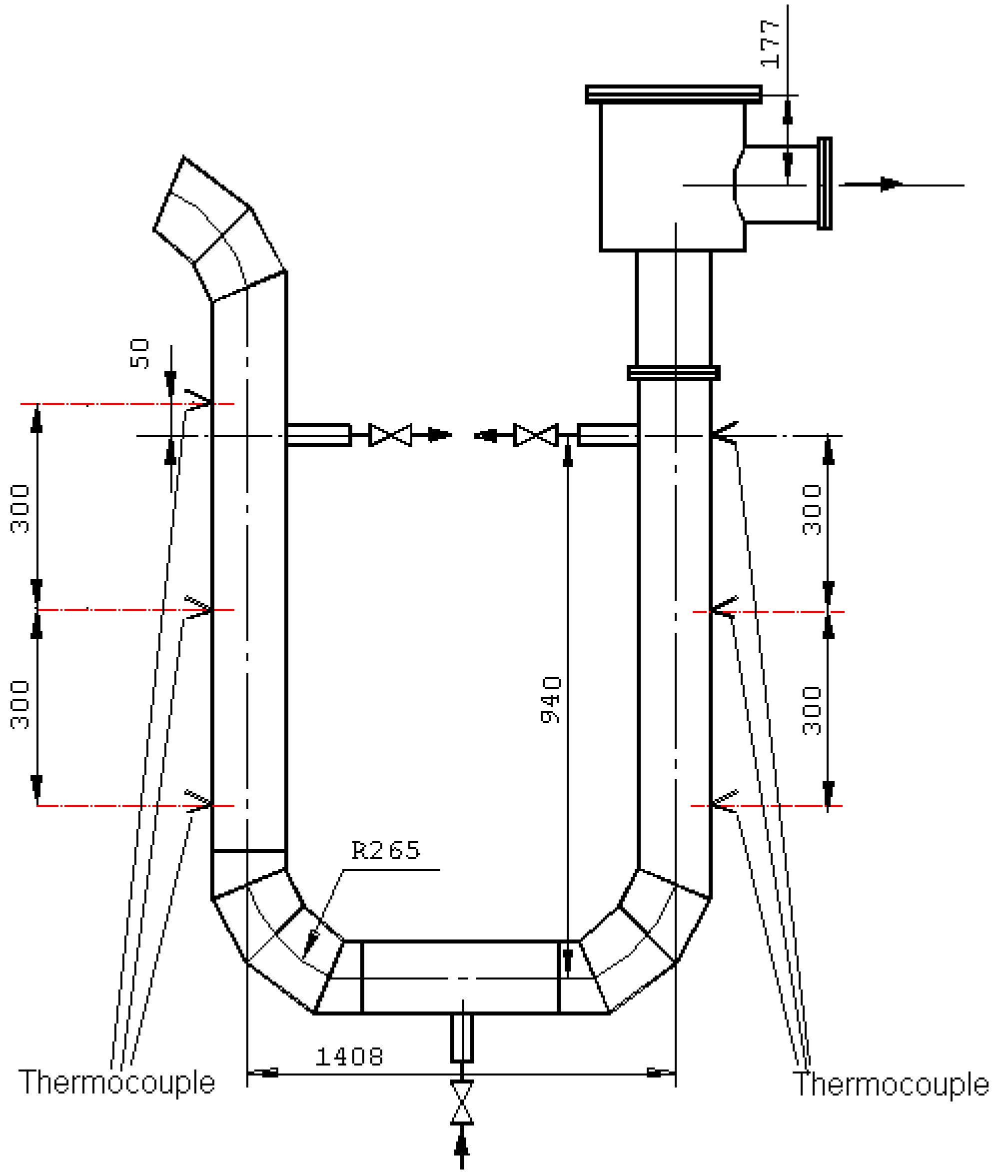

Fig. 4.2.10 Loop seal with positions of the thermocouples and the drain valves

The experiments were carried out in the following way:

- Opening the gate valve between the loop seal and reactor model completely
- switching-on of data acquisition system
- simultaneously start-up of the circulation pump and switch-on of the electric motor of the gate valve actuator at the loop seal inlet

The time of complete opening of motor-driven valve during all experiments was adjusted to 29.6 s.

4.3 Representation of the results

The change in the coolant flow rates through the model loop is given as the “flow rate – time” diagrams. The results of change in the temperature (boron concentration) at the core inlet in the thermocouple locations are presented as the "relative temperature - time" diagrams. The value of relative temperature was determined by the formula:

,
$$\Theta = \frac{t_i - t_c}{t_h - t_c} \cdot 100\% \qquad \text{(Equ. 4.3.1)}$$

where t$_i$ - water temperature at the core inlet, °C;

t$_c$ – cold water temperature in the loop seal, °C;

t$_h$ - hot water temperature in the reactor model, °C.

The relative temperature value characterizes a degree of coolant dilution. The value of $\theta = 100\ \%$ indicates that in the given point no decrease in boron concentration has occurred, $\theta = 0$ – denotes that in the given point the boron concentration is equal to zero, that is only pure condensate comes from the loop seal.

On the basis of the obtained values of the relative temperature for the entire points of measurements the average relative temperature value (boron concentration) at the core inlet for each time moment was calculated by the formula:

$$\theta_{av} = \frac{1}{84} \cdot \sum_{i=1}^{n=84} \theta_i \qquad \text{(Equ. 4.3.2)}$$

By the values of θ_{av} obtained in real time for each coolant flow rate through the loop the diagrams of change in the average boron concentration at the core inlet during the whole time of passage of the condensate slug from the loop seal through the reactor were plotted.

If the moment of ingress of the first portion of the condensate at the core inlet is assumed as a benchmark, then the time of ingress of the maximum condensate quantity (minimum average concentration) can be used to determine the relative time of passage of the diluted coolant through the core:

$$\eta = \frac{\tau}{\Delta\tau_0} \qquad \text{(Equ. 4.3.3)}$$

The dependences of relative average boron concentration on relative time allowed to analyze the process of mixing independent on the coolant flow rate value through the loop.

4.4 Results of the experiments

4.4.1 Methodical experiments

To justify correctness of application of temperature method and reveal the basic features of the experiments on study of mixing of flows with different boron concentration at first methodical experiments were carried out.

When using the temperature method it is possible an additional error owing to unsteady heat exchange between the cold water from the loop seal and the hotter structural components, and also due to the difference of density of the simulated coolant flows being increased as compared with the real object.

To check the influence of unsteady heat exchange on the mixing degree the experiments with the flow rates through the model loop of 180 and 650 m^3/h (without reversal flow through the idle loops) were carried out at the various temperature difference of the hot and cold water - 20, 30 and 40 ^oC.

The analysis of a set of these experiments showed:

- the values of the largest and least relative temperatures coincide for all experiments with similar flow rates through the loop and similar initial conditions. However, in the various experiments the boundaries of the ranges of the largest and least relative temperature values at the separate fuel assembly inlet were shifted and redistributed, especially round the core periphery;
- displacement of the boundaries of the areas with an equal degree of dilution is caused by the casual differences in the character of the coolant flow through the downcomer and through the core barrel bottom being of a complex three-dimensional nature and accompanied by the large-scale vortexes;

- influence of unsteady heat exchange, if any, is much less than that of casual differences in the character of coolant flow through the downcomer and core barrel bottom;
- maximum value of relative difference in densities between the cold and hot coolants amounts to 1.5 through 2.5 %; in view of the large velocities of the flow during the MCP start-up such difference in the densities does not influence upon the mixing process.

On the basis of methodical experiments the following conclusions were made:

- unsteady heat exchange and relative difference in coolant densities do not have a noticeable influence on the mixing character. Therefore when studying the mixing of flows with different boron concentration during the MCP start-up the temperature methods may be applied;
- under the same initial conditions in the various experiments the vortex flow with the various boundary configurations is formed at the core inlet. Because of this phenomenon the minimum number of the experiments was required to be determined during the further studies and when averaging the results of these experiments there occurs the most probable (statistically reliable) picture of passage of the condensate slug from the loop seal through the core.

With the purpose of determination of the minimum number of the experiments to obtain the statistically most probable picture of mixing process eight experiments with flow rate through the model loop of 630 m^3/h were carried out. The change in the average relative temperature (relative boron concentration) at the core inlet determined by (Equ. 4.3.2) depending on the number of the performed experiments was selected as a criterion. As the criterion of sufficiency the deviation of 1 % was assumed. It was found out that for reaching the desirable result it is necessary and enough to carry out a series from five experiments.

4.4.2 Experiments with the MCP start-up

To study the character of distribution of boron concentration at the core inlet during the MCP start-up three series of the experiments with the flow rates through the model loop of 175; 470 and 815 m^3/h without back flow through the non-operating loops were carried out. Each series of the experiments consisted of five or six experiments.

The averaged character of increase in the flow rate through the model loop for each series of the experiments is presented in Fig. 4.4.1. From the diagrams it is seen that the qualitative character of increase in the flow rate through the model loop for all three flow rates practically is similar, but the more flow rate, the more time is required for reaching the steady-state condition. The dependence of increase in the flow rates in the experiments as correlation is given in Tab. 4.2.

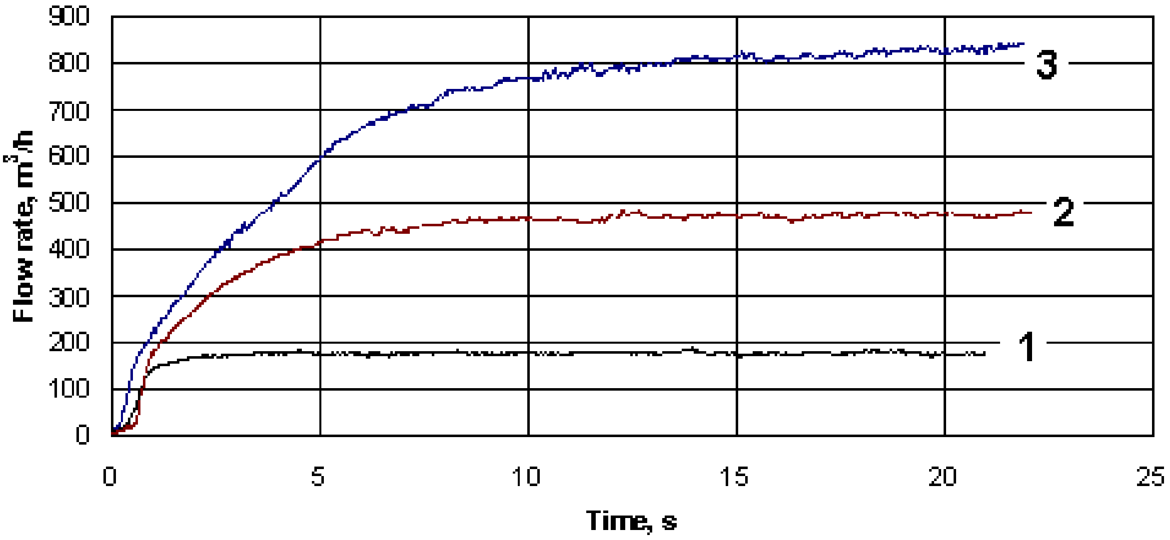

Fig. 4.4.1 Change in flow rate in the model loop

Tab. 4.2 Parameters of the experiments

N°	**Steady-state value of flow rate, m^3/h**	**Time of flow rate increase, s**	**Time dependence for flow rate increase**	**Status of idle loops**
1	175	2.0	$Q^2=(16.872+22312.4*\tau^2)/(1+0.7017*\tau^2)$	closed
2	470	8.0	$Q=(-7.175+265.69*\tau+4.753*\tau^2)/(1+0.4346*\tau+0.0132*\tau^2)$	closed
3	815	16.0	$Q=29.051+187.795*\tau-18.133*\tau^2+0.8144*\tau^3-0.01384*\tau^4$	closed

The primary experimental data as dependence of change in the relative temperature (concentration) on time are obtained in 84 positions at the core inlet. Fig. 4.4.2, Fig.

4.4.3 and Fig. 4.4.4 show as an example the character of change in the relative concentration in some positions along the core cross-section. Thus in each series of the experiments with similar flow rate three experiments wherein the largest spread in the indications of thermocouples was observed.

The change in the average boron concentration at the core inlet in real time for each series of the experiments is given in Fig. 4.4.5, and in relative time - in Fig. 4.4.6.

From consideration of diagrams in Fig. 4.4.6 it is seen that over the entire range of the studied flow rates for the same relative time of passage of the condensate slug the character of change in the average relative boron concentration at its inlet is the same.

From the joint consideration of the contour diagrams for all flow rate values under study it is to be seen that:

- the character of passage of the slug through the core over the studied range of flow rates practically does not depend on the flow rate value (Reynolds number);
- the first portions of the diluted coolant start coming into the peripheral fuel assemblies to the left of the working nozzle, gradually penetrating inside the core and covering simultaneously the most part of periphery. Thus the coolant becomes more and more deborated;
- the basic mass of deborated coolant passes through the core section located from the opposite side from the working nozzle, thus the minimum concentration value at the inlet of several fuel assemblies amounts to 55 % of the initial value;
- for the same relative time moment the configurations of the areas with the similar degree of boron dilution for all three flow rate values are close among themselves.

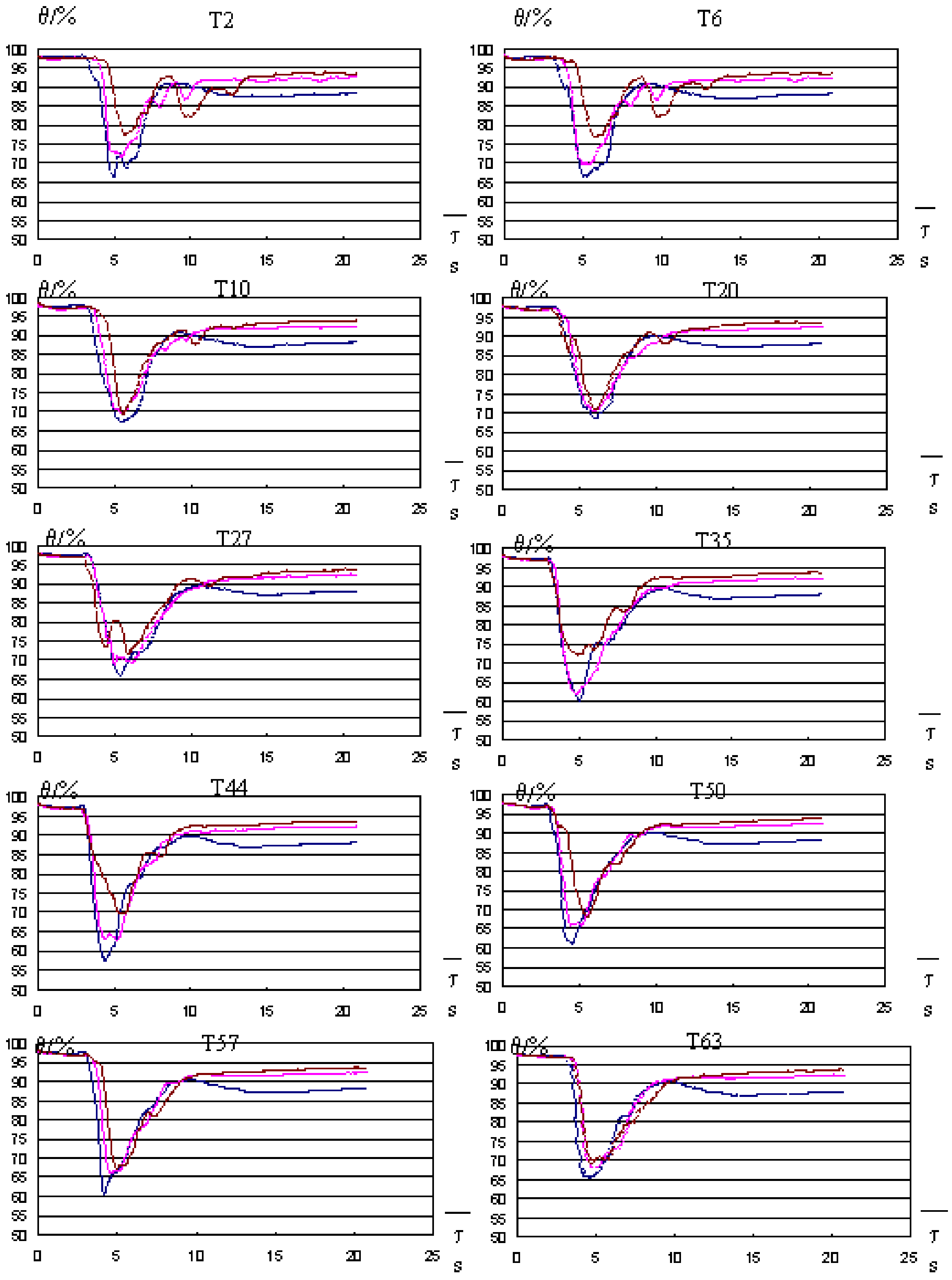

Fig. 4.4.2 Change in boron concentration at the fuel assembly inlet (Q = 175 m^3/h)

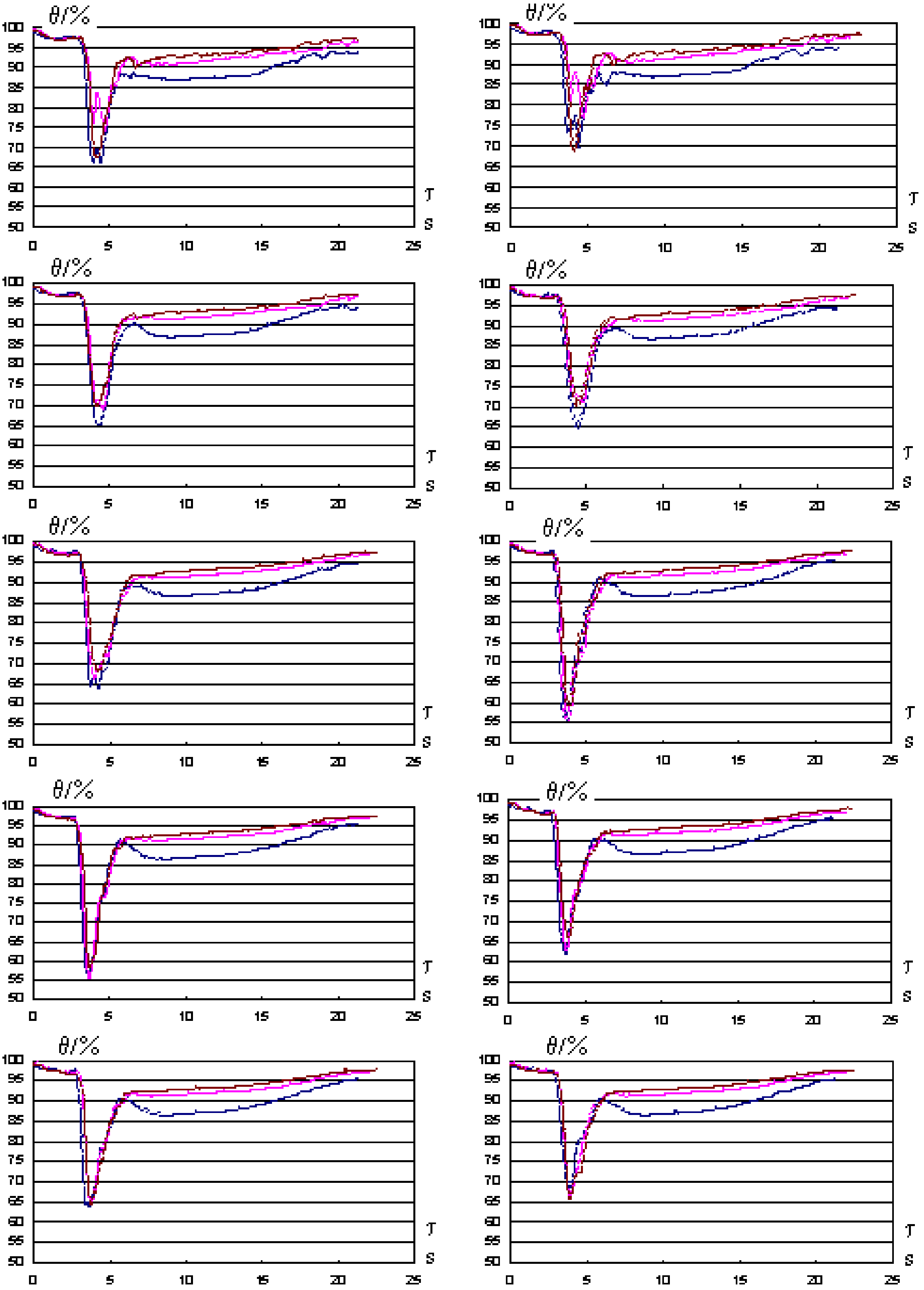

Fig. 4.4.3 Change in boron concentration at the fuel assembly inlet (Q = 470 m^3/h)

•

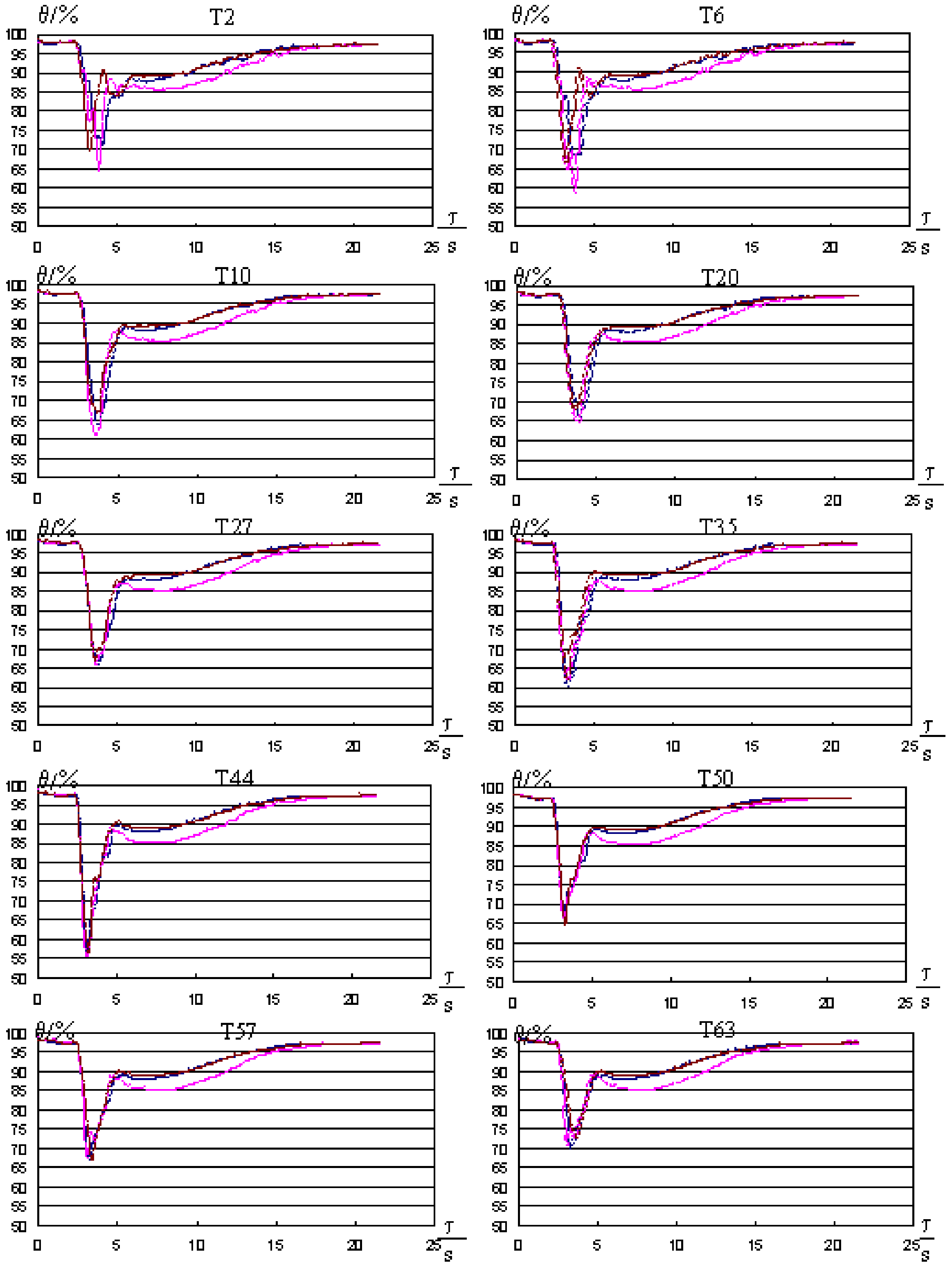

Fig. 4.4.4 Change in boron concentration at the fuel assembly inlet (Q = 815 m^3/h)

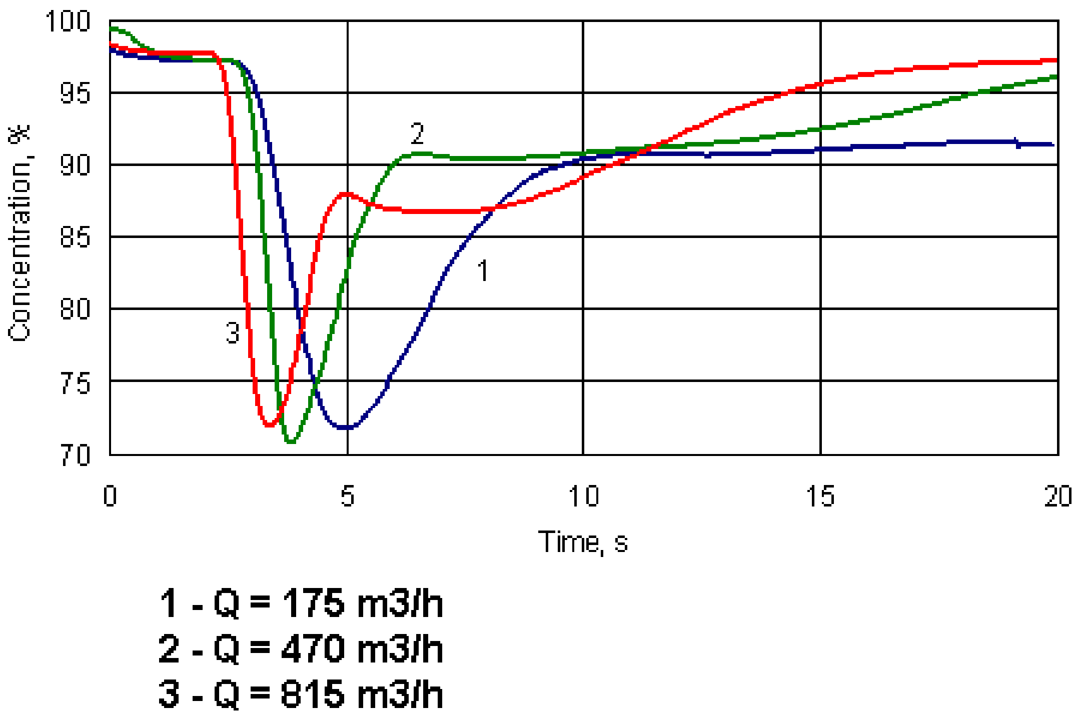

Fig. 4.4.5 Average boron concentration at the core inlet

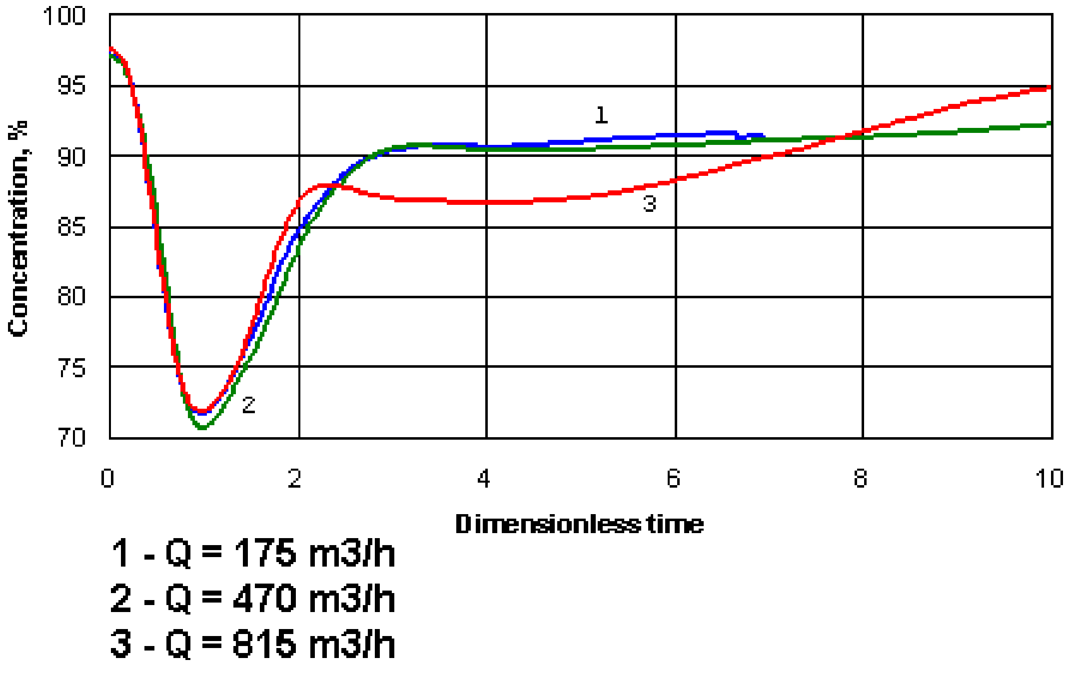

Fig. 4.4.6 Average boron concentration at the core inlet

The mixing of the condensate slug coming from the loop seal into the reactor during the MCP start-up with the primary coolant at the core inlet was investigated. The influence of the flow rate value through the circulation loop (Reynolds number) on the character and degree of mixing of flows with different boron concentration was studied.

The analysis of the experimental data showed the following picture of the dilution process in the experiments with the MCP start-up.

The first portions of the condensate slug (for relative time η = 0 - 0.2) come into the peripheral fuel assemblies to the left of the working nozzle approximately in the middle of the arch between loops 3 and 4, gradually going deep into the core and covering clockwise the more peripheral fuel assemblies (η = 0.4 – 0.7). In this case the minimum value of boron concentration in the peripheral fuel assemblies did not fall below 55 %.

With η = 0.9 – 1.1 through the reactor flowing part there passes the main mass of the condensate slug. Thus on the opposite side from the working nozzle the area with the minimum boron concentration is formed. Then the main mass of deborated water passes just through this area.

The character of change in the average boron concentration at the core inlet in the coordinates “relative concentration - relative time” over all range of flow rates through the model loop is the same. The configuration of the areas with the similar degree of boron dilution at the core inlet for the same moments of relative time is also the same. It gives the basis to consider that under the conditions with the MCP start-up there is no influence of the Reynolds number on the character of mixing of flows with the different boron concentration.

The minimum average boron concentration for all studied conditions with the MCP start-up always was more than 70 % of the initial boron concentration in the primary coolant.

4.5 Conclusions from the slug mixing experiments at the three test facilities

At three different test facilities (all in the scale of 1:5), experiments were carried out to investigate the mixing of deborated slugs with the ambient water in the downcomer. These three test facilities represent three different reactor types: the four-loop PWR KONVOI, the three-loop PWR from Westinghouse and the four-loop PWR VVER-1000.

Although the geometry of the test facilities is quite different, some general conclusions can be drawn, being valid for all three facilities.

- A significant mixing of the deborated slug with the ambient coolant on the through the downcomer and the lower plenum takes place.
- The maximum deboration for nearly identical initial slug sizes is quite similar (see Tab. 4.3).
- The first deborated coolant is registered at the side opposite to the position of the loop with the starting-up pump.
- The deborated slug divides into two parts in the downcomer. At the core inlet, two nearly symmetrical areas with deborated coolant are observed. (see Fig. 4.5.1 for ROCOM and VATENFALL).
- A scaling of the Reynolds-Number at constant Strouhal-Number gives for all test facilities similar results.
- The fluctuations due to the turbulent flow field in the downcomer were observed in both facilities, where velocity measurements were carried out.
- These fluctuations of the velocity start with a certain delay after the start of the pump.
- A comprehensive analysis of the measurement error and the turbulent fluctuations was carried out for the Vattenfall and the ROCOM-experiments. For both experimental series it was confirmed, that the contribution of the turbulent fluctuations is significantly higher than the error of the measurement devices.

Tab. 4.3 Overview on measured maximum deboration values at the different test facilities

N°	Facility	Slug size [m^3]*	Maximum deboration [%]
1	ROCOM	8.0	48.5
2	Vattenfall	8.0	45.7
3	Gidropress	8.5	45.0

* related to the original reactor

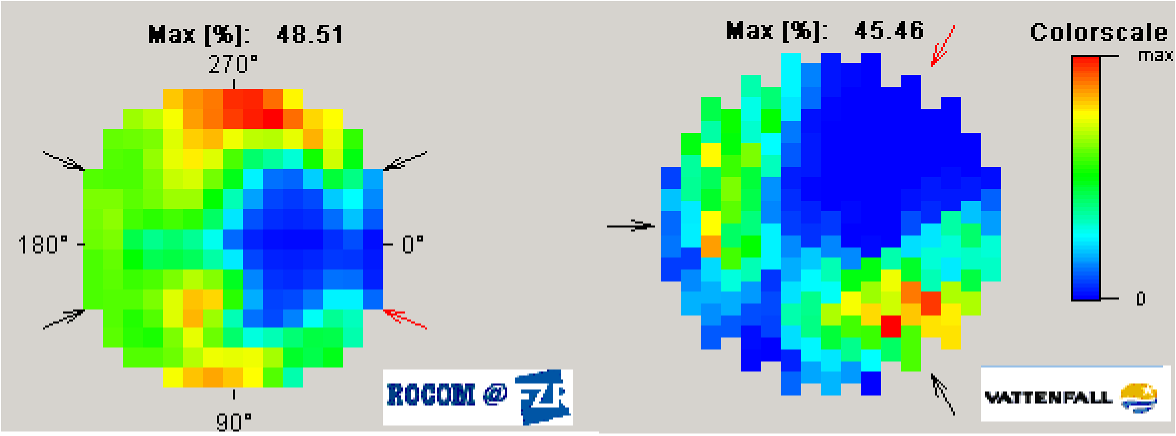

Fig. 4.5.1 Distribution of the deboration (mixing scalar) at the time point of maximum in the ROCOM_12 and the VATT_04 tests

5 Buoyancy driven mixing experiments at the ROCOM test facility

For the investigation of the influence of density effects, generic experiments have been carried out at the ROCOM test facility. It is expected, that density differences can be neglected, if the flow rates are sufficiently high, that means, if mixing is momentum controlled. To find the conditions for transition between momentum controlled and buoyancy driven mixing, generic experiments with variation of density differences between the mixing fluids were performed. To simulate the mixing of colder ECC water, an accurately modeled ECC injection nozzle has been connected to one of the cold legs of ROCOM.

5.1 Boundary conditions

Due to the fact, that the test facility cannot be heated up, the necessary density differences were simulated by adding sugar (glucose) to the water that is injected into the cold leg. To observe the mixing of the ECC water, this water was tracered by small amounts of sodium chloride, as in previous experiments. Generating density differences by high salt concentrations is not possible, because the measurement system is very sensitive and would be saturated at high salt concentrations.

The goal of the experiments was the generic investigation of the influence of density differences between the primary loop inventory and the ECC water on the mixing in the downcomer. To separate the density effects from the influence of other parameters, a constant flow in the loop with the ECC injection nozzle was assumed in this study. The mass flow rate was varied in the different experiments between 0 and 15 % of the nominal flow rate, i.e. it was kept in the magnitude of natural circulation. The other pumps were switched off. The density difference between ECC and loop water has been varied between 0 and 10 %. Fig. 5.1.1 summarizes the boundary conditions of the experiments. Altogether 21 experiments have been carried out (dots in Fig. 5.1.1). In all experiments, the volume flow rate of the ECC injection system was kept constant at 1.0 l/s. The normalized density is defined as the ratio between ECC water density and density of fluid in the circuit. All other boundary conditions are identical. Due to the fluctuations of the flow field in the RPV observed earlier, each experiment was repeated several times to average over these fluctuations.

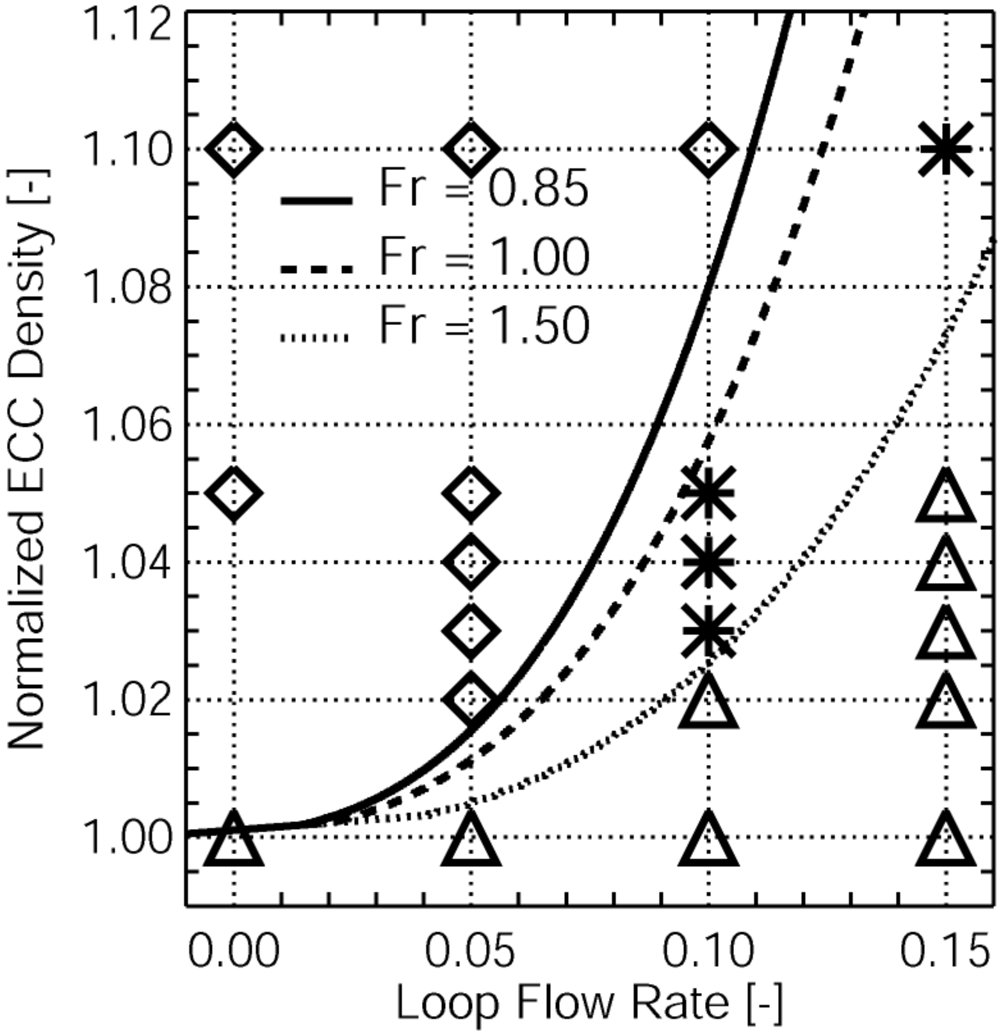

Fig. 5.1.1 Matrix of the experiments carried out and Froude-number isolines acc. to eq. (5.1.1)

5.2 Experimental results and interpretation

5.2.1 Reference experiment

The experiments without density effects serve as reference experiments for the comparison. Fig. 5.2.1 (left) visualises in an unwrapped view the time evolution of the tracer concentration measured at the two downcomer sensors. The downwards directed arrow indicates the position of the loop with the running pump, in that case delivering 10 % of the nominal flow rate. At the upper downcomer sensor, the ECC water (injected in each experiment from t = 5 to t = 15 s) appears directly below the inlet nozzle. Due to the momentum created by the pump, the flow entering the downcomer is divided into two streams flowing right and left in a downwards directed helix around the core barrel. At the opposite side of the downcomer, the two streaks of the flow fuse together and move down through the measuring plane of the lower downcomer sensor into the lower plenum. Almost the whole quantity of ECC water passes the measuring plane of the lower downcomer sensor at the side opposite to the azimuthal position of the affected loop.

Such a velocity field is typical for single-loop operation. It has its maximum at the opposite side of the downcomer and a minimum at the azimuthal position of the running loop, which has been found in velocity measurements by means of a laser-Doppler anemometer at the ROCOM test facility, too.

The maximum tracer concentration of the ECC water in the downcomer is 20 % of the injected water concentration at the upper sensor and 8 % at the lower sensor.

5.2.2 Experiment with 10 % density difference

Fig. 5.2.1 (right) shows the experiment, carried out at the same flow conditions, but the density difference between the injected ECC water and the primary loop coolant is now 10 %. In that case a streak formation of the water with higher density is observed. At the upper sensor, the ECC water covers a much smaller azimuthal sector. The density difference partly suppresses the propagation of the ECC water in horizontal direction. The ECC water falls down in an almost straight streamline and reaches the lower downcomer sensor directly below the affected inlet nozzle. Only later, coolant containing ECC water appears at the opposite side of the downcomer. The maximum concentration values observed at the two downcomer sensors are in the same region as in the case without density differences, i.e. 20.0 % and 9.5 % from the initial concentration in the ECC water tank. The visualizations of the behaviour of the ECC water in the downcomer reveals that in case of momentum driven flow, the ECC water covers nearly the whole perimeter of the upper sensor and passes the measuring plane of the lower sensor mainly at the opposite side of the downcomer. When the density effects are dominating, the sector at the upper measuring device covered by the ECC water is very small. The ECC water falls down straightly and passes the sensor in the lower part of the downcomer below the inlet nozzle of the working loop. Furthermore, variations of the density were carried out to identify the transition region between momentum driven and density driven flow.

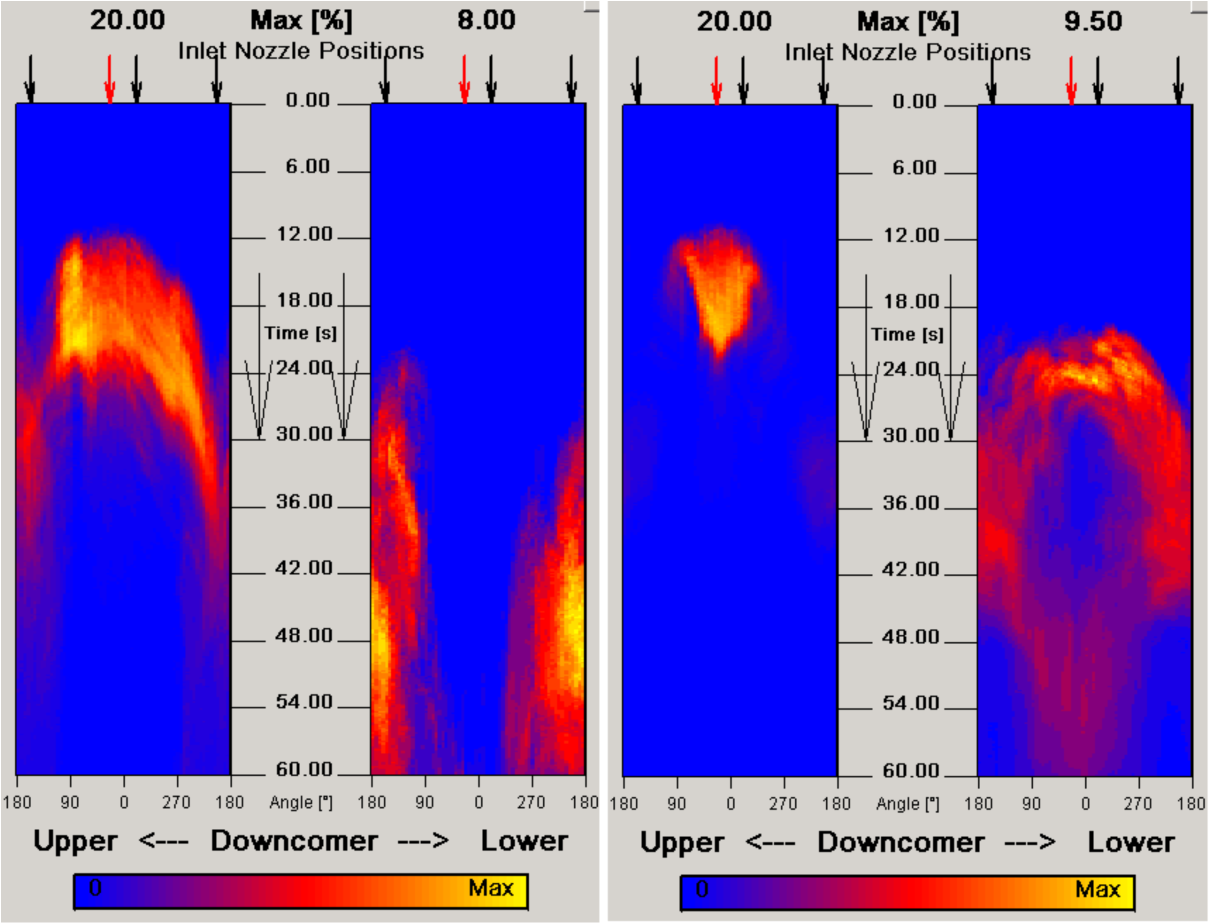

Fig. 5.2.1 Time evolution of the mixing scalar in the experiment with 10 % flow rate and 0 % density difference (left) and 10 % flow rate and 10 % density difference (right)

5.2.3 Experiment with 4 % density difference

Fig. 5.2.2 shows in the left part an experiment with a density difference of 4 %, while the flow rate was again 10 % of the nominal. At the upper sensor, the width of the azimuthal sector covered by the ECC water is in-between the two cases with 0 % respectively 10 % density difference. Near the lower sensor, the ECC water reaches the opposite side of the downcomer and the region below the inlet nozzle position almost at the same time. That means, that one part of the ECC water follows the stream lines of the external momentum driven flow field and another part directly falls down due to the internal momentum created by density differences. We consider this as an intermediate state between momentum and density driven flow. The experiment shown in the left part of Fig. 5.2.2 was therefore assigned to the transition region between the two flow regimes.

Based on these observations, the set of experiments conducted according to the matrix in Fig. 5.1.1, was divided into three groups: buoyancy dominated flow (◊), momentum dominated flow (Δ) and the transition region (*). The conditions at the inlet into the downcomer were used to calculate Froude-numbers of the experiments according to the following formula:

$$Fr = \frac{v_{in}}{\sqrt{g \cdot s \cdot \frac{rho_{in} - rho_{a}}{rho_{in}}}} \qquad \text{(Equ. 5.2.1),}$$

where v_{in} is the velocity at the reactor inlet (combined loop and ECC flow), g is the gravitational acceleration, s is the height of the downcomer, rho_{in} the density of the flow entering the downcomer, calculated with the assumption of homogeneous mixing between ECC and loop flow, and rho_{a} the density of the ambient water in the downcomer. Lines of constant Froude-numbers calculated by means of this formula are shown in Fig. 5.1.1. All experiments, identified as density dominated are located in the region left of the isoline Fr = 0.85 and all momentum dominated points are found right of the isoline Fr = 1.5. These two numbers are critical Froude numbers separating the two flow regimes for the ROCOM test facility. Therefore, the critical Froude number for transition between momentum controlled and buoyancy driven mixing is about 1.0.

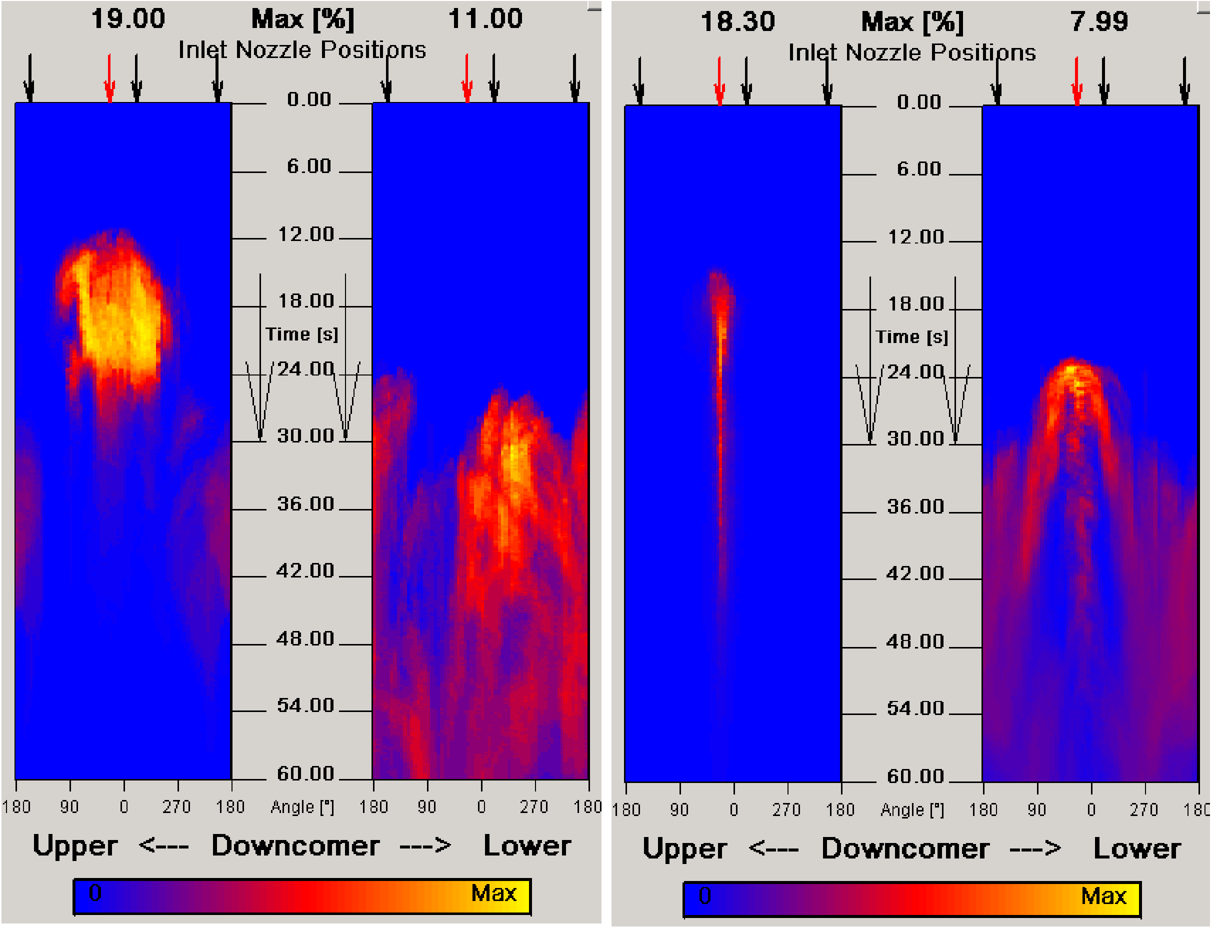

Fig. 5.2.2 Time evolution of the mixing scalar in the experiment with 10 % flow rate and 4 % density difference (left) and 5 % flow rate and 10 % density difference (right)

5.2.4 Experiment for code validation

Beside the code validation on basis of density driven experiments, conclusions on the flow regime in different test facilities with identical boundary conditions should be drawn. From the two available sets of density driven experiments (at the ROCOM and at the Fortum PTS test facility (see chapter 6)) experiments for post-test calculations were selected, belonging to the same Froude number region. Therefore, from the available ROCOM-experiments, the experiment with 10 % density difference and 5 % volume flow rate was chosen for code validation. The time evolution of the mixing scalar at the two downcomer sensors is shown on Fig. 5.2.2 (right).

6 Buoyancy driven mixing experiments at the FORTUM PTS test facility

In 1983 a test facility was constructed by Fortum (former IVO) to study thermal mixing phenomena of cold high-pressure injection (HPI) water with hot primary coolant in the Loviisa VVER-440 reactor. A series of experiments was performed and conclusions made about the mixing in the downcomer and the cold leg. [Tuo87]

Selected tests were now used in Flomix-R project for validation and testing of CFD methods for simulation of buoyancy driven flow and mixing. For corresponding use in the future the original experimental facility and measurement methods with summary of basic experimental results are presented in this chapter. More detailed geometry data with detailed boundary conditions and the results of selected experiments are in separate data files and will be available for use as defined by Flomix-R project partners. The description of CFD model and the results of CFD simulations of these experiments made in Flomix-R project are presented in report [Top04] in appendices of the final report of Flomix-R work package 4 [Flo04].

6.1 Facility description

The test facility is a scaled down model of the Loviisa VVER-440 reactor. The length scale of facility is 1:2.56. A half of the circumference of the real geometry is modeled including parts of the three cold legs (total of six in the real plant) and 180 degree part of the downcomer and the lower plenum. The material used for facility is transparent acrylic plastic allowing flow visualization but limiting the maximum temperature of water.

The main components of the test facility are three cold legs where the middle one has the HPI injection nozzle in the bottom of the pipe, downcomer, lower plenum, drain tank and pipes and ponds needed for maintaining the water flow through the test facility. A photo and a schematic view of the test facility are presented in Fig. 6.1.1.

The cold leg loop seals do not influence to the mixing and are not modeled. The lower plenum with a perforated bottom plate is included to the facility geometry.

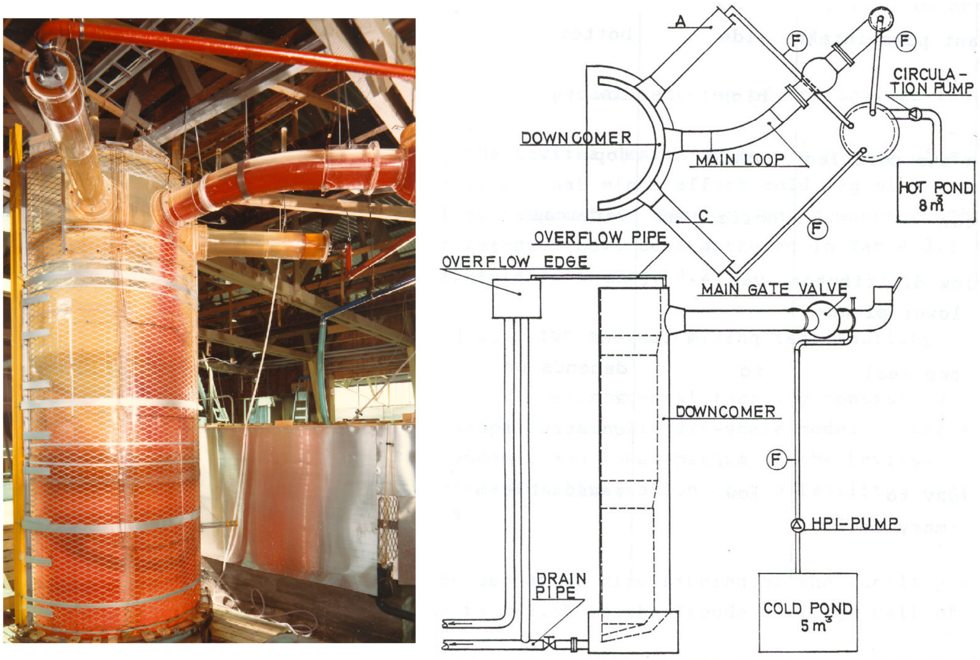

Fig. 6.1.1 Test facility [Tuo87].

6.2 Measurements

The density difference between injection and main flow was induced with temperature difference and salt ($CaCl_2$) addition. The main flow temperature and the initial temperature was about 75 ˚C and the minimum injection temperature was about 10 ˚C. The degree of mixing was measured using temperature measurements with 62 thermocouples located in the downcomer and the injection cold leg as presented in Fig. 6.2.1.

The thermocouples were read once in two seconds and the duration of one test was about 10 minutes.

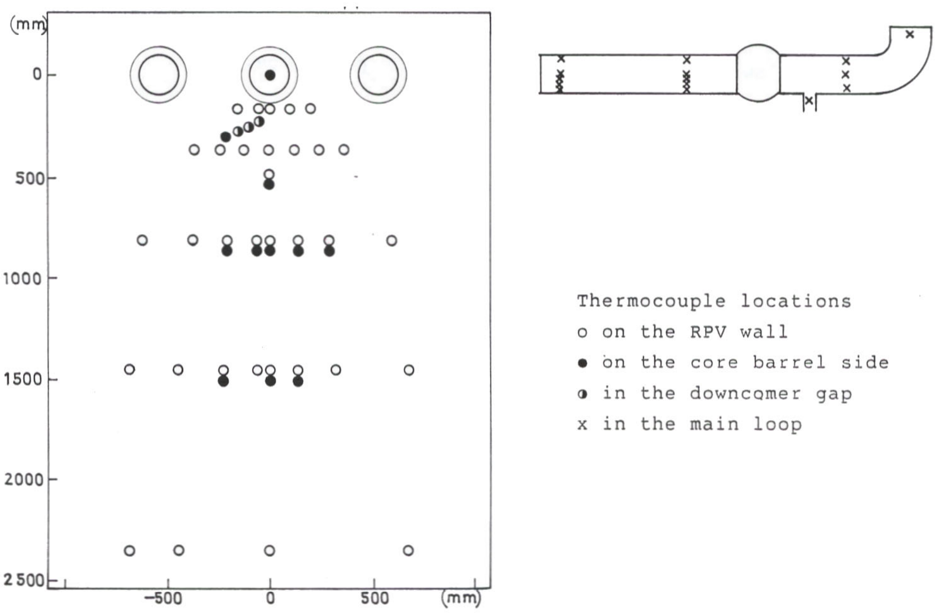

Fig. 6.2.1 Thermocouple locations [Tuo87].

6.3 Test program

6.3.1 Total experimental program

The experimental program consist about 50 tests. The test parameters, flow rates and density difference ratio, were varied as following:

Injection flow rate Q_{HPI}:	0.10 - 4.0 l/s,
side loop flows Q_{LoopA} and Q_{LoopC}:	0 - 2.0 l/s,
main loop flow Q_{LoopB}:	0 - 1.87 l/s and
density difference ratio $\Delta\rho/\rho$:	0.022 - 0.16,

where the density difference ratio between injection and main loop flow was defined as

$$\frac{\rho_{HPI}-\rho_{LoopB}}{\rho_{HPI}} = \frac{\Delta\rho}{\rho}\ . \tag{Equ. 6.3.1}$$

The tests can be divided to three subgroups:

1. All loop flows are stagnant and there is injection to the main loop.
2. The main loop flow is stagnant, side loops have hot water flow and there is injection to the main loop.
3. There is main loop and side loop flows and injection to the main loop.

The modified Froude number defined as

$$Fr_{LoopB,HPI} = \frac{Q_{HPI} / A_{LoopB}}{\left(gD_{LoopB}\Delta\rho / \rho\right)^{1/2}} \qquad \text{(Equ. 6.3.2)}$$

is about 0.006 - 0.65 for HPI flow rate in the main cold leg. This can be compared to typical maximum Froude number in small break LOCA simulations of Loviisa VVER-440 power plant of about 0.15.

6.3.2 Flomix-R test cases used for CFD validation

Three test cases we used for CFD code testing in Flomix-R project. The selected cases represent all three subgroups presented above and have modified Froude number of about 0.15.

The parameters of these test cases are presented in Tab. 6.1.

Tab. 6.1 Test matrix of CFD validation tests.

Test #	Q_{HPI} **l/s**	Q_{LoopA} **l/s**	Q_{LoopB} **l/s**	Q_{LoopC} **l/s**	$Fr_{LoopB,HPI}$	$\Delta\rho/\rho$
10	2.31	0	0	0	0.147	0.16
20	2.31	1.87	0	1.87	0.146	0.16
21	2.31	1.87	1.87	1.87	0.147	0.16

6.4 Results of experiments

Test results and conclusion presented here are based on more comprehensive presentation of reference [Tuo87]. The main areas of interest here are the stratification in the cold leg having the HPI injection and the plume mixing and stratification in the downcomer.

6.4.1 Stratification in the main loop

Mixing at the injection point depends on the injection Froude number and on the injector geometry. The bottom injection prevents any mixing in the injection pipe and a relatively small diameter of the nozzle gives high Froude numbers which leads to mixing behaviour as presented in Fig. 6.4.1a. With a low injection Froude number the mixing behaviour is more like presented in Fig. 6.4.1b.

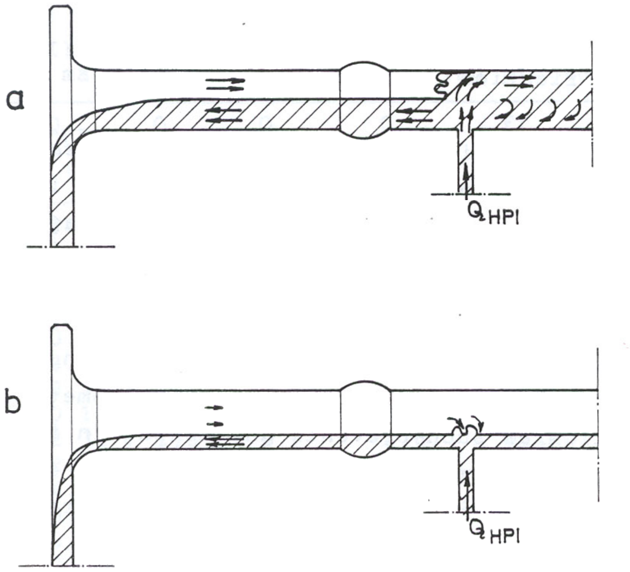

Fig. 6.4.1 Bottom injection with high (a) and low (b) injection Froude number [Tuo87]

If the counter-flowing hot stream from the downcomer is Q_h and the injection flow rate is Q_{HPI} the backflow ratio $Q^* = Q_h/Q_{HPI}$ can be defined and calculate in the experiments using temperature data from thermocouple at the botton of the main cold leg. In Fig. 6.4.2 the backflow ratio of tests is drawn as a function of $\mathrm{Fr}_{\mathrm{LoopB,HPI}}$.

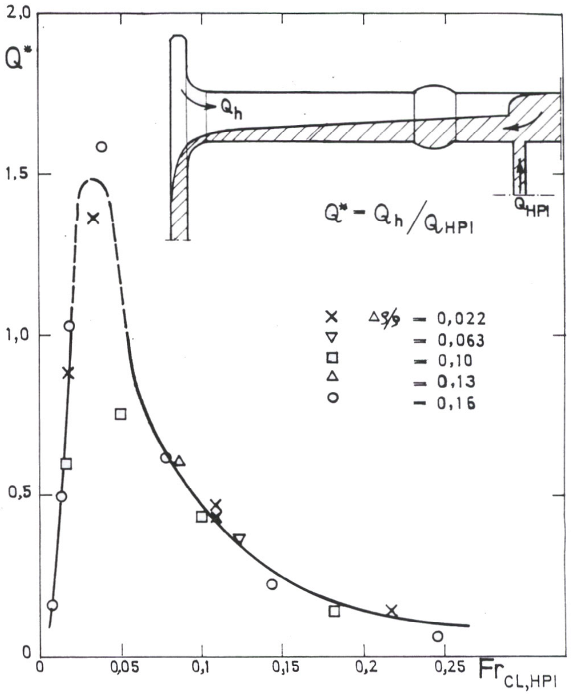

Fig. 6.4.2 Backflow ratio Q^* in the main loop as a function of $\mathrm{Fr}_{\mathrm{LoopB,HPI}}$ [Tuo87].

With small Fr numbers ($\mathrm{Fr}_{\mathrm{LoopB,HPI}} < 0.03$) there is not enough initial turbulence and no vertical plume mixing for bottom injection. With decreasing injection rate the Q^* approached zero and stratification is perfect. With $\mathrm{Fr}_{\mathrm{LoopB,HPI}} \approx 0.04$ and larger jet mixing becomes very effective.

6.4.2 Plume behaviour in the downcomer

The cold stream stratified in the cold leg enters to the downcomer and accelerated downwards due to the buoyancy forces. In the semi-annular downcomer the plume always turns to side if there is no flow from the side loops. In most tests the plume turned to right but also in some cases to the left. This turning effect is induced by the recirculation flows to the mixing regions in the main loop and the semi-annular downcomer geometry. With fully annular geometry as in real plant that do not happen.

With a side loops flows the plume is balanced in the middle of the downcomer. The plume behaviour is shown in Fig. 6.4.3

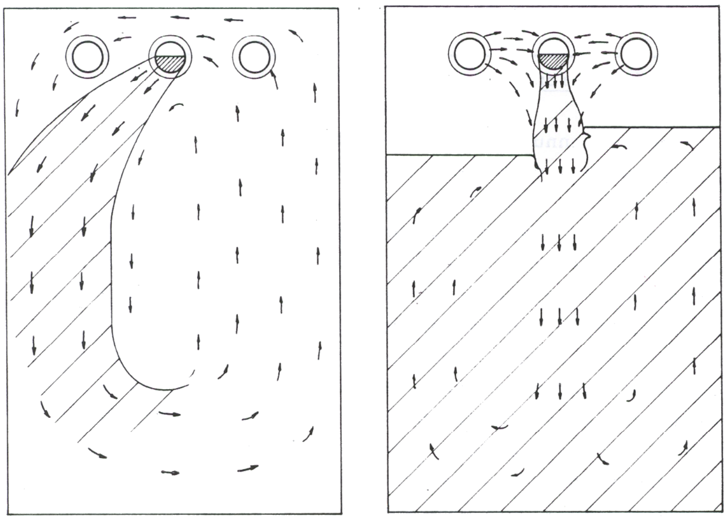

Fig. 6.4.3 Plume in the downcomer with all loop flows stagnated (left) and with side loop flows (right) [Tuo87].

There is a clear stratification in the downcomer when the side loops are on. Side loop flows feed the mixing process in the main loop and in the downcomer. The mixing of the plume occurs with a mixture that stratifies in the downcomer. There is no other flow through the clear separation level of the hot and mixture layer. The stratification height depends on flow rates and it can be different in different sides of the plume.

6.5 Qualitative comparison between the ROCOM and the Fortum PTS buoyancy mixing tests

In spite of the fact, that the ROCOM and the Fortum PTS test facilities differ in geometry, scaling, boundary conditions of the injection and parameter range of the density differences, the basic loop mass flow rate and the HPI mass flow, a qualitative comparison of the mixing patterns was performed. Tab. 6.2 shows a compilation of experiments suitable for comparison. No side loops flow should be present in these experiments. Detailed results are given in this report only for experiment #10 from Tab. 6.1. However, looking at Fig. 6.4.3 it can be seen, that due to the specifics of the Fortum PTS model (sector model of the downcomer), an internal circulation is initiated, when there is no side loops flow.

Tab. 6.2 List of selected experiments at the Fortum PTS facility suitable for comparison with ROCOM tests

N°	**Q_{CL}(l/s)**	**Q_{HPI} (l/s)**	ρ_{HPI}/ρ
3	1.87	2.31	1.0200
8	1.87	2.00	1.1600
9	0	2.02	1.1600
10	0	2.31	1.1600
12	0	0.62	1.1600
14	0.62	0.62	1.1600
16	0	0.31	1.1600
44	0	4.00	1.1000
45	0	4.00	1.1600
47	0	4.00	1.0200
50	1.87	1.87	1.0200
51	0	2.31	1.0200
52	1.87	0.62	1.0200

Due to this circulation, the downwards directed stream of injected HPI water is perturbed in an asymmetric way. The jet is stabilized in symmetric position, when side loop flow exists. This was observed also in corresponding ROCOM experiments (without side loop flow). Therefore, for qualitative comparison, Fortum PTS experiments with symmetric side loop flow can also be considered. This is e.g. experiment #21 from Tab. 6.1.

The results of ROCOM and Fortum PTS tests were both assessed based on Froude scaling, while different definitions of the Froude number were used. While the Froude number according to Equ. 5.2.1 is related to the downcomer mixing, Froude number definition in Equ. 6.3.1 corresponds to the cold leg mixing. The experimental results could be compared with respect to both effects. The cold leg Froude number describes the mixing with respect to stratification in cold leg and back flow ratio. However, these phenomena have not been investigated systematically in the ROCOM tests. To have a basis for comparison, a classification of experiments from both facilities based on unified definition of the Froude number according to Equ. 5.2.1 (downcomer Froude number) was considered. The Fig. 6.5.1 shows the results of this classification. However, in Fig. 6.5.1 the normalised density is not the density ratio occurring in Equ. 5.2.1, but for better clearness, the ration between ECC water and ambient water densities is used.

As it can be seen from Fig. 6.5.1, all Fortum experiments are located in the Froude map in the region of low Froude numbers, while the ROCOM test comprise momentum controlled mixing and the transition region as well.

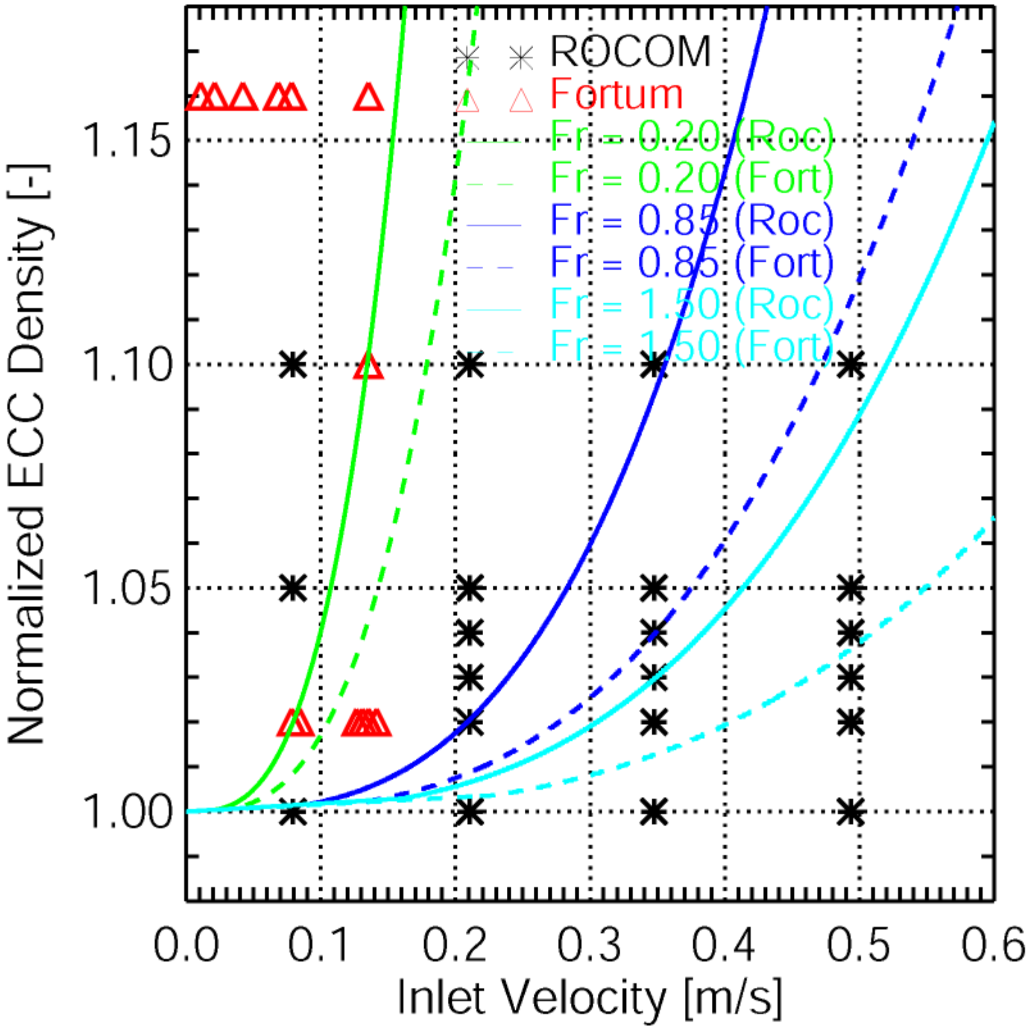

Fig. 6.5.1 Classification of ROCOM and Fortum PTS buoyancy mixing tests with respect to downcomer Froude number

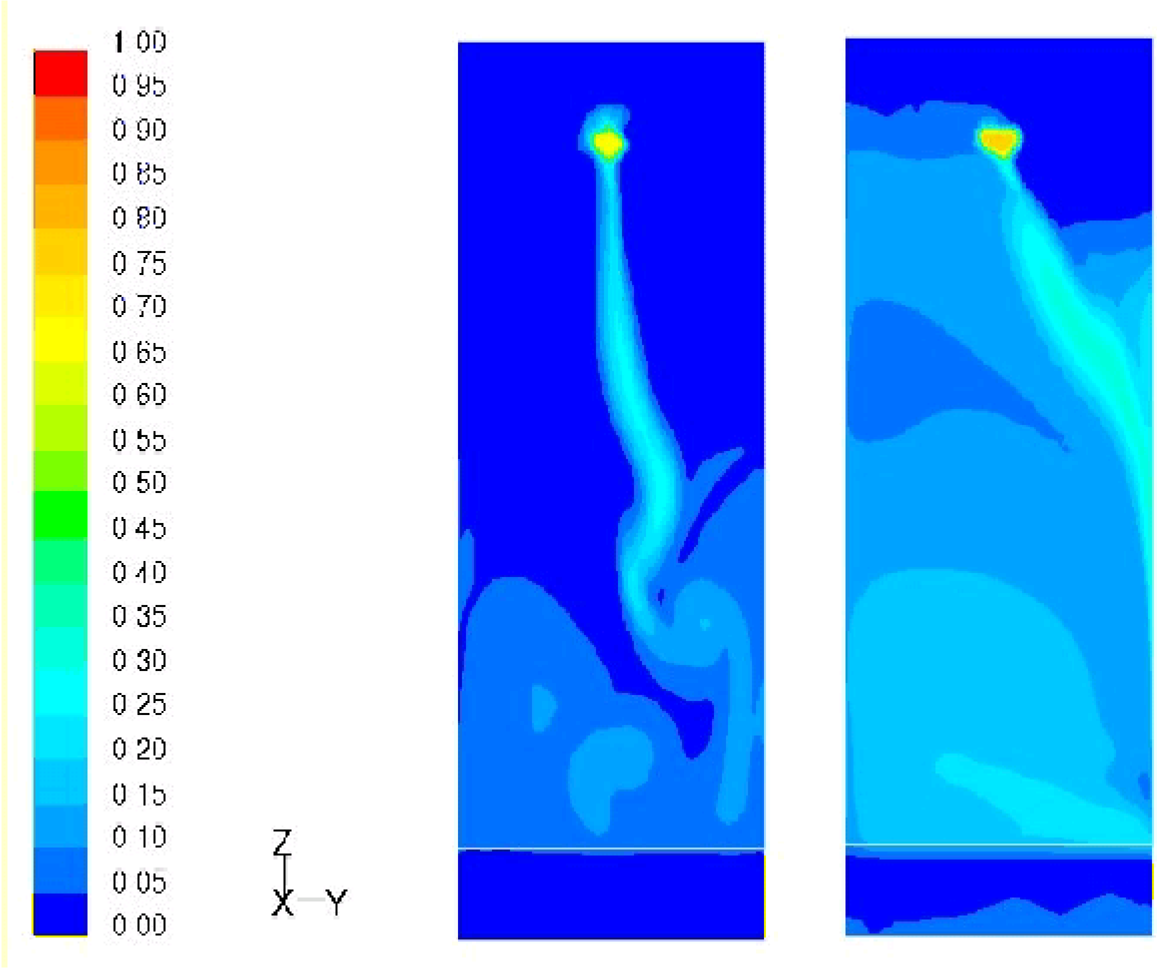

Fig. 6.5.2 Visualisation of mixing in the downcomer in the Fortum PTS test #10

Fig. 6.5.2 shows a visualization of the mixing pattern in the downcomer for the Fortum PTS test #10. It is a visualization of CFD results, which reproduce the mixing pattern observed in the experiment well. The left picture in Fig. 6.5.2 is qualitatively similar to Fig. 5.2.2 (right), where the ROCOM test with 5% of nominal flow rate and 10 % density difference is visualized. The downcomer Froude number for this test is 0.343, while it is 0.039 for the Fortum PTS test #10. A weakly mixed jet of water with higher density in the upper part of the downcomer and good mixing in the lower downcomer are seen. Later on, the asymmetric behaviour of the jet caused by recirculation in the downcomer sector is seen (right part of Fig. 6.5.2). The mixing pattern in the Fortum PTS test #21 is very similar to that of test #10 before the occurrence of asymmetry.

7 Conclusions

A new quality of research in turbulent mixing inside the RPV of nuclear reactors has been achieved in the frame of the work package 2 of the FLOMIX-R project. Experimental data on slug mixing with enhanced resolution in space and time have been gained from the ROCOM, Vattenfall, Gidropress and FORTUM PTS test facilities covering the geometry of various European reactor types and a wide range of flow conditions. Comprehensive analysis of measurement errors was performed, especially for the ROCOM and Vattenfall tests. Repeated realizations of the same experiments allow to estimate uncertainty bands of the measurement data. These uncertainty bands are mainly caused by turbulent fluctuations of the flow, the contribution of measurement errors is low. The measurements and uncertainty analysis are very valuable for the comparison with CFD results.

The basic understanding of momentum controlled mixing in turbulent flow and buoyancy affected mixing in the case of relevant density differences between the mixing fluids has been improved significantly. The impact of various parameters (pump start-up time, mass flow rate, position and size of the slug) on mixing in the case of a boron dilution transients with start-up of the first main coolant pump was investigated systematically. Scalability was considered with respect to application of the results for real reactors. While Reynolds and Strouhal scaling are relevant for momentum controlled slug mixing, Froude scaling can be applied to mixing affected by density differences. A clear criterion was found for transition between momentum controlled and buoyancy driven mixing. Measurement data on stratification and mixing in the case of cold ECC water injection were made available.

Therefore, the results of WP 2 are relevant for nuclear reactor safety issues, but also for physical understanding of turbulent mixing, and form a unique data base for the CFD code validation for turbulent mixing applications in nuclear reactor safety analysis.

Nomenclature

Abbrevation	**Unit**	**Meaning**
A	m^2	cross section
C, c	ppm; -	concentration
CAD	-	computer aided design
CFD	-	computational fluid dynamics
CL	-	cold leg
d	m	diameter
DC-l	-	lower downcomer (sensor)
DC-u	-	upper downcomer (sensor)
ECC		emergency core cooling
Fr	-	Froude number
FS	-	error amount
g	m/s^2	gravity constant
HPI	-	high pressure injection
L	m	length, flow path
LOCA	-	loss of coolant accident
LDV	-	laser Doppler velocitymeter
MCP	-	main coolant pump
min		minimum
n	-	number of values/positions
NPP		nuclear power plant
NV	-	Novo-Voronezh
p	-	calibration coefficient
PWR	-	pressurized water reactor
PTS	-	pre-stressed thermal shock
PVC	-	polyvinyl chloride
Q	m^3/h	volume flow rate
RCS	-	reactor coolant system
Re	-	Reynolds number
ROCOM	-	Rossendorf Coolant Mixing Model
RPV		reactor pressure vessel
s	-, m	standard deviation; height of the downcomer
s	g salt/ kg water	salinity

Sr	-	Strouhal number
t	s, °C	time, temperature
t_p	-	Student factor
U	mV	voltage
u_z	-	confidence interval
v	m^3	volume
$\dot{V}$	m^3/h	volume flow rate
VVER	-	Russian pressurized water reactor (water/water energetic reactor)
w	m/s	velocity
x	m	x-coordinate
y	m	y-coordinate
z	m	z-coordinate

greek

γ	$1/\Omega m$	conductivity
σ	S/cm;-	electrical conductivity; variance of the distribution
η	-	dimensionless time
ν	m^2/s	kinematic viscosity
Θ	-	dimensionless mixing scalar
ρ	Kg/m^3	density
τ	s	time

indexes

0	-	Initial
1; max	-	maximum
a	-	ambient
A	-	Loop A
av	-	average
b	-	Boron; borated
B	-	Loop B
c	-	cold
C	-	Loop C
cal	-	calculated

calib - calibration
discr - discretisation
fluct - fluctuation
h - hot
i - current position
in - inlet
m - model
meas - measured
r - real
sum - summation
u - unborated

8 References

[Ala95] F. Alavyoon, B. Hemström, N.G. Andersson, R.I. Karlsson (1995) Experimental and computational approach to investigating rapid boron dilution transients in PWRs. Report no. US 95:4, presented at the OECD Specialist Meeting on Boron Dilution Reactivity Transients, State Collage, PA, U.S.A., 18-20 October 1995

[And94] N.G. Andersson (1994), Vidareutveckling av konduktivitetsmätutrustning. Teoretisk genomgång av mätmetodik. Report no. VU-S 94:B12. Vattenfall Utveckling AB

[And95] N.G. Andersson, B. Hemström, R.I. Karlsson, S. Jacobson (1995), Physical modelling of a Rapid Boron Dilution Transient. Proceedings of Nureth 7, Saratoga Springs, USA

[Dra87] P. Dräger (1987), Macroscopic coolant mixing in pressurized water reactors (in German), PhD. Thesis, Technical Highschool Zittau (Germany), 106p.

[Flo04] Flomix-R (2004), Final Report on WP 4.

[Gru94] U. Grundmann; U. Rohde (1994), Investigations on a Boron Dilution Accident for a VVER-440 Type Reactor by the Help of the Code DYN3D, Proc. ANS Topical Meeting on Advances in Reactor Physics: Reactor Physics Faces the 21st Century, Knoxville (Tennessee), 11. - 15. April 1994, Vol. 3, pp. 464 – 471

[Hem94] B. Hemström, N.G. Andersson (1994), Physical modelling of a Rapid Boron Dilution Transient. The EDF Case. Report no. VU-S 94:B16. Vattenfall Utveckling AB

[Hem95] B. Hemström, N.G. Andersson (1995), Physical modelling of a Rapid Boron Dilution Transient. Reynolds number sensitivity study for the Ringhals Case. Report no. US 95:5, Vattenfall Utveckling AB

[Hem97] B. Hemström, N.G. Andersson (1997), Physical modelling of a Rapid Boron Dilution Transient. Study for the Ringhals Case, using a more complete model. Report no. US 97:20. Vattenfall Utveckling AB

[Hem04] B. Hemström (2004), Data sets of the slug mixing experiments at the Vattenfall test facility, EU/FP5 FLOMIX-R report, FLOMIX-R-D06, Vattenfall Utveckling AB, CDROM

[Her95] E. Hering, R. Martin und M. Stohrer (1995), Physikalisch-Technisches Taschenbuch, 2. Auflage, ISBN 3-18-401431-2, VDI-Verlag Düsseldorf

[Hoe98] T. Höhne (1998), Vergleich von Kühlmittelströmung und - vermischung in einem skalierten Modell des DWR KONVOI mit den Vorgängen im Originalreaktor, FZR-Report, FZR-210, 7S.

[Hoe99] T. Höhne, G. Grunwald, H.-M. Prasser (1999), Das 1:5 skalierte Vermischungsmodell des DWR Konvoi, Arbeitsbericht, FZR, 29 S.

[Kli03] S. Kliem, U. Rohde, T. Höhne (2003), Data sets of the 1/5-scale slug mixing experiments at ROCOM facility, EU/FP5 FLOMIX-R report, FLOMIX-R-D05, FZ Rossendorf, Germany, 47 p. + CDROM

[Kli04] S. Kliem, U. Rohde, F.-P. Weiß (2004), Core response of a PWR to a slug of under-borated water, Nucl. Eng. and Design 230, 121-132

[Roh02] U. Rohde, S. Kliem, T. Toppila, B. Hemström et al. (2002), Identification of mixing and flow distribution key phenomena, EU/FP5 FLOMIX-R report, FLOMIX-R-D02, FZ Rossendorf, Germany, 40 p.

[Tuo87] H. Tuomisto (1987), Thermal-hydraulics of the Loviisa reactor pressure vessel overcooling transients, Research report, Fortum, Finland

[Top04] T. Toppila (2004), FLOMIX-R, Work Package 4, CFD Code Benchmarking Based on the Mixing Experiments, Simulation of Fortum PTS Mixing Experiments Number 10, 20 and 21, Fortum Nuclear Services, report TERMO-343, August 2004.

[Uly98] V.N. Ulyanovsky, Yu.A. Bezrukov, S.A. Logvinov, L.A. Saly (1998), Study of mixing of flows with different boron concentration at the core inlet. Proc. Int. Conf. ”Thermophysical WWER safety aspects“. vol. 1, pp. 37 - 46,Obninsk, Russia

[Log00] S.A. Logvinov., V.N. Ulyanovsky, Yu.A. Bezrukov, A.N. Kozlov (2000), Mixing of coolant with different boron concentration at the VVER-1000 core inlet during RCP start-up. Proc. Ann. Mtg. Nucl. Techn. ‘00. Bonn, Germany

[Tin93] H. Tinoco, B. Hemström, N.G. Andersson (1993), Physical modelling of a Rapid Boron Dilution Transient. Report no. VU-S 93:B21. Vattenfall Utveckling AB

Appendix A. Supplementary information for the Vattenfall test facility

A.1 Error estimates for boron concentration measurements

In the measurements of boron concentration the following sources of inaccuracy have been identified.

- inaccuracy due to changes in probe characteristics during a test series.
- inaccuracy due to non-linearity in relationship between conductivity and salinity/temperature.
- inaccuracy due to uncertainty of conductivity of slug.
- inaccuracy due to uncertainty of conductivity of tap water.
- inaccuracy due the limited (five) number of tests.
- inaccuracy due to air bubbles present in the vicinity of the probes.
- inaccuracy due to long time constant of probes.

These sources of inaccuracy are discussed below.

A.1.1 Inaccuracy due to changes in probe characteristics during a test series

The probe constant defines the relationship between conductivity and measured voltage. During a test series the probe constant changes significantly, probably due to deposits, corrosion etc. The probe constant that is used is therefore calibrated based on measurements of conductivity for water with known conductivities before and after each test series of five tests. Tap water (flowing through the model) and salt water (injected into the model in the same way as when filling up the slug) were used. The true conductivity is measured for water leaving the model through a valve at the bottom of the lower plenum. The original probe constant is then linearly modified based on the average probe constant from these four measurements. This procedure also gives an upper bound of the inaccuracy for each probe, given that the probe constant changes linearly during the tests. This is exemplified in Fig. A.1.1, which gives the probe constant for each calibration test divided by the average probe constant, i.e. the one that is being used. This ratio should, of course, ideally be exactly equal to 1. Probes with a deviation of more than 5% for at least one of the calibrations were rejected, and not used in the evaluation of the results from the measurements of boron concentration during a transient.

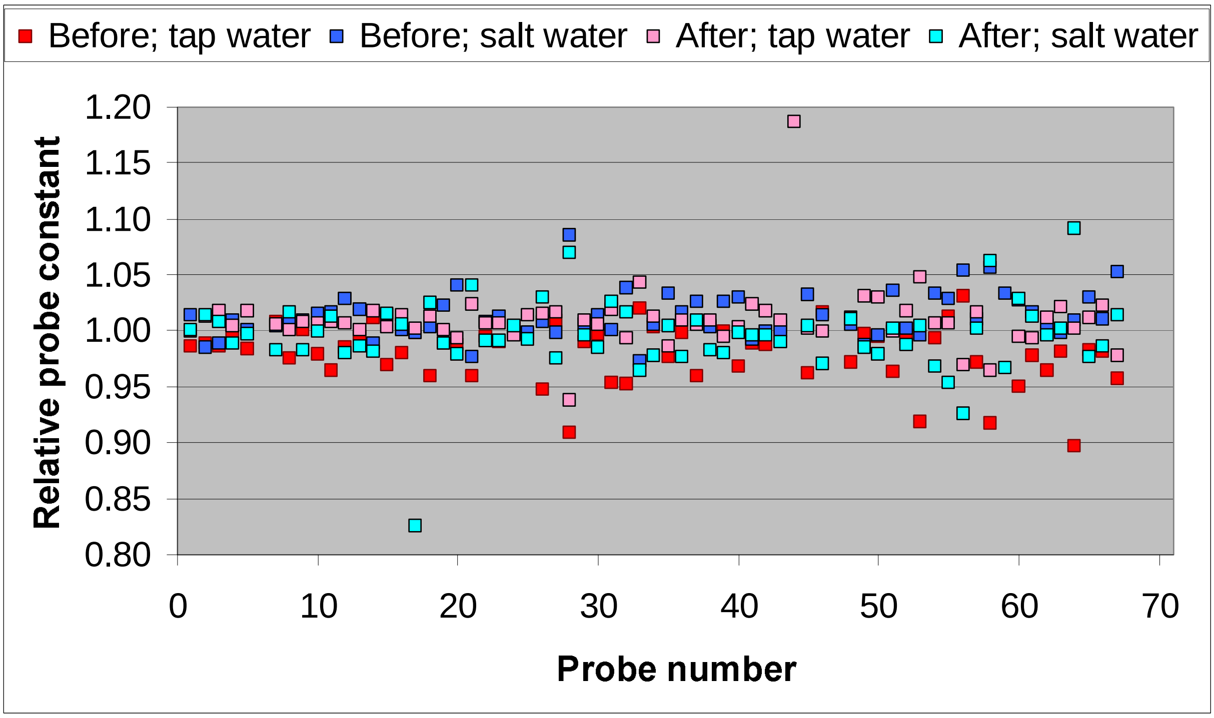

Fig. A.1.1 Probe constant for a calibration test divided by the average probe constant from all four calibration tests

Due to the continuous drift of the probe constant during the coarse of the project the relationship between conductivity and salinity became less and less linear and an increased number of probes had an inaccuracy in conductivity that was higher than 5%. The probe constant was during the coarse of the project in average changed with a factor of around 2. Fig. A.1.2 gives the percentage of probes rejected for each test series. Only very few of the rejected probes were however situated in regions where low boron concentrations were measured. To minimise the problems with non-linearity the salinity of the tap water was increased.

This inaccuracy, along with most other types of inaccuracies, differ with the salinities and temperatures used in the tests. In Tab. A.1 the temperatures and conductivities used for the test cases are shown. A typical value for this type of inaccuracy is 0.015 dimensionless boron concentration units.

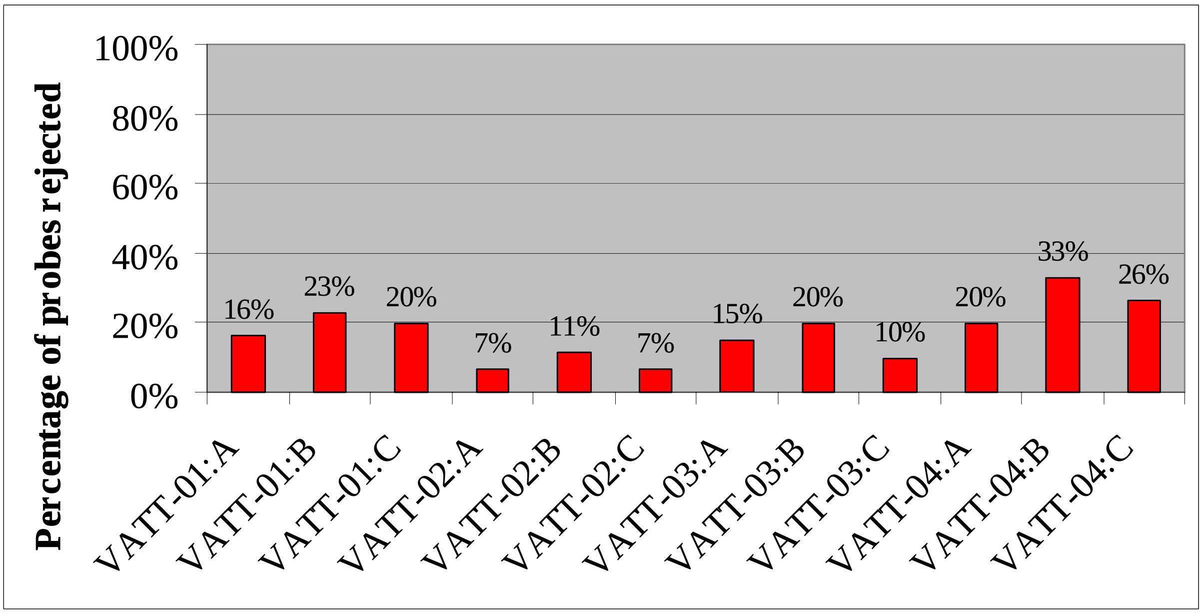

Fig. A.1.2 Percentage of rejected probes for all test series.

Tab. A.1 Temperatures and conductivities used for the test cases

Test case	**Temperature of slug (°C)**	**Temperature of tap-water (°C)**	**Conductivity of slug (1/Ωm)**	**Conductivity of tap-water (1/Ωm)**
VATT-01:A3	52.5	53.8	0.876	0.274
VATT-01:A4	52.4	54.1	0.875	0.281
VATT-01:A5	52.3	54.3	0.875	0.287
VATT-01:A6	52.2	54.3	0.876	0.293
VATT-01:A7	52.0	54.2	0.879	0.297
VATT-01:B2	50.8	51.5	0.812	0.281
VATT-01:B3	50.8	51.4	0.812	0.285
VATT-01:B4	50.8	51.3	0.863	0.289
VATT-01:B5	50.7	51.2	0.862	0.287
VATT-01:B6	50.6	51.1	0.816	0.291
VATT-01:C3	50.7	50.8	0.879	0.274
VATT-01:C4	50.6	50.7	0.879	0.279
VATT-01:C5	50.5	50.6	0.879	0.283
VATT-01:C6	50.5	50.6	0.874	0.287
VATT-01:C7	50.4	50.6	0.874	0.292

VATT-02:A3	51.7	51.6	0.789	0.100
VATT-02:A5	51.9	52.2	0.794	0.108
VATT-02:A7	51.5	52.5	0.790	0.111
VATT-02:A8	50.7	52.0	0.791	0.115
VATT-02:A9	50.0	51.4	0.791	0.132
VATT-02:B1	55.6	53.8	0.787	0.116
VATT-02:B3	55.0	54.1	0.777	0.121
VATT-02:B4	54.6	54.5	0.769	0.124
VATT-02:B5	54.2	54.7	0.764	0.127
VATT-02:B6	53.6	54.8	0.752	0.130
VATT-02:C2	54.1	54.5	0.763	0.101
VATT-02:C3	53.9	55.8	0.761	0.104
VATT-02:C4	53.8	56.0	0.759	0.107
VATT-02:C5	53.6	55.8	0.759	0.110
VATT-02:C6	53.4	55.7	0.757	0.114
VATT-03:A1	53.1	53.0	0.873	0.268
VATT-03:A2	53.0	53.0	0.869	0.270
VATT-03:A3	52.9	52.9	0.873	0.272
VATT-03:A4	52.9	52.8	0.871	0.273
VATT-03:A5	52.8	52.9	0.873	0.274
VATT-03:B1	55.0	56.4	0.755	0.283
VATT-03:B3	54.8	56.8	0.743	0.288
VATT-03:B4	54.7	56.7	0.743	0.289
VATT-03:B5	54.7	56.6	0.741	0.289
VATT-03:B7	54.6	56.5	0.733	0.291
VATT-03:C1	52.4	55.2	1.015	0.240
VATT-03:C4	52.3	55.9	0.995	0.249
VATT-03:C5	52.5	56.0	1.001	0.251
VATT-03:C6	53.3	56.0	1.013	0.253
VATT-03:C7	52.2	56.0	1.016	0.256
VATT-04:A2	51.5	51.8	0.951	0.344
VATT-04:A3	52.0	51.5	0.948	0.345
VATT-04:A4	52.4	51.4	0.956	0.348
VATT-04:A5	52.3	51.3	0.956	0.351

VATT-04:A6	52.1	51.3	0.959	0.353
VATT-04:B1	52.9	56.0	0.942	0.356
VATT-04:B3	53.3	56.4	0.946	0.364
VATT-04:B5	53.1	56.9	0.944	0.373
VATT-04:B6	53.0	57.2	0.945	0.377
VATT-04:B7	52.9	57.4	0.941	0.381
VATT-04:C1	49.2	50.1	0.934	0.304
VATT-04:C2	49.1	50.0	0.936	0.307
VATT-04:C5	49.1	49.8	0.944	0.316
VATT-04:C6	49.6	49.8	0.946	0.318

A.1.2 Inaccuracy due to non-linearity in relationship between conductivity and salt/temperature.

The dimensionless boron concentration is calculated assuming that conductivity is a linear function of salinity and temperature. This is not quite that case, as discussed in Chapter 3.3.2.1. A typical value for this type of inaccuracy is 0.010 dimensionless boron concentration units.

A.1.3 Inaccuracy due to uncertainty of conductivity of slug

The mean conductivity of the slug at t=0, which defines the conductivity corresponding to a dimensionless boron concentration of 0.0, is determined by using the maximum measured conductivities for one or two of the probes X.1 and X.2 in the inlet pipe. These are measured at the centre of the pipe, which of course does not give exactly the same conductivity as the average conductivity in the slug. There are for example some heat losses at the pipe walls during the time (approximately 3 minutes) between starting to fill up the slug and the start of the transient that will give a decreased temperature and consequently a decreased conductivity. This inaccuracy has not been possible to quantify. The inaccuracy is also a function of the inaccuracy of X.1 and X.2, given by the pre- and post-calibrations discussed above. This inaccuracy varies from test to test. A typical value for this type of inaccuracy is 0.010 dimensionless boron concentration units.

The conductivity of the slug, determined in the way described above, can also be compared with the conductivity of the water in the salt-water tank. The measured difference between the conductivity in the salt-water tank and the conductivity of X.1/X.2 varies between –0.04 and +0.04 1/Ωm.

A.1.4 Inaccuracy due to uncertainty of conductivity of tap water

The dimensionless boron concentration of 1.0 is defined as the measured average conductivity for each probe between t=3 seconds to t=4 seconds, i.e. before the slug has reached the probe. There are some small heat losses in the inlet pipe during the approximately 5 minutes of standstill before t=0 and also heat production from the pump during the last half minute before t=0. There are also heat losses at the walls of the model itself. These temperature changes will act as an equivalent of a change in slug volume. These inaccuracies are small and an upper bound for them in terms of boron concentration have not been possible to quantify.

A.1.5 Inaccuracy due the limited (five) number of tests

The inaccuracy due to the limited (five) number of tests can be estimated in the following way:

Based on measured values for corresponding times in the five tests a standard deviation (s) can be estimated. The confidence interval for a confidence of 95%, which is used here, is $2.776 \cdot s/\sqrt{5}=1.241 \cdot s$. This means that the probability that the true mean value, i.e. the mean value from an infinite number of tests, differs from the measured mean value from five tests with more than $1.241 \cdot s$ is approximately 5%. A typical value for this type of inaccuracy is 0.065 dimensionless boron concentration units.

A.1.6 Inaccuracy due to air bubbles appearing in the vicinity of the probes

If air bubbles occur at the tip of a probe the measured conductivity will decrease. It is of course not easy to judge if measured fluctuations in conductivity are due to air bubbles or low salinity. If the fluctuations are dominated by decreases in conductivity one can expect effects of air bubbles. Such disturbances exist for X.1 and X.2, for some of the tests. There are however very few such indications for the probes at the inlet to the core. It has not been possible to quantify this inaccuracy.

A.1.7 Inaccuracy due to long time constant of probes

When exposed to deposits, the time constant for the probes will increase. This was clearly seen from some of the tests. These tests were rejected and repeated using clean probes. From measurements of conductivity during emptying of the model, when the sinking water level passed by the probes, the probes have been shown to have a response time in the order of the sampling frequency of 60 Hz.

A.1.8 Examples of inaccuracies of measured boron concentrations

Tab. A.2, Tab. A.3 and Fig. A.1.3 below show examples of values of the different types of inaccuracies. The examples are taken from the positions where the lowest average boron concentration was measured for each test series. One can see that, for most tests, the dominating source of inaccuracy is due to too few tests performed for each test case. The average inaccuracy for these positions is 0.1 dimensionless boron concentration units. The maximum inaccuracy is 0.164 and the minimum inaccuracy 0.059.

Tab. A.2 Averages of inaccuracies for the probes presented in Tab. A.3

Type of inaccuracy	**Probe constant**	**Non-linearity**	**Slug conduc-tivity**	**Number of tests**	**Total**
Value of inaccuracy	0.014	0.010	0.011	0.065	0.100

Tab. A.3 Inaccuracies for selected positions

Test case	**Boron concen-tration**	**at probe**	**Probe con-stant**	**Non-linearity**	**Slug condu-ctivity**	**Number of tests**	**Total**
VATT-01:A3	0.347	4:8	0.022	0.011	0.023	0.018	0.074
VATT-01:A4	0.347	4:8	0.023	0.013	0.023	0.018	0.076
VATT-01:A5	0.347	4:8	0.023	0.014	0.024	0.018	0.078
VATT-01:A6	0.347	4:8	0.023	0.014	0.024	0.018	0.079
VATT-01:A7	0.347	4:8	0.023	0.014	0.024	0.018	0.079
VATT-01:B2	0.468	6:25	0.007	0.010	0.007	0.050	0.074
VATT-01:B3	0.468	6:25	0.008	0.009	0.007	0.050	0.074
VATT-01:B4	0.468	6:25	0.007	0.010	0.007	0.050	0.074
VATT-01:B5	0.468	6:25	0.007	0.010	0.007	0.050	0.074
VATT-01:B6	0.468	6:25	0.008	0.009	0.008	0.050	0.074
VATT-01:C3	0.518	4:19	0.006	0.009	0.002	0.057	0.074

VATT-01:C4	0.518	4:19	0.006	0.009	0.002	0.057	0.074
VATT-01:C5	0.518	4:19	0.006	0.009	0.002	0.057	0.074
VATT-01:C6	0.518	4:19	0.006	0.009	0.002	0.057	0.074
VATT-01:C7	0.518	4:19	0.006	0.009	0.002	0.057	0.074
VATT-02:A3	0.403	5:8	0.019	0.008	0.001	0.101	0.130
VATT-02:A5	0.403	5:8	0.020	0.009	0.001	0.101	0.131
VATT-02:A7	0.403	5:8	0.020	0.012	0.001	0.101	0.134
VATT-02:A8	0.403	5:8	0.020	0.013	0.001	0.101	0.135
VATT-02:A9	0.403	5:8	0.021	0.013	0.001	0.101	0.137
VATT-02:B1	0.621	6:25	0.016	0.002	0.000	0.080	0.098
VATT-02:B3	0.621	6:25	0.016	0.005	0.000	0.080	0.101
VATT-02:B4	0.621	6:25	0.017	0.007	0.000	0.080	0.104
VATT-02:B5	0.621	6:25	0.017	0.009	0.000	0.080	0.106
VATT-02:B6	0.621	6:25	0.017	0.011	0.000	0.080	0.108
VATT-02:C2	0.657	4:19	0.011	0.009	0.001	0.038	0.059
VATT-02:C3	0.657	4:19	0.011	0.013	0.001	0.038	0.064
VATT-02:C4	0.657	4:19	0.011	0.014	0.001	0.038	0.065
VATT-02:C5	0.657	4:19	0.011	0.014	0.001	0.038	0.065
VATT-02:C6	0.657	4:19	0.011	0.015	0.001	0.038	0.065
VATT-03:A1	0.696	5:7	0.011	0.006	0.011	0.062	0.091
VATT-03:A2	0.696	5:7	0.011	0.007	0.011	0.062	0.092
VATT-03:A3	0.696	5:7	0.011	0.007	0.011	0.062	0.092
VATT-03:A4	0.696	5:7	0.011	0.006	0.011	0.062	0.091
VATT-03:A5	0.696	5:7	0.011	0.007	0.011	0.062	0.092
VATT-03:B1	0.635	6:27	0.012	0.010	0.024	0.095	0.141
VATT-03:B3	0.635	6:27	0.012	0.012	0.025	0.095	0.144
VATT-03:B4	0.635	6:27	0.012	0.012	0.025	0.095	0.144
VATT-03:B5	0.635	6:27	0.012	0.012	0.025	0.095	0.144
VATT-03:B7	0.635	6:27	0.012	0.012	0.025	0.095	0.144
VATT-03:C1	0.749	5:24	0.016	0.015	0.010	0.119	0.160
VATT-03:C4	0.749	5:24	0.016	0.017	0.010	0.119	0.163
VATT-03:C5	0.749	5:24	0.016	0.017	0.010	0.119	0.162
VATT-03:C6	0.749	5:24	0.016	0.015	0.010	0.119	0.160
VATT-03:C7	0.749	5:24	0.016	0.018	0.010	0.119	0.164

VATT-04:A2	0.554	7:10	0.016	0.009	0.020	0.035	0.081
VATT-04:A3	0.554	7:10	0.016	0.007	0.020	0.035	0.078
VATT-04:A4	0.554	7:10	0.016	0.005	0.020	0.035	0.076
VATT-04:A5	0.554	7:10	0.016	0.005	0.021	0.035	0.077
VATT-04:A6	0.554	7:10	0.016	0.005	0.021	0.035	0.077
VATT-04:B1	0.542	6:25	0.014	0.019	0.007	0.065	0.105
VATT-04:B3	0.542	6:25	0.014	0.019	0.007	0.065	0.105
VATT-04:B5	0.542	6:25	0.014	0.021	0.007	0.065	0.108
VATT-04:B6	0.542	6:25	0.015	0.023	0.007	0.065	0.109
VATT-04:B7	0.542	6:25	0.015	0.024	0.007	0.065	0.111
VATT-04:C1	0.597	6:28	0.012	0.012	0.007	0.064	0.094
VATT-04:C2	0.597	6:28	0.012	0.012	0.007	0.064	0.094
VATT-04:C5	0.597	6:28	0.012	0.011	0.007	0.064	0.094
VATT-04:C6	0.597	6:28	0.012	0.009	0.007	0.064	0.092
VATT-04:C7	0.597	6:28	0.012	0.009	0.007	0.064	0.092

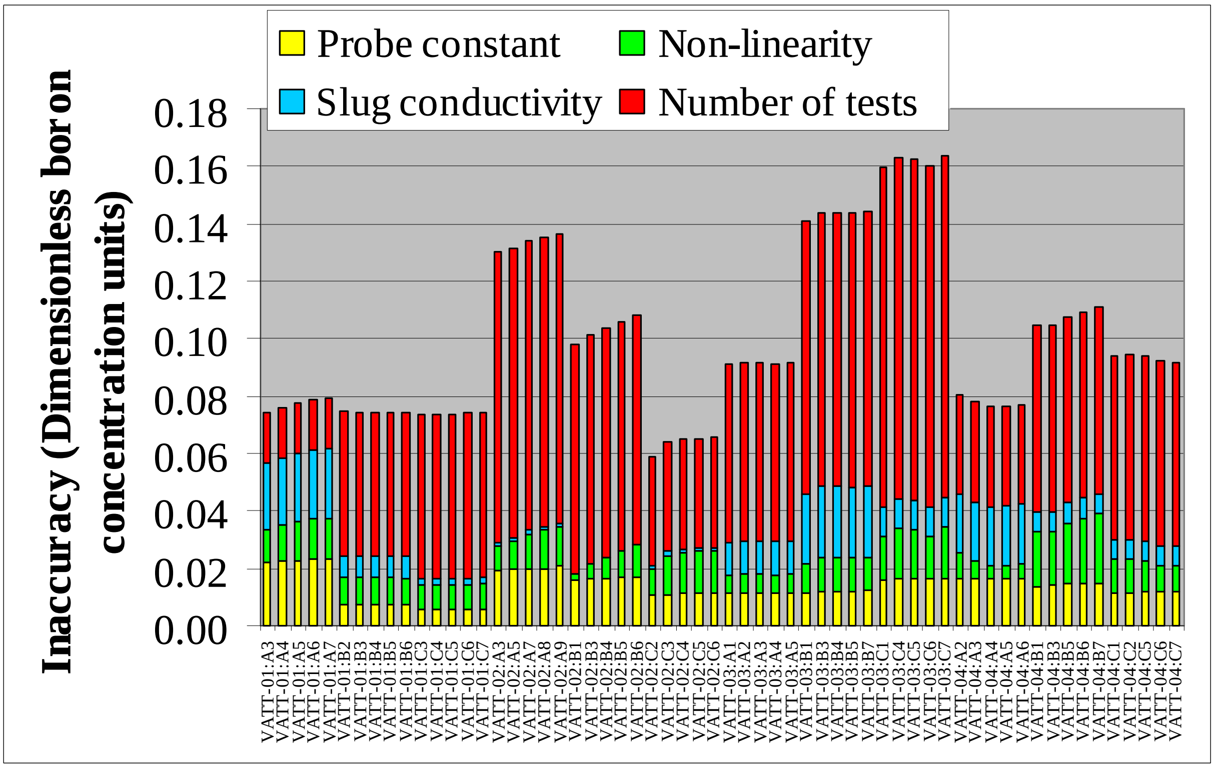

Fig. A.1.3 Inaccuracies for the probes presented in Tab. A.3

A.2 QUALITY CHECKS

A.2.1 Slug volume

Mass continuity of the slug can be checked based on the measured volume flow rate in the RCS pipe and in the idle loops and measured concentration at the core inlet and in the loops.

Fig. A.2.1 gives measured boron concentrations in the loops. Averages are made from the averages of the two probes at each loop. The positions of the probes are indicated in Fig. A.2.2. They are 2.4 m from the inlet to the secondary loops from the downcomer. The two probes are at the same axial position, both at the mid horizontal level and D/3 out from the pipe wall on either side.

For some of the tests one of the probes in a loop did not pass the quality criteria for accuracy and was therefore not used. The two probes in each loop do, however, give approximately the same boron concentration.

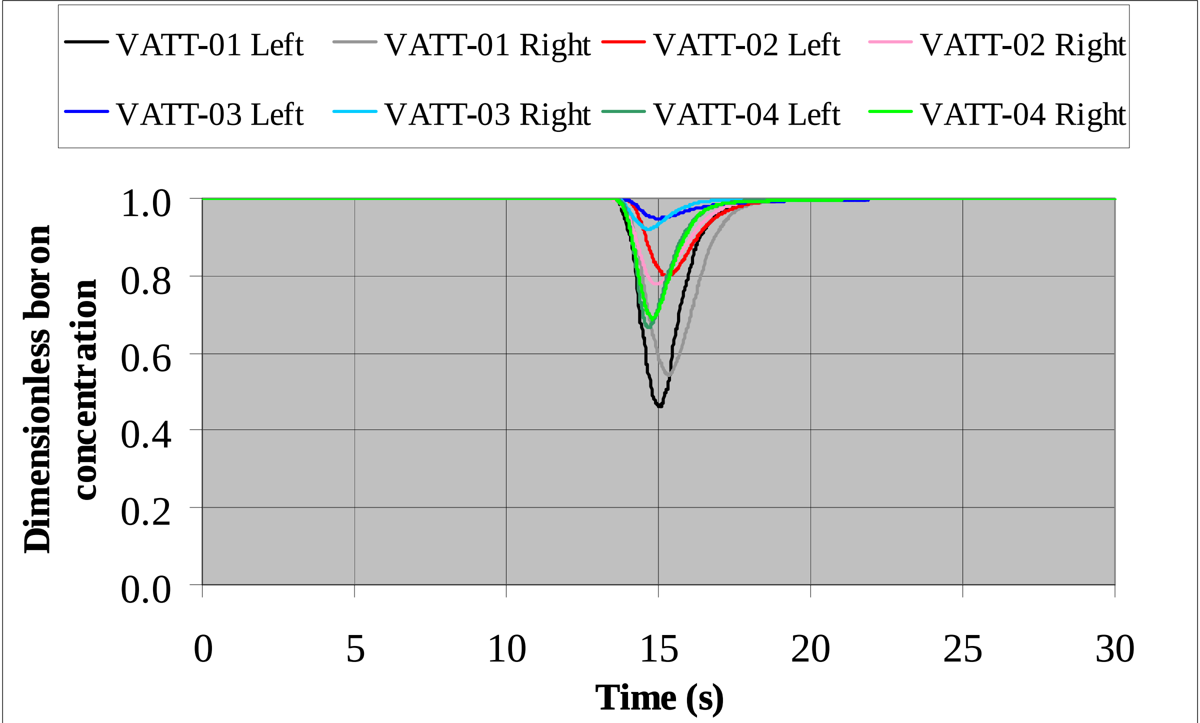

Fig. A.2.1 Boron concentration in loops

Tab. A.4 below shows measured and actual values of slug volumes for the four test cases. The calculated volume based on the measurements assumes that the velocity at the inlet to the core and in the loops are uniform over the respective areas and that the concentration measurements give good averages for the mean concentration for the respective areas. This assumption is not completely true. The measured slug volumes can therefore not be expected to be in exact agreement with the actual slug volume. The calculated differences are therefore considered to be acceptable.

Tab. A.4 Measured and actual values of slug volumes

	Actual slug volume m^3	**Measured volume**	**Measured/actual volume**
VATT-01	0.112	0.108	0.96
VATT-02	0.064	0.068	1.07
VATT-03	0.036	0.034	0.96
VATT-04	0.064	0.065	1.02

A.2.2 Boron concentration at position 0:1

The boron concentration at position 0:1, at the centre of the model at the core inlet, is present for all probe package positions. It is therefore measured 15 times for a test case, instead of only 5 times for the other positions. This leaves us with a possibility to check the repeatability for measurements of concentration at 0:1 and if there is any systematic error for the measurements for a specific probe package position. Fig. A.2.2 gives all measured average values for position 0:1.

One can see that the repeatability is quite satisfactory. The biggest variations are for VATT-04:B and VATT-01:C.

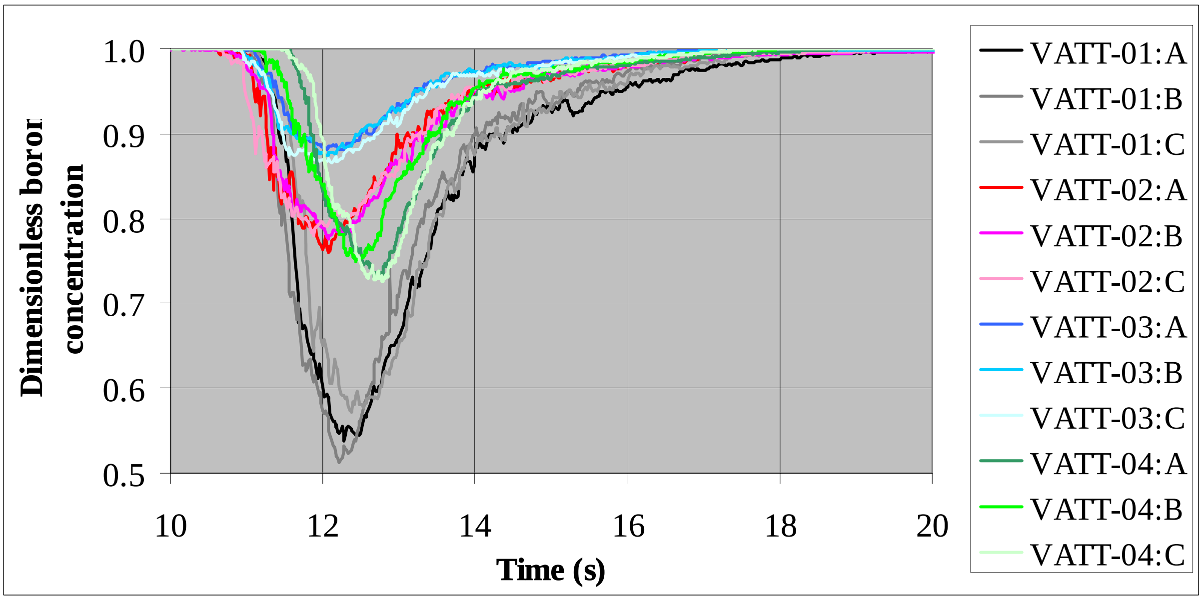

Fig. A.2.2 Average boron concentration at position 0:1

.

A.3 Description of MPG files of the visualisations

Description	**File name**
Local injections of dye during steady state flow.	FLOMIX-R_VATT-02_LOCAL_VIS1.MPG (from tangential position 0° to +90°) FLOMIX-R_VATT-02_LOCAL_VIS2.MPG (from tangential position +90° to +180°) FLOMIX-R_VATT-02_LOCAL_VIS3.MPG (from tangential position +180° to +270°) FLOMIX-R_VATT-02_LOCAL_VIS4.MPG (from tangential position +270° to 0°)
Local injections of dye during a VATT-02 transient.	FLOMIX-R_VATT-02_LOCAL_TRANS_VIS.MPEG
Visualisations of a coloured slug passing through the downcomer during a VATT-02 transient.	FLOMIX-R_VATT-02_SLUG_+35.MPG (Covering from -35° to +100°) FLOMIX-R_VATT-02_SLUG_+110.MPG (Covering from +45° to +180°) FLOMIX-R_VATT-02_SLUG_-160.MPG (Covering from +135° to -90°) FLOMIX-R_VATT-02_SLUG_-70.MPG (Covering from -140° to -5°) (+35, +110, -160 and –70 in the file names indicate tangential position for the camera, in degrees)
Laser sheet visualisations of a coloured slug passing through the downcomer during a VATT-02 transient.	FLOMIX-R_VATT-02_LASERSHEET_%&#.MPG (% = H for horizontal sheet, V for vertical sheet) (& = (only for horizontal sheets) L for lower level, M for middle level and U for upper level) (# = tangential position of the sheet (for vertical sheets) and tangential position of the camera (for horizontal sheets)) Coverage for horizontal sheets:

	# = +60 covers from +15° to +110° # = +150 covers from +105° to -165° # = -120 covers from -165° to -75° # = -30 covers from -75° to +15° All vertical sheets cover from approximately z=-1.1 m to z= -0.5 m, i.e. most of the visible part of the downcomer.
Visualisations of slug quality in inlet pipe during a VATT-02 transient.	FLOMIX-R_VATT-02_INLET_VIS.MPG

A.4 Coordinates for measured data

Name	Measured quantity	x (m)	y (m)	z (m)
6:15	boron concentration	-0.187	0.152	-1.134
5:12	boron concentration	-0.15	0.13	-1.134
4:10	boron concentration	-0.112	0.108	-1.134
3:7	boron concentration	-0.075	0.087	-1.134
2:5	boron concentration	-0.038	0.065	-1.134
1:2	boron concentration	0.000	0.043	-1.134
1:1	boron concentration	0.037	0.022	-1.134
8:8	boron concentration	-0.225	0.217	-1.134
7:14	boron concentration	-0.187	0.195	-1.134
6:14	boron concentration	-0.15	0.173	-1.134
5:11	boron concentration	-0.112	0.152	-1.134
4:9	boron concentration	-0.075	0.13	-1.134
3:6	boron concentration	-0.038	0.108	-1.134
2:4	boron concentration	0	0.087	-1.134
2:3	boron concentration	0.037	0.065	-1.134
2:2	boron concentration	0.075	0.043	-1.134
7:13	boron concentration	-0.15	0.217	-1.134
6:13	boron concentration	-0.113	0.195	-1.134
5:10	boron concentration	-0.075	0.173	-1.134
4:8	boron concentration	-0.038	0.152	-1.134
3:5	boron concentration	0	0.13	-1.134
3:4	boron concentration	0.037	0.108	-1.134
3:3	boron concentration	0.075	0.087	-1.134
3:2	boron concentration	0.112	0.065	-1.134
8:7	boron concentration	-0.15	0.26	-1.134
7:12	boron concentration	-0.113	0.238	-1.134
6:12	boron concentration	-0.075	0.217	-1.134
5:9	boron concentration	-0.038	0.195	-1.134
4:7	boron concentration	0	0.173	-1.134
4:6	boron concentration	0.037	0.152	-1.134
4:5	boron concentration	0.075	0.13	-1.134

4:4	boron concentration	0.112	0.108	-1.134
4:3	boron concentration	0.15	0.087	-1.134
8:4	boron concentration	0.15	0.26	-1.134
7:11	boron concentration	-0.075	0.26	-1.134
6:11	boron concentration	-0.038	0.238	-1.134
5:8	boron concentration	0	0.217	-1.134
5:7	boron concentration	0.037	0.195	-1.134
5:6	boron concentration	0.075	0.173	-1.134
5:5	boron concentration	0.112	0.152	-1.134
5:4	boron concentration	0.15	0.13	-1.134
5:3	boron concentration	0.187	0.108	-1.134
8:6	boron concentration	-0.075	0.303	-1.134
7:10	boron concentration	-0.038	0.281	-1.134
6:10	boron concentration	0	0.26	-1.134
6:9	boron concentration	0.037	0.238	-1.134
6:8	boron concentration	0.075	0.217	-1.134
6:7	boron concentration	0.112	0.195	-1.134
6:6	boron concentration	0.15	0.173	-1.134
6:5	boron concentration	0.187	0.152	-1.134
6:4	boron concentration	0.225	0.13	-1.134
7:9	boron concentration	0	0.303	-1.134
7:8	boron concentration	0.037	0.281	-1.134
7:7	boron concentration	0.075	0.26	-1.134
7:6	boron concentration	0.112	0.238	-1.134
7:5	boron concentration	0.15	0.217	-1.134
7:4	boron concentration	0.187	0.195	-1.134
7:3	boron concentration	0.262	0.152	-1.134
8:5	boron concentration	0.075	0.303	-1.134
8:3	boron concentration	0.225	0.217	-1.134
6:27	boron concentration	-0.038	-0.238	-1.134
5:22	boron concentration	-0.038	-0.195	-1.134
4:18	boron concentration	-0.038	-0.152	-1.134
3:13	boron concentration	-0.037	-0.108	-1.134
2:9	boron concentration	-0.037	-0.065	-1.134

1:4	boron concentration	-0.037	-0.022	-1.134
1:3	boron concentration	-0.038	0.022	-1.134
8:4	boron concentration	-0.075	-0.303	-1.134
7:26	boron concentration	-0.075	-0.26	-1.134
6:26	boron concentration	-0.075	-0.217	-1.134
5:21	boron concentration	-0.075	-0.173	-1.134
4:17	boron concentration	-0.075	-0.13	-1.134
3:12	boron concentration	-0.075	-0.087	-1.134
2:8	boron concentration	-0.075	-0.043	-1.134
2:7	boron concentration	-0.075	0	-1.134
2:6	boron concentration	-0.075	0.043	-1.134
7:25	boron concentration	-0.113	-0.238	-1.134
6:25	boron concentration	-0.113	-0.195	-1.134
5:20	boron concentration	-0.112	-0.152	-1.134
4:16	boron concentration	-0.112	-0.108	-1.134
3:11	boron concentration	-0.112	-0.065	-1.134
3:10	boron concentration	-0.112	-0.022	-1.134
3:9	boron concentration	-0.113	0.022	-1.134
3:8	boron concentration	-0.113	0.065	-1.134
8:13	boron concentration	-0.15	-0.26	-1.134
7:24	boron concentration	-0.15	-0.217	-1.134
6:24	boron concentration	-0.15	-0.173	-1.134
5:19	boron concentration	-0.15	-0.13	-1.134
4:15	boron concentration	-0.15	-0.087	-1.134
4:14	boron concentration	-0.15	-0.043	-1.134
4:13	boron concentration	-0.15	0	-1.134
4:12	boron concentration	-0.15	0.043	-1.134
4:11	boron concentration	-0.15	0.087	-1.134
8:10	boron concentration	-0.3	0	-1.134
7:23	boron concentration	-0.188	-0.195	-1.134
6:23	boron concentration	-0.187	-0.152	-1.134
5:18	boron concentration	-0.187	-0.108	-1.134
5:17	boron concentration	-0.187	-0.065	-1.134
5:16	boron concentration	-0.187	-0.022	-1.134

5:15	boron concentration	-0.187	0.022	-1.134
5:14	boron concentration	-0.188	0.065	-1.134
5:13	boron concentration	-0.188	0.108	-1.134
8:12	boron concentration	-0.225	-0.217	-1.134
7:22	boron concentration	-0.225	-0.173	-1.134
6:22	boron concentration	-0.225	-0.13	-1.134
6:21	boron concentration	-0.225	-0.087	-1.134
6:20	boron concentration	-0.225	-0.043	-1.134
6:19	boron concentration	-0.225	0	-1.134
6:18	boron concentration	-0.225	0.043	-1.134
6:17	boron concentration	-0.225	0.087	-1.134
6:16	boron concentration	-0.225	0.13	-1.134
7:21	boron concentration	-0.262	-0.152	-1.134
7:20	boron concentration	-0.262	-0.108	-1.134
7:19	boron concentration	-0.262	-0.065	-1.134
7:18	boron concentration	-0.262	-0.022	-1.134
7:17	boron concentration	-0.262	0.022	-1.134
7:16	boron concentration	-0.262	0.065	-1.134
7:15	boron concentration	-0.262	0.152	-1.134
8:11	boron concentration	-0.3	-0.087	-1.134
8:9	boron concentration	-0.3	0.087	-1.134
6:3	boron concentration	0.225	0.087	-1.134
5:2	boron concentration	0.188	0.065	-1.134
4:2	boron concentration	0.15	0.043	-1.134
3:1	boron concentration	0.112	0.022	-1.134
2:1	boron concentration	0.075	0	-1.134
1:6	boron concentration	0.038	-0.022	-1.134
1:5	boron concentration	0	-0.043	-1.134
8:2	boron concentration	0.3	0.087	-1.134
7:2	boron concentration	0.263	0.065	-1.134
6:2	boron concentration	0.225	0.043	-1.134
5:1	boron concentration	0.187	0.022	-1.134
4:1	boron concentration	0.15	0	-1.134
3:18	boron concentration	0.112	-0.022	-1.134

2:12	boron concentration	0.075	-0.043	-1.134
2:11	boron concentration	0.038	-0.065	-1.134
2:10	boron concentration	0	-0.087	-1.134
7:1	boron concentration	0.263	0.022	-1.134
6:1	boron concentration	0.225	0	-1.134
5:30	boron concentration	0.188	-0.022	-1.134
4:24	boron concentration	0.15	-0.043	-1.134
3:17	boron concentration	0.113	-0.065	-1.134
3:16	boron concentration	0.075	-0.087	-1.134
3:15	boron concentration	0.038	-0.108	-1.134
3:14	boron concentration	0	-0.13	-1.134
8:1	boron concentration	0.3	0	-1.134
7:36	boron concentration	0.263	-0.022	-1.134
6:36	boron concentration	0.225	-0.043	-1.134
5:29	boron concentration	0.188	-0.065	-1.134
4:23	boron concentration	0.15	-0.087	-1.134
4:22	boron concentration	0.113	-0.108	-1.134
4:21	boron concentration	0.075	-0.13	-1.134
4:20	boron concentration	0.038	-0.152	-1.134
4:19	boron concentration	0	-0.173	-1.134
8:16	boron concentration	0.15	-0.26	-1.134
7:35	boron concentration	0.263	-0.065	-1.134
6:35	boron concentration	0.225	-0.087	-1.134
5:28	boron concentration	0.188	-0.108	-1.134
5:27	boron concentration	0.15	-0.13	-1.134
5:26	boron concentration	0.113	-0.152	-1.134
5:25	boron concentration	0.075	-0.173	-1.134
5:24	boron concentration	0.038	-0.195	-1.134
5:23	boron concentration	0	-0.216	-1.134
8:18	boron concentration	0.3	-0.087	-1.134
7:34	boron concentration	0.263	-0.108	-1.134
6:34	boron concentration	0.225	-0.13	-1.134
6:33	boron concentration	0.188	-0.152	-1.134
6:32	boron concentration	0.15	-0.173	-1.134

6:31	boron concentration	0.113	-0.195	-1.134
6:30	boron concentration	0.075	-0.217	-1.134
6:29	boron concentration	0.038	-0.238	-1.134
6:28	boron concentration	0	-0.26	-1.134
7:33	boron concentration	0.262	-0.152	-1.134
7:32	boron concentration	0.225	-0.173	-1.134
7:31	boron concentration	0.188	-0.195	-1.134
7:30	boron concentration	0.15	-0.216	-1.134
7:29	boron concentration	0.113	-0.238	-1.134
7:28	boron concentration	0.075	-0.26	-1.134
7:27	boron concentration	0	-0.303	-1.134
8:17	boron concentration	0.225	-0.216	-1.134
8:15	boron concentration	0.075	-0.303	-1.134
0:1	boron concentration	0	0	-1.134
P1L1	velocities	0.34	0.196	-1.033
P1L2	velocities	0.331	0.191	-1.033
P1L3	velocities	0.323	0.186	-1.033
P1L4	velocities	0.314	0.181	-1.033
P2L1	velocities	0	0.393	-1.033
P2L2	velocities	0	0.383	-1.033
P2L3	velocities	0	0.373	-1.033
P3L1	velocities	-0.34	0.196	-1.033
P3L2	velocities	-0.331	0.191	-1.033
P3L3	velocities	-0.323	0.186	-1.033
P3L4	velocities	-0.314	0.181	-1.033
P4L1	velocities	-0.34	-0.196	-1.033
P4L2	velocities	-0.331	-0.191	-1.033
P4L3	velocities	-0.323	-0.186	-1.033
P4L4	velocities	-0.314	-0.181	-1.033
P5L1	velocities	0	-0.393	-1.033
P5L2	velocities	0	-0.383	-1.033
P5L3	velocities	0	-0.373	-1.033
P6L1	velocities	0.34	-0.196	-1.033
P6L2	velocities	0.331	-0.191	-1.033

P6L3	velocities	0.323	-0.186	-1.033
P6L4	velocities	0.314	-0.181	-1.033
P1U1	velocities	0.34	0.196	-0.773
P1U2	velocities	0.331	0.191	-0.773
P1U3	velocities	0.323	0.186	-0.773
P1U4	velocities	0.314	0.181	-0.773
P2U1	velocities	0	0.393	-0.773
P2U2	velocities	0	0.383	-0.773
P2U3	velocities	0	0.373	-0.773
P3U1	velocities	-0.34	0.196	-0.773
P3U2	velocities	-0.331	0.191	-0.773
P3U3	velocities	-0.323	0.186	-0.773
P3U4	velocities	-0.314	0.181	-0.773
P4U1	velocities	-0.34	-0.196	-0.773
P4U2	velocities	-0.331	-0.191	-0.773
P4U3	velocities	-0.323	-0.186	-0.773
P4U4	velocities	-0.314	-0.181	-0.773
P5U1	velocities	0	-0.393	-0.773
P5U2	velocities	0	-0.383	-0.773
P5U3	velocities	0	-0.373	-0.773
P6U1	velocities	0.34	-0.196	-0.773
P6U2	velocities	0.331	-0.191	-0.773
P6U3	velocities	0.323	-0.186	-0.773
P6U4	velocities	0.314	-0.181	-0.773